

REPORT DOCUMENTATION PAGE				Form Approved OMB No. 0704-0188	
Public reporting burden for this collection of information is estimated to average 1 hour per response, including the time for reviewing instructions, searching existing data sources, gathering and maintaining the data needed, and completing and reviewing this collection of information. Send comments regarding this burden estimate or any other aspect of this collection of information, including suggestions for reducing this burden to Department of Defense, Washington Headquarters Services, Directorate for Information Operations and Reports (0704-0188), 1215 Jefferson Davis Highway, Suite 1204, Arlington, VA 22202-4302. Respondents should be aware that notwithstanding any other provision of law, no person shall be subject to any penalty for failing to comply with a collection of information if it does not display a currently valid OMB control number. PLEASE DO NOT RETURN YOUR FORM TO THE ABOVE ADDRESS.					
1. REPORT DATE (DD-MM-YYYY) 20-05-2009		2. REPORT TYPE Dissertation		3. DATES COVERED (From - To)	
4. TITLE AND SUBTITLE Acoustic Excitation of Liquid Fuel Droplets and Coaxial Jets				5a. CONTRACT NUMBER	
				5b. GRANT NUMBER	
				5c. PROGRAM ELEMENT NUMBER	
6. AUTHOR(S) Juan I. Rodriguez (AFRL/RZSA)				5d. PROJECT NUMBER	
				5f. WORK UNIT NUMBER 23080533	
7. PERFORMING ORGANIZATION NAME(S) AND ADDRESS(ES) Air Force Research Laboratory (AFMC) AFRL/RZSA 10 E. Saturn Blvd. Edwards AFB CA 93524-7680				8. PERFORMING ORGANIZATION REPORT NUMBER AFRL-RZ-ED-TP-2009-205	
9. SPONSORING / MONITORING AGENCY NAME(S) AND ADDRESS(ES) Air Force Research Laboratory (AFMC) AFRL/RZS 5 Pollux Drive Edwards AFB CA 93524-7048				10. SPONSOR/MONITOR'S ACRONYM(S)	
				11. SPONSOR/MONITOR'S NUMBER(S) AFRL-RZ-ED-TP-2009-205	
12. DISTRIBUTION / AVAILABILITY STATEMENT Approved for public release; distribution unlimited (PA #09224).					
13. SUPPLEMENTARY NOTES PhD dissertation final defense for submission to UCLA, Los Angeles, CA.					
14. ABSTRACT This experimental study focuses on two important problems relevant to acoustic coupling with condensed phase transport processes, with special relevance to liquid rocket engine and airbreathing engine combustion instabilities. The first part of this dissertation describes droplet combustion characteristics of various fuels during exposure to external acoustical perturbations. Methanol, ethanol, a liquid synthetic fuel derived from coal gasification via the Fischer-Tropsch process, and a blend of aviation fuel and the synthetic fuel are used. The second part of this work consists of an experimental study on coaxial jet behavior with direct applications to flow mixing and unstable behavior characterization in liquid rocket engines. The experiments span a range of outer to inner jet momentum flux ratios from 0.013 to 23, and explore subcritical, nearcritical and supercritical pressure conditions, with and without acoustic excitation, for two injector geometries.					
15. SUBJECT TERMS					
16. SECURITY CLASSIFICATION OF:			17. LIMITATION OF ABSTRACT	18. NUMBER OF PAGES	19a. NAME OF RESPONSIBLE PERSON
a. REPORT	b. ABSTRACT	c. THIS PAGE			19b. TELEPHONE NUMBER (include area code)
Unclassified	Unclassified	Unclassified	SAR	271	N/A

UNIVERSITY OF CALIFORNIA

Los Angeles

Acoustic Excitation of Liquid Fuel Droplets and Coaxial Jets

A dissertation submitted in partial satisfaction
of the requirements for the degree
Doctor of Philosophy in Aerospace Engineering

by

Juan Ignacio Rodriguez

2009

© Copyright by
Juan Ignacio Rodriguez
2009

Distribution A: Approved for public release; distribution unlimited

The dissertation of Juan Ignacio Rodriguez is approved.

Stanley J. Osher

Jeff D. Eldredge

Ivett A. Leyva

Owen I. Smith, Committee Co-chair

Ann R. Karagozian, Committee Co-chair

University of California, Los Angeles

2009

A mis padres

TABLE OF CONTENTS

1. Introduction.....	1
<i>1.1 Acoustically Coupled Droplet Combustion</i>	<i>2</i>
1.1.1 Burning of Spherical and Non-spherical Fuel Droplets.....	2
1.1.2 Acoustic Excitation Effects on Condensed Phase Combustion	3
1.1.3 Alternative Fuels	6
<i>1.2 Acoustic Driving of Coaxial Jets.....</i>	<i>8</i>
1.2.1 Basic Flow Configuration.....	8
1.2.2 Motivations and Objectives of Coaxial Jet Study	10
1.2.3 Previous Work on Coaxial Jets.....	14
1.2.4 Dark Core Length	17
1.2.5 Shear Layers and Spreading Angles	20
1.2.6 Stability Analysis of the Coaxial Jet.....	22
<i>1.3 Present Studies.....</i>	<i>25</i>
1.3.1 Droplet Combustion Experiment	25
1.3.2 Coaxial Jet Experiment.....	26
2. Experimental Setup – Acoustically Coupled Fuel Droplet Combustion	35
<i>2.1 Acoustic Waveguide</i>	<i>35</i>
<i>2.2 Droplet Generation</i>	<i>37</i>
<i>2.3 Measurement Methods</i>	<i>38</i>
<i>2.4 Experimental Procedure</i>	<i>39</i>
<i>2.5 Uncertainty Analysis</i>	<i>41</i>

3. Results – Acoustically Coupled Fuel Droplet Combustion.....	44
3.1 Baseline Burning Rate Constants.....	44
3.2 Burning Rate Constants under Acoustic Excitation	45
3.3 Pressure Node Location Offset	47
3.4 Relation between Acoustic Acceleration and Burning Rate Increase	50
3.5 Fuel Extinction Studies	54
4. Experimental Setup – Acoustically Excited Coaxial Jet.....	70
4.1 Cryogenic Supercritical Chamber and Coaxial Jet Facility	70
4.2 Original and New Injectors.....	74
4.3 Measurement Methods	75
4.4 Uncertainty Analysis	80
5. Results – Acoustically Excited Coaxial Jet	90
5.1 Quantification of Dark Core Length and Inner and Outer Jet Spreading Angles.....	90
5.1.1 Dark Core Length	90
5.1.2 Inner Jet Spreading Angles	92
5.1.3 Outer Jet Spreading Angles	94
5.2 Results with the Original Coaxial Jet Injector Geometry	95
5.2.1 Behavior in the Absence of Acoustic Excitation	95
5.2.2 Dark Core Length Results in the Absence of Acoustic Excitation	100
5.2.3 Inner Jet Spreading Angle Results in the Absence of Acoustic Excitation	104
5.2.4 Outer Jet Spreading Angle Results in the Absence of Acoustic Excitation	107
5.2.5 Acoustic Field in the Test Chamber	110
5.2.6 Behavior during Exposure to Acoustic Excitation	117

5.2.7	Dark Core Length Results in the Presence of Acoustic Excitation.....	122
5.2.8	Spreading Angle Results in the Presence of Acoustic Excitation.....	129
5.3	<i>Results with the New Coaxial Jet Injector Geometry.....</i>	<i>134</i>
5.3.1	Behavior with and without Acoustic Excitation	135
5.3.2	Dark Core Length Results with and without Acoustic Excitation	142
5.3.3	Spreading Angle Results with and without Acoustic Excitation	149
5.4	<i>Stability of Coaxial Jet Flows</i>	<i>152</i>
6.	Conclusions and Future Work.....	190
6.1	<i>Acoustically Coupled Droplet Combustion.....</i>	<i>190</i>
6.2	<i>Acoustic Driving of Coaxial Jets.....</i>	<i>192</i>
6.2.1	Summary and Conclusions	192
6.2.2	Future Work	196
A.	Detailed Schematic of Coaxial Jet Experimental Facility	199
B.	Coaxial Jet Experimental Procedures.....	205
C.	Summary of Coaxial Jet Experimental Data.....	227

LIST OF FIGURES

Figure 1.1. In microgravity, effect of sound pressure level, SPL, on the mean burning rate constant K normalized by its mean value in the absence of acoustic excitation, K_{unf} , (a) at a pressure antinode, PAN, and (b) at a pressure node, PN. From Dattarajan (14).	28
Figure 1.2. In normal gravity, effect of sound pressure level, SPL, on the mean burning rate constant K normalized by its mean value in the absence of acoustic excitation, K_{unf} , (a) at a pressure antinode, PAN, and (b) at a pressure node, PN. From Dattarajan (14).	29
Figure 1.3. Photographs of a burning droplet in microgravity (a) with no forcing and (b) forced at a pressure node at 770 Hz; and in normal gravity (c) with no forcing and (d) with forcing at a pressure node at 770 Hz. From Dattarajan (14).	30
Figure 1.4. Schematic of coaxial jet flow.	31
Figure 1.5. Schematic of a 2D shear layer spreading angle.	31
Figure 1.6. Schematic of the dark core region and the inner jet spreading angle of a shear coaxial jet.	32
Figure 1.7. Consecutive frames from high-speed shadowgraph movies with the acoustic driver turned off (in rows 1, 3 and 5) and on (in rows 2, 4, and 6) at $\sim 3\text{kHz}$. Time increases from left to right with an interval of $55.6\ \mu\text{s}$ between frames. The first two rows are at a subcritical chamber pressure ($\sim 1.5\ \text{MPa}$), the third and fourth rows are at a near-critical chamber pressure ($\sim 3.5\ \text{MPa}$), and the fifth and sixth rows are	

at a supercritical chamber pressure (~ 4.9 MPa). The light gray lines in the first and second rows connect fluid structures as they evolve in time. Images from Davis and Chehroudi (21).....	33
Figure 1.8. Comparison of dark-core length measurements by Davis and Chehroudi (21) with all other data available in the literature of core-length vs. momentum flux ratio. Amongst the data reported by others, Eroglu, et al., Englebert, et al., and Woodward are two-phase flows and the rest are single phase. The references for the data are found in Table 1 of Ref. (21).	34
Figure 2.1. Experimental setup of the acoustic waveguide and feed droplet system. The tank and microvalve arrangement was used for the tests with methanol, while the syringe pump was used for all other fuels.	42
Figure 2.2. Acoustic characterization of the waveguide as measured by pressure transducers at P1 and P2. From Dattarajan (14). The distance between the speaker and reflector was 62 cm.	43
Figure 2.3. Photograph of a burning fuel droplet showing standoff distance ($d_{standoff}$) and velocity perturbation (u') used to obtain strain rate estimates of the droplet at extinction.....	43
Figure 3.1. Photographs of fuel droplets burning in the absence of acoustic excitation. Backlighting accounts for the light portion of the background observed outside of the flame.....	57
Figure 3.2. Photographs of various fuel droplets burning during acoustic excitation, situated at or near the waveguide center for the “original” locations of the speaker and reflector, based on a measured maximum in P2/P1. Acoustic excitation corresponded to 780 Hz with an amplitude of	

138.6 dB for ethanol, the pure F-T, and the JP-8/F-T fuel blend, and
 140.2 dB for methanol..... 57

Figure 3.3. Location of the pressure node relative to the droplet (y) and the droplet relative to the pressure node (y'), based on positioning of the speaker and reflector (S&R). (a) $y = 0$ and $y' = 0$, (b) $y > 0$ and $y' < 0$, where S&R move to the right, and (c) $y < 0$ and $y' > 0$, where S&R move to the left. From Dattarajan (14)..... 58

Figure 3.4. Photographs of a burning ethanol droplet with acoustic excitation at 780 Hz (PN) and 138.6 dB. The distances to which the speaker and reflector (S&R) have been moved, relative to their original locations, are indicated. 59

Figure 3.5. Photographs of a burning methanol droplet with acoustic excitation at 540 Hz (PAN) and 139.9 dB. The distances to which the speaker and reflector (S&R) have been moved, relative to their original locations, are indicated. 60

Figure 3.6. Photographs of a burning JP-8/FT fuel droplet with acoustic excitation at 785 Hz (PN) and 138.6 dB. The distances to which the speaker and reflector (S&R) have been moved, relative to their original locations, are indicated. 61

Figure 3.7. For ethanol, measured values of K and d_{eqvs} , and estimated absolute value of g_a as a function of the displacement of the speaker and reflector relative to their original positions, for a 780 Hz PN. The solid line on the K plot represents a fit of the experimental data points, while the solid line on the g_a plot represents the theoretical variation in g_a assuming an average SPL of 138.6 dB. The data points for g_a represent absolute values estimated from the locally measured SPL value. 62

Figure 3.8. For methanol, measured values of K and d_{eqvs} , and estimated absolute value of g_a as a function of the displacement of the speaker and reflector relative to their original positions, for a 540 Hz PAN. The solid line on the K plot represents a fit of the experimental data points, while the solid line on the g_a plot represents the theoretical variation in g_a assuming an average SPL of 139.9 dB. The data points for g_a represent absolute values estimated from the locally measured SPL value. 63

Figure 3.9. For JP-8/F-T fuel, measured values of K and d_{eqvs} , and estimated absolute value of g_a as a function of the displacement of the speaker and reflector relative to their original positions, for a 785 Hz PN. The solid line on the K plot represents a fit of the experimental data points, while the solid line on the g_a plot represents the theoretical variation in g_a assuming an average SPL of 138.6 dB. The data points for g_a represent absolute values estimated from the locally measured SPL value. 64

Figure 3.10. For ethanol, measured values of K and d_{eqvs} , and estimated absolute value of g_a as a function of the displacement of the speaker and reflector relative to their original positions, for a 540 Hz PAN. The solid line on the K plot represents a fit of the experimental data points, while the solid line on the g_a plot represents the theoretical variation in g_a assuming an average SPL of 138.8 dB. The data points for g_a represent absolute values estimated from the locally measured SPL value. 65

Figure 3.11. For ethanol, measured values of K and d_{eqvs} , and estimated absolute value of g_a as a function of the displacement of the speaker and reflector relative to their original positions, for a 290 Hz PN. The solid line on the K plot represents a fit of the experimental data points,

while the solid line on the g_a plot represents the theoretical variation in g_a assuming an average SPL of 137.8 dB. The data points for g_a represent absolute values estimated from the locally measured SPL value. 66

Figure 3.12. For ethanol, measured values of K and d_{eqvs} , and estimated absolute value of g_a as a function of the displacement of the speaker and reflector relative to their original positions, for a 800 Hz PN. The solid line on the K plot represents a fit of the experimental data points, while the solid line on the g_a plot represents the theoretical variation in g_a assuming an average SPL of 138.5 dB. The data points for g_a represent absolute values estimated from the locally measured SPL value. 67

Figure 3.13. Consecutive photographs showing the extinction process of a pure F-T fuel droplet. Images (a) and (b) show the flame before extinction, image (c) shows a “wake” flame and image (d) shows a flameless droplet. The time interval between images is 33.37 ms, with forcing at 141.1 dB or a perturbation pressure of 228 Pa, and maximum velocity perturbation of 0.79 m/s. 68

Figure 3.14. Consecutive photographs showing the extinction process of a JP-8/F-T fuel droplet. Images (a) and (b) show the flame before extinction, image (c) shows a “wake” flame and image (d) shows a flameless droplet. The time interval between images is 33.37 ms, with forcing at 141.3 dB or a perturbation pressure of 233 Pa, and maximum velocity perturbation of 0.82 m/s. 68

Figure 3.15. Consecutive photographs showing the extinction process of an ethanol droplet. Images (a) and (b) show the flame before extinction, images (c) and (d) show a flameless droplet. The time interval between

images is 33.37 ms, with forcing at 142.2 dB or a perturbation pressure of 257 Pa, and maximum velocity perturbation of 0.90 m/s..... 69

Figure 3.16. Consecutive photographs showing the extinction process of a methanol droplet. Images (a) and (b) show the flame before extinction, image (c) shows a “wake” flame and image (d) shows a flameless droplet. The time interval between images is 33.37 ms, with forcing at 143.3 dB or a perturbation pressure of 292 Pa, and maximum velocity perturbation of 1.0 m/s. 69

Figure 4.1. Experimental test chamber and supporting systems of the Experimental Cell 4 at AFRL, Edwards AFB, CA. 84

Figure 4.2. Chamber section view of the flow schematic for Experimental Cell 4 with the upgrades for the new coaxial injector. For a complete schematic refer to Appendix A..... 84

Figure 4.3. Photograph of the inner chamber within the test chamber in EC 4..... 85

Figure 4.4. (a) First (“original”) coaxial injector used in this study. (b) Exit plane view of the original coaxial injector..... 85

Figure 4.5. (a) Second (“new”) coaxial injector used in this study. (b) Exit plane view of the new coaxial injector. 86

Figure 4.6. Thermocouple and pressure transducer probes near the exit of the coaxial injector. 86

Figure 4.7. (a) Linear positioning stages that moved perpendicular to the vertical axis. (b) Larger view of the positioning stages and the thermocouple and pressure probe they support. 87

Figure 4.8. (a) Diagonal view of the mechanical stage used to move the thermocouple in the vertical direction inside the main chamber. (b) View of the mechanical stage from above. The bottom of the test chamber can be seen in the upper part of the image.	87
Figure 4.9. High speed camera used in this study.....	88
Figure 4.10. Simplified diagram of the two acoustic drivers at a 0° and 180° phase angle, indicating relative flow perturbation directions.....	88
Figure 4.11. (a) One of two piezo-siren elements used to produce the acoustic field for this study. (b) Waveguide used to transmit the acoustic waves from the piezo-siren to the inner chamber.....	89
Figure 5.1. (a) Raw image from high-speed camera. (b) Dark core boundary extracted from the raw image using the image processing routine. (c) Black and white image after image processing threshold had been applied. (d) Schematic of the left and right contours used in this study to obtain inner jet spreading angles.	156
Figure 5.2. Left and right angles derived using the maximum displacement of the dark core region at each row over a sample of 998 images.	156
Figure 5.3. Image showing how outer jet spreading angles are measured.	157
Figure 5.4. Collection of coaxial jet images without acoustic forcing at subcritical pressure from lowest to highest J. Original injector geometry.	157
Figure 5.5. Collection of coaxial jet images without acoustic forcing at nearcritical pressure from lowest to highest J. Original injector geometry.	158
Figure 5.6. Collection of coaxial jet images without acoustic forcing at supercritical pressure from lowest to highest J. Original injector geometry.	158

Figure 5.7. Dark core length normalized by the inner jet post inner diameter, L/D_1 , for the subcritical pressure regime. The results shown are for all the cases studied with the original injector geometry.	159
Figure 5.8. Dark core length normalized by the inner jet post inner diameter, L/D_1 , for the nearcritical pressure regime. The results shown are for all the cases studied with the original injector geometry.	159
Figure 5.9. Dark core length normalized by the inner jet post inner diameter, L/D_1 for the supercritical pressure regime. The results shown are for all the cases studied with the original injector geometry.	160
Figure 5.10. Dark core length normalized by the inner jet post inner diameter, L/D_1 for all pressure regimes using the original injector geometry. Results are shown in the $0.02 < J < 10$ range.....	160
Figure 5.11. Dark core length normalized by the inner jet post inner diameter, L/D_1 for all pressure regimes. Results include previous research work using the original injector geometry in the same facility this study was performed.	161
Figure 5.12. Spreading angle of the inner jet in degrees for all pressure regimes using the original injector geometry. Dark circular markers are data points from Leyva et al. (22).	162
Figure 5.13. Single phase coaxial jet images without acoustic excitation at subcritical pressures. Original injector geometry.....	162
Figure 5.14. Outer jet spread angle measurements with original injector geometry for one-phase coaxial jet at subcritical pressures. The bars indicate one standard deviation above and below the mean spreading angle.	163

Figure 5.15. Outer jet spread angle measurements compared to jet divergence angle theoretical predictions and other single jet and coaxial jet spreading angle experimental data.....	163
Figure 5.16. (a) Approximate location during testing of the absolute pressure transducer used to measure the acoustic field inside the inner chamber. (b) Absolute pressure transducers used to quantify the pressure oscillations at three different transversal locations within the inner chamber for tests performed with the original injector. (c) Differential pressure transducers used to quantify the pressure oscillations within the inner chamber for tests performed with the new injector.....	164
Figure 5.17. RMS of chamber pressure fluctuations measured at the bottom of the inner chamber versus phase angle between acoustic sources for the nearcritical case with $J = 2.1$ with the original injector geometry. The data with only one acoustic source on was obtained immediately before recording data with both sources on for the corresponding phase angle on which they are plotted.	164
Figure 5.18. Graphs of the RMS value of the chamber pressure fluctuations at different phase angles between the acoustic sources on the left with chamber pressure as a function of time on the right for one subcritical case, one nearcritical case and one supercritical case with the original injector geometry.....	165
Figure 5.19. Collection of subcritical coaxial jet images at $P_{\text{chamber}} = 1.50 \text{ MPa}$, $J = 0.17$. Original injector geometry	166
Figure 5.20. Collection of subcritical coaxial jet images at $P_{\text{chamber}} = 1.45 \text{ MPa}$, $J = 2.6$. Original injector geometry.	166

Figure 5.21. Collection of subcritical coaxial jet images at $P_{\text{chamber}} = 1.50$ MPa, $J = 9.6$. Original injector geometry.	167
Figure 5.22. Collection of subcritical coaxial jet images at $P_{\text{chamber}} = 1.50$ MPa, $J = 23$. Original injector geometry.	167
Figure 5.23. Collection of nearcritical coaxial jet images at $P_{\text{chamber}} = 3.58$ MPa, $J = 0.55$. Original injector geometry.	168
Figure 5.24. Collection of nearcritical coaxial jet images at $P_{\text{chamber}} = 3.56$ MPa, $J = 4.9$. Original injector geometry.	168
Figure 5.25. Collection of nearcritical coaxial jet images at $P_{\text{chamber}} = 3.56$ MPa, $J = 9.3$. Original injector geometry.	169
Figure 5.26. Collection of supercritical coaxial jet images at $P_{\text{chamber}} = 4.96$ MPa, $J = 0.33$. Original injector geometry.	169
Figure 5.27. Collection of supercritical coaxial jet images at $P_{\text{chamber}} = 4.96$ MPa, $J = 2.4$. Original injector geometry.	170
Figure 5.28. Collection of supercritical coaxial jet images at $P_{\text{chamber}} = 4.96$ MPa, $J = 9.9$. Original injector geometry.	170
Figure 5.29. Dark core length with acoustics ($L_{\text{acoustics}}$) over dark core length without acoustics ($L_{\text{no acoustics}}$), shown in diamonds, versus phase angle between acoustic sources for subcritical pressures. The the peak-to-peak pressure perturbation as a percentage of the mean chamber pressure ($\Delta p_{\text{peak-to-peak}}/p_{\text{mean}}$), in squares, is also plotted. Original injector geometry.....	171
Figure 5.30. Dark core length with acoustics ($L_{\text{acoustics}}$) over dark core length without acoustics ($L_{\text{no acoustics}}$), shown in diamonds, versus phase angle	

between acoustic sources for nearcritical pressures. The the peak-to-peak pressure perturbation as a percentage of the mean chamber pressure ($\Delta p_{\text{peak-to-peak}}/p_{\text{mean}}$), in squares, is also plotted. Original injector geometry..... 172

Figure 5.31. Dark core length with acoustics ($L_{\text{acoustics}}$) over dark core length without acoustics ($L_{\text{no acoustics}}$), shown in diamonds, versus phase angle between acoustic sources for supercritical pressures. The the peak-to-peak pressure perturbation as a percentage of the mean chamber pressure ($\Delta p_{\text{peak-to-peak}}/p_{\text{mean}}$), in squares, is also plotted. Original injector geometry..... 173

Figure 5.32. Peak-to-peak pressure perturbation ($\Delta p_{\text{peak-to-peak}}$) as a percentage of the mean chamber pressure (p_{mean}) and dark core length with acoustics ($L_{\text{acoustics}}$) over dark core length without acoustics ($L_{\text{no acoustics}}$) versus phase angle between acoustic sources for sub, near and supercritical pressures at $J \approx 1.0, 2.5$ and 9.5 for the original injector geometry. 174

Figure 5.33. Maximum dark core length reduction between dark core length without acoustics and dark core length with acoustics for all phase angles $(L_{\text{no acoustics}} - L_{\text{acoustics}})_{\text{MAX}}$ for a given case divided by the dark core length without acoustics ($L_{\text{no acoustics}}$) as a function of J for all cases obtained with the original injector in this study..... 175

Figure 5.34. Maximum spread angles as a function of acoustic phase angle for different J values at subcritical pressures for original injector geometry..... 176

Figure 5.35. Maximum spread angles as a function of acoustic phase angle for different J values at nearcritical pressures for original injector geometry..... 177

Figure 5.36. Maximum spread angles as a function of acoustic phase angle for different J values at supercritical pressures for original injector geometry.....	178
Figure 5.37. Coaxial jet images with the new injector at subcritical pressure ($P_{\text{chamber}} = 1.48 \text{ MPa}$, $J = 0.089$).	179
Figure 5.38. Coaxial jet images with the new injector at subcritical pressure ($P_{\text{chamber}} = 1.49 \text{ MPa}$, $J = 0.43$).	179
Figure 5.39. Coaxial jet images with the new injector at subcritical pressure ($P_{\text{chamber}} = 1.49 \text{ MPa}$, $J = 2.0$).	180
Figure 5.40. Coaxial jet images with the new injector at subcritical pressure ($P_{\text{chamber}} = 1.49 \text{ MPa}$, $J = 7.8$).	180
Figure 5.41. Coaxial jet images with the new injector at subcritical pressure ($P_{\text{chamber}} = 1.48 \text{ MPa}$, $J = 18$).	181
Figure 5.42. Coaxial jet images with the new injector at nearcritical pressure ($P_{\text{chamber}} = 3.56 \text{ MPa}$, $J = 0.50$).	181
Figure 5.43. Coaxial jet images with the new injector at nearcritical pressure ($P_{\text{chamber}} = 3.58 \text{ MPa}$, $J = 2.2$).	182
Figure 5.44. Coaxial jet images with the new injector at nearcritical pressure ($P_{\text{chamber}} = 3.58 \text{ MPa}$, $J = 9.4$).	182
Figure 5.45. Coaxial jet images with the new injector at nearcritical pressure ($P_{\text{chamber}} = 3.56 \text{ MPa}$, $J = 19$).	183
Figure 5.46. Coaxial jet images with the new injector at supercritical pressure ($P_{\text{chamber}} = 4.95 \text{ MPa}$, $J = 2.6$).	183

Figure 5.47. Dark core length with acoustics ($L_{\text{acoustics}}$) over dark core length without acoustics ($L_{\text{no acoustics}}$), shown in diamonds, versus phase angle between acoustic sources for subcritical pressures. The the peak-to-peak pressure perturbation as a percentage of the mean chamber pressure ($\Delta p_{\text{peak-to-peak}}/p_{\text{mean}}$), in squares, is also plotted. The cases which had their x coordinate marked with an asterisk (*) denote cases that had a dark core length that was longer than the field of view in more than 10% but less than 50% of the images. The ones marked with two asterisks (**) had dark cores larger than the examination window for at least half of the images. New injector geometry. 184

Figure 5.48. Dark core length with acoustics ($L_{\text{acoustics}}$) over dark core length without acoustics ($L_{\text{no acoustics}}$), shown in diamonds, versus phase angle between acoustic sources for pressures above the critical point. The the peak-to-peak pressure perturbation as a percentage of the mean chamber pressure ($\Delta p_{\text{peak-to-peak}}/p_{\text{mean}}$), in squares, is also plotted. See caption of Figure 5.47 for further details. New injector geometry. 185

Figure 5.49. Peak-to-peak pressure perturbation ($\Delta p_{\text{peak-to-peak}}$) as a percentage of the mean chamber pressure (p_{mean}) and dark core length with acoustics ($L_{\text{acoustics}}$) over dark core length without acoustics ($L_{\text{no acoustics}}$) versus phase angle between acoustic sources for sub, near and supercritical pressures at $J \approx 5, 10$ and 20 for the new injector geometry. 186

Figure 5.50. Maximum dark core length reduction between dark core length without acoustics and dark core length with acoustics for all phase angles $(L_{\text{no acoustics}} - L_{\text{acoustics}})_{\text{MAX}}$ for a given case divided by the dark core length without acoustics ($L_{\text{no acoustics}}$) as a function of J for moderate and higher momentum flux ratio cases obtained with the new injector. 187

Figure 5.51. Comparison of the maximum dark core length reduction as a function of momentum flux ratio between the original injector geometry and the new injector geometry.	187
Figure 5.52. Maximum spread angles as a function of acoustic phase angle for different J values at subcritical pressures for the new injector geometry. The cases which had their x coordinate marked with an asterisk (*) denote cases that had a dark core length that was longer than the field of view in more than 10% but less than 50% of the images. The ones marked with two asterisks (**) had dark cores larger than the examination window for at least half of the images.	188
Figure 5.53. Maximum spread angles as a function of acoustic phase angle for different J values at near and supercritical pressures for the new injector geometry. See caption of Figure 5.52 for further details.	189
Figure A.1. Detailed schematic showing the flow path of the experimental setup of this study.	200
Figure A.2. Expanded view of the upper left section of the flow path schematic in Figure A.1.	201
Figure A.3. Expanded view of the upper right section of the flow path schematic in Figure A.1.	202
Figure A.4. Expanded view of the lower left section of the flow path schematic in Figure A.1.	203
Figure A.5. Expanded view of the lower right section of the flow path schematic in Figure A.1.	204

LIST OF TABLES

Table 3.1. Comparison of measured values of burning rate constant K for various fuel droplets, with combustion in the absence of acoustic excitation. Comparison with available established values is also given.	56
Table 3.2. Acoustic conditions of various fuels at extinction. The corresponding sound pressure level in decibels (dB), pressure perturbation in Pascals (Pa), and velocity perturbation in meters per second (m/s) is given. A rough estimate of the strain rate is also shown.	56
Table C.1. Summary of experimental conditions for tests performed with the original injector including single phase subcritical experimental conditions and results.	228
Table C.2. Summary of two-phase subcritical experimental results for tests performed	229
Table C.3. Summary of nearcritical experimental results for tests performed with the original injector.	230
Table C.4. Summary of supercritical experimental results for tests performed with the original injector.	231
Table C.5. Summary of experimental conditions for tests performed with the new injector.	232

NOMENCLATURE

Symbols or Abbreviations

α	angle, spreading angle, density coefficient
ϵ	strain rate
g	gravitational acceleration
g_a	acoustic acceleration
\dot{m}	mass flow rate
μ	dynamic viscosity
p	pressure
ρ	density
u	mean velocity
A	area
C	carbon
CFD	computational fluid dynamics
D	diameter
D_{eqvs}	equivalent diameter of a sphere with the same volume
Δ	change
H	hydrogen
HE	heat exchanger
J	outer jet to inner jet momentum flux ratio, $J = \rho_o u_o^2 / \rho_i u_i^2$

K	burning rate constant
L	length, dark core length, distance between S&R; left
LRE	liquid rocket engine
N	nitrogen
O	oxygen
P	pressure
PAN	pressure antinode
PN	pressure node
PT	pressure transducer
R	radius; right
Re	Reynolds number, $Re = \rho uL/\mu$
RMS	root-mean-square, root-mean-square value
RTD	resistance temperature detector
S&R	speaker and reflector
SPL	sound pressure level
T	temperature
TC	thermocouple
VR	outer jet to inner jet velocity ratio, $VR = u_o/u_i$

Subscripts

_{cr}	critical
_i	inner, inner jet, inner wall or post (of coaxial injector)
_o	outer, outer jet, outer wall or post (of coaxial injector), air outside the flame
_s	surrounding products (of droplet combustion)

ACKNOWLEDGMENTS

This work would not have been possible without the help and support of many individuals and groups who directly or indirectly provided the time, knowledge, and/or financial support that I needed to successfully accomplish this endeavor. First and foremost, I would like to sincerely thank my advisor Professor Ann Karagozian who even before I met her encouraged me to pursue graduate studies right away instead of taking a year off school after finishing my undergraduate education. She, since then, has been involved in basically all the research and funding opportunities I have had a chance to take part of as a graduate student. From the NSF funded AGEP Scholars Program, which I started as soon as I arrived to UCLA, and the opportunity to perform part of my research work at the Air Force Research Laboratory at Edwards AFB, to the current possibility to perform postdoctoral work overseas at the Laboratoire EM²C at École Centrale Paris in France. I am indebted to her for all her time, support and advice and I truly feel honored to be one of her PhD students.

I would also like to thank my advisor Professor Owen Smith who always gave me helpful and practical research advice when I needed it and for trusting in me twice as his teaching assistant. I also appreciate the help of Dr. Srinivasan Dattarajan whose work I continued during my first years as a graduate student. The support of my lab and classmate Dr. Juliett Davitian throughout our graduate school careers has also been invaluable. To Reinaldo Santos, Alec Pezeshkian, Hann-Shin Mao, and Sophonias Teshome for their support with my droplet combustion research at its various stages. I would also like to acknowledge the support of the NASA Microgravity Combustion program which made possible the completion of this research and Maj. Gen. Curtis Bedke, Commander of the Air Force Research Laboratory, for supplying the aviation and Fischer-Tropsch synthetic fuels.

For the second part of my research work, which took place at Edwards, AFB, CA, I would like to especially thank my mentor, Dr. Ivett Leyva, who put an incredible amount of time and effort into preparing me for the type and level of research that I would eventually be in charge of at AFRL. I share her sincere interest and passion for the work we perform at the Air Force Research Lab. I also deeply appreciate the invaluable discussions and expert advice of Dr. Douglas Talley and Dr. Behrouz Chehroudi and from whom I continuously learn how to be a better researcher. To Mr. Randy Harvey, Lt. Jeffrey Graham, Mr. Earl Thomas, Mr. David Hill, Mr. Todd Newkirk, Mr. Mark Pilgram, and Mr. Matt Billingsley many sincere thanks for your help supporting my research at Edwards AFB. My acknowledgments would of course be incomplete if I did not thank the Air Force Office of Scientific Research, grant FA 9550-07-1-0156, and Dr. Mitat Birkan, program manager of the supercritical fluids work I performed while at AFRL.

I would like to thank Professor Richard Weiss, Dr. Barbara Ige, Professor Odvar Bendiksen, Dr. Jeffrey Murphy, Dr. Atul Mathur, Ms. Angie Castillo, Ms. Cory Castro and Mr. Abel Lebon and all my professors and instructors from my earliest school years to undergraduate and graduate school for their support, for believing in me and for always helping me improve as a student and as a person. Last, but not least, to my doctoral committee members, Professor Stanley Osher and Professor Jeff Eldredge for their time, patience, and helpful insights.

Also, thank you to all my family and friends: you are who makes it all worth it.

Finally, for everyone I have failed to mention in the previous paragraphs who have given their time and effort so that I can accomplish the goal of completing my PhD, I sincerely thank you very, very much.

VITA

1982	Born, San Diego, CA.
1989 - 1997	Attended Instituto Lux Elementary School, Leon, Guanajuato, Mexico.
1997 - 2000	Attended ITESM Campus León High School, Leon, Guanajuato, Mexico.
2000	Participated in MIT's Project Interphase 2000.
2001	Summer Internship, Raytheon Electronic Systems.
2003	Summer Internship, Center for the Advancement of Hispanics in Science and Engineering Education
2004	Undergraduate Teaching Assistantship, Thermal Energy, Aeronautics and Astronautics Department, MIT.
2004	B.S., Aerospace Engineering, MIT.
2004	Summer Internship, MIT Department of Aeronautics and Astronautics
2004	NSF/AGEP Fellowship, UCLA Graduate Division.
2005	Winter Teaching Assistantship, Preliminary Design of Aircraft, MAE Department, UCLA.
2005	Spring Teaching Assistantship, Rocket Propulsion, MAE Department, UCLA.
2005	Summer Graduate Research Assistantship, advisory by Professor Ann Karagozian and Professor Owen Smith, Thesis Topic
2005	Fall Teaching Assistantship, Aircraft Propulsion, MAE Department, UCLA.
2006	Winter Graduate Research Assistantship, advisory by Professor Ann Karagozian and Professor Owen Smith, Thesis Topic.
2006	Spring Teaching Assistantship, Rocket Propulsion, MAE Department, UCLA.

2006 M.S., Aerospace Engineering, UCLA.

2006 Summer Graduate Research Assistantship, advisory by Professor Ann Karagozian and Professor Owen Smith, Thesis Topic.

2006 Fall Teaching Assistantship, Aircraft Propulsion, MAE Department, UCLA.

2007 Winter Research Assistantship, advisory by Professor Ann Karagozian and Professor Owen Smith, Thesis Topic.

April 2007 Passed PhD Candidacy Exam.

2007 - 2009 Graduate Student Researcher, Air Force Research Laboratory, Propulsion Directorate, Edwards AFB.

PUBLICATIONS AND PRESENTATIONS

Rodriguez, J. I., Graham, J. J., Leyva, I. A., Talley, D., “Effects of Variable Phase Transverse Acoustic Fields on Coaxial Jet Forced Spread Angles”. AIAA Paper No. 2009-0231, 47th AIAA Aerospace Sciences Meeting, Orlando, FL, 5-8 January 2009.

Rodriguez, J. I., Graham, J. J., Leyva, I. A., Lyu, H.-Y., Talley, D., “On the Inner Jet Spread Angles of Coaxial Jets from Subcritical to Supercritical Conditions with Preliminary Numerical Results”. Paper 4D-LPS-II, 55th JANNAF Propulsion/4th Liquid Propulsion Subcommittee Meeting, Orlando, FL, 8-12 December 2008.

Leyva, I. A., Rodriguez, J. I., Chehroudi, B., Talley, D., “Effect of Phase Angle on Coaxial Jet Behavior Spanning Sub- To Supercritical Pressures”. Paper 14-2, 22nd European Conference on Liquid Atomization and Spray Systems, ILASS Europe, Como, Italy. 8-10 September 2008.

Rodriguez, J. I., Leyva, I. A., Chehroudi, B., Talley, D., “Results on Subcritical One-Phase Coaxial Jet Spread Angles and Subcritical to Supercritical Acoustically-Forced Coaxial Jet Dark Core Lengths”. AIAA Paper No. 2008-4561, 44th AIAA/ASME/SAE/SEE Joint Propulsion Conference and Exhibit, Hartford, CT, 20-23 July 2008.

Rodriguez, J. I., Leyva, I. A., Chehroudi, B., Talley, D., "Effects of a Variable-Phase Transverse Acoustic Field on a Coaxial Injector at Subcritical and Near-Critical Conditions". Paper M32-A-2, 21st Annual Conference on Liquid Atomization and Spray Systems, ILASS Americas, Orlando, FL, 18-21 May 2008.

Rodriguez, J. I., Leyva, I. A., Chehroudi, B., Talley, D., "Preliminary Results on Coaxial Jets Spread Angles and the Effects of Variable Phase Transverse Acoustic Fields". 2nd Southern California Symposium on Flow Physics, University of California, Los Angeles, Los Angeles, CA, 12 April 2008.

Rodriguez, J., Teshome, S., Mao, H.-S., Pezeshkian, A., Smith, O. I., Karagozian, A. R., "Acoustically Driven Droplet Combustion with Alternative Liquid Fuels". AIAA Paper No. 2008-1002, 46th AIAA Aerospace Sciences Meeting and Exhibit, Reno, NV, 7-10 January 2008.

Leyva, I. A., Rodriguez, J. I., Chehroudi, B., Talley, D., "Preliminary Results on Coaxial Jets Spread Angles and the Effects of Variable Phase Transverse Acoustic Fields". AIAA Paper No. 2008-0950, 46th AIAA Aerospace Sciences Meeting and Exhibit, Reno, NV, 7-10 January 2008.

Rodriguez, J., Mao, H.-S., Teshome, S., Pezeshkian, A., Smith, O. I., Karagozian, A. R., "Combustion of Condensed Phase Alternative Fuels in an Acoustic Field". 60th American Physical Society, Division of Fluid Dynamics Meeting, Salt Lake City, UT, 18-20 November 2007.

Rodriguez, J. I., Smith, O. I., Karagozian, A. R., "Acoustically Coupled Droplet Combustion with Alternative Fuels". Southern California Symposium on Flow Physics, California Institute of Technology, Pasadena, CA, 7 April 2007.

Rodriguez, J. I., Smith, O. I., Karagozian, A. R., "Acoustically Coupled Droplet Combustion with Alternative Fuels". Paper G-09, 5th US Combustion Meeting, San Diego, California, 25-28 March 2007.

ABSTRACT OF THE DISSERTATION

Acoustic Excitation of Liquid Fuel Droplets and Coaxial Jets

by

Juan Ignacio Rodriguez

Doctor of Philosophy in Aerospace Engineering

University of California, Los Angeles, 2009

Professor Ann R. Karagozian, Co-chair

Professor Owen I. Smith, Co-chair

This experimental study focuses on two important problems relevant to acoustic coupling with condensed phase transport processes, with special relevance to liquid rocket engine and airbreathing engine combustion instabilities. The first part of this dissertation describes droplet combustion characteristics of various fuels during exposure to external acoustical perturbations. Methanol, ethanol, a liquid synthetic fuel derived from coal gasification via the Fischer-Tropsch process, and a blend of aviation fuel and the synthetic fuel are used. During acoustic excitation, the droplet is situated at or near a pressure node condition, where the droplet experiences the largest velocity perturbations, and at or near a pressure antinode condition, where the droplet is exposed to minimal velocity fluctuations. For unforced conditions, the values of the droplet burning rate constant K of the different fuels are consistent with data in the literature. The location of

the droplet with respect to a pressure node or antinode also has a measurable effect on droplet burning rates, which are different for different fuels and in some cases are as high as 28% above the unforced burning rate value. Estimates of flame extinction due to acoustic forcing for different fuels are also obtained.

The second part of this work consists of an experimental study on coaxial jet behavior with direct applications to flow mixing and unstable behavior characterization in liquid rocket engines. The experiments span a range of outer to inner jet momentum flux ratios from 0.013 to 23, and explore subcritical, nearcritical and supercritical pressure conditions, with and without acoustic excitation, for two injector geometries. Acoustic forcing at 3 kHz is utilized to maximize the pressure fluctuations within the chamber acting on the jet, reaching maximum values of 4% of the mean chamber pressure. The effect of the magnitude and phase of the acoustic field generated within the chamber on the dark core length and the inner jet spreading angles is presented and the stability of coaxial flows in the current flow regime is discussed with respect to evidence for convective and absolute jet instabilities under different operating conditions.

CHAPTER 1

Introduction

Acoustics play an important role in the performance of combustion systems. There is a strong interest in knowing the response of such reactive systems to acoustic excitation, since the acoustic and combustion processes can couple and enhance instabilities that might lead to the destruction of the combustion device (1). A particular area that is not well understood is the response and behavior of a range of alternative fuels in the environment of an acoustically resonant engine, which can occur in airbreathing engines and other combustion devices. The different reactive time scales associated with different fuels could modify the nature of combustion coupling to acoustic resonances and thus alter the performance of the combustion device. Therefore, it is of interest to investigate the response of various fuels when acoustic disturbances are present.

Such acoustically coupled, condensed phase combustion also occurs in liquid rocket engines (LREs). Combustion instabilities in LREs have been a long-standing challenge, and the fundamental mechanisms underlying such instabilities and the means by which they can be controlled remain largely not well understood. Because supercritical pressures and transcritical (i.e., transitioning from subcritical to supercritical) temperatures are typically found in LREs, it has been of interest to conduct fundamental experiments and numerical simulations in these flow regimes to better

understand acoustic coupling associated with these instabilities. Davis and Chehroudi (2), for example, have explored supercritical coaxial nitrogen jets and have shown that changes in the behavior of the jet as it leaves the injector can be enhanced by acoustic excitation. Since the injectors in LREs feature coaxial jet configurations, the effects of acoustic excitation on mixing and transport, which are flow features that are closely related to the reactive phase of the combustion process, of coaxial jets is a relevant topic. The present study focuses on both burning fuel droplets and coaxial jet behavior in a transverse acoustic field.

1.1 Acoustically Coupled Droplet Combustion

1.1.1 Burning of Spherical and Non-spherical Fuel Droplets

Fuel droplet combustion is a heterogeneous and reactive process. The condensed-phase combustion features of this phenomenon can be obtained from studying the characteristics of its associated diffusion flame. For a quasi-steady, burning spherical droplet, classical studies show that the variation in the diameter of the droplet d with time t follows the “ d^2 ” law (3):

$$d^2(t) = d^2(t = 0) - Kt. \quad (1.1)$$

The burning rate constant K is usually characterized in units of mm^2/s . In microgravity conditions, the observed droplet diameter follows a d^2 type of dependence on time due to a more spherical droplet geometry. One of the many motivations for

microgravity droplet combustion studies is aimed at understanding the applicability of the d^2 law to burning droplets (4).

However, in normal gravity conditions, a suspended droplet cannot maintain a spherical geometry due to surface tension and gravitational forces. Thus, the droplet and its surrounding diffusion flame cannot be assumed to be spherical. To be able to analyze the non-spherical droplets, the equivalent diameter of a sphere with the same volume as the non-spherical droplet d_{eqvs} is obtained via optical means to determine K using equation (1.1) for different burning scenarios (5).

1.1.2 Acoustic Excitation Effects on Condensed Phase Combustion

Several studies show that an increase in heat and mass transfer rates can take place in droplets burning under the effects of an external acoustical field (6; 7; 8; 9). Saito et al. (8; 9) explored how evaporating and burning kerosene droplets reacted when they are placed near a pressure node or antinode associated with standing waves inside a closed acoustic waveguide. This group finds an increase of 2 to 3 times in evaporative and burning rate constants when the droplet is situated at a pressure node (where velocity perturbations are high) compared to little or no change when the droplet is situated at a pressure antinode (where velocity perturbations are small or non-existent).

Some acoustic excitation studies involving droplet combustion have been performed under microgravity conditions. These experiments essentially eliminate natural convection effects and permit an undisturbed analysis of the acoustic forcing effects on the burning droplets. For instance, the work of Okai et al. (10) featured n-

octane droplet combustion in an acoustic field at different amplitudes and frequencies in a microgravity environment. It was observed that for droplets situated at a pressure node location at frequencies over 2 kHz the increase in burning rates is about 40% from the unforced values.

Tanabe et al. (11; 12), exposed a burning n-decane droplet to a pressure node and a location between the pressure node and the pressure antinode of a standing wave inside a duct in a microgravity environment. This research group found that the burning rate of the fuel increased significantly with the magnitude of velocity perturbation. A burning rate increase as high as 85% over the unforced value was observed for velocity perturbations up to 1 m/s. The effects of standing acoustic waves on burning rates and flame deflections are related to acoustic streaming processes, which describe the time-averaged motion induced in a fluid flow by its dominating fluctuating components (13). The concept of an acoustic radiation force, F_R , acting on a sphere of hot gases surrounding the burning droplet is used by Tanabe et al. (11; 12) to interpret their observations. The magnitude and orientation of this acoustic radiation force are presumed to directly affect burning rate constants and the degree of deflection of the flame surrounding the droplet. The expression for the acoustic radiation force is

$$F_R = \alpha(\rho_s - \rho_o)V \frac{\partial(\overline{u'^2})}{\partial x}, \quad (1.2)$$

where ρ_s is the density of the hot combustion products surrounding the diffusion flame, ρ_o is the density of the air outside the flame and the combustion products, V is the volume of a sphere containing the hot combustion products, x is the position of the droplet

measured from the point where the velocity node or antinode is located, and $\overline{u'^2}$ is the mean of the square of the amplitude of the local perturbation velocity, u' , within the waveguide. The coefficient α takes the following form when the density of the combustion products is lower compared to that of the ambient air:

$$\alpha \equiv \frac{3\rho_o}{2(2\rho_s + \rho_o)}. \quad (1.3)$$

The expression for the buoyancy force on an object of density ρ_s and volume V surrounded by a heavier fluid of density ρ_o , has the same form as the expression in equation (1.2). Thus, Tanabe et al. (11; 12) suggest that the acoustic radiation force has an influence on droplet combustion similar to the effect that gravity has on unforced droplet combustion. Their observations of the direction of flame deflection of burning droplets lying away from a pressure node are consistent with this theory.

In an effort to compare the effects of acoustic excitation in normal gravity and microgravity, Dattarajan et al. (14; 15) studied the droplet combustion characteristics of these fuels exposed to different acoustic excitation conditions in a laboratory environment and during free-fall (microgravity) conditions in a NASA drop tower. For these experiments, the droplet was located near a pressure node, where the droplet experiences the greatest effects of velocity perturbations and near a pressure antinode where the droplet is exposed to minimal velocity fluctuations. Results show that droplet burning rates in microgravity increase over 75% when the droplet is located near a pressure antinode and over 200% when the droplet is situated near a pressure node for

sound pressure levels greater than 135 dB compared to the unforced values (see Figure 1.1).

For burning droplets in normal gravity, no appreciable change is observed from the unforced values when the droplet is located near a pressure node and only moderate increases up to 15% are observed when the droplet is located near a pressure node (see Figure 1.2). Overall, the observed flame deformations when the droplet is located to either side of a pressure node or a pressure antinode are consistent with acoustic radiation forces associated with the acoustic field present (see Figure 1.3). When the droplet location is extremely close or coincident with the pressure node, flame oscillations are observed, in contrast to an absence of flame deflection suggested by acoustic radiation forces as in eqn. (1.2). Moreover, the theoretical acoustic acceleration to which the droplet is exposed when it is moved with respect to a pressure node or a pressure antinode did not completely explain the significant increases in burning rate observed in microgravity. While displacements of the droplet with respect to node or antinode locations are observed to have a measurable effect on droplet burning rates, acoustic accelerations associated with such displacements, as an analogy to gravitational acceleration, do not completely explain the significant increases in burning rate resulting from the excitation in microgravity.

1.1.3 Alternative Fuels

It is of great interest to study the performance and characteristics of potential substitutes to conventional fuels. These alternative sources of fuel are receiving

increasing attention due to sharp fluctuations in crude oil prices and a surge in competition for fossil fuels mostly from emergent economies (16). There is a wide range of options for alternate sources of energy. Some potential fuels, such as liquid hydrogen, have still major technological challenges to address, such as synthesis in sufficient quantity for transportation systems. In the short term, the solution for aircraft propulsion systems involves undoubtedly hydrocarbons. For automotive applications bio-diesel and ethanol have promise as non-fossil fuel derived sources, while synthetic fuels derived from natural gas or coal via the Fischer-Tropsch process (17) show promise as an aviation fuel replacement. To make efficient recommendations for the transition between alternative and conventional fuels for current propulsion systems, it is necessary to understand the differences in combustion and other characteristics of these alternative fuels as compared to conventional fuels. One example is the effect that liquid Fischer-Tropsch synthetic fuel has on the polymer seals of an aircraft engine. The synthetic fuel is found to degrade the seal over time due to its high content of aromatic naphta (18).

In the present study, two alcohols (ethanol and methanol), synthetic fuel (Fischer-Tropsch or F-T), and a blend of aviation fuel (JP-8) and synthetic fuel (F-T) were examined to assess differences and similarities in their combustion characteristics under acoustic excitation. It is interesting to note that this blend of JP-8 and synthetic fuel has been used in a B-52 aircraft during flight tests at Edwards AFB and is currently undergoing exploration at the Air Force Research Laboratory as an alternative aviation fuel (19).

1.2 Acoustic Driving of Coaxial Jets

1.2.1 Basic Flow Configuration

The type of flow analyzed for the second part of this dissertation is a coaxial jet flow. There are two types of coaxial flows depending on the jet dynamics: shear coaxial flows and swirl coaxial flows. In the former, the mean velocity of the outer jet and the mean velocity of the inner jet are parallel. In the latter, either the mean outer jet or the mean inner jet velocity has a tangential or rotational component and it is not parallel to the mean velocity of the other jet. Shear coaxial flows consist of two concentric jets or streams. The stream in the center of this flow configuration has a circular cross section and is referred to as the inner jet. The annular stream which surrounds the center stream is referred to as the outer jet. The boundary between the inner and outer streams is denoted as the inner jet post or tube and the boundary between the outer annular stream and the surrounding environment is denoted as the outer jet post or tube.

This study focuses solely on shear coaxial flows and the schematic in Figure 1.4 is representative of the type of shear coaxial flow investigated. The inner stream has a set of properties that characterize it, such as chemical composition of the fluid, temperature, density and the velocity of the flow. The inner diameter of the inner jet post, D_{ii} , constitutes the diameter of the circular inner jet. From the diameter of the inner jet, the cross sectional area, A_i , can be calculated:

$$A_i = \pi D_{ii}^2 / 4, \quad (1.4)$$

and using the average inner jet velocity, u_i , the mass flow rate, \dot{m}_i , can be found as $\dot{m}_i = \rho_i u_i A_i$, where ρ_i is the density of the inner jet fluid.

The outer stream is characterized by the same set of properties as the inner jet, and the values of the properties of the outer jet are mostly independent from those of the inner jet, the only exception being pressure which is the same for both inner and outer jets. The outer jet cross sectional area is:

$$A_o = \pi D_{oi}^2/4 - \pi D_{io}^2/4, \quad (1.5)$$

and the mass flow rate of the outer jet is given by $\dot{m}_o = \rho_o u_o A_o$, where ρ_o is the density of the outer jet fluid and u_o is the average outer jet velocity.

This basic coaxial jet flow configuration is used in the design of flow injection elements, commonly referred to as injectors, in cryogenic liquid rocket engines or LREs. One of the streams is used for the injection of the fuel and the other stream is used for the injection of the oxidizer. Commonly for cryogenic engines, the inner jet is the oxidizer and the outer jet is the fuel. Both fuel and oxidizer can be referred to as propellants. Examples of both cryogenic and non-cryogenic oxidizer fluids are oxygen, O_2 , hydrogen peroxide, H_2O_2 , and dinitrogen tetroxide, N_2O_4 ; while some fuels include hydrogen, H_2 , kerosene, a hydrocarbon with an approximate chemical formula of $C_{12}H_{26}$, hydrazine, N_2H_4 , monomethylhydrazine, CH_6N_2 and unsymmetrical dimethylhydrazine, $C_2H_8N_2$. Such coaxial flow injectors were used in the J-2 engine which powered the Saturn V

rocket, and are used in the RS-24 engine, also known as the Space Shuttle Main Engine or SSME, and the Vulcain engine that is used to lift the Ariane 5 rocket (20). As LREs evolve into higher specific impulse rocket designs, maximum combustion chamber pressures increase, reaching or surpassing the supercritical pressure values of most propellants. Hence, when propellants are injected into the combustion chamber of an LRE, they mix and the thermodynamic properties of the mixture can deviate significantly from those of the individual propellants. A better understanding of how the propellants behave under these supercritical conditions is of utmost importance.

1.2.2 Motivations and Objectives of Coaxial Jet Study

One of the most important requirements for an injector or a group of injectors in an LRE is to provide homogeneous mixing of the fuel and oxidizer within a short distance from the location where these propellants enter the combustion chamber. Two factors that strongly influence the mixing process are the geometry of the injector and the flow and thermodynamic properties of the propellants as they exit the injector.

The design of the injector plays a very important role in the performance of the device. For a coaxial injector, the thickness of the inner jet post dictates the separation between the inner jet and the outer jet flows after they exit the injector. A thinner post will allow for the fuel and oxidizer streams to come in contact with each other and develop a shear layer as soon as they exit the injector, while a thick inner jet post will delay the contact between the fuel and oxidizer, creating a recirculation region and a different mixing flow pattern between the two streams as they exit the injector. The

thickness of the outer jet post also affects the type of interaction between the outer jet and the mean flow of the combustion chamber.

Another geometry parameter that affects the flow is the axial distance from the end of the inner jet post to the end of the outer jet post; this distance is usually referred to as the inner jet “recess” length (see Figure 1.4) since usually the inner jet post ends before the outer jet post does, leaving no solid boundary between the inner jet and the outer jet for a short distance before both streams leave the coaxial injector exit, which in this case is defined as coincident with the end of the outer jet post.

The other factors that inherently influence the mixing process are the properties of both the inner and the outer jet flows. The local pressure and temperature can be used to find the local density of each jet, which along with their average velocities at the exit of the injector can be used to find parameters such as the outer jet to inner jet velocity ratio, VR , and outer jet to inner jet momentum flux ratio, J . These parameters are defined as follows, respectively: $VR = u_o/u_i$ and $J = \rho_o u_o^2 / \rho_i u_i^2$, and are used to determine which combination of temperatures, pressures and mass flow rates are the most effective to enhance mixing of the propellants as they enter the combustion chamber. For example, empirical evidence from previous experiments at AFRL suggests that as the outer jet to inner jet momentum flux ratio increases, the dark core length, a quantity to be defined in chapter 5, decreases (21; 22), which constitutes evidence that mixing between the two jets increases at relatively short distances from the exit plane.

Combustion instability constitutes a very challenging phenomenon when working with LREs and its components. Any incidents featuring high-frequency unstable behavior

in the pressure or heat flux in the combustion chamber of an LRE can cause severe engine damage and vehicle destruction. There are several factors that can contribute to high frequency combustion instabilities in LREs and each component of the engine could potentially have a role in the development of these instabilities. In fact, the same factors that affect the mixing process, such as the injector geometry and the outer jet and inner jet flow properties, could have a large influence in the development of such unwanted instabilities (23).

The main motivation of the second part of this work is to study shear coaxial jet flows in order to understand fundamental problems associated with LREs. How propellant fluids come in contact with each other and mix, and how they interact with each other in the combustion chamber when there are strong acoustic fields and resonances present are issues of great interest. It is thus the objective of the present work to analyze the response of a nonreactive coaxial jet when factors such as the injector geometry and the flow properties are varied in a systematic fashion, including exposure to strong acoustic forcing, to obtain a better understanding of the mixing processes of propellants and the high frequency interactions that are most destructive to a rocket engine. The main goal is to gather the knowledge acquired from this study and apply it to the early stages of LRE design so that efficient propellant use is achieved and predisposition to combustion instabilities is assessed and corrective actions are taken.

For the present experimental study, there was only one fluid used to simulate the fuel and oxidizer. The fluid was molecular nitrogen, N_2 , which has a critical temperature, T_{cr} , of 126.2 K and a critical pressure, P_{cr} , of 3.39 MPa. Having only one working species

allowed for a clear boundary between the gas, liquid, and supercritical phases of the fluid, avoiding the added complexity introduced when working with mixtures. Further, having a non-reactive shear coaxial injector flow also allowed the fluid mechanic effects to be isolated from the combustion-related phenomena observed in a reactive combustion chamber.

For instance, in a typical application of a coaxial injector with jets of liquid O_2 /liquid H_2 present, the oxygen is injected at subcritical temperatures through the inner jet and the hydrogen is injected at supercritical temperatures through the outer jet. The temperature of the outer hydrogen jet is higher than that of the inner jet as the hydrogen is used to remove heat from the combustion chamber walls. Therefore in the combustion chamber, since there are at least two species present, there is no single critical point, but instead there are critical mixing lines that define the thermodynamic state of the mixture (24). Hence, the reactive flow increases the difficulty of the thermodynamic analysis by adding more species to the chamber (reactants and products). Thus, this study is comprised of single species flows, either one-phase, when both the inner jet and the outer jet are in a gaseous state or when they both are in a supercritical state, or two-phase flows, when the outer jet is in a gaseous or supercritical state and the inner jet is in a liquid or liquid-like state. This greatly simplifies the analysis of the thermodynamic properties of both the coaxial injector and chamber flows.

Given the connection between this study and LREs, one of the major parameters considered was the mean pressure of the combustion chamber. Both the Space Shuttle and the Ariane 5 launch vehicles have LREs designed to operate above the critical

pressures of each of its propellants individually. Therefore, for this work, experiments were performed at three different mean chamber pressures, a subcritical pressure of 1.5 MPa, a nearcritical pressure of 3.6 MPa and a supercritical pressure of 5.0 MPa. The parameters affecting the interaction between the outer jet and the inner jet, which include their flow properties, were varied by changing the outer jet to inner jet momentum flux ratio, J . Varying J also indirectly modified the velocity ratio, VR . Commonly, the velocity ratio between the outer and inner jets of coaxial injectors in LREs is about 10 or higher. This practice was adopted after empirical evidence showed that injectors operating at these VR s were the most effective in preventing combustion instabilities (25). In this work J was varied from less than 0.02 to over 20, which in turn produced a variation of outer to inner jet velocity ratio in the $0.25 < VR < 23$ range.

1.2.3 Previous Work on Coaxial Jets

To meet the objective of studying the effects of acoustic forcing in a coaxial jet flow configuration, a transverse acoustic field was generated inside the test chamber. A transverse acoustic field was chosen because transverse acoustic modes lead to more destructive instabilities in LREs than longitudinal ones (20; 26). Specifically, this work focused on the effects of varying the pressure and velocity perturbations, by varying the phase difference between the acoustic sources producing the imposed transverse acoustic field, on the coaxial jet flow.

From the information above, it is important to highlight that one of the unique characteristics of this study is the exposure of the coaxial jet flow to the different

conditions found in a transverse acoustic field. To accomplish this, two acoustic sources were situated in the same plane of the coaxial jet and turned on simultaneously at the same frequency and very similar amplitudes, only varying the phase of the signal sent to them. The objective was to find the effect of the phase difference or phase angle in the coaxial jet, leaving the other acoustic properties the same.

In earlier studies involving acoustic excitation of reactive gaseous $\text{CH}_4/\text{liquid O}_2$ swirl coaxial jets, Marshall et al. (27) performed experiments at a mean chamber pressure of 1.53 MPa with maximum peak-to-peak pressure perturbations ($\Delta p_{\text{peak-to-peak}}$), as a fraction of mean chamber pressure (p_{mean}), of 4%. They studied the influence of mass flow rate, mixture ratio, injector and nozzle positions and chamber pressure on the spontaneous excitation of the transverse modes of their three-dimensional rectangular chamber. They found that the first mode of the largest dimension of the chamber produced a strong response in the jet when the injector was positioned near a velocity node location, where pressure fluctuations were the largest.

In another study, Richecoeur et al. (28) studied an acoustically excited, multiple element, and reactive coaxial injector configuration at elevated but still subcritical pressure conditions, with a mean chamber pressure of 0.9 MPa. Their experiments were performed at conditions where combustion became sensitive to external acoustic oscillations, which corresponded to outer to inner jet momentum flux ratios in the $4.6 < J < 20$ range. They obtained strong coupling between the combustion products from the three coaxial CH_4/O_2 injectors used in the study with pressure amplitude oscillations reaching 7% $\Delta p_{\text{peak-to-peak}}/p_{\text{mean}}$. This strong coupling between acoustics and combustion

was manifested by an enhancement of the flame spread, which is often associated with improved mixing; however, if the acoustic perturbations that enhance mixing result from or lead to combustion instabilities, they are clearly something to avoid. Interestingly, it was also found by a phase analysis study that the flame location (measured indirectly by tracking the emission of OH radicals) and the pressure oscillate in phase at the modulating frequency, a behavior they also observed with their high-speed camera. This could indicate that flame enhancement was observed at the rough equivalent of the pressure antinode location as reported in the present work.

Some of the previous work on coaxial jets has focused on the mixing properties of this concentric flow configuration. For instance, Gutmark et al. (29) concluded in their single phase coaxial vs. free jet experimental studies that in coaxial flow configurations, more of the surrounding fluid is entrained deeper into the inner jet as compared to the free jet case, enhancing the overall mixing process. These researchers also found that the geometry of the injector plays a role as well, with better mixing performance achieved by rectangular injectors as compared to circular ones. Gautam and Gupta (30) reported, in their cryogenic coaxial injector studies at atmospheric pressures, an increase in the evaporation of the inner jet and enhanced mixing with the surrounding flow with increasing outer to inner momentum flux ratio. They also altered the geometry of their injector setup by modifying the recess length between the inner jet and the outer jet exits. They found that larger recess lengths promote higher jet expansion and more entrainment of surrounding gases into the flow. Their shear layer analysis confirms that mixing enhancement and jet expansion are slower at lower J values.

In terms of reactive flows, Zong and Yang (31) also find in their numerical study of high pressure coaxial reactive flow that as J increases, turbulent mixing is enhanced, which reduces the inner jet dark core. One of the earliest studies on the subject, by Chigier and Beér (32), provides a very detailed description of the region near the injector exit in their coaxial jet experiments in which they varied the outer to inner velocity ratio from ∞ to 0.024. They present an explanation for the fluid processes they observe as the inner jet and outer jet leave the injector exit, such as the influence of the recirculation zone between the streams and the mixing process once the flows meet. They observe that at the low VR values the inner jet is less affected by the recirculation zone and is capable of entraining more flow from the outer jet. However, at high VR values, the inner jet gets entrained more by the outer jet because of the way the recirculation zone acts to push the inner jet towards the outer jet.

1.2.4 Dark Core Length

In a coaxial flow configuration, the region between the end of the coaxial injector and the location in the fluid stream where the density or the velocity, depending on the definition, starts to deviate from its initial value at the exit of the injector can be referred to as the potential core of the jet (33). Given the definition above, both the inner jet and outer jet can have their own potential core regions. The inner or outer potential core length is thus the axial distance from the end of the coaxial injector (either the inner jet or outer jet exit) to the end of their respective potential core region.

Intact surface length, intact core length, liquid intact length, liquid core length, undisturbed jet length, primary and secondary breakup length or simply unbroken, intact or breakup length are other common length scales used in the literature (34; 35; 36; 37; 38; 39) to characterize single and coaxial jets, although some of these variables are almost exclusively applied to the potential region of a single jet or the inner jet of a coaxial flow only. For instance, in a two phase coaxial jet, the term ‘liquid core length’ refers to the length needed for the liquid inner jet to be completely broken into drops and ligaments (36). A similar definition is that of the ‘intact or breakup length’ which refers to the distance between the exit of the injector and the location just before the first drop is formed as the inner jet liquid stream brakes apart from the liquid core (37).

The shape of the core in a two dimensional plane intersecting the axis of symmetry of the coaxial flow configuration resembles a triangle. Thus, for the three dimensional coaxial jet, the potential core has an appearance that is very similar to that of a cone. Thus the words “core” and “cone” are used interchangeably in some of the variable names mentioned above. For this work, the term ‘dark core’ will be used to describe the same variable referred to by the various definitions above. Any term involving the word ‘liquid’ cannot be used in this study since we analyze supercritical inner jets as well. Also, in the supercritical regime, both jets have the same phase, and words such as ‘intact’, ‘undisturbed’ or ‘unbroken’ become more ambiguous. Thus, a ‘dark core region’ based on the flow density, and the corresponding ‘dark core length’ will be precisely defined, discussed and compared to other equivalent potential core measurements in chapter 5.

Regardless of the name used, such length scales are important parameters to study because, among other considerations, they are related to the degree of mixing that has taken place at a critical distance from the injector exit. The shorter these length scales are, the higher the amount of fluid from the inner jet that has been entrained by the outer jet and mixed with the surroundings.

Given the significance of the dark core length as a qualitative indication of mixing in an LRE, it is important to analyze also the effects that an external acoustic field can have in the behavior of the dark core. External forcing can be introduced in an LRE by means of vibration, especially when the vehicle that the engine will be lifting is being launched. During take-off, high-frequency phenomena within the engine can interact with the combustion processes in the chamber, driving the energy release to unstable and potentially destructive patterns. Analyzing the effects of an acoustic field on the dark core length can lead to an improved understanding of how these acoustic modes couple with the mixing processes taking place in the combustion chamber, thus providing information on potential causes of combustion instabilities in LREs.

Previous experiments performed in the same facility at AFRL in which this study took place (2; 21; 22; 40; 41) feature one acoustic source at one end of the test chamber and a non-movable reflective wall at the other end. This type of acoustic set up only allowed for a fixed position of the jet with respect to the acoustic wave profile for pressure or velocity. By adding a second identical resonator at the location of the reflective surface, the magnitude and relative position of the pressure and velocity acoustic field with respect to the jet could be varied. Therefore, studying the effects of

having the injector positioned at a pressure or velocity node or at positions in between was now possible, and the effects of both the magnitude and gradient of the pressure and acoustic field on the coaxial jet flow could now be carefully analyzed.

The experiments performed by Leyva et al. (22) in the present facility with one acoustic source found that the effects of acoustics on the dark core length are greatest at subcritical pressures and for outer to inner jet momentum flux ratios in the $1 < J < 4$ range. In the experiments performed for the present work the addition of a second acoustic driver allowed changes of the relative position of the acoustic field with respect to the fixed location of the coaxial jet injector, and hence greater variability in the flowfield. Thus the effects of the magnitude and phase of the pressure oscillations on the jet could be characterized and the answer to the question on whether a similar range of J values for which the effects of acoustics are enhanced could be found. Quantities such as the mean chamber pressure, p_{mean} , the peak-to-peak pressure perturbation over the chamber pressure, $\Delta p_{\text{peak-to-peak}}/p_{\text{mean}}$, and the outer to inner jet momentum flux ratio, J , were also considered to characterize the effects of this transverse acoustic field on the coaxial injector flow.

1.2.5 Shear Layers and Spreading Angles

The study of the growth of shear layers between two planar flows is relevant because the rate of growth of the shear layer is indicative of the mixing process between the two layers (42; 43; 44; 45; 46). In an idealized 2D shear layer a spreading angle starts to develop at the point where both flows meet. Since the velocity of the particles in the

shear layer achieves an intermediate value between the two flows that bound it, the points in the flow where the velocity changes from its original value to a higher or lower one form two lines. The angle between these two lines is the shear layer spreading angle (see Figure 1.5).

One classic shear layer study is described in the work of Brown and Roshko (42), who proposed an equation for the growth rate of a shear layer while studying subsonic two dimensional incompressible turbulent gas-gas flows. Dimotakis (43) in turn proposed an equation for the vorticity growth rate of a planar free jet while Papamoschou and Roshko (44) proposed an equation for the growth of the visual thickness of the shear layers for compressible (subsonic to supersonic) two dimensional turbulent mixing layers. More relevant to the present studies, Chehroudi et al. (45; 46) showed for the first time that the near field spreading angle or growth rate of single round jets at supercritical pressure and temperature agrees quantitatively with experimental data and theoretical predictions for 2D shear layer growth from the single phase investigations discussed above.

For a single round jet, the spreading angle can also be referred to as the spray angle, spread angle or jet divergence angle (36; 38; 47). It can be defined experimentally using a visual method that averages a sample of images and approximates the left and right contours of the jet as straight lines using the least-squares method (47). In their studies, Chehroudi et al. (45; 46) analyzed the spreading angles of single round jets under pressure conditions spanning from subcritical to supercritical. The study also included experimental data on gas phase variable density jets from different researchers in which

the main variable investigated was the ratio of the chamber density to the jet density. This variable is important when considering the interaction between a single jet and a quiescent atmosphere.

For a coaxial flow, the spreading angle of the inner jet can be defined in a similar manner to the spreading angle of a single round jet. One can also consider the spreading angle of the outer jet, for which a different definition is needed since it has an annular shape. The spreading angle of the outer jet is the sum of the angle spanned by a line parallel to one side of the outer jet and the vertical axis of the jet and the angle spanned by a line parallel to the opposite side of the jet and the same vertical axis. In coaxial flows, a shear layer is created when the wall or tube between the inner jet and the outer jet ends (see Figure 1.6).

The development and effect of shear layers in a flow becomes important when analyzing coaxial jet behavior. For the case of a coaxial jet, the inner jet spreading angle provides an experimental indication of the growth of the shear layer between the inner and outer streams. However, to accurately represent a shear layer, the wall between the inner and outer streams must be very thin. In this work, the spreading angles of both the inner and outer jet with and without exposure to an acoustic field will be defined and analyzed in chapter 5.

1.2.6 Stability Analysis of the Coaxial Jet

A liquid jet owes its behavior to numerous factors, including the geometry of the orifice from where it is being issued, the properties of the flow when it exits such orifice

and the environmental conditions that it encounters as it leaves the exit location. But regardless of how these factors are varied, a liquid jet cannot be prevented from ultimately breaking up at some distance downstream from the exit location. To study the physical reasons for the breakup of a liquid sheet or jet, linear stability analysis is an important tool which predicts the onset of the instability in this class of flows (37). In stability analysis, disturbances should be allowed to grow both temporally and spatially to reach an accurate description of the breakup process. The breakup process leads to two different major regimes, the creation of large drops or fine atomization of the liquid, which are the result of very distinct physical phenomena. These two main regimes and others in between are the consequence of how the jet responds to disturbances.

Many different effects influence the absolute or convective instability of the inviscid liquid jet flow. Exit conditions, surrounding gas and slip velocity are some of them. For instance, in actual experiments, before the flow leaves the exit orifice, the velocity is zero at the wall due to the no-slip boundary condition and reaches a maximum at the axis; however, according to Scriven and Pigford (48) as the liquid jet flow leaves the exit, the velocity profile does achieve a uniform distribution. This notion was used by Leib and Goldstein (49) in their instability analysis to show that if the Weber number at the orifice exit is less than 3.3 the convectively unstable jet becomes absolutely unstable before the flow has an opportunity to recover a uniform velocity profile. If the Weber number is above 3.3, the jet remains convectively unstable and attains a top-hat distribution. This “velocity relaxation” seems to preclude the disturbance from travelling upstream. The effect of surrounding gas on a liquid jet is also important. When the

density ratio is increased by a factor of ten the effect of the ambient air is to increase the spatial growth rate of the disturbances by the same factor since the gas inertial force is an important factor in the enhancement of such growth rate. Likewise, the increase of the relative velocity between the gas and the liquid augments the disturbance growth rate and cut-off wave number, which is the basis for the Kelvin-Helmholtz instability.

The review by Huerre and Monkewitz (50) on local and global instabilities in spatially developing flows classifies open shear flows according with their local/global and absolute/convective instability features. They point out that flows that are locally convectively unstable everywhere are more prone to external disturbances, which determine the evolution in space of the unsteady flow. These flows, such as mixing layers, are susceptible to acoustic excitation and therefore a certain degree of control can be exercised over their behavior. In contrast, flows that have regions of absolute instability of large enough size are not easily affected by external dynamics. Instead, the source of their absolute instability relies on the temporal growth of the initial perturbations in these absolutely unstable regions of the flow. Low density jets are an example of these kinds of flows. Finally, flows that are locally convectively unstable but a latent absolute instability is present at some point in the field are referred to as marginally globally stable flows. In these flows, the global mode can be excited if forcing is applied at or near the frequency of the mode, which otherwise would be damped slowly over time. This is the case of homogeneous jets.

Raynal (51) extends the classical stability analysis of two parallel flows with different densities from previous authors to the particular case of coaxial jets with high

momentum flux ratios. The main goal of this analysis is to study the main instability that develops at the interface between the liquid and the gas streams. In the particular case of coaxial flows, he points out that a proper model should include the vorticity layers produced by the walls of the nozzle. He also suggests that the gaseous flow sets the velocity and length scales and the liquid flow damps high frequency perturbations and only allows the amplification of large wavelengths. His empirical observations led him to postulate that the vorticity layer of the gaseous stream is responsible for the instability and not the surface tension between the two fluid streams.

Perrault-Joncas and Maslow (52) performed a linear stability study of a compressible coaxial jet with velocity and temperature profiles characteristic of a turbofan engine exhaust, with outer to inner velocity ratio varying between 0.5 and 0.8. They conclude that there are two primary modes of instability for the velocity profiles they investigate. The secondary mode, associated with the outer stream, is found to have a larger growth rate; however, the two modes seem to behave independently. The outer to inner velocity ratio primarily affects the mode of the inner stream and the diameter ratio has more influence on the mode of the outer stream. They point out that it is simple to diminish the effects of the most unstable outer stream mode by increasing the momentum thickness of the outer stream through changes in the geometry of the flow.

1.3 Present Studies

1.3.1 Droplet Combustion Experiment

The main focus of the droplet combustion experiment consisted of measuring the flame deflection and burning rate constant of different alternative and conventional fuels. Results were compared to previous studies by our research group at UCLA (14; 15) and others (9; 10; 12). Chapter 2 introduces the experimental setup of the droplet combustion experiment and chapter 3 presents the results.

1.3.2 Coaxial Jet Experiment

Another example where condensed phase material is affected by acoustic excitation is in supercritical coaxial jets in LREs. Investigation of the interaction between high-amplitude acoustic waves and the flow present at the exit of a coaxial jet injector has useful applications in cryogenic liquid rockets. Understanding the effects of acoustic excitation on mixing and fluid mechanics of subcritical and supercritical jets can provide useful information for improved processes in injector design (25).

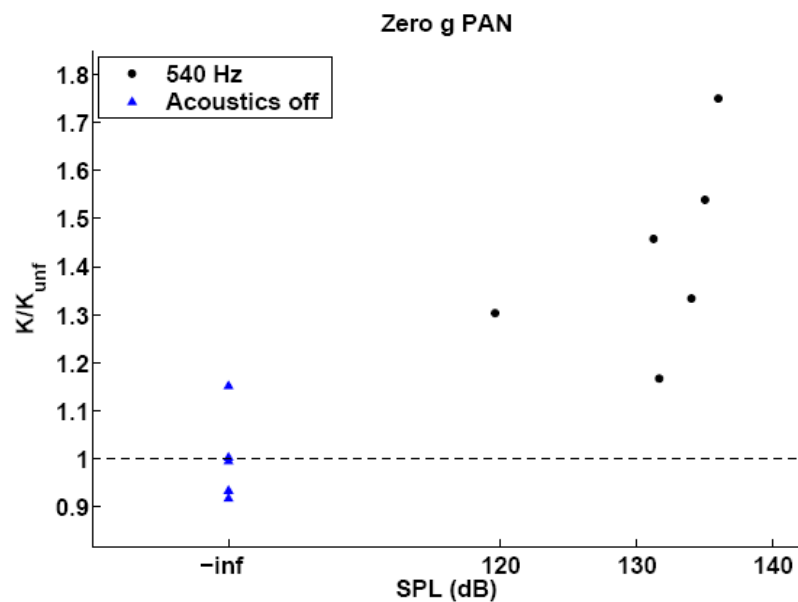
Previous studies have shown the relevance of changes in the exit area of a coaxial jet injector and the physical processes taking place in the vicinity of the device due to acoustic forcing (53; 54; 55). Richecoeur, et al. (28) found correlation between the intact core-length of the coaxial jet and the enforced acoustic excitation. For several years, Chehroudi and co-workers (40; 46; 56) have investigated supercritical jet flows at high Reynolds numbers, which are of interest to practical applications in propulsion systems.

In recent experiments, Davis and Chehroudi (21) explored large scale acoustic excitation of a liquid(interior)/gaseous(exterior) coaxial nitrogen jet injected into a gaseous nitrogen chamber at high pressures. Subcritical, near-critical, and supercritical

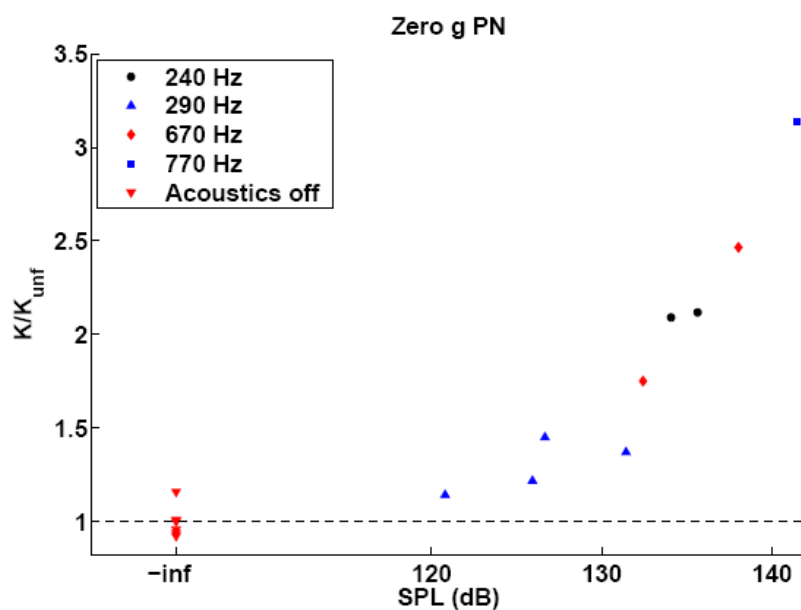
chamber pressures were explored, with acoustic excitation of the jet in the vicinity of the pressure node (or velocity antinode) and with amplitudes as high as 180 dB at pressures up to 5 MPa. As indicated, for example, in Figure 1.7 (from their paper), the strongest effect of acoustic excitation was observed under subcritical pressures, whereby strong jet oscillations and liquid jet spread and breakup were enhanced. The cause of this behavior is not completely understood, but there is the suggestion that the operation of the acoustic driver (operating at constant power for different pressure amplitudes) may be a limitation. Detailed quantification of the jet dark-core length via high speed shadowgraph movies and image processing allowed scaling with the momentum flux ratio for the different regimes explored (see Figure 1.8).

Data from Davis and Chehroudi (21) constitute the first exploration of subcritical conditions in the vicinity of momentum flux ratio $M = 10$. They also have found that there is correlation between the outer-to-inner velocity ratios of the injector and the root-mean-square value of the fluctuations in dark-core length of the jet under acoustic excitation. It is thought that an important driving mechanism of the processes leading to combustion instabilities in a rocket engine is inhibited at high outer-to-inner coaxial jet injector velocity ratios. The present study aims to answer these questions.

Also, in the present study, the different response of the coaxial jet to acoustic excitation for different conditions and properties of the flow will be used to present a qualitative stability analysis that will identify convective/absolute and local/global modes and the regimes for which the coaxial jet flow can be assigned any of these instability characteristics.

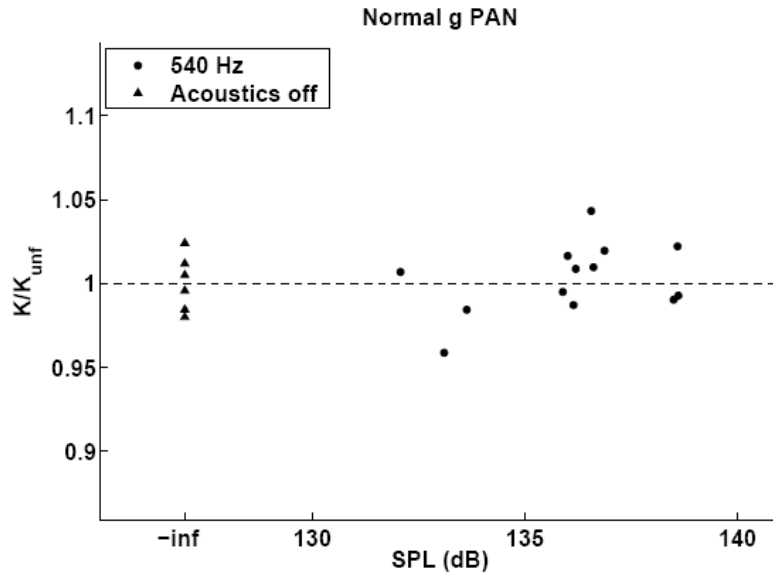


(a)

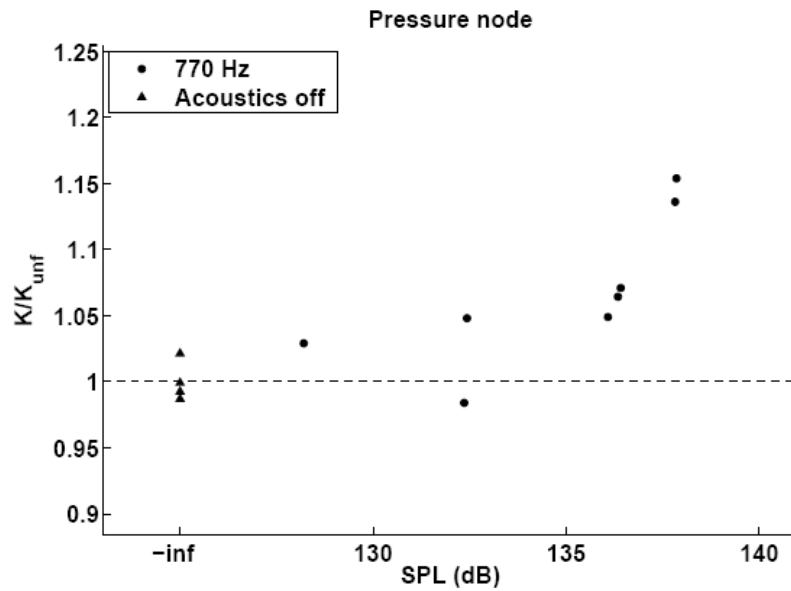


(b)

Figure 1.1. In microgravity, effect of sound pressure level, SPL, on the mean burning rate constant K normalized by its mean value in the absence of acoustic excitation, K_{unf} , (a) at a pressure antinode, PAN, and (b) at a pressure node, PN. From Dattarajan (14).



(a)



(b)

Figure 1.2. In normal gravity, effect of sound pressure level, SPL, on the mean burning rate constant K normalized by its mean value in the absence of acoustic excitation, K_{unf} , (a) at a pressure antinode, PAN, and (b) at a pressure node, PN. From Dattarajan (14).



(a)



(b)



(c)



(d)

Figure 1.3. Photographs of a burning droplet in microgravity (a) with no forcing and (b) forced at a pressure node at 770 Hz; and in normal gravity (c) with no forcing and (d) with forcing at a pressure node at 770 Hz. From Dattarajan (14).

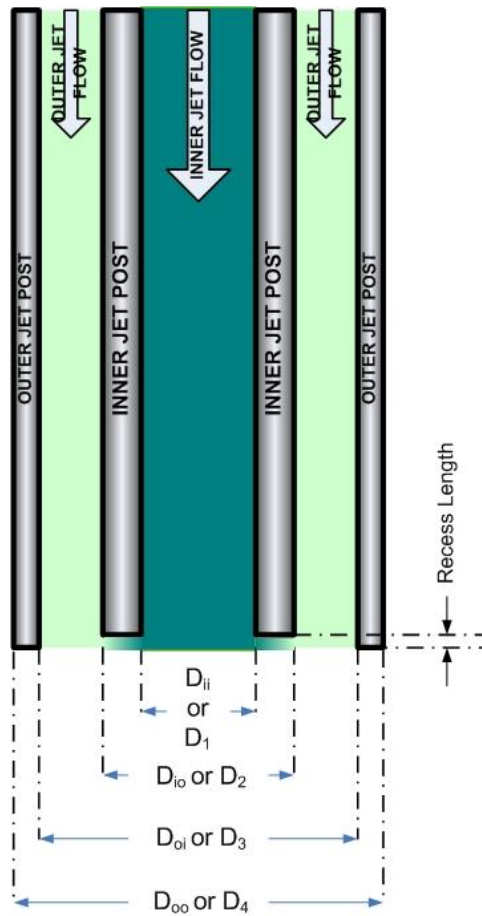


Figure 1.4. Schematic of coaxial jet flow.

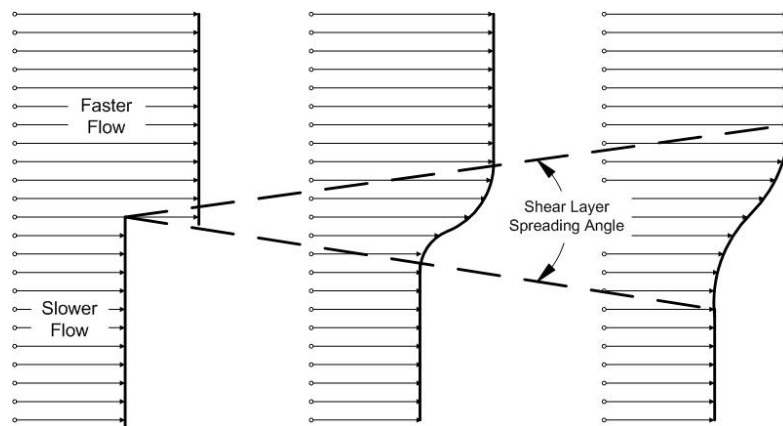


Figure 1.5. Schematic of a 2D shear layer spreading angle.

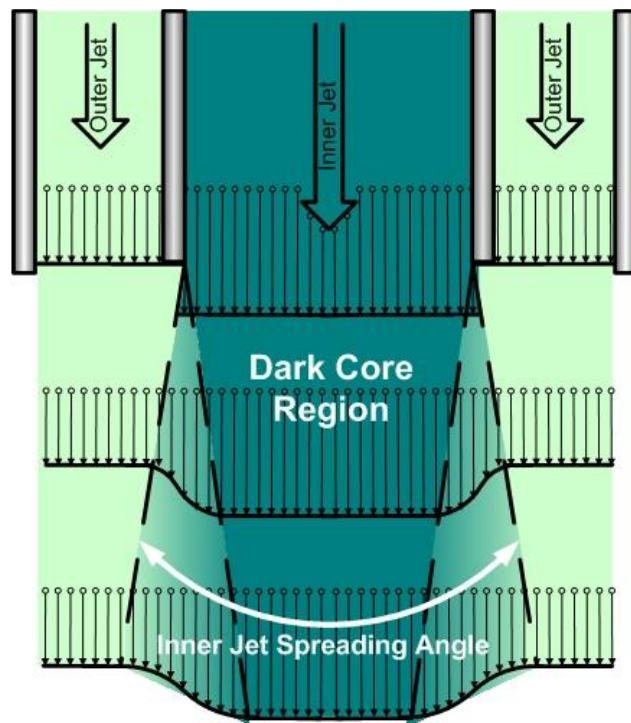


Figure 1.6. Schematic of the dark core region and the inner jet spreading angle of a shear coaxial jet.

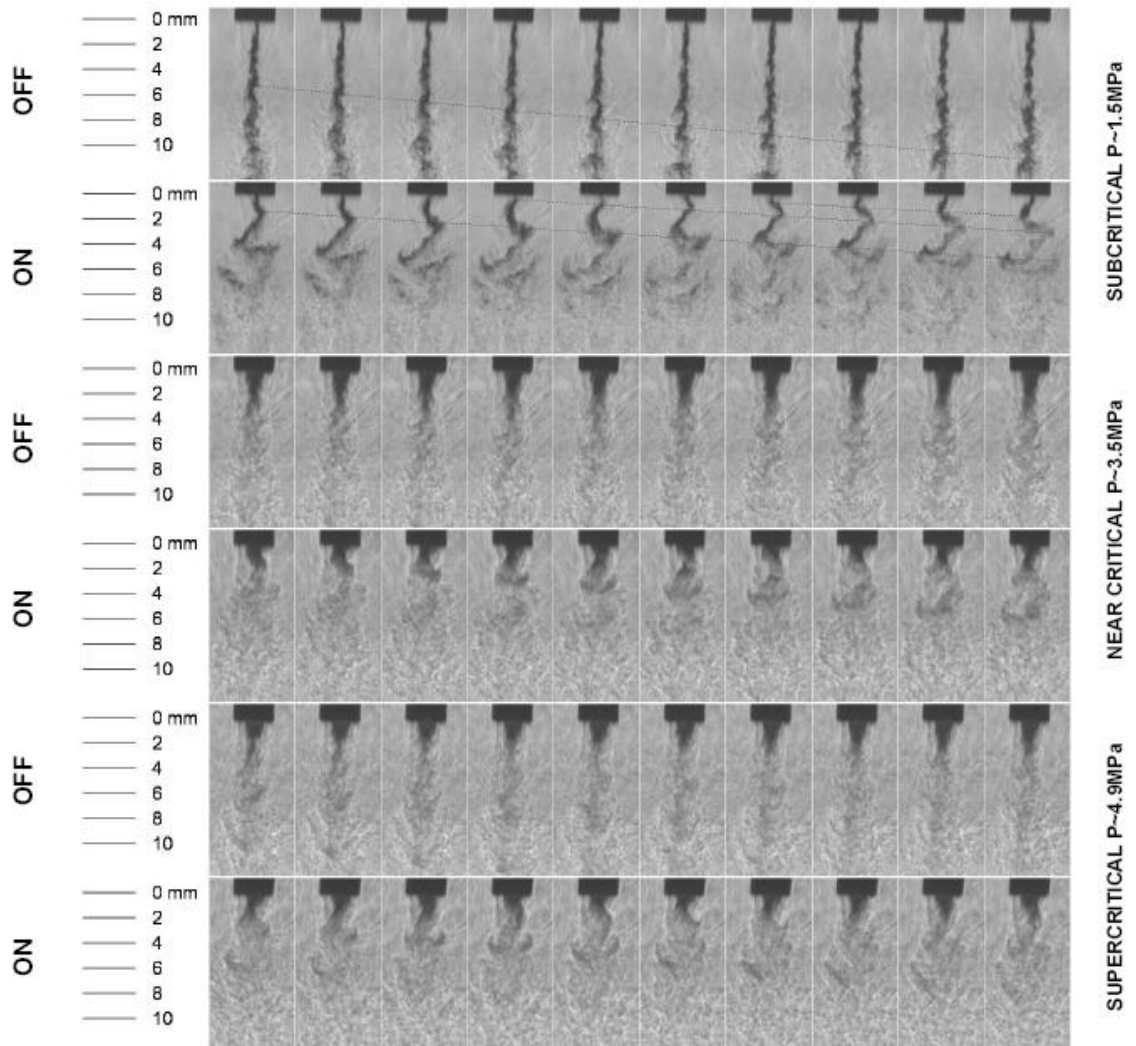


Figure 1.7. Consecutive frames from high-speed shadowgraph movies with the acoustic driver turned off (in rows 1, 3 and 5) and on (in rows 2, 4, and 6) at $\sim 3\text{kHz}$. Time increases from left to right with an interval of $55.6\ \mu\text{s}$ between frames. The first two rows are at a subcritical chamber pressure ($\sim 1.5\ \text{MPa}$), the third and fourth rows are at a near-critical chamber pressure ($\sim 3.5\ \text{MPa}$), and the fifth and sixth rows are at a supercritical chamber pressure ($\sim 4.9\ \text{MPa}$). The light gray lines in the first and second rows connect fluid structures as they evolve in time. Images from Davis and Chehrودي (21).

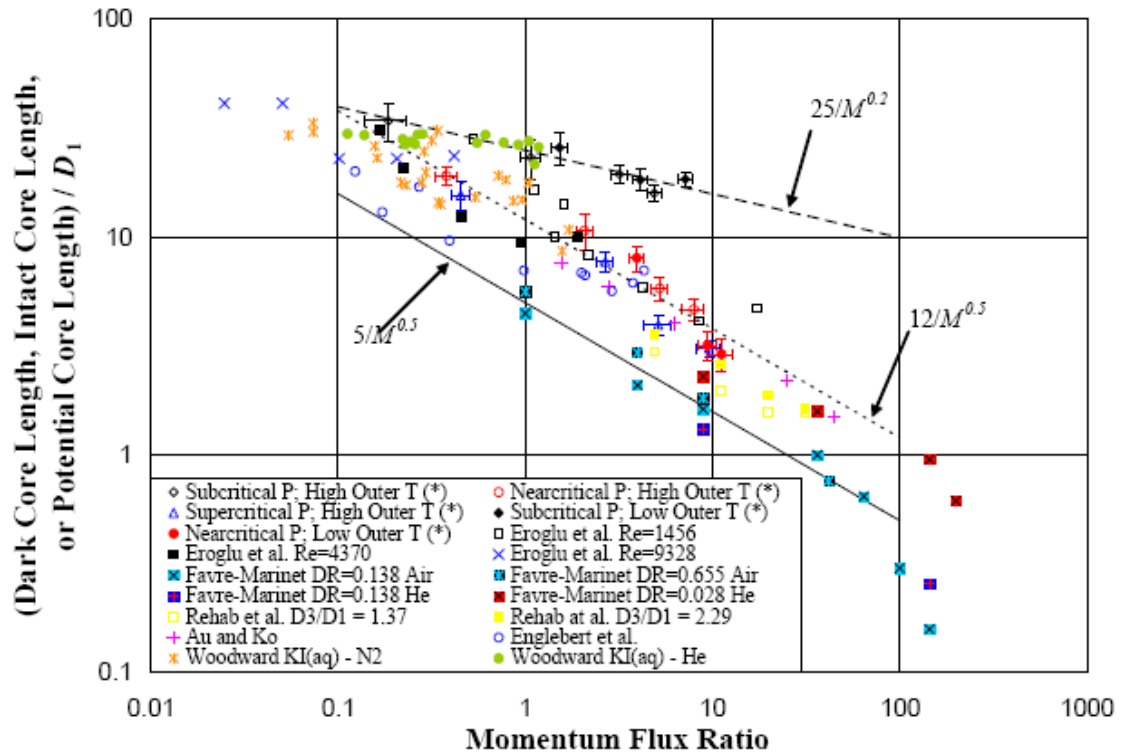


Figure 1.8. Comparison of dark-core length measurements by Davis and Chehroudi (21) with all other data available in the literature of core-length vs. momentum flux ratio. Amongst the data reported by others, Eroglu, et al., Englebert, et al., and Woodward are two-phase flows and the rest are single phase. The references for the data are found in Table 1 of Ref. (21).

CHAPTER 2

Experimental Setup – Acoustically Coupled Fuel

Droplet Combustion

The present studies involving fuel droplet combustion were performed using the same experimental apparatus used by Dattarajan, et al. (14; 15) to analyze the behavior of methanol burning droplets under microgravity and normal gravity conditions. The current setup at UCLA was slightly modified to study the combustion behavior of various liquid alternative fuels in the presence of acoustic disturbances.

2.1 Acoustic Waveguide

In the present experiments, standing acoustic waves were generated by a loudspeaker inside a cylindrical acoustic waveguide. The frequency and amplitude were adjusted with a function generator and a signal amplifier. The continuously fed burning fuel droplet was situated at the center of the waveguide, which operated at atmospheric pressure and room temperature and featured quartz windows situated at either side of the center of the waveguide for optical access.

Figure 2.1 shows a detailed schematic diagram of the experimental device. The aluminum waveguide has an inner diameter of 11.4 cm and a maximum length of 90 cm. An 8-ohm speaker with a maximum power output of 40W and a wave reflector placed at

the opposite end, consisting of a flat aluminum disc, were used to generate the standing waves. The distance L between the speaker and the reflector was fixed using an internal movable rod assembly connected the speaker and reflector. This distance was chosen to be an integral multiple of half the acoustic wavelength, $\frac{1}{2} \lambda = \frac{1}{2} c/f$, where c is the speed of sound in the waveguide and f is the applied frequency of acoustic excitation. The standing waves produced by this configuration allowed the droplet to be exposed to conditions corresponding to either a pressure node or a pressure antinode, depending on the applied frequency f .

In order to assess the response of the burning droplet to different acoustic conditions, the speaker and reflector were moved relative to the droplet, enabling the location of the pressure node or antinode to be moved relative to the droplet as well. For the current experiments, the pressure node was estimated to be at or very close to the burning droplet by moving the fixed speaker and reflector and applying different loudspeaker excitation frequencies so that eventually the local pressure at the location of droplet within the waveguide (at the pressure transducer labeled P1 in Figure 2.1) was a minimum and the pressure at the end of the waveguide (at P2 in Figure 2.1) was a maximum. A pressure antinode at the location of the droplet was estimated when the local pressures measured by P1 and P2 were both local maxima.

Figure 2.2 shows a series of pressure transducer measurements in the present device made by Dattarajan et al (14; 15). Based on maxima and minima noted above, pressure nodes were found at 290 Hz and 780 Hz, and a pressure antinode was found at 540 Hz, for the fixed waveguide length of approximately 62 cm.

It is important to note that the position of the droplet at a pressure node or at a pressure antinode was actually approximate here, since the vibrating diaphragm of the speaker and the diameter of the flush-mounted pressure transducer P1, about 1.5 cm, introduced ambiguity in the exact location of the maximum or minimum pressure. Dattarajan, et al. (14; 15) attributed an observed offset between the pressure node or antinode location as estimated by pressure-transducer measurements and the “true” pressure node or antinode, based on flame orientation and the acoustic radiation force F_R (eqn. (1.2)), to this ambiguity. The nature and magnitude of this offset were explored in the present experiments as well.

2.2 Droplet Generation

The experimental setup featured a 0.38 mm outer diameter hollow glass capillary that was used to suspend the droplet inside the waveguide. This uncommon feature allowed continuous liquid fuel delivery to the droplet. Ethanol and methanol experiments were conducted using a nitrogen-pressurized 300 ml tank, and a filter to eliminate particulate contaminants. The fuel was then diverted to the capillary by a solenoid valve. The volumetric flow rate Q_v of the fuel delivered to the capillary could be altered by changing the duty cycle of the solenoid valve. For the JP-8/F-T blend, due to degradation of internal components of the microvalve, a syringe pump was used instead for controlled fuel delivery to the capillary.

The range of volume flow rates Q_v delivered by the syringe pump matched those used for the alcohol fuels, which were of the order of 1 mm³/s. The volumetric flow rate

Q_v and the droplet size were used to determine the burning rate constant K , as will be described below. A protective shroud was placed above the end of the glass capillary in order to prevent vaporization of the fuel within the glass capillary just above the droplet. Further details on the droplet delivery system may be found in the dissertation of Dattarajan (14).

2.3 Measurement Methods

For the experimental work of Dattarajan, et al. (14; 15), the instantaneous fuel droplet width was examined by back-lighting the droplet and imaging the magnified droplet shadow onto a linear photodiode array. This system was used during microgravity tests along with a closed loop control algorithm that used the width measurements to control fuel delivery to achieve a constant droplet size. The present experiments were only performed in normal gravity, and the droplet width measurements were only monitored and not used for control. A constant volumetric flow rate Q_v was used in each set of experiments, determined from calibration of the microvalve or direct input of the volume flow rate on the syringe pump, and from this information the droplet burning rate K could be determined.

From continuity, for a *spherical* droplet of diameter d , the instantaneous K may be evaluated according to (Dattarajan et al. (14; 15)):

$$K = \frac{4Q_v(t)}{\pi d(t)} - 2d\dot{d}. \quad (2.1)$$

Because of the non-spherical geometry of the droplet in normal gravity tests, video images of the burning droplet were used to determine the cross-sectional area of the oblong droplet. An image processing algorithm in MATLAB, incorporating specially written edge-detection software, was used to estimate the effective volume of the actual oblong droplet. This volume was then equated to that of a spherical droplet of equivalent diameter d_{eqvs} , a procedure also followed by Struk et al. (5) as well as Dattarajan et al. (14; 15) in normal gravity and microgravity droplet combustion experiments. Droplet burning rate constants based on d_{eqvs} in equation (2.1) were then determined, and average K values over time computed. Typically the transient term in equation (2.1) is not large, per the detailed investigation by Dattarajan (14), but it was nevertheless incorporated into the present measurements of K .

2.4 Experimental Procedure

To perform the experiments for droplets burning in the absence of acoustic excitation, fuel was loaded into the tank or the syringe pump, then the valve was calibrated or the syringe pump flowrate was set to the desired constant value. Then an incandescent ignitor was used to ignite the droplet and initiate quasi-steady combustion. A video cassette recorder was used to store the images that a video camera, with optical access to the burning droplet, provided. The video of the burning droplet was later processed by the previously mentioned edge-detection software to obtain an equivalent diameter d_{eqvs} over time. A curve fit for $d_{eqvs}(t)$ as described in Dattarajan (14) is then used to calculate K values according to equation (2.1), K may then be averaged over the

2-3 seconds of data acquisition. After two or three burning cases, the waveguide was purged with air to discard the products of combustion accumulated.

For acoustically excited cases, before droplet combustion commenced, the loudspeaker was turned on and the frequency was adjusted to achieve a P2/P1 maximum for an estimation of a pressure node or a P2/P1 minimum for a pressure antinode. The amplitude was adjusted to the maximum value that could be achieved without having flame extinction.

A different type of test was conceived after observing different extinction conditions for different fuels at high sound pressure levels: a flame extinction study. This study consisted of exposing a burning droplet to increasingly high amplitudes near (but not precisely at) a pressure node until the flame was instantaneously extinguished. These pressure amplitudes at extinction were recorded, and estimates of the velocity perturbation at those amplitudes and the associated strain rates could be approximated.

With the assumption that the flow in the vicinity of the burning droplet may be approximated as stagnation point flow, a rough estimate of the strain rate close to extinction may be obtained in terms of the velocity perturbation u' and the droplet standoff distance:

$$\varepsilon = \frac{|u'|}{2d_{standoff}}. \quad (2.2)$$

A photograph depicting $d_{standoff}$ and u' is shown in Figure 2.3. The velocity perturbation u' was obtained from measurements with the pressure transducer P1 in

Figure 2.1. The pressure transducer output in volts (V) was converted to Pascals (Pa) using calibration information from the manufacturer and then the following relation was used to obtain the velocity measurements:

$$u' = \frac{p'}{\rho c}, \quad (2.3)$$

where ρ is the density of the air surrounding the flame and c is the local speed of sound.

2.5 Uncertainty Analysis

The uncertainty analysis of the measurement of the burning rate constant K for the acoustically excited droplet experiment was carried out by Dattarajan (14). For the cases in the present study where the syringe pump was used to deliver the flow to the droplet, the overall uncertainty of the measurement was lower. When the volumetric flow rate, Q_v , was measured using a solenoid valve the precision uncertainty found by Dattarajan was 8-10% (14). However, the syringe pump has an accuracy of $\pm 1\%$. Thus a precision uncertainty of the same magnitude (1%) can be assigned to the syringe pump and a precision error of approximately 10% for the burning rate constant K is obtained instead of the original 13% found by Dattarajan (14) when using the solenoid valve to deliver the flow. In addition, the syringe pump reproducibility of $\pm 0.1\%$ should bring the flow rate bias error indicated by Dattarajan from 10% to less than 1 %.

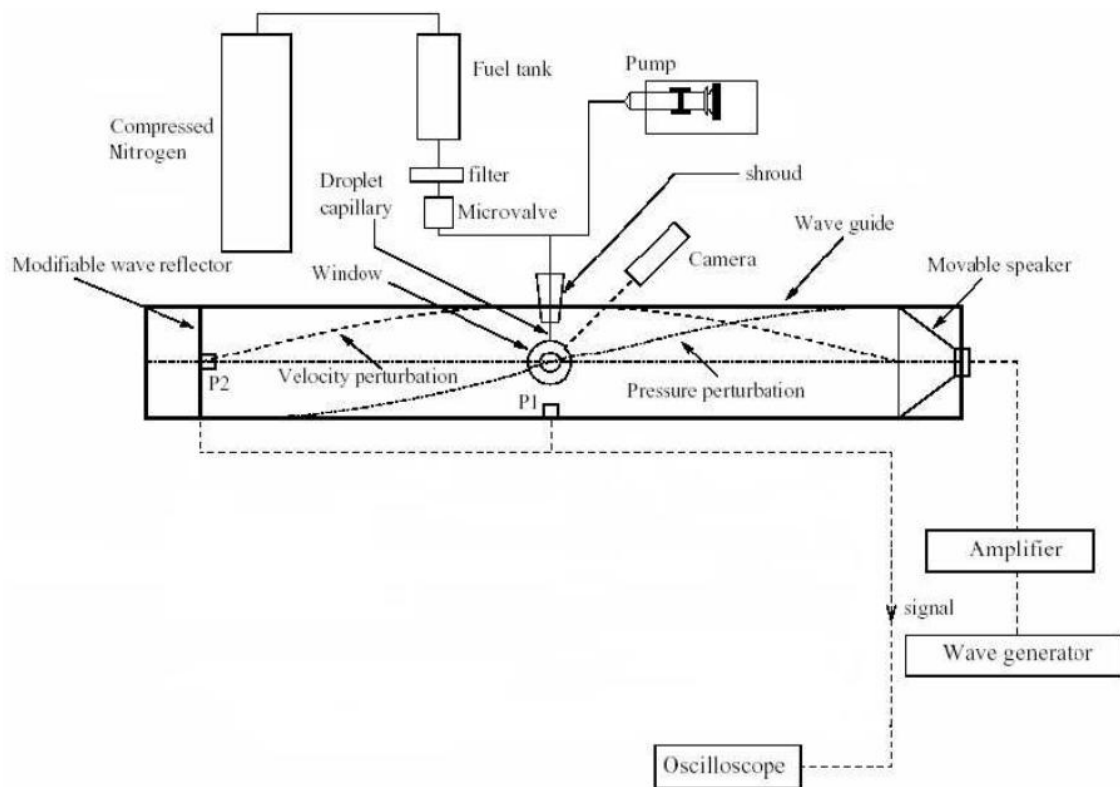


Figure 2.1. Experimental setup of the acoustic waveguide and feed droplet system. The tank and microvalve arrangement was used for the tests with methanol, while the syringe pump was used for all other fuels.

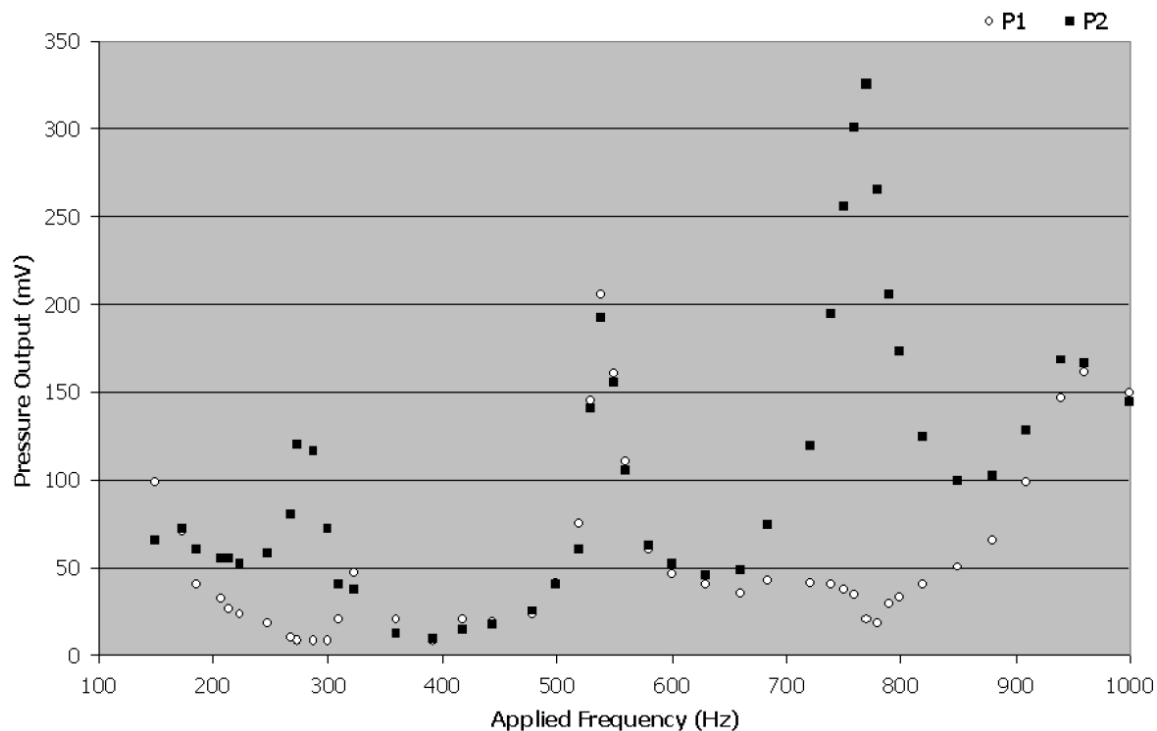


Figure 2.2. Acoustic characterization of the waveguide as measured by pressure transducers at P1 and P2. From Dattarajan (14). The distance between the speaker and reflector was 62 cm.

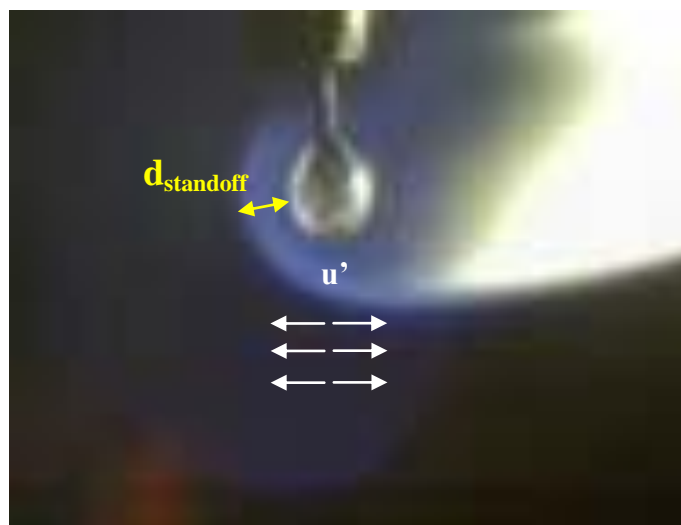


Figure 2.3. Photograph of a burning fuel droplet showing standoff distance ($d_{standoff}$) and velocity perturbation (u') used to obtain strain rate estimates of the droplet at extinction.

CHAPTER 3

Results – Acoustically Coupled Fuel Droplet Combustion

3.1 Baseline Burning Rate Constants

The initial set of experiments took place in the absence of acoustic forcing. The burning rate constants of four alternative liquid fuels, including ethanol, methanol, pure Fischer-Tropsch synthetic fuel and a 50% - 50% blend (by volume) of the F-T and JP-8 aviation fuel was obtained. Representative images of the burning droplets without the effects of acoustic excitation are shown in Figure 3.1. The oblong droplets and surrounding symmetric non-premixed flames burned in a relatively steady fashion when fuel was delivered at a constant volumetric rate. These tests were designed to quantify “baseline” droplet combustion processes for a comparison with the behavior of acoustically coupled burning droplets. K values were obtained from the equivalent diameter, d_{eqvs} , extracted using the edge-detection software and video imaging from the droplet. Instantaneous K values were found to be approximately constant over time for constant volumetric flow rates, as seen for methanol by Dattarajan et al (14; 15).

Table 3.1 shows that K values for methanol and ethanol based on d_{eqvs} were close to available data for fuel droplets burning in normal gravity. K values for the JP-8/F-T

blend were compared to available data for JP-4 fuel and found in agreement. No conclusion could be made for the pure F-T fuel since no burning rate data could be found for this synthetic fuel. Effects such as water adsorption, capillary length and distillation on methanol droplet burning rates were relatively minimal, as documented by Dattarajan (14). Adsorption was minimized in the current configuration due to continuous fuel replenishment and, according to Dattarajan (14), alterations in the capillary length between 2.0 mm and 3.2 mm did not yield significant or systematic changes in K for methanol. Thus, a capillary length of approximately 3.2 mm was used, which isolated the droplet from the shroud while at the same time prevented fuel boiling. Distillation of volatiles was observed to occur with the pure F-T fuel and the JP-8/F-T blend and was often visible within the droplets in video images; it is not likely that this affected the burning rate constant significantly, since the magnitudes of the unforced K values were in the correct range.

3.2 Burning Rate Constants under Acoustic Excitation

The effects of acoustic excitation on droplet burning rates were explored by first placing the estimated pressure node (maximum velocity perturbation) or pressure antinode (no velocity perturbation) near the droplet, by using pressure transducer measurements described previously. The distance between the speaker and reflector, 62 cm, produced pressure nodes at the waveguide center for applied frequencies of around 290 Hz and 780 Hz, and a pressure antinode at a frequency of 540 Hz. These estimates were obtained in the absence of combustion, at room temperature conditions.

As noted in Dattarajan et al. (14; 15), there was some uncertainty in the specific conditions creating a pressure node or antinode at the center of the waveguide where the burning droplet was placed. Because of the relatively large diameter of the pressure transducer P1 (1 cm) compared with the diameter of the droplet (of about 1.6 mm), and the ambiguity introduced by the precise location of the loudspeaker (i.e., with a vibrating membrane), only an approximation for the exact location of the pressure node or antinode near the center of the waveguide could be made using the pressure transducers.

Video images showing a burning droplet that was supposedly located at a pressure node or antinode according to pressure transducer readings showed flames that were actually deflected to one side or the other. According to the theory of Tanabe et al. (11; 12), per eqn. (1.2), this suggests that an actual offset of the droplet from the “true” pressure node or antinode exists. Examples of this phenomenon for all four fuels are shown in Figure 3.2, for droplets burning near the vicinity of a pressure node (determined by a maximum in P2/P1), with forcing at approximately 780 Hz. The acoustic radiation force in eqn. (1.2) reduces, for a standing wave, to:

$$F_R = (\rho_s - \rho_o)V \left[\mp 4\alpha \left(\frac{I}{z_a} \right) \left(\frac{2\pi f}{c} \right) \sin \left(\frac{2\pi x}{\lambda} \right) \cos \left(\frac{2\pi x}{\lambda} \right) \right]. \quad (3.1)$$

Here c is the speed of sound ($= f\lambda$), z_a the acoustic impedance ($= \rho c$), and I the acoustic intensity. An equivalent acoustic acceleration term, $g_a \equiv \alpha \frac{\partial(\overline{u'^2})}{\partial x}$, is represented by the term in square brackets. A minus sign in the bracketed term corresponds to the case of a pressure node positioned at the center of the waveguide ($x = 0$); and a plus sign corresponds to a pressure antinode at the same location. Therefore, if the droplet is

located to the right ($x > 0$) or left ($x < 0$) of the waveguide center, a finite acoustic radiation force would try to deflect the flame and hot gas zone surrounding the droplet, scaling with frequency as indicated in eqn. (3.1). The observed flame deflection in Figure 3.2 is similar to that observed by Dattarajan et al. (14; 15) for methanol droplet combustion in both microgravity and normal gravity, and is also seen by Tanabe et al. (11; 12) in their microgravity studies with n-decane droplets.

3.3 Pressure Node Location Offset

As noted above, Figure 3.2 shows the flame deflection when the speaker and reflector were placed so that the transducer readings indicated a maximum in P_2/P_1 at the waveguide center. This suggested that there was actually an offset of the burning droplet from the “true” pressure node. To assess the magnitude and the influence of the offset on fuel burning rates, the speaker and reflector were moved systematically to the right or left during these experiments, keeping L constant. Since the droplet and pressure transducer P_1 were each fixed at their original locations, by moving the speaker and reflector, the pressure node or antinode relative to the fixed droplet could be moved. In the present tests, the 780 Hz pressure node with $L \approx 0.62$ m was moved up to 7 cm to the left of the originally estimated pressure node location (slightly more than an eighth of a wavelength), and up to 8 cm to the right. This tests were also conducted for the 540 Hz pressure antinode.

A diagram of the displacements of speaker and reflector is shown in Figure 3.3, where y corresponds to the location of the pressure node (PN) relative to the position of

the droplet, and y' corresponds to the location of the droplet relative to the pressure node. The figure shows that when the speaker and reflector (S&R) were moved substantially to the right, one approaches a condition where the PN was located to the right of the droplet, or the droplet was located to the left of the PN ($y' < 0$ as in Figure 3.3b). In this case, if the droplet was positioned to the left of the PN, the sign of the acoustic radiation force in eqn. (3.1) would become negative, shifting the flame and hot gases away from the pressure node toward the wave reflector on the left side of the waveguide.

In contrast, when the S&R were moved substantially to the left, so that $y' > 0$ as in Figure 3.3c, the opposite would occur, causing the flame to deflect to the right, away from the PN. For the pressure antinode (PAN) case, e.g., at 540 Hz, the opposite behaviors should take place when the S&R are moved to one side or the other. The flame deflection observed during PN acoustic excitation in Figure 3.2 suggests that the conditions produced by a maximum in P_2/P_1 actually may have placed the droplet to the right of the true PN, with $y' > 0$ and the flame deformation to the right.

To assess this supposition, burning droplets of three fuels (ethanol, methanol, and the fuel blend) were exposed to situations where a pressure node or antinode would lie to either left or right of the droplet. The S&R were moved systematically to the left and to the right in relation to their original positions (e.g., as shown for the PN at 780 Hz in Figure 3.2). Images extracted from video of the burning ethanol droplet situated at different locations relative to the pressure transducer estimated pressure node, for 780 Hz forcing, are shown in Figure 3.4a-f. These images show that as the speaker and reflector were displaced relative to the burning droplet, the direction of the flame deflection

changed its orientation. This switch occurred when the speaker and reflector were displaced between 2.4 cm (Figure 3.4c) and 4.9 cm (Figure 3.4d) to the right of their original positions, suggesting that the “true” pressure node was likely coincident with the burning droplet for conditions lying between Figure 3.4c and Figure 3.4d. It can be surmised that in Figure 3.4a-c, the droplet must have been located to the right of the PN (so that y' or x in eqn. (3.1) was positive), and in Figure 3.4d-f, the droplet probably was located to the left of the PN (so that y' or x was negative). These characteristic flame shifts were also observed during droplet combustion of methanol (e.g., shown near a PAN at 540 Hz in Figure 3.5a-f) and for the JP-8/F-T fuel blend (e.g., shown near a PN at 785 Hz as in Figure 3.6a-f).

While the change in orientation for the alcohols occurred in roughly the same location, when the S&R were displaced between 2.7 cm and 5.2 cm to the right of their original positions, the flame switch location for the JP-8/F-T blend occurred further to the right, when S&R were displaced between 5.1 cm and 6.4 cm in that direction. Further exploration of the phenomena by Sophonias Teshome and Hann-Shin Mao indicated that placing two speakers in the waveguide, rather than a speaker and reflector, made the acoustic field much more symmetric and the flame switch location more repeatable (57). During tests with either configuration, however, an interesting highly unstable flame oscillatory behavior was exhibited when the droplet was positioned very close to the PN. This was also observed by Dattarajan et al. (14; 15) in microgravity.

3.4 Relation between Acoustic Acceleration and Burning Rate Increase

The acoustic radiation force ideas of Tanabe et al. (11; 12) are generally consistent with results obtained in the offset studies presented in the previous section. Flame orientations were consistent with the sign predicted by eqn. (3.1). The approximate positions of the S&R at which flame switch occurred were quantified for all fuels and excitation conditions. The location of the “true” $x = 0$ location (for a PN or a PAN) was then set at the location of flame switch from the experiments where $x = 0$ was presumed to be coincident with the burning droplet. Once the range for x was determined in this manner, the acoustic acceleration term, g_a , was estimated from the term in square brackets in eqn. (3.1). Since the relative magnitude of the term α is approximate in any case for each fuel (e.g., for methanol, α is approximately 1.15, but might vary due to temperature dependence, etc.), α was set to unity in the relation for g_a .

Tanabe et al. (11; 12) as well as Dattarajan et al. (14; 15) suggest that a direct correlation between the amplitude of the acoustic radiation force F_R and the droplet burning rate K might exist. In principle, the influence of a vertical buoyancy force in normal gravity conditions could limit the influence of an acoustic radiation force acting horizontally. However, the higher amplitudes of forcing here (over 138 dB) acting perpendicularly to gravity, allowed the influence of the acoustics to have a somewhat greater impact than in previous studies. For example, prior experiments by Dattarajan et al. (14; 15) did not allow strong enough excitation at the 540 Hz PAN to be able to

produce flame distortion in normal gravity, a phenomenon that was always routinely observed at high forcing amplitudes in the present experiments. Hence, at least in terms of magnitude, the correlation between F_R or g_a and K could be studied for several alternative fuels.

Ethanol, methanol, and the JP-8/F-T fuel droplets were exposed to pressure node conditions (at approximately 780 Hz and 290 Hz) and pressure antinode conditions (at approximately 540 Hz). Average burning rate constants based on time averages over a 2-second period were obtained for a range of different droplet positions relative to the waveguide center. Measured average K and d_{eqvs} values for different positions of the speaker and reflector (measured relative to their original position as determined by the magnitude of P2/P1), are plotted in Figure 3.7 for ethanol at the 780 Hz PN, in Figure 3.8 for methanol at the 540 Hz PAN, in Figure 3.9 for the JP-8/F-T blend at a 785 Hz PN, in Figure 3.10 for ethanol at the 540 Hz PAN, in Figure 3.11 for ethanol at the 290 Hz PN, and in Figure 3.12 for ethanol at the 800 Hz PN. The first three figures correspond to the flame photos shown in Figure 3.4, Figure 3.5 and Figure 3.6, respectively. A value of acoustic acceleration g_a equalling zero is assumed at the position of the S&R where the flame switch occurred, corresponding to the “true” node location at $x = 0$ in eqn. (3.1). The solid lines on the K plots represent a curve fit of the experimental data. The solid lines on the g_a plots represent the theoretical dependence of the absolute value of g_a on x , assuming an average value of the acoustic intensity I . In reality, however, the sound pressure level and hence I were slightly different for the different conditions explored, and the data points on the plots for g_a represent the more accurately determined values

based on the local I values. In addition to the previous results, data for one pure F-T fuel test is also included in Figure 3.9. For this test, the S&R were located at the pressure transducer estimated pressure node at 785 Hz. A droplet image of this test is shown in Figure 3.2d.

In theory, droplets burning near the “true” pressure node or pressure antinode should have the same burning rate constant K as for the unforced burning droplet. This is due to a zero acoustic radiation force F_R or acoustic acceleration g_a (see eqn. (3.1)) at the node location. Most of the present results, when compared with unforced values in Table 3.1, suggest that this proposition holds; however, in some cases, such as methanol at the 540 Hz PAN, a reduction in the burning rate constant might be taking place. On the other hand, when the droplet was placed away from the “true” PN or PAN, a general trend of increasing burning rates was observed. The increases were at most about 20% for the alcohol fuels (see Figure 3.10) and the JP-8/F-T blend, and in recent studies, up to 28% for the pure F-T fuel (see Figure 3.9). Although the K value of the pure F-T fuel is not necessarily greater than the K value of the JP-8/F-T blend in the figure, the increase over the unforced value is higher for the pure F-T fuel given its lower unforced burning rate constant value compared to that of the JP-8/F-T fuel (see Table 3.1)

An exception to the previous trends is found at low frequencies, such as ethanol at the 290 Hz PN (see Figure 3.11). There is little discernible trend in the burning rate constant as the location of the speaker and reflector is changed, or actually, one that is somewhat the opposite to the trend in g_a . This behavior could be explained by the low acoustic radiation forces acting on the hot combustion products around the droplet. Since

the acoustic acceleration depends on the frequency applied, its maximum value for this case ($\sim 1.3 \text{ m/s}^2$) is very low compared to the 540 Hz ($\sim 4 \text{ m/s}^2$) and 780 Hz ($\sim 5 \text{ m/s}^2$) cases.

The general consistency between the experimental increases in burning rate constant K and the theoretical increases in acoustic acceleration for $g_a \geq 4 \text{ m/s}^2$ is important and seems to confirm the suppositions of Tanabe et al. (11; 12) and Dattarajan et al. (14; 15) about the relation between K and F_R . Even more significant is the fact that increases were observed for both pressure node and antinode forcing conditions. One important experimental observation is the fact that, as flame deflection increased, the flame front got closer to the droplet. A closer flame front enhances the rate of release or vaporization of reactants due to increased heat transfer between the flame and the droplet. This mechanism could be directly related to the observed increases in K at the conditions mentioned above. This could also explain the lack of a trend in K for the low frequency experiments with ethanol at the 290 Hz, since little or no deflection of the flame was observed in this case.

To our knowledge, investigation of acoustic forcing effects on a burning fuel droplet near a pressure antinode has not been explored to any significant degree in the past and it might provide information on whether enhancement of condensed phase fuel consumption at a pressure antinode could promote or suppress flow instabilities. The similarities in combustion properties for the alcohol fuels and the F-T fuels were remarkable, given their differences in reaction and diffusion time scales.

3.5 Fuel Extinction Studies

In further investigations, fuel droplets were exposed to excitation when situated at a fixed location with respect to a pressure node at 780 Hz. The location was selected so that the theoretical acoustic acceleration was above 2 m/s^2 . Then the droplet was ignited and, after it reached quasi-steady burning conditions, it was exposed to a standing wave of increasing acoustic intensity. The forcing amplitudes at which extinction (flame burnout) was observed were recorded. Photographs of the extinguishing flames for various fuels are shown in Figure 3.13 -Figure 3.16. In some cases the flames extinguished near the stagnation region of the droplet but persisted in the wake of the droplet before complete burnout. It was found that the perturbation amplitudes at extinction for the F-T fuel (see Figure 3.13), the JP-8/F-T blend (see Figure 3.14), and ethanol (see Figure 3.15) all corresponded to sound pressure levels close to 141 dB, and velocity perturbations of approximately 0.75 m/s. However, for methanol, the corresponding sound pressure level at extinction was 143 dB, for a velocity perturbation of approximately 1.0 m/s (see Figure 3.16).

Estimated values for the equivalent local strain rate in the vicinity of the droplet were calculated using a rough approximation of the definition for the strain rate as the “radial velocity gradient at the flame position” (58). The radial velocity gradient was approximated using eqn. (2.2) where the velocity perturbation u' is divided by a characteristic length of the flow, in this case twice the flame standoff distance $2d_{\text{standoff}}$, or twice the distance from the flame sheet to the surface of the droplet (see Figure 2.3).

Table 3.2 shows the corresponding velocity perturbations and estimated strain rates for each fuel at extinction. Interestingly, the extinction strain rate associated with methanol and ethanol were higher than the F-T fuel and the JP-8/F-T blend. While these results are only preliminary, requiring further exploration in the new symmetric waveguide configuration utilized by Sophonias Teshome, the extinction strain rates were found to be comparable to those measured in opposed-flow diffusion flame configurations.

Table 3.1. Comparison of measured values of burning rate constant K for various fuel droplets, with combustion in the absence of acoustic excitation. Comparison with available established values is also given.

Fuel	K , present (mm^2/s)	K , established (mm^2/s)
Methanol	0.85 – 0.95	0.85 – 1.2
Ethanol	0.85 – 1.1	0.81 – 0.86
JP-8/F-T	0.78 – 0.90	0.87, 1.04 (JP-4)
Pure F-T	0.80	-

Table 3.2. Acoustic conditions of various fuels at extinction. The corresponding sound pressure level in decibels (dB), pressure perturbation in Pascals (Pa), and velocity perturbation in meters per second (m/s) is given. A rough estimate of the strain rate is also shown.

Fuel	SPL (dB)	Amplitude (Pa)	Δv (m/s)	ϵ (s^{-1})
Pure F-T	140.4	210	0.73	$3.7 \cdot 10^2$
JP-8/F-T	140.9	222	0.77	$3.7 \cdot 10^2$
Ethanol	141.1	228	0.79	$4 \cdot 10^2$
Methanol	142.9	280	0.98	$4 \cdot 10^2$

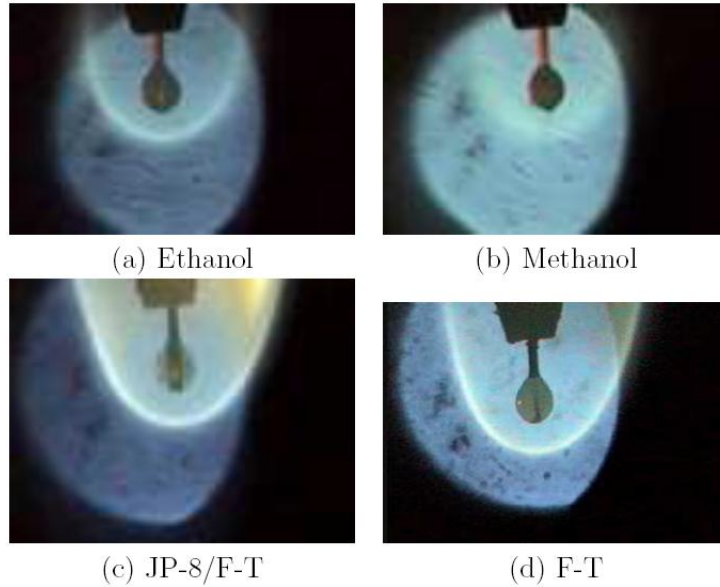


Figure 3.1. Photographs of fuel droplets burning in the absence of acoustic excitation. Backlighting accounts for the light portion of the background observed outside of the flame.

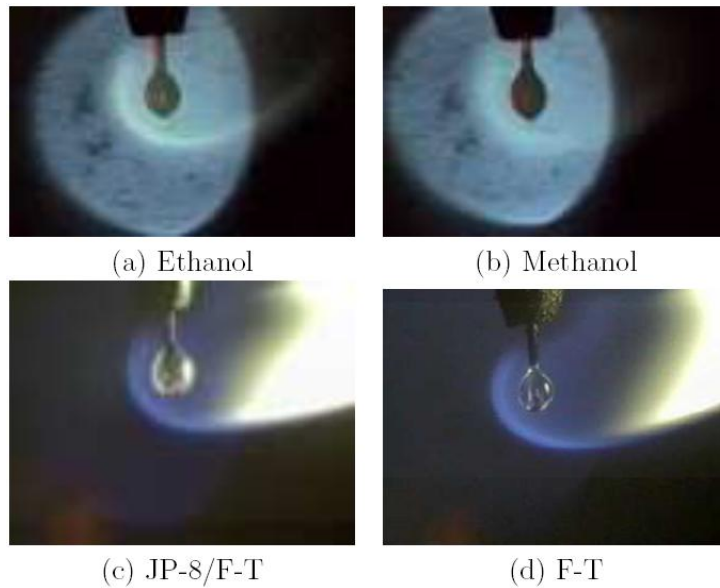
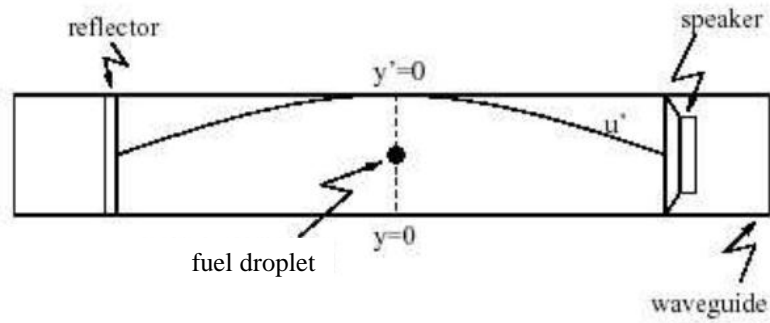
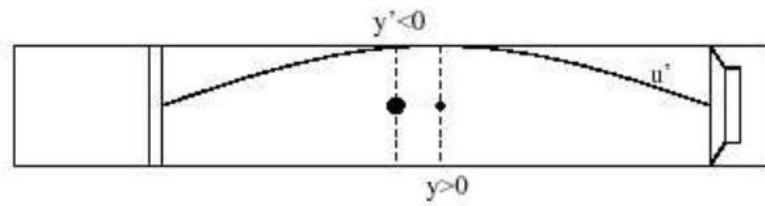


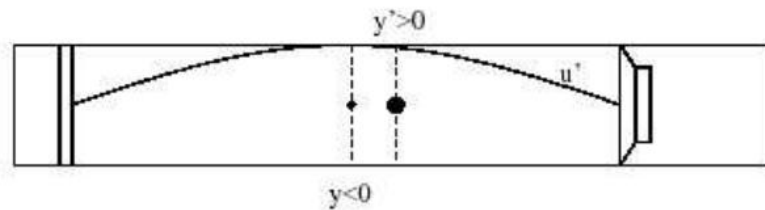
Figure 3.2. Photographs of various fuel droplets burning during acoustic excitation, situated at or near the waveguide center for the “original” locations of the speaker and reflector, based on a measured maximum in P2/P1. Acoustic excitation corresponded to 780 Hz with an amplitude of 138.6 dB for ethanol, the pure F-T, and the JP-8/F-T fuel blend, and 140.2 dB for methanol.



(a)



(b)



(c)

Figure 3.3. Location of the pressure node relative to the droplet (y) and the droplet relative to the pressure node (y'), based on positioning of the speaker and reflector (S&R). (a) $y = 0$ and $y' = 0$, (b) $y > 0$ and $y' < 0$, where S&R move to the right, and (c) $y < 0$ and $y' > 0$, where S&R move to the left. From Dattarajan (14).

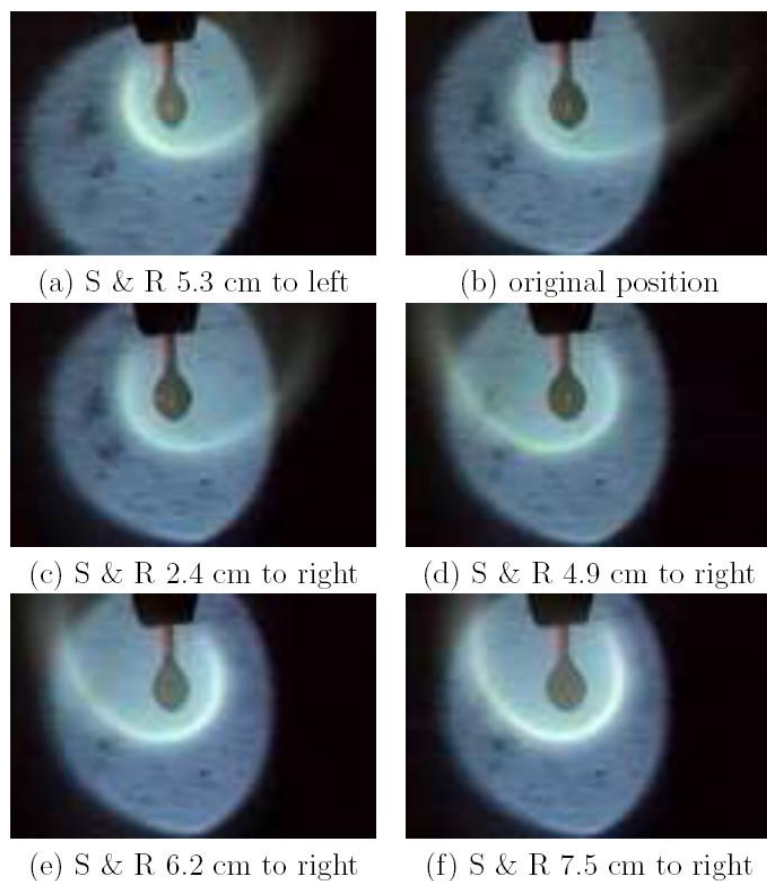


Figure 3.4. Photographs of a burning ethanol droplet with acoustic excitation at 780 Hz (PN) and 138.6 dB. The distances to which the speaker and reflector (S&R) have been moved, relative to their original locations, are indicated.

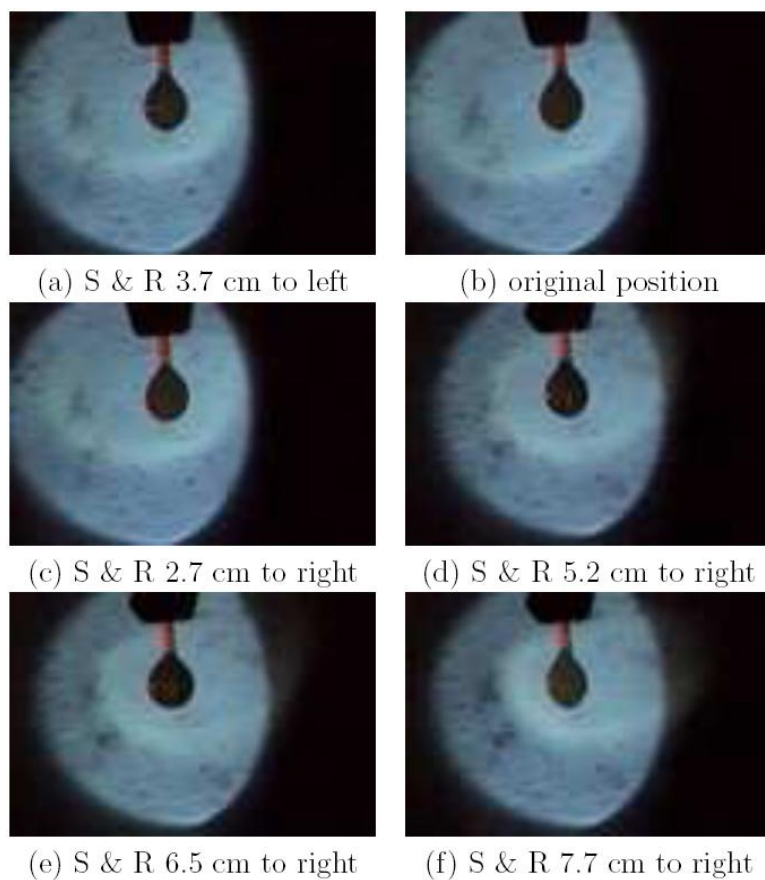


Figure 3.5. Photographs of a burning methanol droplet with acoustic excitation at 540 Hz (PAN) and 139.9 dB. The distances to which the speaker and reflector (S&R) have been moved, relative to their original locations, are indicated.

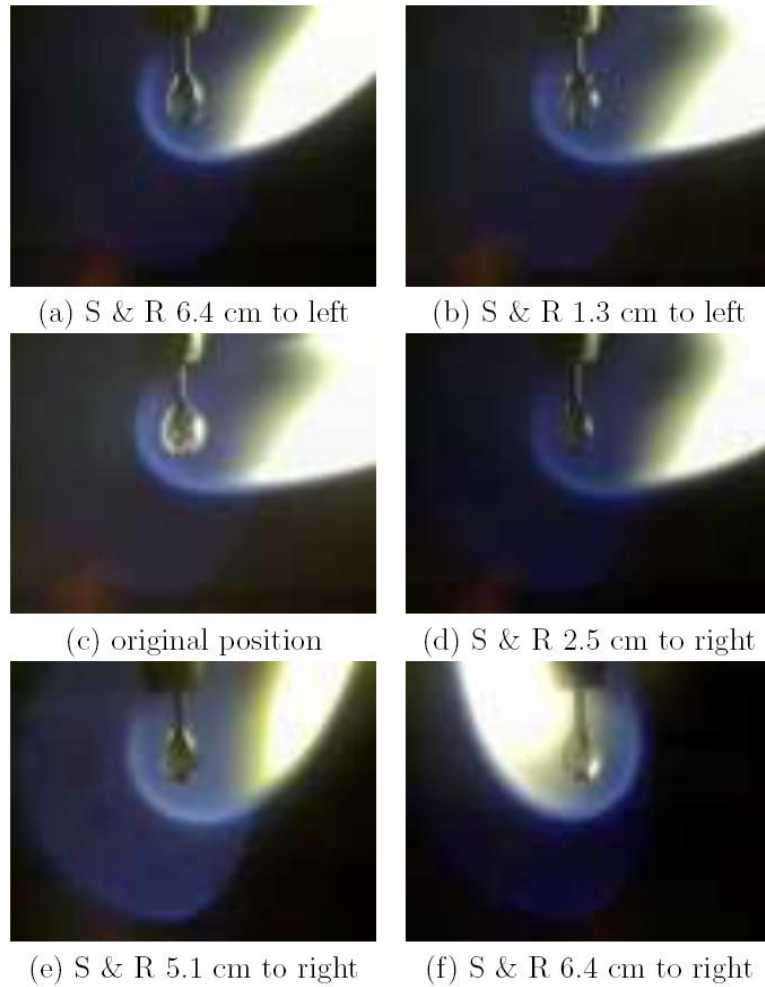


Figure 3.6. Photographs of a burning JP-8/FT fuel droplet with acoustic excitation at 785 Hz (PN) and 138.6 dB. The distances to which the speaker and reflector (S&R) have been moved, relative to their original locations, are indicated.

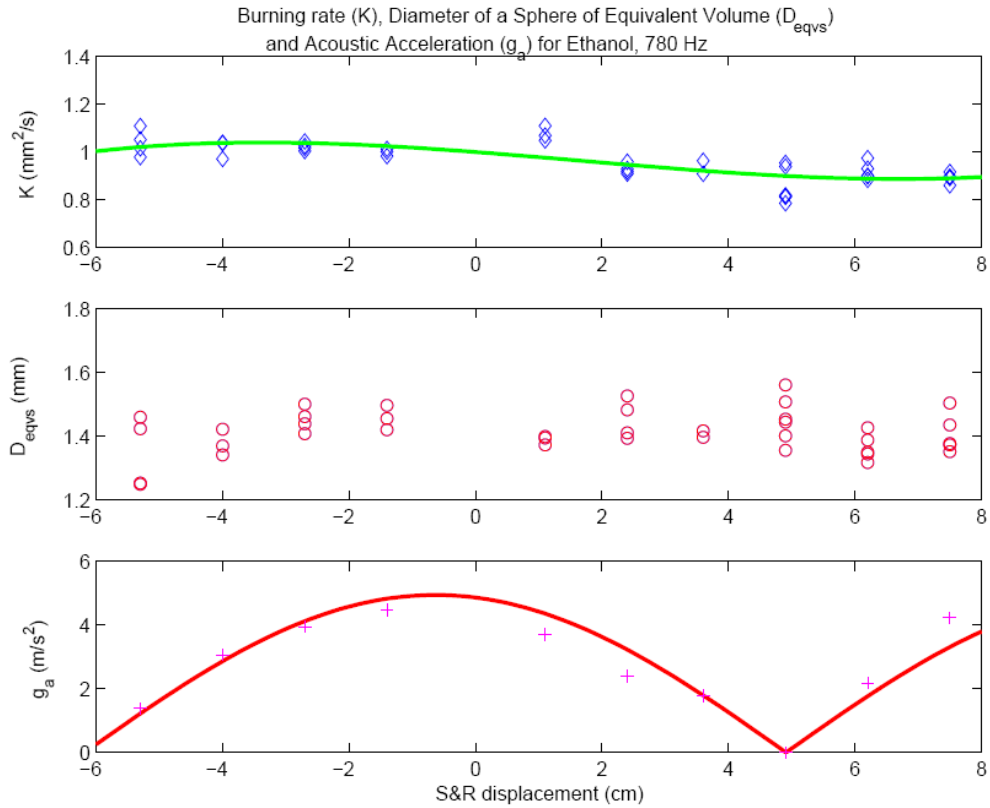


Figure 3.7. For ethanol, measured values of K and d_{eqvs} , and estimated absolute value of g_a as a function of the displacement of the speaker and reflector relative to their original positions, for a 780 Hz PN. The solid line on the K plot represents a fit of the experimental data points, while the solid line on the g_a plot represents the theoretical variation in g_a assuming an average SPL of 138.6 dB. The data points for g_a represent absolute values estimated from the locally measured SPL value.

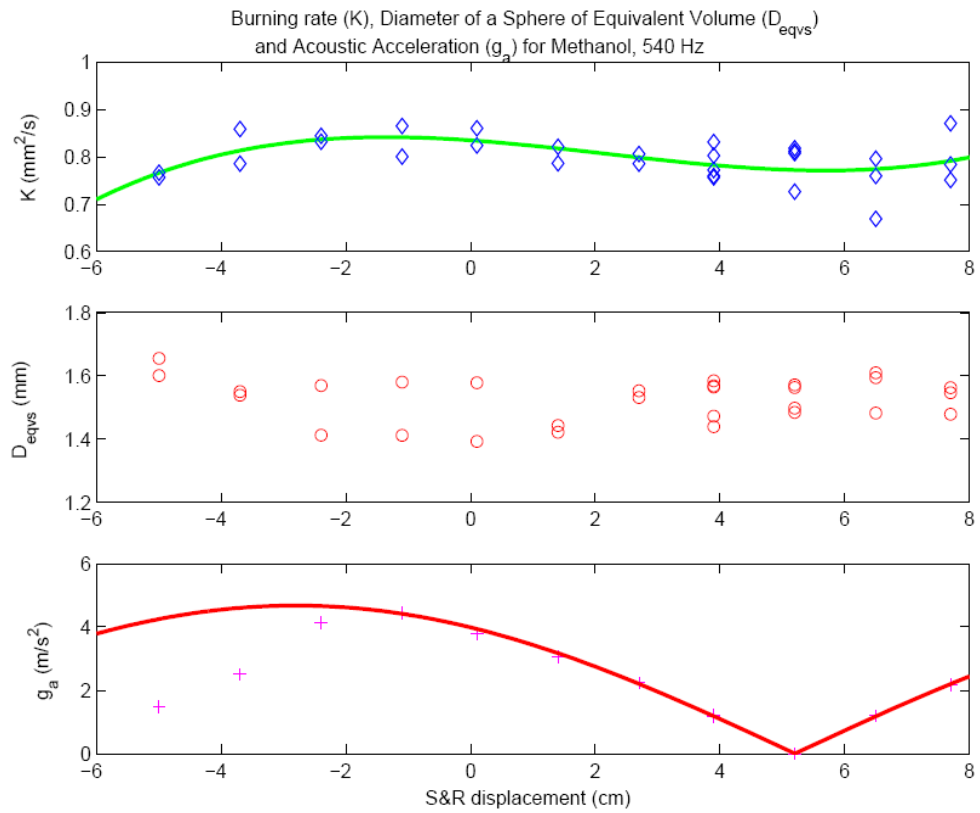


Figure 3.8. For methanol, measured values of K and d_{eqvs} , and estimated absolute value of g_a as a function of the displacement of the speaker and reflector relative to their original positions, for a 540 Hz PAN. The solid line on the K plot represents a fit of the experimental data points, while the solid line on the g_a plot represents the theoretical variation in g_a assuming an average SPL of 139.9 dB. The data points for g_a represent absolute values estimated from the locally measured SPL value.

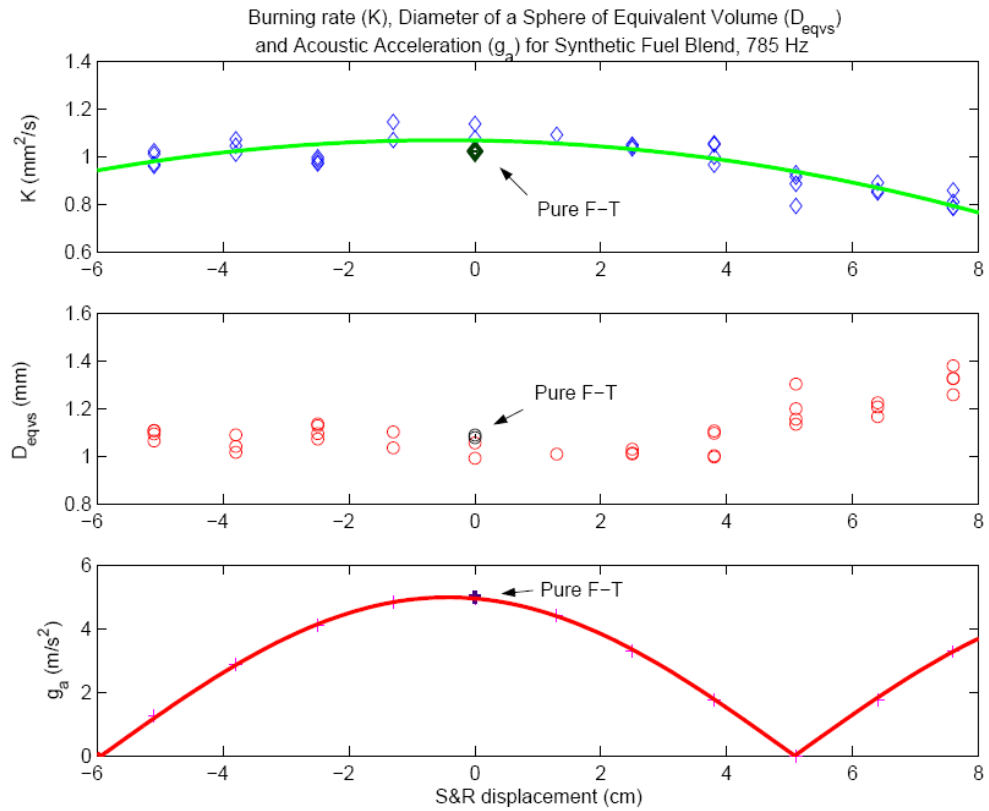


Figure 3.9. For JP-8/F-T fuel, measured values of K and d_{eqvs} , and estimated absolute value of g_a as a function of the displacement of the speaker and reflector relative to their original positions, for a 785 Hz PN. The solid line on the K plot represents a fit of the experimental data points, while the solid line on the g_a plot represents the theoretical variation in g_a assuming an average SPL of 138.6 dB. The data points for g_a represent absolute values estimated from the locally measured SPL value.

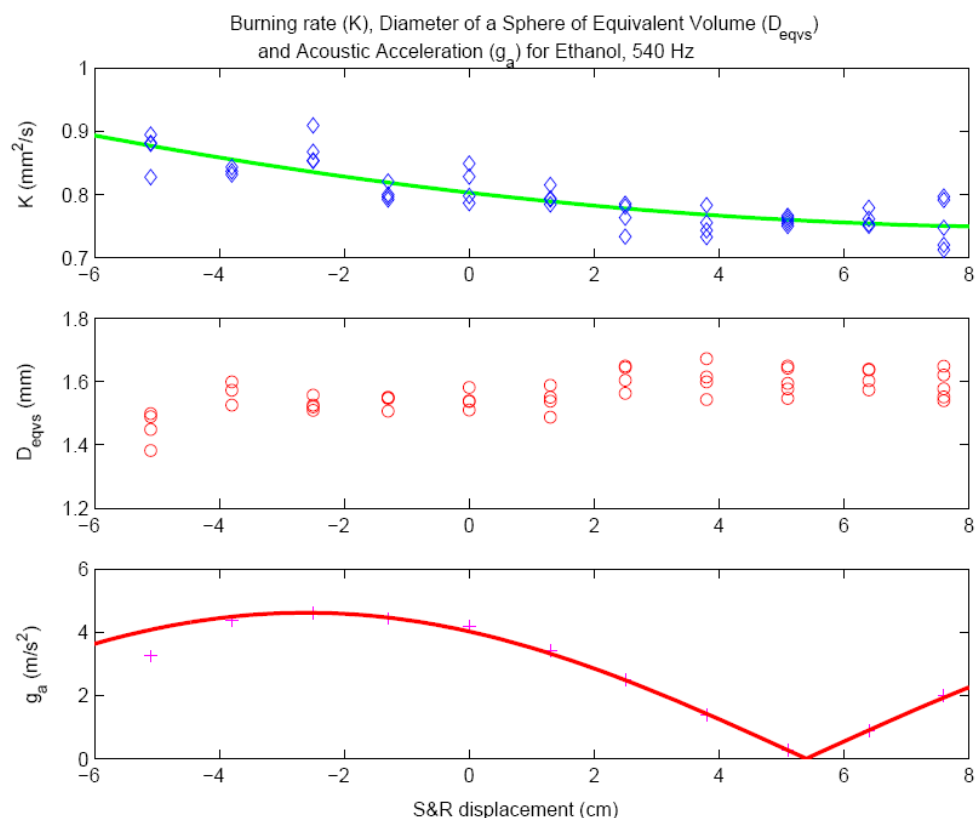


Figure 3.10. For ethanol, measured values of K and d_{eqvs} , and estimated absolute value of g_a as a function of the displacement of the speaker and reflector relative to their original positions, for a 540 Hz PAN. The solid line on the K plot represents a fit of the experimental data points, while the solid line on the g_a plot represents the theoretical variation in g_a assuming an average SPL of 138.8 dB. The data points for g_a represent absolute values estimated from the locally measured SPL value.

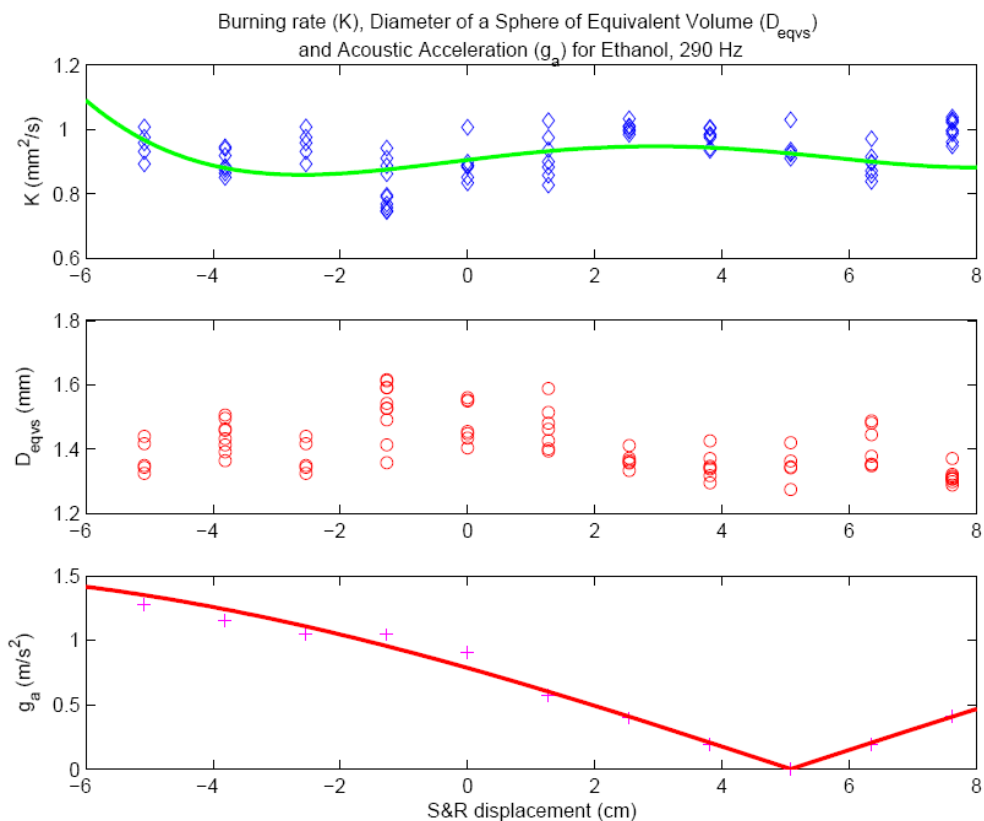


Figure 3.11. For ethanol, measured values of K and d_{eqvs} , and estimated absolute value of g_a as a function of the displacement of the speaker and reflector relative to their original positions, for a 290 Hz PN. The solid line on the K plot represents a fit of the experimental data points, while the solid line on the g_a plot represents the theoretical variation in g_a assuming an average SPL of 137.8 dB. The data points for g_a represent absolute values estimated from the locally measured SPL value.

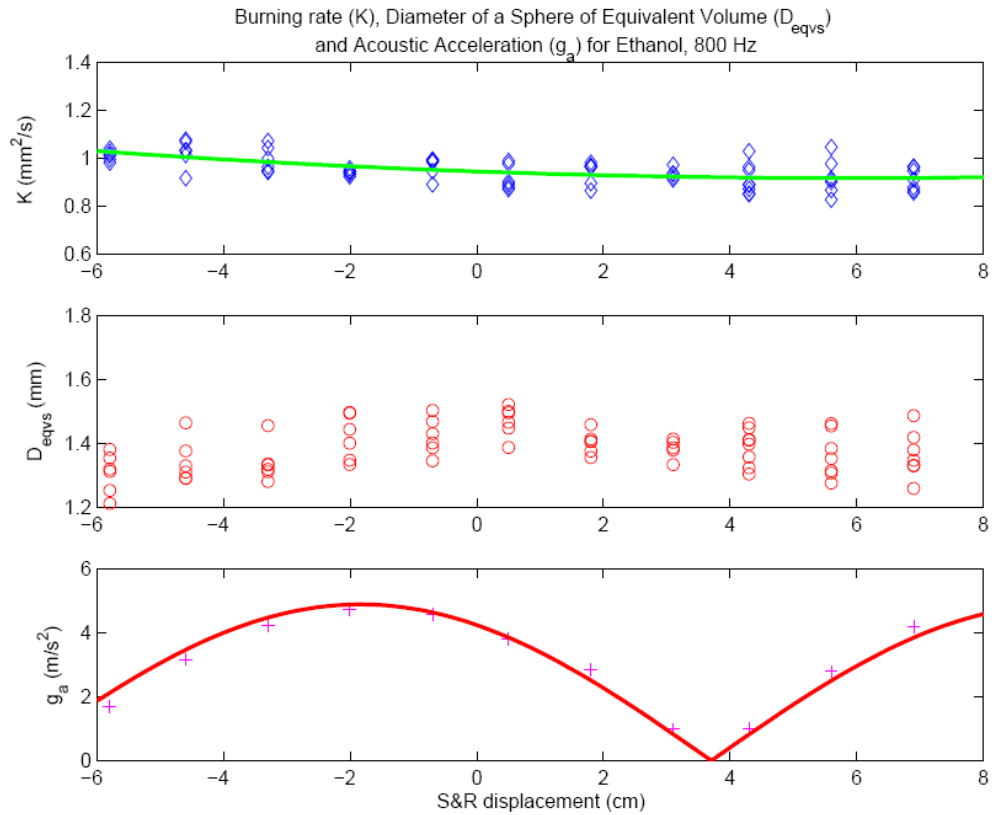


Figure 3.12. For ethanol, measured values of K and d_{eqvs} , and estimated absolute value of g_a as a function of the displacement of the speaker and reflector relative to their original positions, for a 800 Hz PN. The solid line on the K plot represents a fit of the experimental data points, while the solid line on the g_a plot represents the theoretical variation in g_a assuming an average SPL of 138.5 dB. The data points for g_a represent absolute values estimated from the locally measured SPL value.

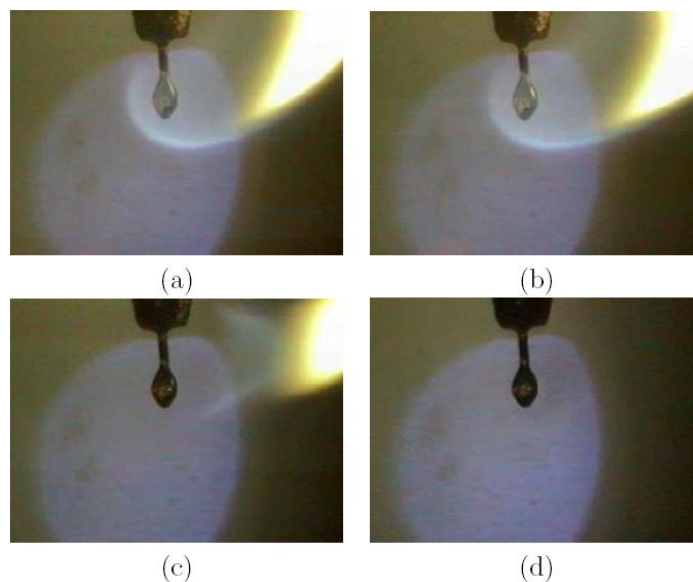


Figure 3.13. Consecutive photographs showing the extinction process of a pure F-T fuel droplet. Images (a) and (b) show the flame before extinction, image (c) shows a “wake” flame and image (d) shows a flameless droplet. The time interval between images is 33.37 ms, with forcing at 141.1 dB or a perturbation pressure of 228 Pa, and maximum velocity perturbation of 0.79 m/s.

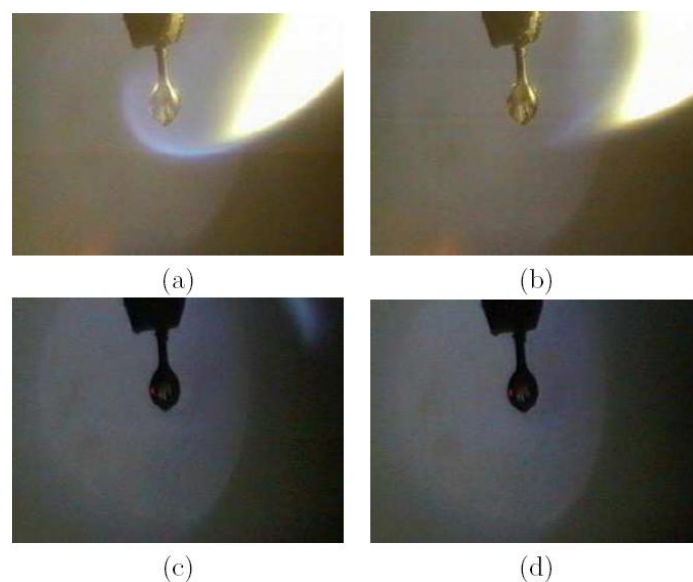


Figure 3.14. Consecutive photographs showing the extinction process of a JP-8/F-T fuel droplet. Images (a) and (b) show the flame before extinction, image (c) shows a “wake” flame and image (d) shows a flameless droplet. The time interval between images is 33.37 ms, with forcing at 141.3 dB or a perturbation pressure of 233 Pa, and maximum velocity perturbation of 0.82 m/s.

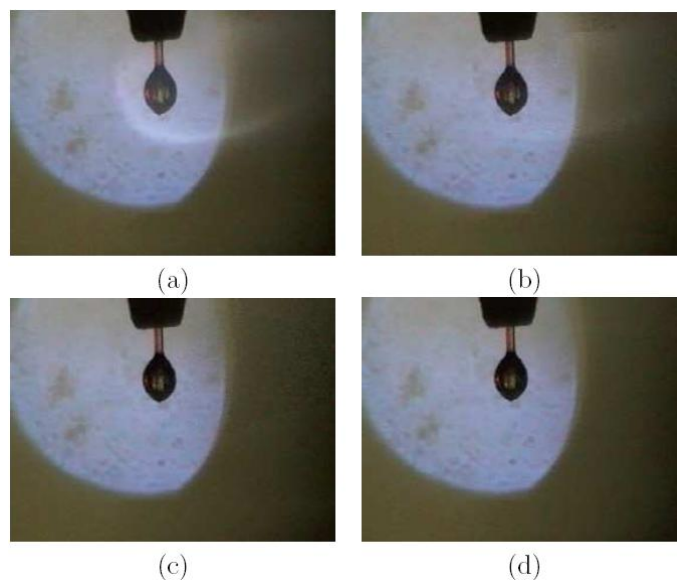


Figure 3.15. Consecutive photographs showing the extinction process of an ethanol droplet. Images (a) and (b) show the flame before extinction, images (c) and (d) show a flameless droplet. The time interval between images is 33.37 ms, with forcing at 142.2 dB or a perturbation pressure of 257 Pa, and maximum velocity perturbation of 0.90 m/s.

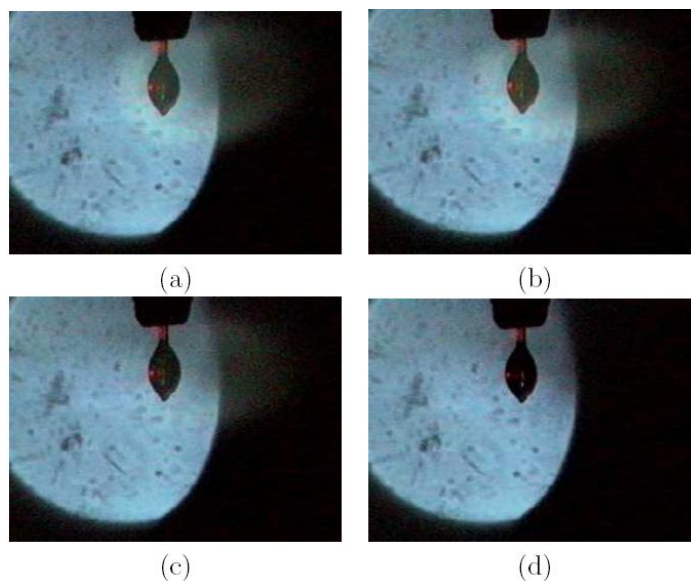


Figure 3.16. Consecutive photographs showing the extinction process of a methanol droplet. Images (a) and (b) show the flame before extinction, image (c) shows a “wake” flame and image (d) shows a flameless droplet. The time interval between images is 33.37 ms, with forcing at 143.3 dB or a perturbation pressure of 292 Pa, and maximum velocity perturbation of 1.0 m/s.

CHAPTER 4

Experimental Setup – Acoustically Excited Coaxial Jet

4.1 Cryogenic Supercritical Chamber and Coaxial Jet Facility

The experimental studies of the acoustically excited coaxial jet were performed at the Air Force Research Laboratory (AFRL) located at Edwards Air Force Base, CA. The Cryogenic Supercritical Laboratory (EC 4) was used to run all the tests. A photograph of the facility is shown in Figure 4.1 and a schematic of the experiment is shown in Figure 4.2. The photograph shows the test chamber in the center and the acoustic drivers on each side. Specific features of the facility such as the inner chamber, which is a smaller chamber within the main test chamber, the coaxial jet injector, and the pressure transducer and thermocouple probe used to obtain measurements very near the exit of the coaxial jet will be discussed in detail below.

The photograph in Figure 4.1 is intended as a visual aid to provide a perspective of the actual facility and the main components of the experimental setup. The chamber flow is exhausted through a vent line located at the center bottom of the chamber. Other diagnostic equipment also is introduced to the chamber from the center bottom. Above the chamber there is a thick insulation that houses the inner jet heat exchanger which cools the nitrogen inner jet as much as possible before it enters the chamber. On top of

the chamber, to the sides of the insulation, there are orifices that allow more probes, such as thermocouples and pressure transducers, to reach inside the test chamber. On the back, towards the right side of the photograph, part of the control panel can be observed, where valves, flow meters and pressure regulators were used to monitor and distribute the right amount of flow to the experimental setup.

The schematic in Figure 4.2 shows how the different flow lines interact with each other in order to produce an inner jet and an outer jet that satisfied testing requirements. The chamber section of the schematic represents the most updated version of the experimental setup. It shows the three differential pressure transducers that were used to measure the pressure fluctuations in three equally spaced locations with one placed just above the location of the coaxial injector exit and the other two to its sides. It also shows the pressure transducer and thermocouple that were brought from the bottom of the chamber to the injector exit inside the inner chamber. The schematic also shows that both the inner jet and outer jet have a pressure transducer and a thermocouple at the coaxial injector location.

The ability to measure the pressure and the temperature of the inner jet and the outer jet just as they enter their corresponding coaxial channel within the injector was only possible with the newly designed coaxial injector (described in section 4.2), since only the new injector featured probe lines through which pressure transducers and thermocouples could be introduced. This upgrade allowed a better understanding of the effects of acoustics on the flow upstream the injector and how fast the temperature of the inner and the outer jets could change as they flow across the injector.

Also shown in the schematic in Figure 4.2 are heat exchangers that allowed the cooling of the inner and outer flows, and the window purge flow that was used to prevent water vapor condensation on the test chamber windows so as to allow proper visualization of the coaxial jet flow. Several thermocouples were used across the heat exchanger and in other locations to keep track of the conditions of the flow in order to maintain the required flow properties for each test.

The flow process started with a high pressure and a low pressure gaseous N₂ supply, ended with a carefully regulated coaxial jet flow inside the test chamber, and consisted of several steps. First, gaseous N₂ was used to supply the inner and outer flows of the coaxial jet and to pressurize the chamber. Then the outer jet was cooled by either one or two heat exchangers (HEs), depending on the test requirements. A third HE was used to decrease the temperature of the inner jet. The coolant that ran through the HEs for both the inner and outer jets consisted of liquid N₂ obtained from a cryogenic pressure vessel located outside EC 4, which had a capacity of 5 m³. The temperatures of the two jets were controlled by adjusting the flow rate of liquid N₂ through the HE's. The mass flow rates through the inner and outer jets were measured before they were cooled with Porter mass flow meters (models 122 and 123-DKASVDAA), since it was less cumbersome to measure mass flow rates at ambient temperature than to measure them at cryogenic conditions.

Once the desired mass flow rates for the inner and outer jet were achieved, the mean chamber pressure required for the experiment was adjusted. The chamber pressure was measured with a Stellar 1500 transducer. After the mean chamber pressure was

obtained, the mass flow rates were adjusted for minor changes due to the pressure increase. Finally, the liquid N₂ flow through the HEs was carefully controlled to stabilize the inner and outer jet temperatures to produce the desired outer to inner jet momentum flux ratio for that particular test. For a complete description of the operating procedures of the facility used to perform these studies, refer to Appendix B. To see a summary of the operating conditions achieved for all cases reported in this study, refer to Table C.1 and Table C.5 in Appendix C.

In order to maximize the effect of the available acoustic energy on the jet, an inner chamber was created into which the jet is injected. A photograph of the inner chamber while running a trial test is shown in Figure 4.3. This inner chamber had a nominal height of 6.6 cm, a width of 7.6 cm and a depth of 1.3 cm. The photograph in Figure 4.3 shows a gray object that surrounds the outside of the test chamber. It is foam insulation that was placed between the outside of the test chamber and an acrylic window in order to provide an enclosed space through which gaseous nitrogen at low pressures (10 to 15 kPa) could flow in a continuous fashion, removing all air inside it. The square shape insulation was hollowed at the center to allow visual access of the coaxial jet. Flowing nitrogen through this enclosure prevented water vapor in the ambient air from condensing on the test chamber window, which was a recurrent problem when the chamber was first used for experiments at very low temperatures.

At the center of the photograph, slightly shifted down, we observe the inner chamber. It was bounded by two small acrylic windows in the front and back, and to both sides by the end of the acoustic waveguides, which will be described later in this chapter.

Three round holes can be observed in one of the windows. They show the original location for the three pressure transducers that were flushed with the window to measure the pressure oscillations inside the inner chamber. This configuration was used for tests with the original injector. They were raised to a location between the center and the top of the acrylic windows for the tests performed with the new injector. A description of the “original” and “new” injectors will be given below. At the bottom an aluminum piece served as support for the entire inner chamber and on the top there was a plate that acted as the ‘ceiling’ of the inner chamber. Both the top and bottom pieces had orifices at their centers. The top plate’s orifice allowed the coaxial jet tip to enter the inner chamber and the bottom orifice was used to provide an exit for the flow. It was also used to introduce a thermocouple and pressure transducer to study the properties of the flow near the jet, as can be observed in the photograph as well.

4.2 Original and New Injectors

Two images of the first or “original” coaxial injector used in the majority of these studies are shown in Figure 4.4a and b. Figure 4.4a presents the full injector and Figure 4.4b shows a plane view of the end where the jets exited. The inner diameter of the inner jet, D_1 , or $2R_1$ as shown in the picture, was 0.51 mm. The outer jet had an inner diameter, D_2 , of 1.59 mm and outer diameter, D_3 , of 2.42 mm. The length to inner diameter ratio was 100 for the inner jet and 67 for the outer jet (taking as reference the mean width of the annular passage, $R_3 - R_2$). The coaxial injector was installed so that the inner and outer jets were concentric and the inner jet exit plane was recessed by 0.3 mm from the

outer jet exit plane. This recess length was chosen to represent one half of D_1 , in order to mimic realistic coaxial jet configurations used in industry. This recess length will be varied in a future study.

The second or “new” coaxial injector used in these studies is shown in Figure 4.5a and b. The inner diameter of the inner jet, D_{new1} , or $2R_{\text{new1}}$, was 1.40 mm. The outer jet had an inner diameter, D_{new2} , of 1.65 mm and outer diameter, D_{new3} , of 2.44 mm. The length to inside diameter ratio was 65 for the inner jet and 105 for the outer jet (taking as reference the mean width of the annular passage, $R_{\text{new3}} - R_{\text{new2}}$). The injector was installed so that the inner and outer jets were concentric and the inner jet exit plane was recessed by 0.7 mm from the outer jet exit plane, which was chosen to represent one half of D_{new1} , to be able to compare it with the results obtained with the original injector. Notice that the inner post thickness decreased dramatically from the old injector to the new injector. The post thickness of the old injector was 110% of its inner diameter ($1.1D_1$) whereas the post thickness of the new injector is only 9.1% of its inner diameter ($0.091D_{\text{new1}}$).

4.3 Measurement Methods

The temperature of the fluid in the jets was measured with unshielded type E thermocouples with a bead diameter of 0.1 mm. The accuracy of the thermocouples used in the study was checked with an RTD and found to be within ± 1 K. A miniature pressure transducer was placed next to the thermocouple, using a small metallic post as support, and used to measure the pressure at a sampling frequency of 20 kHz. The manufacturer of

the miniature pressure transducers was Kulite Semiconductor Products, Inc. (models CCQ-062-1000A and CCQ-093-750A). These pressure transducers had an absolute pressure range of either 6.9 MPa or 5.2 MPa, respectively. The thermocouple and pressure transducer probe used are shown in Figure 4.6. In this photograph, the upper boundary or ‘ceiling’ of the inner chamber and the tip of the injector discussed above can be clearly seen.

Two linear positioning stages built by Attocube Systems AG were used to move the pressure transducer and the thermocouple in a plane perpendicular to the jet axis. Each stage had a range of 3 mm in 1 dimension with step sizes in the order of 0.01 mm. One stage was placed on top of the other with their axis of movement perpendicular to each other for a total maximum examination area of 3 mm by 3 mm, as shown in Figure 4.7a and b.

With the configuration described above, the thermocouple tip could easily reach the exit plane of both the outer jet and inner jet. It was even possible to measure the temperature within the recess of the inner jet. During the actual measurements, the thermocouple was placed as close to the exit plane of the outer jet as possible without compromising its integrity as can be seen in Figure 4.6. The thermocouple and pressure transducer were attached to a custom made probe stand, shown in the cone-shaped aluminum part on the top positioning stage in Figure 4.7a. The devices were mounted on top of the linear positioning assembly using a small custom made base (circular base under the bottom positioning stage in Figure 4.7b), which in turn was placed at the top end of a shaft that rested on a large, linear mechanical stage with a 10-cm range built by

SETCO and shown in Figure 4.8a and b, which allowed the probe to get to the desired interrogation region within the inner chamber.

Properties such as density and viscosity were computed from the measured flow rates, chamber pressure and jet temperature, using the National Institute of Standards and Technology's REFPROP Software (59) and its thermophysical properties online database (60). From these properties, Reynolds number, Re , outer to inner jet velocity ratio, VR , and outer to inner jet momentum flux ratio, J , for a given set of conditions were then calculated. The jet was visualized by taking backlit images using a Phantom v7.1 high-speed camera (see Figure 4.9) capable of recording up to 160,000 frames per second at a resolution of 32 pixels by 32 pixels. For a resolution of 128 pixels by 256 pixels the camera was capable of recording 41,300 pictures per second. The resolution of the images in the present experiments varied from 128 pixels x 224 pixels to 196 pixels x 400 pixels, depending on chamber pressure and outer to inner momentum flux ratio. These in turn determined the size of the visible features of the jet that this study was characterizing. Each pixel represents an approximate area of 0.08 mm x 0.08 mm. Depending on the resolution chosen, the framing rate (frequency at which pictures were recorded) was 20, 25 or 41 kHz.

To focus the camera on the coaxial jet flow an AF Nikkor 35-105 mm lens with an extension tube was used. Since focusing on the outer jet structures while at the same time having a clear view of the inner jet was always a difficult process when setting up the camera and related optical equipment, the quality of the coaxial jet images was not

always the same. In some cases, to be described in chapter 5, the images were blurred and made it more difficult to characterize the inner and outer jet.

The jet was backlit using a Newport variable power arc lamp set at 160 W or 300W. The exposure time generally was 1-2 μ s and the number of images saved per run was 1000 on average. The dark core length and the inner jet spreading angles were measured from 998 images using a MATLAB subroutine based on the Otsu technique (61), which analyzes an image and finds a threshold which helps differentiate the dark core of the inner jet from the rest of the image.

The acoustic waves were generated using two piezo-sirens placed at each end of the chamber, custom-designed for the Air Force Research Laboratory by Hersh Acoustical Engineering, Inc. A Fluke 100 MS/s arbitrary waveform generator (model 292) was used to produce two sinusoidal waves with the same frequency but with a prescribed phase between them. The signals were then sent to two amplifiers, one for each piezo-siren. The amplifiers were a Krohn-Hite (model 7500) and a Trek (model PZD2000A), which amplified the signals and fed them to the piezo-sirens. The amplified signals were in the 200 to 540 V range. The principle by which the piezo-sirens work as acoustic drivers is relatively simple, with a piezo element moving an aluminum cone attached to it, which in turn vibrates to produce acoustic waves. The distance from each cone to the location of the coaxial jet is 44 cm.

The frequency at which the piezo-sirens were driven was chosen by manually varying the frequency on the signal generator until the highest amplitudes of the pressure perturbations were obtained. These pressure perturbations were measured using the three

differential Kulite pressure transducers (model XCQ-093-25D) flushed with the acrylic window of the inner chamber (see Figure 4.3) and shown real time and recorded for further processing using Pacific Instruments PI660 Acquisition and Control Software.

The phase difference, also referred to in this work as phase angle, between the signals sent to the piezo-siren elements was varied to expose the coaxial jet to different effective positions relative to the pressure node or antinode of the generated acoustic field. When the two piezo-siren elements produce waves with a zero degree phase angle between them, the movement of the piezo-siren cones is synchronized and in opposite directions, that is, towards and away from each other. This produces conditions of high pressure perturbations and low velocity fluctuations at the center of the chamber, where the coaxial jet is located. This condition is called a pressure antinode or velocity node. In contrast, when the two drivers present a 180-degree phase difference, then the cones move in the same direction, generating high velocity fluctuations with very small variations in pressure at the jet location. This condition is called a pressure node or velocity antinode. A schematic of this behavior is reproduced in Figure 4.10. The method for creating pressure node and antinode conditions in the chamber differed from that used in the UCLA droplet waveguide, but the effect created was the same.

In these experiments, the voltage supplied to the two acoustic drivers was maintained at the same level for all conditions during each case. Efforts were made to keep the amplitudes of both piezo-siren elements the same. A photograph of one of the piezo-sirens can be seen in Figure 4.11a. Since the experimental setup uses a rectangular test section, the jet was excited with a transverse acoustic field. A transverse mode on a

rectangular chamber would be the equivalent of a tangential mode on a cylindrical chamber, which are the most dangerous for the integrity of such systems and an important reason to analyze its effects on a coaxial jet. To accommodate for the rectangular chamber, a waveguide with a catenary contour was used to transmit the waves from a circular cross-section to a rectangular cross-section as seen in Figure 4.11b. The maximum peak-to-peak acoustic pressure fluctuations generated by the two piezo-ceramic acoustic sources in the inner chamber varied from 7 to 30 kPa (1 to 5 psi) and were produced in the 2.9 to 3.3 kHz range.

4.4 Uncertainty Analysis

It is fundamental, for a useful interpretation of the data, to assess the uncertainty of the measurements for the experiments described in this work. An analysis of the impact that the errors of the measured variables have in the reported quantities is therefore necessary. Of particular interest are those measured quantities that the experimenter identifies as the most sensitive to small changes in experimental conditions or most likely to vary from one experiment to another, increasing the bias error of the measurement, or those quantities that are most difficult to measure with the probes and sensors available to the experimenter, which impact the precision error of the measurement.

The uncertainty of an experimental quantity, u_q , is given by the general formula (62; 63):

$$u_q = \sqrt{\frac{\partial q}{\partial x_1} u_{x_1} + \frac{\partial q}{\partial x_2} u_{x_2} \dots + \frac{\partial q}{\partial x_n} u_{x_n}} . \quad (4.1)$$

The quantities x_1 , x_2 , to x_n are the experimentally measured variables and u_{x_1} , u_{x_2} , to u_{x_n} their corresponding experimental uncertainties. This is the formula used to derive the uncertainties of the experimentally derived quantities shown throughout this study.

For the acoustically excited coaxial injector experiment there were several experimental quantities used to find test parameters such as J or VR. The pressure of the chamber was measured with a precision of $\pm 0.1\%$ of full scale reading. Mass flow meters report $\pm 1\%$ of full scale output. Temperatures were measured within 1 K after calibration with an RTD, which represents less than $\pm 1\%$ of the lowest absolute temperatures recorded (in the vicinity of 105K). The largest source of error appeared when finding the density near the critical temperature of nitrogen, due to the large density gradients occurring at that temperature range. For further details on the uncertainty analysis of the coaxial jet experiment see Davis (41).

For the dark core lengths reported in this study, the quantity L/D_1 was obtained from a sample of 998 images. The number of pixels spanning the width of the outer post of the injector (D_4) was used as the basis to calculate D_1 . The end of the injector was at least 40 pixels for the majority of the cases. The pixel uncertainty was 1 to 2 pixels at each side. That brings a maximum uncertainty of 10% in the calculation of D_1 . The data from each sample were used to create a distribution from which the mean and standard deviation were calculated. This mean value was reported as L/D_1 . The value of the corresponding standard deviation was used to assign an uncertainty value to these

measurements. A 68% confidence level (1σ) was used to report error limits in the length measurements. This means that the dark core length for any given image will stay within those error bars on 68% of the cases. A 95% confidence value could be attained if 1.96σ was used instead.

However, if the uncertainty of the *mean* dark core length and not only of one image is desired, the uncertainty value will decrease by a factor of

$$\sigma_{mean} = \frac{\sigma_{single\ image}}{\sqrt{N}}, \quad (4.2)$$

where N is the number of images from which the mean value is derived (62; 63). In our case $N = 998$ and the uncertainty will decrease by a factor of 31.6. Thus the uncertainty of the mean is only 3.2% that of a single image. Of course, one must be aware that these confidence factors and standard deviation calculations depend on the underlying assumption that the working variable (L/D_1 in our case) assumes a normal distribution as N goes to infinity.

Uncertainties were not reported for the inner jet spreading angles reported in this study since they were based on the measurement of the *maximum* value achieved at each row by all contours. Thus the method searched for the outer most regions of the dark core regardless of the number of images in which they appeared. For most conditions this was a representative method for estimating how much the inner jet will spread during a few milliseconds of operation. If a particular case was found not to accurately depict the observed spreading angle, certain parameters, such as the region of the contour from which the angles were measured, were adjusted to eliminate the sources of inconsistency.

Finally, outer jet spreading angles were extracted from a sample of 20 images. A mean and standard deviation were obtained and the mean reported as the outer jet spreading angle, $\alpha_1 + \alpha_4$. The error bars represent $\pm 1 \sigma$ which gives a 68% confidence that an angle extracted from any image at that condition will remain within the reported error bars. If the uncertainty of the *mean* instead of a single image is desired, its value will only be 22% that of the original uncertainty for one image only per eqn. (4.2).

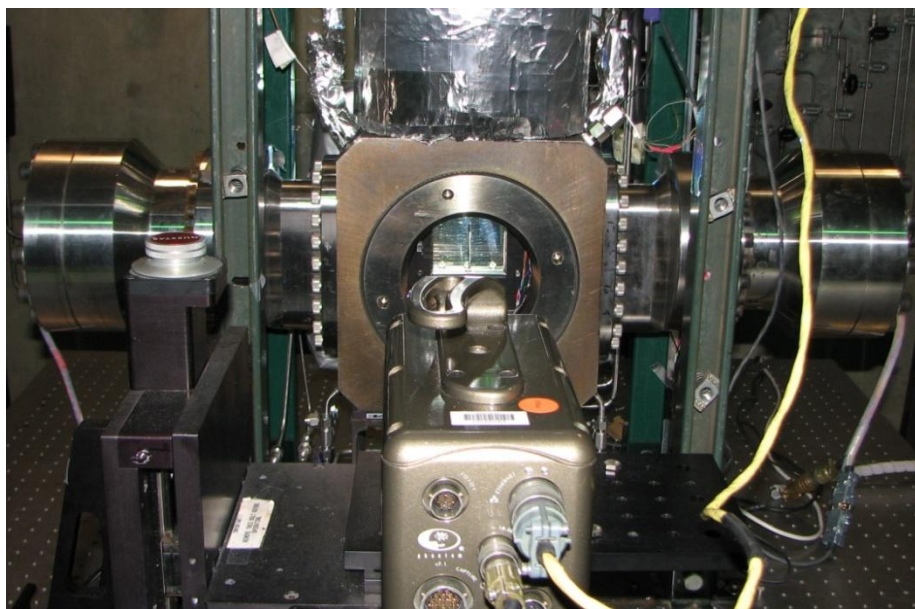


Figure 4.1. Experimental test chamber and supporting systems of the Experimental Cell 4 at AFRL, Edwards AFB, CA.

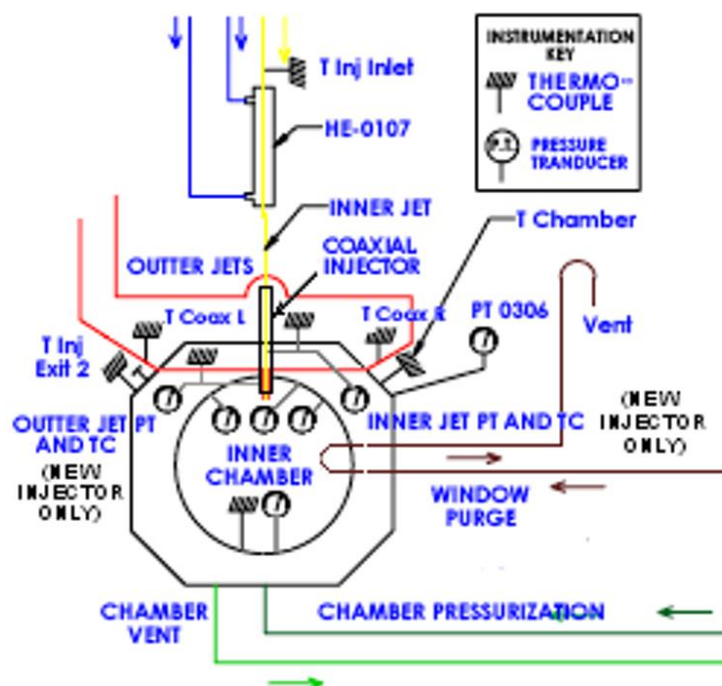


Figure 4.2. Chamber section view of the flow schematic for Experimental Cell 4 with the upgrades for the new coaxial injector. For a complete schematic refer to Appendix A.

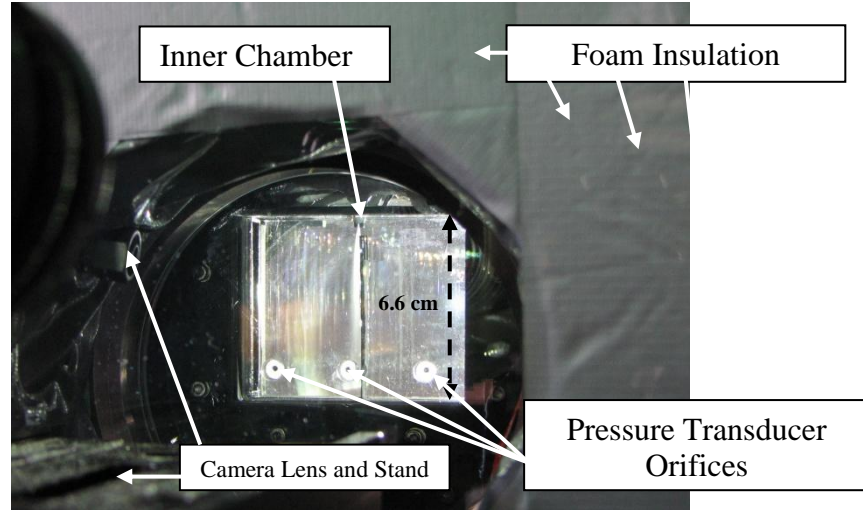


Figure 4.3. Photograph of the inner chamber within the test chamber in EC 4.

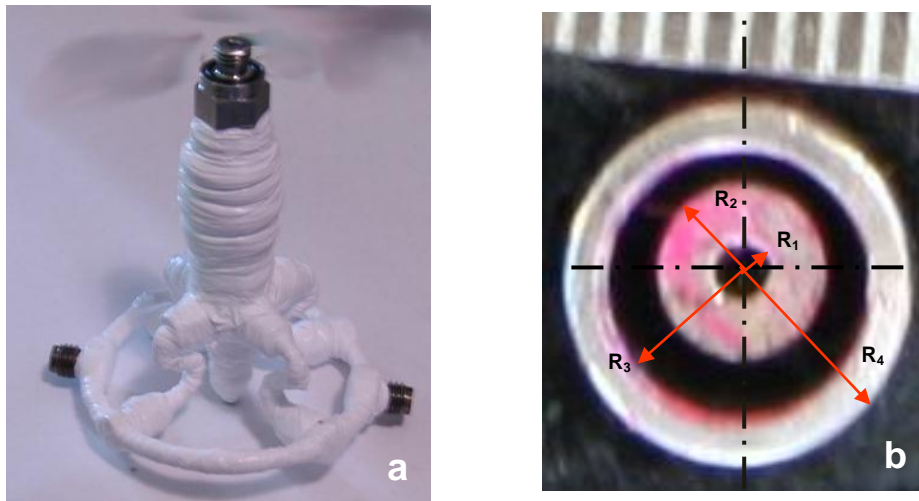


Figure 4.4. (a) First (“original”) coaxial injector used in this study. (b) Exit plane view of the original coaxial injector.

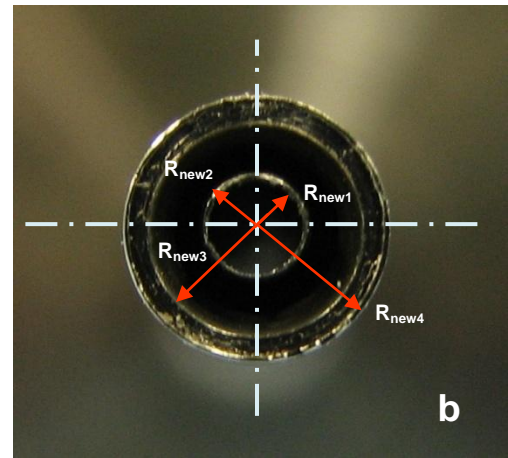
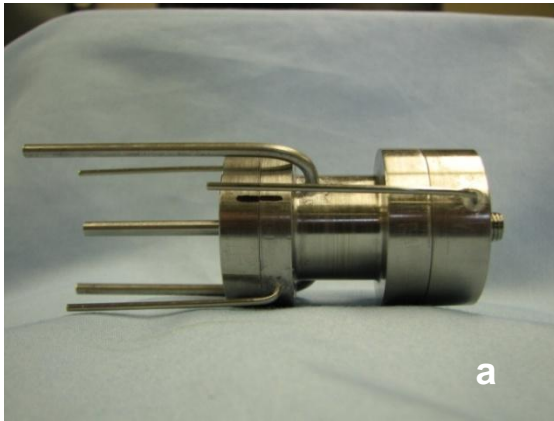


Figure 4.5. (a) Second (“new”) coaxial injector used in this study. (b) Exit plane view of the new coaxial injector.



Figure 4.6. Thermocouple and pressure transducer probes near the exit of the coaxial injector.

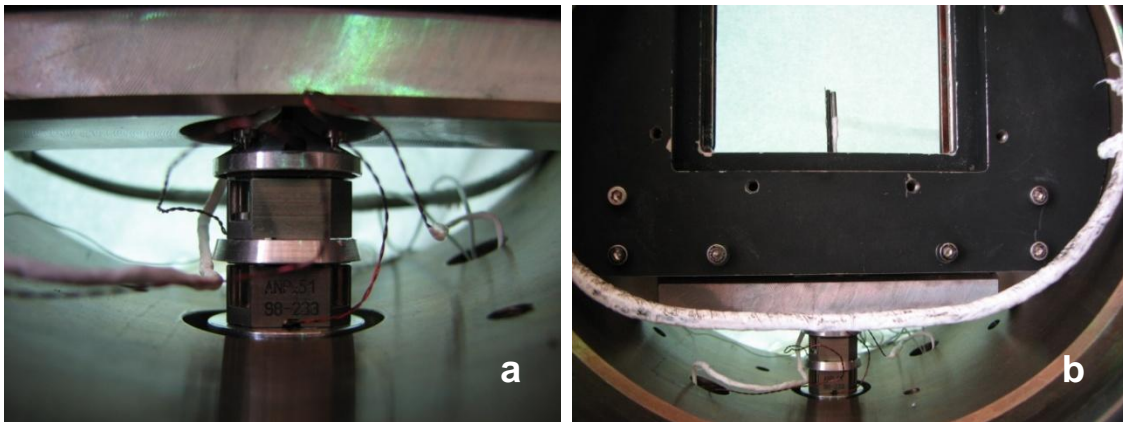


Figure 4.7. (a) Linear positioning stages that moved perpendicular to the vertical axis. (b) Larger view of the positioning stages and the thermocouple and pressure probe they support.

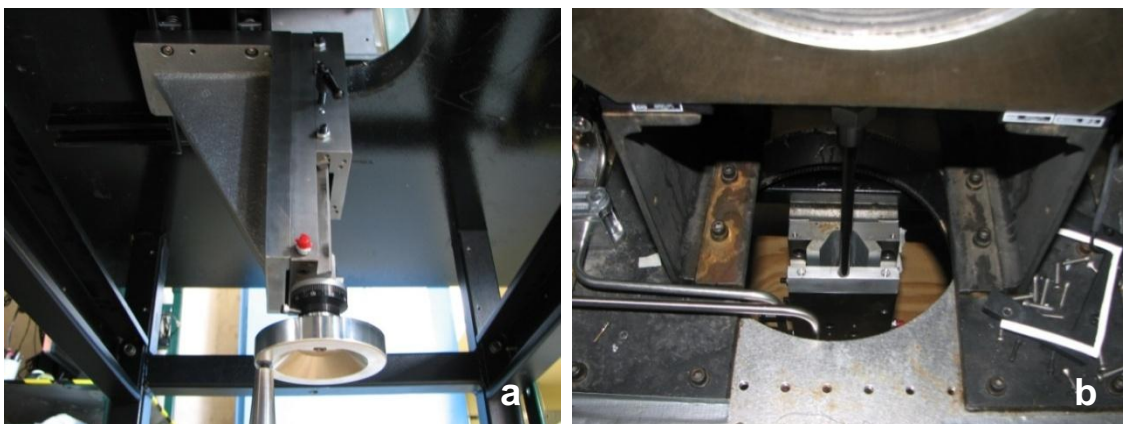


Figure 4.8. (a) Diagonal view of the mechanical stage used to move the thermocouple in the vertical direction inside the main chamber. (b) View of the mechanical stage from above. The bottom of the test chamber can be seen in the upper part of the image.

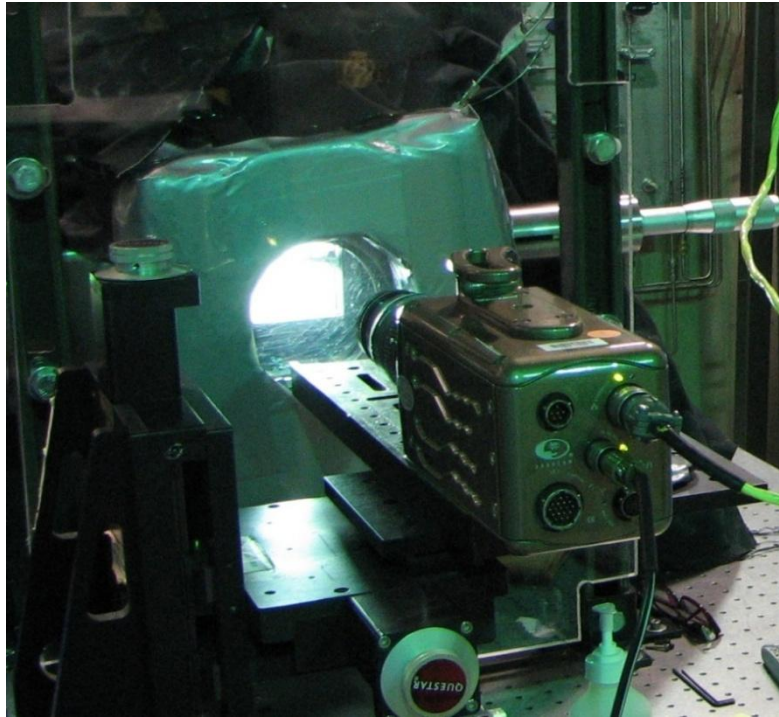


Figure 4.9. High speed camera used in this study.

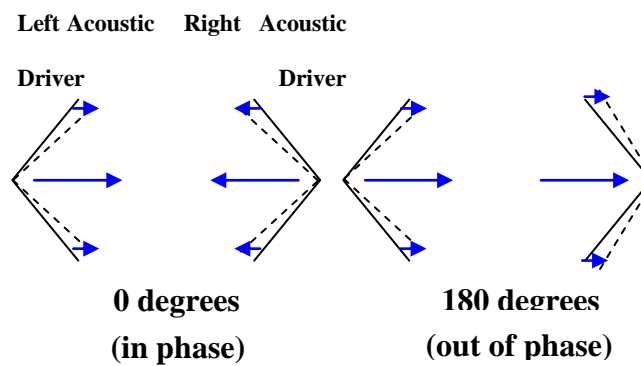


Figure 4.10. Simplified diagram of the two acoustic drivers at a 0° and 180° phase angle, indicating relative flow perturbation directions.

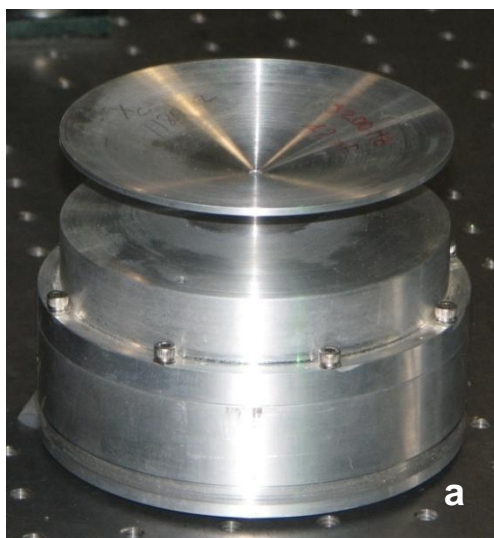


Figure 4.11. (a) One of two piezo-siren elements used to produce the acoustic field for this study. (b) Waveguide used to transmit the acoustic waves from the piezo-siren to the inner chamber.

CHAPTER 5

Results – Acoustically Excited Coaxial Jet

5.1 Quantification of Dark Core Length and Inner and Outer Jet Spreading Angles

The parameters investigated in the present experiments were the mean dark core length of the inner jet, the maximum spreading angle of the inner jet, and the average spreading angle of the outer jet. These specific parameters are relevant to LRE combustion stabilities and propellant mixing in the combustion chamber. In this section the method used to quantify each of these parameters will be explained and in subsequent sections the results obtained from applying this method to the experimental data will be presented.

5.1.1 Dark Core Length

The visualization method for the experiments performed for this work consisted of backlit images obtained with a high speed camera. Since the coaxial jet was located between the lens of the camera and the lamp, the denser regions of the inner jet were able to obstruct or deflect the incoming light the most. These denser regions produced dark areas which represented the flow from the inner jet, or the “core” of the coaxial flow. As

the denser inner jet flow starts to combine with the less dense flow of the outer jet and the chamber, its ability to obstruct or deflect light diminishes and the flow appears less dark. When the darkness of the inner jet is reduced below a certain threshold, that region is not considered part of the dark core. It is important to notice that the darker regions, the ones that are above the threshold, are not necessarily connected. It is then possible to find a continuous dark area starting at the exit of the injector and ending a few diameters downstream, then some less dense regions which are not part of the dark core, and then a few disconnected regions or “islands” where the flow is dark enough to go over the threshold.

For this study, the dark core is defined as the continuous dark area starting at the exit of the injector. The dark regions that are not connected with the main “core” that is exiting the injector are not considered part of it, even if their darkness indicates that the fluid in these regions has not been mixed with the outer jet or chamber fluid yet. Once a dark core region was identified, the perimeter of this interconnected area which starts at the exit of the injector was highlighted by a visual processing routine in MATLAB and its projection in the axial direction is reported as the dark core length shown in Figure 5.1a to c. The width of the inner jet inner post was found (see injector exit region in Figure 5.1b) in pixels and used to normalize the dark core length. The visual processing routine was then used to convert the shadowgraph image to a black and white picture. This method for conversion is based on the Otsu technique (61), which defines edges based on the zeroth and first cumulative moments of the gray-level histogram of the image, and its implementation is described in detail in Leyva et al. (22)

Since the dark core length is an instantaneous measurement, its value changes with each frame analyzed. The mean dark core length is an average of a predetermined number of images obtained with the high speed camera. In this work, the mean dark core length for each particular condition consisted of an average of 998 images such as the one shown in Figure 5.1a. The average was taken over a period of at least 24 ms (for cases recorded at 41000 frames per second) and at most of 50 ms (for cases recorded at 20000 frames per second). For data with external forcing between 2.9 and 3.1 kHz, the number of acoustic cycles included in the interrogation window varied from 70 to 155 depending on the time periods indicated above. Forcing at these conditions was chosen because it coincided with a multiple of the transverse mode of the chamber, so that the largest possible pressure fluctuations could be obtained.

5.1.2 Inner Jet Spreading Angles

To measure the inner jet spreading angles for a given condition, 998 images such as the one shown in Figure 5.1a were employed. Then, using the process outlined in the previous section to obtain the dark core length, a dark core region was extracted from each image. From the black and white images such as the one shown in Figure 5.1c, a contour of the dark core region was constructed. In order to measure the inner jet spreading angle, the locations of the left and right contours were recorded for each image as seen in Figure 5.1d. Then the leftmost points from each row for the left contours of all 998 images were selected. With these set of points, a “maximum left contour” was obtained. Likewise, the rightmost points from each row for the right contours of all 998

images were selected and a “maximum right contour” was extracted as indicated in Figure 5.2.

A linear fit through each contour was used to calculate the left and right spreading angles. The linear fit was chosen to start where the contour was the thinnest, usually between $\frac{1}{2}D_1$ (in supercritical cases at high J values, for example) and $5D_1$ (for all pressure conditions at moderate J values) and to end at the mean dark core length, which was found using a modified MATLAB routine based on the routine used to extract the dark core length. The reason to omit the first rows of the contour and instead begin the linear fit where the contour was thinner was to avoid a recirculation zone generated at the exit of the original injector used in this work. This recirculation of the flow occurred due to the thick inner jet post which prevented the inner jet and outer jet from coming into contact right away after the inner jet post ended. The recirculation region appeared in the images to be just as dark as the inner jet dark core, and if taken into account it would bias the measurements. Therefore the upper limits of the fit were chosen a few inner jet diameters downstream the exit of the injector.

Once the limits for the linear fit were chosen, the corresponding line was obtained and its associated angle as well. An example of both left and right angles, α_{Left} and α_{Right} , computed in this manner is shown in Figure 5.2. The sum of the left and right angles was referred to as the “maximum inner jet spreading angle”. This computed spreading angle represented the region the inner jet traveled during the time it takes to record the 998 images, which ranged from 24 to 50 milliseconds. It is important to note that this ‘maximum inner jet spreading angle’ over predicted the mean of the spreading angles that

could be obtained from each of the 998 frames. This is because the maximum contour out of all the images was found and then the linear fit to the composite contour was obtained, instead of fitting a line and finding a spread angle for each image and then taking the average of these angles. When acoustics were present, this maximum spreading angle represented the region the inner jet had traveled during all acoustic cycles captured in the number of images processed, which varied from 70 to 155 acoustic cycles as indicated above. It represented the maximum acoustic spreading angle of the inner jet.

5.1.3 Outer Jet Spreading Angles

The outer jet spreading angle was defined to start from the point where the jet started to grow, approximately $2D_1$ to $4D_1$ downstream of the exit plane, and end at a location $10D_1$ downstream of the exit of the injector. Therefore this measure could be interpreted as an outer jet initial spread angle, $\alpha_1 + \alpha_4$. The main difference between the inner jet spreading angle measurement described in the previous subsection and this outer jet spreading angle measurement is the technique used. The outer jet spreading angles were extracted visually from 20 randomly selected images of the total of 998 available. Figure 5.3 shows an image recorded with the high speed camera with labels and arrows indicating how the spreading angle was obtained. Only α_1 and α_4 were visible and measured. The angles α_2 and α_3 were not visible in the images recorded. Regardless, they are indicated in the figure to complete a conceptual picture of the spreading of the outer jet both outside towards the chamber and inside towards the inner jet.

5.2 Results with the Original Coaxial Jet Injector Geometry

5.2.1 Behavior in the Absence of Acoustic Excitation

This section presents the results obtained for the coaxial jet experiment in the absence of acoustic excitation. Images of the jet for different outer to inner momentum flux ratios at each of the three pressure regimes studied are shown and their features discussed. An analysis of the dark core length measurements and spreading angles follows with observations and conclusions offered at the end.

In this work, the coaxial jet images without acoustic excitation provide a baseline to analyze the behavior of the flow when the effects of acoustic forcing are introduced. The results without acoustic excitation also provide information about inherent features of the flow such as naturally occurring instabilities and interaction between the two fluid streams. For reference, the actual distance from the exit of the injector to the bottom of the images varies between 1.5 and 2.0 cm.

The images in Figure 5.4 were obtained at subcritical pressures and show the coaxial jet with the old injector at different outer to inner jet momentum flux ratios. The feature that stands out the most in every image is the length of the dark core region. For $J = 0.17$, the dark core is long and evidence of breakup is only seen towards the end of the image. The relative smoothness of the dark core region at the exit of the injector disappears as the inner jet travels downstream. The core region then develops into shreds of dense fluid that are as dark as the initial dark core region but are not as well connected. Towards the end of the image regions of very

dense fluid can still be observed, though definitely not connected to the inner jet. In this image, the dark core might appear longer than the field of view but video images confirm that the breakup occurs within the visible area of the image. The spreading angle of the outer jet can be also seen.

The image for $J = 1.0$ features a comparatively thinner and slightly shorter dark core region, but the inner and the outer jets still behave in a similar manner. The reason for the jet to be thin for this and the next case ($J = 2.6$) compared to the other subcritical cases is not known. The inner jet mass flow rates and temperatures are similar for all cases (see Table C.1) and wider inner jets occur above and below the J values for which these thin inner jets are observed. A fact that could potentially explain this discrepancy is that the data for both the $J = 1.0$ and $J = 2.6$ cases were taken the same day, and at least 3 months before the data for the rest of the cases. However, operation procedures (see Appendix B) were the same throughout the study and it is highly unlikely that a different procedure was performed that day.

The next image ($J = 2.6$) has a feature that was not observed in the previous two cases. The inner jet shows a noticeable jet distortion and spread compared to its initial width. After a few inner diameters downstream the jet broadens and starts breaking up. However, denser flow structures are still convected downstream. Towards the bottom of the image an area with almost no darker regions is observed, unlike the first two, which featured dark structures throughout the image. The boundary of the outer jet is also affected by the spreading behavior of the inner jet

and features a wavy pattern; however, the overall angle is still very similar to the previous two conditions.

The next case at $J = 4.2$ shows a thicker, shorter inner jet with a different type of interaction with the outer jet than the previous three. The dark core seems to be entrained by the outer jet right away after it exits the injector region. Gray regions where the denser structures mix with the surrounding outer jet fluid are now noticeable towards the bottom of the image. Both the inner and outer jets shows similar spread compared to the $J = 2.6$ case. The outer jet contour is also wavy to accommodate for the observed behavior of the inner jet.

The next image corresponds to the $J = 9.6$ case with a very wide inner jet, which is attributed to a recirculation region created at the exit of the injector due to the inner jet post thickness discussed in chapter 4. With an outer jet momentum flux that is an order of magnitude larger than the inner jet momentum flux, the inner jet is quickly entrained by the outer jet, expanding as it leaves the inner jet. This phenomenon cannot be seen in the image because of the recess of the injector. The inner jet spread is still similar to the previous case as is will be explained in section 5.2.3 and the dark core length is greatly reduced compared to the previous cases. The inner jet also features a transition between the dark core region and progressively lighter regions of the flow downstream, an evidence of mixing between the inner and outer jets. At the exit of the injector a clear coaxial stream and a dark inner stream can be observed. Then, as they flow away from the exit they combine and form blended structures. This behavior is ideal for propellant mixing.

The last image corresponds to a momentum flux ratio of $J = 23$. Such high value for J was only achieved at the subcritical pressure regime. In this image we observe features that are very similar to the $J = 9.3$. This case features a thick dark core region, an even smaller dark core length and inner jet spreading angle. The momentum flux of the outer jet is so strong that the inner jet and outer jet appear very well mixed just a few diameters downstream the exit of the injector. Since the density and the mass flow rate of the inner jet for all subcritical cases is the same (see Table C.1), the broadness of the inner jet for the last two cases indicates that the inner jet has slowed down due to recirculation zone effects and the flow has been entrained further into the outer jet.

For the nearcritical pressure regime, images for 8 different momentum flux ratios were obtained. Even though at this pressure regime the flow was single phase, the images still feature a dark core and a lighter outer jet region as can be observed in Figure 5.5. The first image was obtained at $J = 0.55$ and shows a long dark core. A series of structures spreading out from the inner core region are observed near the center and towards the bottom of the image. This could be evidence of a particular instability or just the effect of flow entrainment by the outer jet at low J values for pressures over the critical point. The dark core is long and evidence of strong mixing is only seen towards the bottom. The second and third images show the cases at $J = 1.0$ and 1.1 respectively. The dark core lengths are similar and their dark core regions also spread in a similar fashion. The outer jet is not clear in the image corresponding to case $J = 1.1$ but in the case for $J = 1.0$ it follows the curved pattern of the inner jet. Both images show a region

were the inner jet is very well mixed with the outer jet towards the bottom of the image. The first three images show how more homogeneous mixing is accomplished closer to the injector as J increases.

For the case of $J = 1.6$ the dark core length has decreased. The dark core region still shows a wavy contour but it is not as clear as the previous three. The outer jet is clear in this case and shows a very similar spread pattern compared to the outer jets of the subcritical cases. The next image ($J = 2.1$) is not very clear. A dark core region can still be observed through the top portion of the image. Then a mixed region appears in the bottom half. This image resembles a blurred version of the image for $J = 1.6$, both having very similar dark core lengths.

The next two images in Figure 5.5 ($J = 2.9$ and 4.9) are also very similar and feature short dark core lengths. The spreading angles of the dark core region appear negative and the region where the inner and outer jets become well mixed start around the same location. This more homogeneous flow still shows some undulating structures that are clearly observed in the dark core region of the lower momentum flux ratio images.

The last image in Figure 5.5 shows the nearcritical case with the highest momentum flux ratio recorded ($J = 9.3$). It features a very short dark core. This image presents very clear evidence of the strong effect of the outer jet on the inner jet at high J values. The inner jet flow is completely mixed with its surroundings only a couple of millimeters after it leaves the injector. This effect is desirable in an actual engine for a couple of reasons. First, the propellants will burn more efficiently, and second, any

effects of the acoustics on the inner jet will be diminished since its length is very short and there is not much intact dense mass to excite.

The third set of images without acoustic forcing is shown in Figure 5.6. These images correspond to the supercritical pressure regime. The first one features the lowest momentum flux ratio ($J = 0.019$) of all the experimental data presented in this study. This image features a very long and spreading dark core region. It starts very thin at the exit and it expands as it travels downstream. The inner jet did not seem to be affected by the outer jet, most likely due to the very low outer jet momentum flux compared to that of the inner jet. The dark core in the next image ($J = 0.33$) is also long but its thickness is constant through most of the image until it starts to break up towards the end.

At $J = 1.3$ the inner jet shows again a wavy structure that resembles those found at the lower J values of the nearcritical pressure cases. The outer jet was denser than usual and thus appears darker in the image. In the $J = 2.4$ and 2.5 cases, the dark core length is greatly reduced. Also, the distinction between the inner jet and outer jet is not clear towards the end of the image. This is evidence that strong mixing between the dark core and the outer jet occurred. At the highest momentum flux ratio of the supercritical cases ($J = 9.9$), the same phenomenon that occurred for the highest sub and nearcritical cases was observed. The dark core becomes very thick and extremely short. Mixing is accomplished at a very short distance from the exit of the injector and the spreading angle of the inner jet appears negative.

5.2.2 Dark Core Length Results in the Absence of Acoustic Excitation

The dark core length results for the three different pressure regimes are presented next. The dark core length measurements were performed as described in section 5.1.1. The lengths are normalized by the inner diameter of the inner jet or D_1 . Figure 5.7 shows the behavior of the dark core as a function of the outer to inner jet momentum flux ratio for the subcritical cases. There is a general downward trend that is observed in the graph starting at $26D_1$ for $J = 0.17$ and decreasing to about $17D_1$ to $15D_1$ for J values between 5 and 1. The image also shows that the dark core lengths have large uncertainties for momentum flux ratio values less than 5. For $J = 9.6$ the value decreases to $8D_1$ and it decays to approximately $5D_1$ for the highest J value.

An effect of having a very long and thin dark core is the existence of regions that do not appear interconnected in some images. At this condition, the routine used to extract the average length interprets some long dark cores as short ones, especially at the lowest J value. At $J = 0.17$, the images generate mostly very long but some short dark cores, which are averaged and reported as a long mean dark core length with a large uncertainty associated to it.

In the following plot in Figure 5.8 the dark core lengths for the nearcritical cases are shown. Note that the nearcritical cases follow a very clear trend of decreasing dark core length with increasing J . The only case that seems to be just outside the curve is the $J = 2.1$ case. From Figure 5.5 we observe that the image corresponding to this case is somewhat blurred, most likely due to difficulties adjusting the camera lenses, as described in section 4.3. This could have contributed to a slightly larger length than

otherwise expected. The longest dark core of the set is $24D_1$ for $J = 0.55$. Then for $J = 1.0$ and 1.1 the lengths decrease to $15D_1$, with a very good agreement between these two different cases at very similar J values. For $J \approx 2$ they stay in the $15D_1$ to $10D_1$ range. For $J = 2.9$ and 4.9 the dark core lengths decrease to $6D_1$ and at $J = 9.3$, the highest momentum flux ratio, the dark core length is just one tenth of the value at the lowest J .

The dark core lengths for the supercritical cases (see Figure 5.9) show a similar trend to that found in the nearcritical cases. This is expected since both tests are above the critical pressure of the fluid and constitute single phase flow. Here the dark core length at the lowest momentum flux ratio ($J=0.019$) for the supercritical cases is close to $40D_1$. Then it drops close to $25D_1$ for $J = 0.33$ and reaches a value near $20D_1$ for the $J = 1.3$ case. For the two cases at $J = 2.4$ and 2.5 , a very good agreement, similar to the agreement between $J = 1.0$ and 1.1 in the nearcritical regime, is found, with both dark core lengths being very close to $10D_1$. Finally at $J = 9.9$ the dark core length is very short, $3D_1$, a characteristic that is shared by the highest momentum ratio cases from all three pressure regimes.

A plot showing all dark core length measurements but one obtained with the original injector appears in Figure 5.10. The case not shown is the subcritical case with $J = 23$ which had a value of L/D_1 of 5 and extends off the chart. Figure 5.4 shows that the subcritical dark core lengths span, in a broad sense, the whole image for the 2 cases with the lowest J values and almost all the image for the $J = 2.6$ case. However, the actual breakup of the continuous stream captured by the visual processing routine is occurring halfway along the image for the second and third cases, and it is only clear in the image

for the fourth ($J = 4.2$) case. The uncertainty in dark core length for the first three subcritical cases is large compared to the fourth one, since this case features a thicker inner jet and thus breakup location does not fluctuate as much as the first three.

In Figure 5.10 the trend laid out by the sub, near and supercritical cases is quite clear. There is a transition between very large dark core lengths when $J < 1$ and very short lengths when $J > 3$. The images shown in Figure 5.5 and Figure 5.6 for near and supercritical cases, respectively, share several features, such as thicker dark core regions and smeared boundaries between the inner and outer streams. The near and supercritical regimes are also single phase, which clearly alters the dynamics of the jet, which explains in part why the boundaries are less clear than those from the subcritical images.

In the subcritical cases, surface tension in the liquid prevents the molecules from drifting towards the gaseous outer jet fluid, making the boundary between both phases sharper. The surface tension maintains the liquid molecules together until shear forces are strong enough to strip away some fluid particles. These are the unconnected structures that are seen in the lower momentum flux ratios. Surface tension thus prevents the jet from mixing. That is a possible explanation to why higher momentum fluxes are needed to reach the same dark core lengths at subcritical conditions in contrast to near and supercritical conditions.

Momentum transfer due to turbulent motion can also be enhanced by the lack of surface tension above the critical pressure and temperature. The particles of heavier fluid are quickly drawn toward the lighter stream due to the large density and velocity gradient in the otherwise homogeneous supercritical flow. For example, the subcritical image

(Figure 5.4) for a momentum flux ratio of 23 has a dark core length of $5D_1$, similar to the near and supercritical images (Figure 5.5 and Figure 5.6) near a momentum flux ratio of 10, which have dark core lengths between $2D_1$ and $3D_1$. The image for the subcritical condition at $J = 9.6$ also resembles the near and supercritical images in the $2 < J < 3$ range, with dark core lengths around $10D_1$ for all these cases (see Figure 5.4 to Figure 5.6).

The plot shown in Fig. 5.11 shows the results obtained with the original injector with no acoustic excitation gathered over a period of more than 6 years at the Supercritical Cryogenic Laboratory (EC 4) at AFRL in Edwards AFB, CA. For the subcritical data obtained in the present work, the results follow the trend from previous results by Davis (41) and Leyva et al. (22), except at very low supercritical and very high subcritical momentum flux ratios. For the nearcritical results, the present work shows good agreement with the lengths found by Davis. However, the supercritical data only lies close to previous supercritical data by Davis and Leyva at the higher momentum flux ratio case. In the overall sense, the current results fall within the region corresponding to the pressure condition in which they were taken, except for the lowest momentum flux ratio for the supercritical cases. The results in this plot provide a “map” that future researchers using similar coaxial injectors to those employed in this work could use to compare their results in subcritical to supercritical pressure regimes.

5.2.3 Inner Jet Spreading Angle Results in the Absence of Acoustic Excitation

The analysis of the spreading angle provides a measure of the amount of momentum either the inner or outer jet develops in any outward direction that is perpendicular to the axis of motion. In the current experiments, the inner jet spreading angle was easier to identify than the outer jet given the darkness of the inner jet region. Inner and outer jet spreading angles represent a measure of mixing between propellants and how they spread within the chamber. This is useful information for LRE injector design.

In this section we will look at the behavior of the inner jet spreading angles without an externally imposed transverse acoustic field. This study includes inner jet spreading angle results for outer to inner jet momentum flux ratios in the $0.02 < J < 20$ range. The graph in Figure 5.12 shows that the subcritical jets do not spread too much compared to its initial thickness, with all angles below 10° . The maximum spread is observed at $J = 2.6$, consistent with the initial thickness of the inner jets in Figure 5.4 and observing how they spread. The measured changes in spreading angle for the subcritical case could be within the experimental uncertainty; however, more data is required to reach a conclusion. For $J = 4.2$ and 9.6 the spreading is similar but the initial thickness is higher, thus the overall angle is slightly smaller. The smallest angles for the subcritical cases occur at the lowest and highest J values and they are in the 2° to 3° range.

For the near and supercritical cases, the spreading angles reach both higher and lower values than those of the subcritical cases. Starting at the very low J values of 0.019 and 0.33 for the supercritical cases, we observe an initial spread that is comparable to the average value of the angles for the subcritical cases. Looking at the set of supercritical

images of Figure 5.6 these low angles correspond to the relative small thickness of these supercritical jets. Then the cases between $J = 0.5$ and $J = 2.5$ show the largest angles, which vary from 10° to 17° , for both nearcritical and supercritical tests. The dark core regions for these cases show dark core flow structures that oscillate in the transverse direction as the flow travels downstream, which contributes to these large spreads and are likely related to the reduced core length with enhanced mixing. Finally, for values of J near 3 and above, the angles decrease prominently, reaching negative values near 5 and beyond. Previous data by Leyva et al. (22) were used to confirm this trend for supercritical pressures near $J = 5$, since there were no data from the present study near those J values at supercritical pressures. The negative values are the effect of a very thick jet due to the aforementioned circulation zone at the exit of the injector and rapid mixing at very high outer to inner jet momentum flux ratios, which actually make the jet thinner by stripping fluid away from the inner dark core region. These small angles can be observed in the images for the corresponding momentum flux ratios in Figure 5.5 and Figure 5.6.

One important difference between the spreading angles for subcritical cases compared to those for the near and supercritical regimes is the effect of the surface tension of the liquid inner jet and larger density gradients at the boundary between the inner jet and the outer jet for subcritical cases compared to the cases above the critical point. Surface tension forces keep molecules together and could be a factor for the inner jet at subcritical conditions not spreading as much as its nearcritical and supercritical counterparts.

5.2.4 Outer Jet Spreading Angle Results in the Absence of Acoustic Excitation

In this section we analyze the behavior of the outer jet spreading angles without an externally imposed transverse acoustic field. The pressure regime studied is subcritical but the coaxial flow is single phase (gas-gas). The outer to inner jet momentum flux ratios varied from 0.013 to 2.0. The purpose of taking the gas-gas data is to compare the results with the available literature on single phase shear layers and coaxial jets, which is more abundant than two-phase investigations. For subcritical pressures, we generally obtained two phase flow, since the inner jet temperature was either a few degrees below or at the saturation temperature, and the outer jet was in the vapor phase. The experimental procedures were therefore modified to keep the inner jet in a gaseous state. Images of the single phase coaxial jet at subcritical conditions and momentum flux ratios from 0.013 to 2.0 are shown in Figure 5.13.

One of the areas of interest of gas-gas flows in coaxial jet behavior is the situation where both fuel and oxidizer are injected into the combustion chamber in the gaseous phase. For the near and supercritical pressures regimes used for the inner jet spreading angle cases, the inner and the outer jet constituted single phase flows but certainly not in the gaseous state. In order to have a gaseous inner jet and a gaseous outer jet coaxial flow, the flow had to remain at a subcritical pressure and the inner jet had to remain as a gas. To achieve this, the flow of liquid nitrogen through the heat exchanger that cools down the inner jet flow was decreased. This was allowed to provide just enough flow to achieve a density difference between the outer and the inner jet so that the coaxial jet

could be visualized. These single phase tests, to be discussed below, make more complete the outer jet spreading angle measurements and make gas-gas data available for comparison to other researchers. However, since the inner jet flow was not dense enough, it did not appear dark in the backlit images. Thus, a measurement of the dark core length could not be accomplished with the single gaseous phase data.

Outer jet spreading angle measurements in the absence of acoustics were thus the only measure processed from 6 subcritical cases. The momentum flux ratios are low because of the density of the inner jet could not be increased. To generate these cases, the inner jet mass flow rate was fixed and the outer jet mass flow rate was varied. A visual inspection of at least 20 randomly-selected images for each case was performed. From each picture a left angle (α_1) and a right angle (α_4) as described in Figure 5.3 were obtained. These angles were added and a total spread angle was found as shown in Figure 5.14. For these subcritical conditions, the trend starts with a very low J ($= 0.013$) and a negative spreading angle ($- 6^\circ$), which indicates that outer jet width is decreasing as it exits the tip of the injector. The next J is 0.037 and in this case the coaxial jet shows an angle of 5° . The remaining J values surveyed have angles in the 10° to 11° range.

To compare the results from these subcritical gas-gas experiments with other available data, a plot of the spreading angle growth rate as a function of the density of the chamber, the density of the outer jet and the momentum flux ratio is shown in Figure 5.15. The plot also includes experimental, numerical and theoretical data from various researchers on spreading angles of coaxial jets and 2D shear layers. The linear fits are derived for the growth of a 2D shear layer by Dimotakis (43) and Papamoschou and

Roshko (44). The expression of Papamoschou and Roshko predicts the visual growth of the shear layer and the formula Dimotakis derives predicts the vorticity growth of the shear layer. However, Dimotakis shows how to convert from vorticity growth to visual growth, which is the quantity that the gas-gas data are compared against. The applicability of these expressions to axisymmetric and coaxial jets is limited to the region very close the exit of the injector where the flow of the outer jet and either the flow of the chamber or the inner jet meet.

The experimental work by Brown and Roshko (42) measured the visual growth of the shear layer formed between two incompressible fluid streams of different densities. The experimental results from Favre-Marinet and Camano Schettini (64) are obtained from coaxial jet experiments where the densities of the inner jet, outer jet, and chamber fluid were different. The data from Liu et al. (65) were extracted from velocity and temperature contour images presented in their paper. An interesting characteristic from their study is that the geometry of their injector is modeled after the original injector analyzed in this study. It is thus not so unexpected to find their results more in agreement with the spreading angles found in this study than the rest of the data discussed so far.

The data by Leyva et al. (22) were obtained using the same facility with the same flow configuration and fluid characteristics used to obtain the one-phase gaseous state data presented in this work, which will explain the very close agreement between their data points and the results of this one-phase gaseous state study for $J > 0.1$. The only difference is that none of the angles reported by Leyva et al. (22) are one-phase gaseous state coaxial jet flows, which makes the agreement much more interesting.

In the graph in Figure 5.15, the exact variable against which the spreading angle (defined as $d\delta/dx$ or $\tan \alpha_1 + \tan \alpha_4$) is plotted is the ratio of the chamber density to that of the outer jet multiplied by the square root of the outer to inner jet momentum flux ratio. The reason to incorporate outer to inner jet momentum flux ratio as a parameter instead of just the more widely used chamber to outer jet density ratio is to bring in the effects of the inner jet on the outer jet spreading angle. The square root of J was used instead of just J to avoid cancelling outer jet density from the expression.

A very plausible explanation for the larger angles obtained by the analytical formulas from Dimotakis (43) and Papamoschou and Roshko (44), and experimental data from Brown and Roshko (42) and Favre-Marinet and Camano Schettini (64), as compared to the shorter angles obtained for the rest of the data, involves the type of flow modeled and the injector geometry used. The particular injector configuration used in this work, which is the same geometry used by Leyva et al. (22) and Liu et al. (65), produces a relatively large recirculation zone between the inner jet and the outer jet at the inner jet exit location. This recirculation zone does not exist in coaxial jet geometries where the inner jet and the outer jet are separated by a very thin wall or for two-dimensional shear layer mixing studies where the flows mixing at two different velocities are assumed to have a wall of negligible thickness between them. Further studies in the gas-gas regime with the new injector could provide evidence to prove this claim.

5.2.5 Acoustic Field in the Test Chamber

The results of the behavior of the coaxial jet under acoustic forcing are drawn from a complete set of data where at least 6 cases are reported for each of the three mean chamber pressure conditions surveyed: subcritical, nearcritical and supercritical. The peak-to-peak pressure perturbation as a percentage of the mean chamber pressure varied from less than 1 to 4 %, the outer to inner jet velocity ratio ranged from 0.25 to 23 and the outer to inner jet momentum flux ratio ranged from 0.019 to 23.

Two acoustic sources were used to generate the transverse acoustic field inside the inner chamber of the experimental apparatus. To expose the coaxial jet flow to different acoustic conditions, including conditions near or at the pressure node or antinode, the phase between the two acoustic sources was varied from 0° to 360° in steps of 45° . To characterize the acoustic field inside the inner chamber during each test, pressure measurements were obtained from pressure transducers inside the inner chamber. One absolute pressure transducer was located at the bottom of the inner chamber, very close to the orifice through which the flow exited the enclosure, to minimize as much as possible any effects of the probe on the coaxial jet and vice versa (Figure 5.16a). Three absolute pressure transducers were located at the bottom of the inner chamber for the first injector studied (Figure 5.16b) and three differential pressure transducers were located halfway between the middle and the top for the second injector studied (Figure 5.16c).

A measurement of the root-mean-square (RMS) values of the pressure fluctuations at each phase angle condition is shown for a nearcritical case in Figure 5.17. In the graph, the baseline shows the measurement when there is no acoustic excitation

inside the chamber. The positive number in the RMS of the pressure, between 3 and 4 kPa, represents the noise in the measurement. Thus the pressure transducer cannot discern pressure oscillations with an RMS below 3 kPa.

At each phase angle condition, either three or one data sets were obtained. When three data sets were collected, it consisted of data with both acoustic sources on, only the left acoustic source on, and only the right acoustic source on. When only one data set was collected, it consisted of data with both acoustic sources on. The purpose of recording data with only one source on was to compare the results obtained with each acoustic source and verify that their acoustic amplitudes did not change throughout the test. Phase angle is thus not a meaningful quantity for the single source excitation cases and it is indicated to show the order in which this single source excitation cases were taken.

The number of phase angles for which results for one acoustic source were obtained varied depending on the time available to run the tests. Some cases have no results with only one acoustic source on (i.e. only data with both acoustic sources on was recorded) and others have up to five phase angles for which single-source excitation was recorded. The slight differences in the results obtained with either acoustic source throughout the course of any given test may be attributed to the different times at which the measurements were made.

All pressure measurements reported in this study for the original injector were obtained using the pressure transducer at the bottom of the inner chamber shown in Figure 5.16a. The pressure measurements reported for the new injector were obtained using the center pressure transducer, which was the one closest to the injector exit, of the

three shown in Figure 5.16c. The pressure measurements for the new injector are shown, together with dark core length and spreading angle results, in section 5.3.

Results with only one acoustic source on for the case shown in Figure 5.17 were recorded for only three phase angles. In this nearcritical case with $J = 2.1$, the left acoustic source, in triangles, had RMS values of 7.13, 7.10 and 7.17 kPa and the right acoustic source, in squares, had RMS values of 6.07, 6.02 and 6.26 kPa for 0° , 45° and 315° phase difference, respectively. The data verified that the amplitudes of each acoustic source by itself do not vary with phase angle, which is what is expected. Also, though not exactly the same, the left and right source amplitudes are very close. This fact is important when considering the effect of both acoustic sources on. These data points are represented in Figure 5.17 by the diamond-shaped markers, which show a very well defined curve that has the same RMS value at 0° and 360° and it also shows a minimum (at 225°) and a maximum (at 45°) that are separated by a 180° phase difference. The minimum in pressure fluctuations occurs near the 180-degree phase angle and the maximum near the 0-degree phase angle, which is theoretically where the minimum and maximum pressure fluctuations should occur. The minimum pressure fluctuation at 225° also shows an RMS value just slightly over the baseline value, indicating that the two signals cancelled each other almost completely.

The same type of graph shown in Figure 5.17 was plotted on the left side of Figure 5.18 for three other cases. In these graphs, the effect of the phase difference between the two acoustic sources on the coaxial jet at different chamber pressure conditions can be observed. Higher amplitude forcing and the ability to expose the jet to

different effective positions relative to pressure nodes and antinodes are created when there are two acoustic sources operational. The supercritical case with $J = 9.9$, in the bottom graph on the left side of Figure 5.18, shows the ideal acoustic behavior described above where a maximum pressure perturbation was achieved at a 0° phase angle between the acoustic sources and the minimum achieved at a 180° phase angle between them. In the top graph on the left side of Figure 5.18 for the subcritical case with $J = 9.6$, the maximum and minimum pressure perturbation are observed at 315° (-45°) and 135° respectively. Thus, maximum pressure perturbations were observed at $0^\circ \pm 45^\circ$ and minimum pressure perturbations were observed at $180^\circ \pm 45^\circ$ for the three graphs shown on the left side of Figure 5.18.

The reason for the pressure noded and antinodes to be observed at different phase angles for different tests is not fully understood, but a source of error might be the acoustic sources themselves. One possible explanation for this asymmetry is strong crosstalk between speakers. The vibration of one not being completely shielded from the vibration of the other one. This has been observed in strain gauge measurements with only one acoustic source. One of the piezo-sirens has a strain gauge which generates a signal that is carefully monitored to prevent damage to the piezo. It is supposed to only produce a signal when the acoustic source to which the gauge is attached is on. However, a noticeable signal is also recorded when the piezo-siren to which the strain gauge is attached is off and the other piezo-siren is on.

The observed asymmetry could also be explained by the fact that the piezo elements used by the acoustic sources to produce their oscillatory movement are voltage-

dependent and capacitance-dependent, the latter also changing with temperature. Very slight through moderate differences in the voltage or capacitance values to each piezo-siren element could delay the signal to one or both sources, which in turn would shift the location of the actual 0° degree phase angle between them. However, minima were observed at 180° apart from the maxima for all three cases, and the relative 0° degree phase angle did not go beyond $\pm 45^\circ$. Therefore, the shift between the expected or ideal phase angle and the actual phase angle was consistent in every case.

To have a better understanding of the chamber environment during these tests, the time history of the chamber pressure for a period of 6 ms during different transverse acoustic excitation conditions is plotted on the right set of graphs of Figure 5.18. The 0 ms point does not indicate the moment when data started to be recorded but it was an arbitrarily chosen point during the time the acoustics were on. The acoustic data shown for different phase angles in these set of graphs refers always to the case when both acoustic sources are on. In these graphs, the conditions where maximum and minimum pressure oscillations were obtained along with the baseline condition with no acoustic sources on are plotted. The top graph on the right, which represents a subcritical case, shows the chamber pressure for the 315° phase angle oscillating consistently between 1.51 and 1.56 MPa, compared with 1.52 to 1.54 MPa which then shifts to 1.53 to 1.55 MPa for the 135° phase angle.

The graphs in Figure 5.18 also include the baseline condition which shows that the pressure stays at 1.530 ± 0.005 MPa. For both the 135° and 315° phase angle conditions one can observe that the pressure follows a wave-like pattern, unlike the

baseline condition, and the number of peaks for both phase angles is 18, which corresponds to a frequency of, or very close to, 3kHz for a period of 6 ms. In fact, a wave-like pattern should only be expected for a phase angle of 315° , where the maximum oscillations occur, and for the minimum oscillation condition the signals should cancel as shown in the 225° condition of Figure 5.15. The reason that this does not happen in the top right graph of Figure 5.18 is because the amplitudes of each acoustic source by itself are very different. This can be seen in the top graph on the left side, which shows an RMS value between 11 and 12 kPa for the left acoustic source and a value around 5 kPa for the right acoustic source. Therefore the oscillations reach a minimum at 135° but the signals never cancel because the amplitude of the signal from the right source is smaller than the amplitude of the signal from the left source. Incidentally, the number of peaks in the wave-like signal for the 135° condition is also 18 as expected.

In the middle graph on the right, the chamber pressure history for the nearcritical case is shown. In this case, the condition at 45° presents the maximum oscillations which fluctuate from 3.58 to 3.61 MPa. In contrast, the condition at 225° presents the signal with lowest pressure perturbation. In fact, its behavior is not wave-like but appears more noise-like. Its signal starts at its lowest point around 3.59 and reaches up to 3.61 in the 6 ms period but it is not oscillating between those two extremes but instead drifting from one to the other. The largest oscillations within the 225° condition occur near the 4.5 ms mark with peak-to-peak amplitudes of 0.01 MPa. In this case, the left and right acoustic sources have values just above and below 6 kPa, which allow for better signal cancellation. The third signal is the baseline, which stays near 3.59 MPa up to the 4 ms

point, where it starts going slightly below this value but still very close, showing how little perturbation, if any, the chamber experiences when there are no acoustics present.

Finally, the bottom graph on the right shows a supercritical case where the condition of maximum pressure perturbation took place at 0° , where it is normally expected. The wave-like pattern features 18 peaks with oscillations which range from just under 4.98 MPa to halfway between 5.00 and 5.01 MPa. The minimum pressure oscillations occur at 180° where the oscillations stay between 4.99 and 5.00 MPa for almost the entire 6 ms period. In contrast, the baseline condition performs erratically but does not show any wave-like or high-frequency pattern; its behavior most likely due to a transitional period after adjusting the pressure during testing.

It can be noted that, though sometimes there was some discrepancy in the value of the phase angle at which the minimum and maximum pressure fluctuations occurred for different cases, the coaxial jet was always exposed to a full range of acoustic conditions from a minimum to a maximum in velocity and pressure perturbations. In consequence, an analysis of these different acoustic conditions on the jet behavior could be performed to quantify and understand their effects on the mechanics of the jet by looking at parameters such as the dark core length and the spreading angle of the outer and inner jets.

5.2.6 Behavior during Exposure to Acoustic Excitation

In this section, images of the coaxial jet at each phase angle for three different cases at each of the three pressure regimes studied are shown. The behavior of the jet

is described and the important features are highlighted. The baseline images are also included to compare its dynamics with and without acoustic excitation. The first set of images is shown in Figure 5.19. It corresponds to the case where $J = 0.17$ with and without forcing. At this low momentum flux ratio at subcritical pressures the jet is usually thin. The overall behavior of the jet does not change substantially with and without acoustic forcing but an increase in mixing can be observed. For the 0° and 315° conditions the inner jet starts spreading and breaking up into smaller dark core sections that mix with the outer jet towards the middle of the image. In contrast, the 135° and the baseline conditions show very little spread and the core only starts to break up towards the bottom of the image. These images feature the largest dark core lengths of the subcritical tests.

The second set of subcritical images corresponds to a momentum flux ratio of 2.6. The effects of the acoustics in this set of images, shown in Figure 5.20, are very clear. The inner jet dark core bends significantly for every phase angle reaching a maximum at 180° . Mixing improves significantly with large regions where the dark core structures have almost completely blended with their surroundings. This effect is particularly enhanced for phase angles between 45° and 215° . For the rest of the conditions a few dark fluid structures can still be observed throughout the image, but for the phase angle range mentioned the images show very few dark structures beyond certain point near the center. This sequence of images shows that the effects of high velocity fluctuations (pressure node conditions) due to acoustic forcing are very strong and can make a difference in practical systems operating near this momentum flux ratio.

The next set of images for the subcritical case is shown in Figure 5.21 and corresponds to a momentum flux ratio of 9.6. All the images feature a very thick dark core which differs substantially from the thin dark core regions observed in the previous two sets of images. This thickness is evidence that the high momentum flux of the outer jet is having a strong effect on the inner jet allowing it to expand very rapidly across the recirculation region at the exit of the injector. The recess length of the inner jet hides this phenomenon and we only observe a thick jet emanating from the exit of the injector. Even at this high momentum flux ratio the dark core region is affected by the acoustic forcing as seen by the curvature of the inner jet for all phase angles, an effect that might not be obvious if only the effects of the dark core length are considered.

Finally, the set of images for the subcritical case corresponding to a momentum flux ratio of 23 appears in Figure 5.22. The dark core seems to be even thicker than the case for $J = 9.6$. The shape of the dark core does not seem to vary at all among the images and the only difference is the slight change in curvature at towards the bottom of the dark core for different acoustic conditions, which is evidence of the effects of acoustic excitation even at these high momentum flux ratios. In fact the forcing induces strong oscillations on the already mixed coaxial jet flow towards the middle of the image. However, as pointed out in the previous case, this behavior is not taken into account since only the effects of the dark core length are being considered.

The set of images shown in Figure 5.23 corresponds to the nearcritical case with $J = 0.55$. In this case the inner jet shows an already perturbed behavior with structures emanating from the dark core region in an outward fashion. This could be evidence of the

interaction of the denser, faster inner jet flow with the slower and lighter outer jet. However, this oscillating pattern is not enhanced by acoustic forcing as noticed in the rest of the images. In fact, near the 180° phase angle the wavy structures seem to be suppressed. On the other hand, the dark core length provides visual evidence of acoustic forcing. A specific phase angle for which the dark core is shorter cannot be clearly chosen but the general trend is that the dark core region ends sooner for all phase angles compared to the non acoustics condition. Interestingly, acoustic forcing in this case seemed to affect the dark core length and not change the spreading angle. This behavior is opposite to the one observed for the subcritical case with a large momentum flux ratio, where the curvature of the core was affected but not the dark core length.

The next set of images, shown in Figure 5.24 corresponds to the nearcritical case with a momentum flux ratio of 4.9. In these images the effects of acoustics can be noticed on both the dark core length and its spreading behavior. The baseline image shows a thick jet as it exits the injector that eventually gets thinner as it mixes with the surrounding fluid. This effect is not only enhanced for the dark core under acoustic forcing but it actually adds a curvature to the dark core region that was not present in the baseline case. The overall effect of this transversal motion of the jet is a shorter and slightly thinner dark core that shows noticeable bending which enhances mixing even further.

The nearcritical set of images for the test with the highest momentum flux ratio for this pressure regime is shown in Figure 5.25. The baseline case shows an extremely short dark core region that is completely entrained by the outer jet just a few diameters downstream the exit of the injector. The rest of the images with acoustic forcing are quite

similar to the baseline case. They feature very short dark core regions and the spreading angle is almost non-existent. If there is an effect of the acoustics on the coaxial jet flow, it takes place after the two streams have completely mixed.

A final set of three different supercritical cases for different momentum flux ratios is presented here. The images in Figure 5.26 show the case for a momentum flux ratio of 0.33. This case features an inner jet region that is not smooth, from which fluid structures emanate at right at the exit of the injector, which resembles the momentum flux ratio case $J = 0.55$ of the nearcritical regime. In both cases the difference in velocity and density across the two layers of fluid appear to develop these outward-moving structures. The dark core length of the inner jet under acoustic forcing does not change noticeably. The only clear image that shows a shorter dark core length occurs at 360° whereas the image at 180° shows a dark core length similar to that of the condition with no acoustics. The spreading angle also appears to remain roughly constant. Thus, clear effects of acoustic forcing are not evident here.

The following set of images shown in Figure 5.27 corresponds to the supercritical case at $J = 2.4$ at different acoustic excitation conditions. The dark core length of the baseline is considerably longer than those observed for the cases under acoustic forcing. There is also evidence near the exit of the injector that the inner jet is being bent by the acoustic field. The curvature that is observed in conditions 135° and 225° for the acoustically excited jet does not appear at all in the baseline image. The spreading and bending associated with the forced conditions produced a well mixed flow earlier than the case without acoustics, which shows a grey region that is very dark

towards the bottom of the image, and it does not appear in the rest of the images with acoustics. The closest image to resemble the baseline flow behavior is the condition at 135° and even for that image the dark core length and the spread angle right at the exit are quite different.

The images in Figure 5.28 correspond to a momentum flux ratio of 9.9 at a supercritical pressure. In these images all dark core lengths are very short and therefore look very similar. This case resembles closely the nearcritical case with the momentum flux ratio of 9.3. In both cases the momentum flux of the outer jet is an order of magnitude larger than that of the inner jet. The faster gaseous flow shears off fluid from the thick inner jet very rapidly and leaves a very short dark core region. The only difference that is observed between these two cases is the effect of the acoustics on the spreading angle or bending of the inner jet. The images in this supercritical case do appear to have some curvature due to the effect of acoustics. In particular, the conditions between 135° and 270° feature a short, bent inner jet to the right that is different from the baseline case. Also, some of the images, such as the conditions at 45° and 135° show a gray, less dense structure that continues to show curved features a few diameters downstream; however, their boundaries are difficult to discern.

5.2.7 Dark Core Length Results in the Presence of Acoustic Excitation

The results of the dark core length measurements of the inner jet of the coaxial jet flow are presented in Figure 5.29 to Figure 5.31. The figures show a series of plots with the dark core length measurements on the vertical axis and the different acoustic

conditions on the horizontal axis. A secondary axis shows the amplitude of the pressure oscillations as a fraction of the recorded mean chamber pressure for that case. The first value on the horizontal axis is the baseline measurement without acoustics followed by the measurements of the dark core length with acoustics starting with a 0° phase angle between acoustic sources and then in steps of 45° until a full cycle is achieved at 360° . All the values are normalized by the baseline condition of the case, which is the length of the dark core without acoustics. The error bars show the composite uncertainty of the non-dimensional length variable, $L_{\text{acoustics}}/L_{\text{no acoustics}}$, using one standard deviation as the uncertainty of each measured variable.

The values of the dark core lengths for the tests at subcritical pressures are shown in Figure 5.29. As a reminder, the tests at subcritical pressures represent a two-phase coaxial jet flow, where the inner jet is in liquid state at a temperature below the critical temperature of N_2 , and the outer jet is in a gaseous state at a temperature above the critical temperature of N_2 .

The subcritical tests showed that for $J = 0.17$, the length of the dark core changed noticeably with acoustics. It was shorter or equal to the baseline for all conditions with the exception of the 225° phase angle, where the length was 4% larger, which is not meaningful due to the large uncertainty. The largest dark core also coincided with the condition of lowest pressure perturbations. The dark core length results for $J = 1.0$ do not show any trend, and the corresponding acoustic measurements do not show any wave-like pattern either. The results might be the response to disordered signal input to the acoustic drivers.

For $J = 2.6$, a sinusoidal-like pattern, similar to the $J = 0.017$ case, is observed in the length. The value goes as high as 80% the baseline value and decreases below 60%. The pressure oscillations seem to follow the pattern, so that the lowest pressure oscillations occur at the same conditions as the largest changes in length. For $J = 4.2$, the data shows a clearer trend with smaller uncertainty. It has its lowest length values when acoustic forcing is the largest and vice versa. The pressure data have an evident sinusoidal shape. For $J = 9.6$, there is some change in the length with acoustics, which stays between 80% and 90% of the baseline value. The effects of the outer jet entraining more and more fluid from the inner jet can be seen here. For $J = 23$, the outer jet has even more momentum flux compared to the inner jet, making the dark core very short and irresponsive to the acoustics, the change in length stays between 90% and no change with respect to the baseline value. The large uncertainty in the data did not allow a conclusive statement for most J values but the general trends could still be observed.

The next set of graphs shown in Figure 5.30 show the results for the tests performed at nearcritical pressures. At these pressures, the coaxial jet flow had only one supercritical phase present since both the temperature and pressure of the inner and outer jet, as well as the surrounding environment, was above the critical temperature and pressure of N_2 . The results show that at $J = 0.55$ the change in length of the dark core varies between 60% and 80% of the baseline value, which indicates a definitively strong effect of the acoustics on the jet. A similar effect is observed at $J = 1.0$ and $J = 1.1$, where most of the lengths obtained under acoustic forcing remain between 60% and 80%, although there are a couple of conditions, 90° and 180° at $J = 1.0$ where the length does

not change much with respect to the baseline, and the acoustic data does not have any particular pattern that might account for that behavior.

At $J = 1.6$, the change in length follows very closely the behavior of the pressure perturbations and the dark core lengths remain in a range between 70% and 90% of the baseline values. Then the largest effects of acoustics are observed for $J = 2.1$ and 2.9 . Both cases show an average change of length around 60% with respect to the baseline. Both cases have very similar acoustic fields and dark core length changes. The only difference for the $J = 2.1$ and $J = 2.9$ cases is in the behavior of the conditions at 225° , 270° and 315° , which do not follow a sinusoidal pattern for $J = 2.1$. The effect of the acoustics is also very clear in the $J = 4.9$ case. The length of the dark core changes between 70% and 60% of the baseline value for all conditions except at 45° , where it decreases only to 75% of the baseline value. These results show that at J values near 5, a relatively weak acoustic perturbation, in the order of one percent of the mean acoustic chamber pressure, can reduce noticeably the length of the dark core. For the last case, where $J = 9.3$, the results show that the dark core length hardly changes at different acoustic conditions. At this point, the momentum flux of the outer jet is almost 10 times that of the inner jet and it entrains a large amount of fluid from the inner jet. This results in a very small dark core region at the exit of the injector, and a very short dark core length that does not get influenced by the acoustic field.

Thus from the nearcritical pressure tests and within the limits imposed by the calculated uncertainty, a significant reduction of the dark core length with respect to its non-forced value is observed during acoustic excitation at moderate J values. This

decrease in the length, and therefore enhancement of mixing is achieved in the $1 < J < 5$ range. At higher outer to inner jet momentum flux values the outer jet starts to entrain a significant amount of fluid from the inner jet inhibiting the effects of the acoustic field on the dark core.

The third set of plots in Figure 5.31 presents the values of the dark core lengths for the tests at supercritical pressures. These results also represent single-phase coaxial jet flow since the chamber, the inner jet, and the outer jet are at supercritical temperature and pressure conditions. All the plots show well defined acoustic fields with minima between 180° and 225° . The amplitude of acoustic forcing does not go over 0.75% of the mean chamber pressure. The first two supercritical cases, which are below $J = 1$, show a moderate effect of the acoustics on the dark core. For these cases, most of the dark core lengths with acoustics on fall within the range of 80% to 90% of the baseline length. However, they do not show any trend with phase angle.

For the supercritical case at $J = 1.3$, all the dark core lengths are within 60% to 80% that of the baseline, but no trend is found either. The cases where $J = 2.4$ and 2.5 show a reduction of the dark core that sets the length with acoustics below 60% of the baseline length for some phase angle conditions whereas only one phase angle condition from both cases presents a dark core length that is over 80% of the baseline length. Finally, similar to the nearcritical case for $J = 9.3$ in Figure 5.30 above, a supercritical case for which $J = 9.9$ is shown. This test shows a moderate increase of the dark core length with acoustics for half of the conditions. This might be attributed to a short baseline value extracted. However, since the momentum flux of the outer jet is

significantly higher than the momentum flux of the inner jet, a very small dark core region at the exit of the injector is expected and effects such as a longer dark core length with acoustics are possible.

From the supercritical pressure tests, within the limits of the uncertainty, a reduction of the dark core length similar to that observed for the nearcritical cases was accomplished. Again, the largest effects on length decrease and mixing enhancement were achieved in the $1 < J < 5$ range. For higher values, the inner jet starts to lose its core in a very rapid fashion to the outer jet which makes very difficult to distinguish the effects of the acoustic field on the dark core.

To assess the effect of the pressure on the coaxial jet flow, dark core length changes at different pressures for a given outer to inner jet momentum flux ratio are presented next. The ratio of the length of the dark core with acoustics to the length of the dark core with no acoustics ($L_{\text{acoustics}}/L_{\text{no acoustics}}$) and the peak-to-peak pressure perturbation as a percentage of the mean chamber pressure ($\Delta p_{\text{peak-to-peak}}/p_{\text{mean}}$) both as a function of the phase angle between acoustic sources are shown in Figure 5.32. Although $\Delta p_{\text{peak-to-peak}}/p_{\text{mean}}$ is not 0% for the baseline conditions, it is still below the rest of the values that correspond to the conditions with acoustic forcing. The quantity shown represents the noise measured by the pressure transducer. In this series of plots, the uncertainty of the dark core length results is not included, to avoid cluttering of the graphs. The uncertainty values can be obtained from Figure 5.29 to Figure 5.31.

Despite the relative acoustic excitation intensities varying several times from supercritical to subcritical conditions, the reduction in normalized dark core length (1 -

$L_{\text{acoustics}}/L_{\text{no acoustics}}$) at most phase angles for $J \approx 1.0$ ranged from 20% to 40%. Even with the large uncertainties associated with these results, the large amount of data that fall in this region shows that the acoustics have an effect at a value of J close to 1. When the outer to inner jet momentum flux ratio approaches 2.5 a similar trend is observed. The normalized dark core length now has a broader range reaching values as low as 50% of the baseline length and as high as 90% of the baseline length. The large spread could be a consequence of the inherent uncertainty of the measurements but still shows that acoustic forcing produces a clear shortening effect on the dark core length for J values near 2 to 3 as well.

For outer to inner jet momentum flux ratios near 10, the largest reduction in the dark core length ($1 - L_{\text{acoustics}}/L_{\text{no acoustics}}$) is at most 20%, usually at subcritical pressures. Both nearcritical and supercritical cases show little or no reduction in their dark core length, in fact some of the data indicates that the dark core lengths actually increased in some cases. However, this phenomenon is the consequence of very small dark core lengths at these high J values. Also at these conditions and especially true for near and supercritical conditions, the dark core does not show any response to acoustic forcing since most of the flow has been entrained by the outer jet and thus mixed with the rest of the fluid in the chamber, leaving a short dark core that usually does not show interesting acoustic behavior. Overall, these results show a very interesting trend which suggests that normalized dark core length behavior could be independent of mean chamber pressure; however, the large uncertainties in the measurements still prevent us from a definitive conclusion in this regard.

A plot that compiles all the dark core length data is shown in Figure 5.33. To make this graph, the difference between the baseline length or the average length of the dark core with no acoustics and the average length of the dark core with acoustics ($L_{\text{no acoustics}} - L_{\text{acoustics}}$) was determined for each phase angle at a given p_{mean} and J , and the maximum value was selected. This quantity was termed “maximum dark core length reduction”, ΔL , normalized by the average length of the dark core with no acoustics ($\Delta L/L_{\text{no acoustics}}$), and plotted versus J for all cases. The overall trend for all pressure conditions shows that at very low outer to inner jet momentum flux ratios the normalized maximum dark core length reduction drops below 30%. Next, the range of values of J between 0.5 and 5 shows reductions in normalized dark core length between 30 to 50%. All cases with a J greater than 5 shows that the normalized dark core length decreases at most by 20%. This plot suggests a range of outer to inner jet momentum flux ratios from 0.5 to 5 where acoustic forcing has more influence on the axial dark core length of the coaxial jet and thus in the mixing processes that characterizes it.

5.2.8 Spreading Angle Results in the Presence of Acoustic Excitation

In this section we analyze the behavior of the inner jet spreading angles with an externally imposed transverse acoustic field. The results obtained under acoustic perturbation could perhaps be used by a designer as a measure of the lateral spread expected from one coaxial element under similar conditions. Knowing this would facilitate the selection of a safe distance between injector elements if one wants to avoid

any interaction between them. It also gives the designer a good idea of the amount of mixing that it would be expected from these elements under different conditions.

The analysis will focus on the effects of both the magnitude and gradient of the pressure and velocity fields on the coaxial jet flow, specifically on the inner jet spreading angles at subcritical to supercritical pressures. As previously indicated, the relative position of the jet with respect to the pressure and velocity acoustic field is varied by alternating the phase between the two acoustic resonators.

First we will examine the spreading angles at subcritical pressures. At low momentum flux ratios the maximum spread angles are small. The images for $J = 0.17$ in Figure 5.19 as well as the upper-left plot in Figure 5.34 show this behavior. For this case, the inner jet dominates the behavior of the coaxial jet, entraining and bending the outer jet towards itself since the higher density of the inner jet is 20 to 30 times the density of the outer jet and surrounding plenum. With both jets having similar mass flow rates, the flow surrounding the inner jet is simply not substantial enough to affect its behavior. When the acoustics are turned on, no discernable effect is seen, either visually in Figure 5.19 or quantitatively in Figure 5.34.

Acoustics in the range studied here do not seem to strongly affect low J coaxial jets, since they do not seem to produce a significant reduction of the mean axial dark core length or increase of the maximum spreading angles of the inner jet. As J increases to 1, a slight effect is observed with phase angle (see upper-right plot in Figure 5.34). Specifically, the maximum acoustic spread angle tends to achieve its largest value around a phase angle of 180° . This agrees with subcritical results at $J = 2.6$ where the mean axial

dark core length is reduced the most at or near a phase angle of 180° , which corresponds to a velocity antinode (pressure node). At $J=2.6$, the maximum acoustic spread angle increases continuously with phase angle reaching a maximum at a phase angle of 180° as shown in Figure 5.20 and the middle-left plot in Figure 5.34. In fact, the maximum acoustic spread angle recorded for this case at a phase angle of 180° is the one of highest from all cases at all phase angles.

For the $J = 4.2$ case, we see a slight peak of the maximum acoustic spread angle at a phase angle of 135° , not far from the phase angle where we would expect the largest value which is 180° . Overall, we can conclude that for this range of J values, we observe the largest maximum acoustic spread angles when the jets are exposed to an acoustic field which has a velocity antinode at the location of the jet (for our case, when the two sources are at a 180° phase angle).

As we move to the case where $J=9.6$, shown in Figure 5.21 and the bottom-left plot in Figure 5.34, we see a different behavior. In this case the inner jet achieves a uniformly high maximum acoustic spread angle, reaching a value as high as 38° , compared to its 7° maximum baseline spread angle. This large spreading occurs as long as there is a source of acoustic excitation. This behavior is irrespective of the different acoustic conditions produced by the change in phase angle, which produces no statistically relevant change upon its spreading properties. This is surprising since the results from the previous section show that for $J = 9.6$ the percentage of shrinkage of the mean axial dark core length of the inner jet was smaller than for lower J values suggesting a smaller effect of acoustics on mixing. Also, the mean axial dark core length

changed with phase angle whereas here the spread angle seems independent of phase. Finally as J increases to 23 shown in Figure 5.22, we find a flatter profile of the maximum acoustic spread angle as the phase angle is varied. Also, all the values of maximum spread angles have decreased compared to the case of $J=9.6$.

The eight nearcritical cases are presented in Figure 5.35 with momentum flux ratio varying from 0.55 to 9.3. The behavior of the jet at $J = 0.55$ (see Figure 5.23) shows a very flat distribution of the spreading angles at different acoustic conditions. Most angles, including the condition with no acoustics present, show a value near 10° . The only exceptions are the spreading angles obtained at a phase angle of 0° and 360° . At these conditions, the dark core bends more than the rest of the cases and the inner jet flow penetrates the outer jet and seems to reach the surrounding media.

The following three cases, $J = 1.0$, 1.1 and 1.6 , show a similar behavior. The values of the spreading angles fall between 10° and 20° and their corresponding baseline spreading angle values are also in that range. For these cases where J is near or less than 1, acoustic forcing has little or no effect on the spreading angles. However, for $J = 2.1$ the average angles for the acoustic conditions are higher with a baseline value of 15° , which is similar to the lower J cases.

As J is increased to 2.9 and 4.9 a more enhanced behavior is observed. They have average values for the spreading angles under acoustic forcing that are significantly higher than their respective baselines. Both $J = 2.9$ and 4.9 have an average spreading angle with acoustics of over 20° and a baseline smaller than 10° . The effect of acoustics is the highest for these flow conditions. Finally, at $J = 9.3$, all the spreading angles are

below 10° with an average below 5° . The reason for this behavior is the very short dark core length of the inner jet, pictured in Figure 5.25, which makes very difficult to capture any effect the acoustics might be having on it. The dark core itself is very straight until it mixes completely with its surroundings just a couple of inner jet diameters downstream the injector exit.

The final set of graphs in Figure 5.36 shows the results for the inner jet spreading angles in the supercritical regime. The first graph on the upper left shows the case for $J = 0.019$. The spreading angle shows a coaxial jet that is very slightly affected by the acoustic field. The baseline image (see Figure 5.6) shows a very long dark core with a large spreading. This large cone might be enhanced near the 180° condition due to large velocity perturbations in the transversal direction but otherwise stays close to the baseline value.

The $J = 0.33$ case also shows no response at all which can be somewhat concluded from the very similar coaxial jet images shown in Figure 5.26. Thus, in the first two cases all but one angle remain below 10° . In the following two cases ($J = 1.3$ and $J = 2.4$) the spreading angles remain in the 10° to 20° range. The acoustics do not seem to have an effect on the jet. Even if the overall angles are greater, which can be attributed to a higher momentum flux ratio and thus more entrainment of the inner jet fluid by the outer jet irrespective of the acoustic conditions, the angles under acoustic forcing do not appear to be larger than their respective baselines.

The case at $J = 2.5$ shows some angles that increase beyond the spread of the baseline condition. It is the only set that has angles over 20° . This could occur because of

dark core bending, which is then translated into curved surfaces that are interpreted as larger spreading angles. In contrast, the case for $J = 9.9$ is shown with different limits for its vertical axis. It starts at negative values to account for some negative angles that appear when the inner jet is immediately entrained into the outer jet as it exits the injector. This produces a ‘thinning’ of the jet (see Figure 5.28) that is processed as a negative angle. Eventually some positive angles are recorded when the jet is exposed to acoustic excitation. Figure 5.28 shows images of the inner jet at a very high momentum ratio for the highest pressure regime. Some of these photographs were noticeably curved towards the right, including the 270° condition which appears as the largest spreading angle (near 10°) for this particular case ($J = 9.9$).

An interesting observation from all cases at the three different pressure regimes is that for some moderate momentum flux ratios in the $1 < J < 5$ range, the inner jet seems to spread more when it is located at or near a pressure antinode. This can be seen for the $J = 2.6$ and $J = 4.2$ cases (and slightly in case $J = 1.0$) in Figure 5.34, case $J = 4.9$ and to some extent in case $J = 2.1$ in Figure 5.35 and case $J = 2.5$ in Figure 5.36. This is evidence that the maximum velocity perturbations taking place at this acoustic condition might be enhancing the spreading of the inner jet.

For a detailed summary of all the experimental data obtained with the original injector, refer to Table C.1 to Table C.4 in Appendix C.

5.3 Results with the New Coaxial Jet Injector Geometry

5.3.1 Behavior with and without Acoustic Excitation

As described in chapter 4 a new injector was designed, built and tested at the Cryogenic Supercritical Laboratory. The following paragraphs will describe sets of images that show the response of the coaxial jet to the same levels of acoustic excitation that were employed for the tests with the original injector. To obtain similar outer to inner momentum flux ratios with the new injector than those obtained with the old injector, the mass flow rate of the inner jet had to be increased by a factor of three. This change in mass flow rate was necessary given the difference in the inner jet inner diameter between D_1 and D_{1new} (see Figure 4.4b and Figure 4.5b) between the original and new injectors. The mean velocity of the inner jet with the new injector at the three different pressure regimes remained just under 1 m/s compared with the mean velocity of the original injector which was 2.2 m/s in the subcritical pressure regime and varied between 2.4 m/s and 6.6 m/s for the nearcritical and supercritical regimes (refer to Appendix C, Tables C.1 and C.5)

The first pressure regime to be analyzed with the new injector was the subcritical regime. The images shown in Figure 5.37 correspond to a momentum flux ratio of approximately 0.089. The first image shows the coaxial jet when no acoustics are present. The inner jet can be clearly distinguished from the outer jet and its surroundings. The thickness of the inner jet stays constant throughout the image. The non-dimensional dark core length in this case is longer than $14 L/D_{1new}$, which is expected based on the results from the original injector at similar momentum flux ratios.

The response of the inner jet with acoustic excitation is depicted in the images in Figure 5.37. For the phase angles from 0° to 90° the inner jet bends noticeably too and there is strong atomization taking place near the injector exit. The background flow of the chamber is difficult to notice and the dark core region is somewhat thicker and blurred. The next two images show a perturbed, but straight, inner jet. The images corresponding to a phase difference between 225° and 315° show the liquid stream from the inner jet shortened significantly, with large structures of liquid that have been separated from the inner jet flowing downstream. The last image seems to return to the behavior seen at a 0° phase angle.

It is interesting to notice that the images that show the greatest contrast in the inner jet behavior with acoustics correspond to a phase difference of 135° and 315° , which would correspond to the pressure node and pressure antinode locations. The 135° image shows an inner jet with a fully connected dark core region. In contrast, the 315° image shows the inner jet being completely disintegrated into large liquid structures just a few inner diameters after leaving the exit. A strong response to acoustics at this very low momentum flux ratio was not expected given the results obtained with the original injector. Also, the effect of the acoustic field on the integrity of the inner jet is something that was not observed with the original injector before.

A possible cause of this phenomenon is the change in geometry from the original injector to the new injector. As discussed previously, the original injector featured a very thick inner jet post which created a large recirculation zone between the inner jet and the outer jet at the exit of the injector. This recirculation zone could have damped the

pressure and velocity fluctuations, which instead of affecting the inner jet directly, modified the dynamics of the recirculation zone (41) which in turn altered the dynamics of the inner jet at the exit. That would explain the smooth back-and-forth oscillations of the inner jet that were characteristic of “strong evidence of acoustic excitation” with the original injector. However, without such a large recirculation zone, the pressure and velocity fluctuations could be having a direct impact on the inner jet flow and that might explain the very strong atomization taking place right at the exit of the injector for every acoustic condition regardless of phase angle.

The group of images in Figure 5.38 shows the coaxial jet at a subcritical pressure of 1.49 MPa and a momentum flux ratio of 0.43. The baseline condition has a dark core that spans the whole length of the image; however, compared with the same condition in Figure 5.37, this dark core region is not as smooth and features fluid structures from the inner jet moving outwards to the outer jet. This shreds of fluid that seem to be shed away from the inner jet might be evidence of instability at this momentum flux ratio, since this behavior was also observed in the original injector at nearcritical and subcritical pressures for similar momentum flux ratios (see Figure 5.23 and Figure 5.26).

There is also a striking response of the coaxial jet to acoustic excitation in this case. The flow at 0° and 45° shows an inner jet that starts shearing off fluid outwards just as it exits the injector and is convected downstream, as the fluid travels away from the inner jet, it starts slowing down. It seems to “wrap around” the fluid in the dark core assuming the shape of an inverted mushroom. The excitation is so violent that the dark core is fully mixed by the time the flow reaches the center of the picture and the

spreading angle is very large. This is an “expanding” or “relaxing” effect. However, as the phase angle varies from 135° to 180° a different behavior takes place. The inner jet is widened at the exit but as it reaches the center of the image it gets very thin, just to spread out again in an hourglass shape fashion. This effect seems to “compress” or “contract” the inner jet flow. These two effects are separated by 180° , with the relaxing effect taking place near the pressure antinode location and the compressing effect near the pressure node location. The conditions at 90° and 225° show a transition between these two different responses and the last two images (315° and 360°) show the same behavior as the first two images described in this paragraph (0° and 45°).

The set of images in Figure 5.39 show the coaxial jet behavior at a subcritical pressure of 1.49 MPa and momentum flux ratio of 2.0. The baseline condition shows a dark core region that does not extend the whole length of the image, in contrast with the previous two cases. In the first few inner jet diameters after the exit of the injector the dark core region is thick and connected, then it starts being sheared apart by the outer jet and becomes thinner with shreds of flow extending from the core towards the end. At the bottom of the image only a very thin dark core region, which is most likely unconnected from the main core, remains. In comparison, the response of the coaxial jet to acoustics for this J value is very similar to the response to the previous value of $J = 0.43$. The only noticeable difference is that the images at 135° and 180° do not show an hourglass shape but instead they seem to show similar dynamics to the baseline condition and even a longer dark core region.

The following subcritical case, shown in Figure 5.40, features a momentum flux ratio of 7.8. The high momentum flux of the outer jet is capable of entraining enough flow from the inner jet to end the dark core region towards the middle of the image, and in the bottom portion only a few dark spots are observed with mostly mixed flow. The behavior with acoustics is similar to the “expanding” case for $J = 0.43$ and 2.0 , although the structures are clearer for this case. Again, at 0° and 360° phase angle the structures are periodic, extend outward and wrap around forming eddies and near 180° phase angle the image is very similar to the case with no acoustics.

The last of the subcritical cases presented here is shown in Figure 5.41. It features a baseline that has the shortest dark core of all the five subcritical cases with the new injector, as it would be expected for this case at a momentum flux ratio of 18. In this case the effect of the acoustics are still visible with a very short dark core at a 0° and 360° phase angle and longer dark cores near the 180° phase angle. The no acoustics case does not show eddies and similar structures that extend outwards from the inner jet and seem to bend up but they are very clear in almost all the images showing acoustic excitation conditions. For the new injector, acoustic effects are still noticed in the dynamics of the dark core at subcritical pressures for momentum flux ratios near 20, unlike the original injector where the effects of acoustics could not be adequately quantified by measuring the short dark core region from the images at these high J values.

The following paragraphs describe four sets of images that show the coaxial jet with the new injector exposed to nearcritical pressures. For the new injector tests, the heat exchangers were improved to increase cooling efficiency. The result led to inner jet

temperatures below the critical temperature of nitrogen. In consequence all the following cases features two phase flow, with the inner jet being in a liquid-like phase (nearcritical pressure but below critical temperature) at the exit and the outer jet and surrounding chamber fluid in a supercritical state.

The first set of nearcritical images corresponds to a momentum flux ratio of 0.50 (see Figure 5.42). The baseline case shows a slightly spreading, thick inner jet dark core that extends for the entire image. The outer jet is smooth at the exit and follows the dynamics of the inner jet. The acoustic conditions are not too different from the baseline. Some of the images show a thinner inner jet (90° and 180°) but the most interesting effect is that there is no similar spreading in the acoustic cases. An interesting condition took place at the 315° phase angle. The inner jet was completely obliterated by the acoustic field and the dark core was completely dispersed across the region at the exit of the injector depicted by the image. This could be an indication that there exists a threshold amplitude for this particular injector geometry above which the thin shear layer between the inner jet and outer jet cannot damp the pressure and velocity fluctuations and the liquid inner jet becomes rapidly mixed with its surroundings. Any of these effects could be accentuated by the transition of the outer layer of the inner jet flow from liquid to supercritical state.

The images shown in Figure 5.43 show a nearcritical case with a momentum flux ratio of 2.2. The images are similar to the nearcritical case $J = 0.50$ in Figure 5.42. For this J value, an even more uniform behavior across all conditions, including the baseline, is observed. All images feature a steady spread of the inner jet dark core and evidence of

mixing towards the bottom of the picture where gray areas can be observed between the darker inner jet and the outer jet. In this case, the coaxial jet had no noticeable response to acoustic excitation.

The coaxial jet at a momentum flux ratio of 9.4 for the nearcritical pressure regime is shown in Figure 5.44. It behaves in a similar fashion to its subcritical counterpart with $J = 7.8$ in Figure 5.40 but the structures that shed from the dark core are not as pronounced, with the most noticeable ones taking place at the 45° phase angle condition. This nearcritical case appears to have the shortest dark core length from all the different cases with the new injector. In the 360° condition one can observe a very short dark core that is quickly entrained by the outer jet and thus a gray region downstream that eventually mixes with its surroundings. In fact, all the images show this transition but they do so over longer distances from the injector exit.

A nearcritical case with momentum flux ratio of 19 is presented next in Figure 5.45. It features the shortest dark core of all nearcritical cases, as it is expected for the case with the highest momentum flux ratio, whether using the original or new injector. Unlike the first two nearcritical cases shown, and only slightly perceived in the third one, a noticeable effect of the acoustics on the coaxial jet is observed on the length of the dark core when compared between the baseline condition and the rest of the images at different phase angles. It seems that for this particular geometry, very high momentum flux ratios are needed to shorten the jet to an adequate length so that the pressure and velocity perturbations can interact with it and display visible acoustic phenomena.

The last set of images presented here from the new injector tests show the coaxial jet at a momentum flux ratio of 2.6 at supercritical pressures in Figure 5.46. The behavior is basically the same as the one observed for its nearcritical counterpart in Figure 5.43. It has a slightly spreading inner jet angle with some structures shearing of the dark core towards the bottom of some images. The gray region between the inner jet and the outer jet indicates that mixing is taking place at the boundary between the two streams. At this condition there is no observed response to acoustics at any phase angle.

5.3.2 Dark Core Length Results with and without Acoustic Excitation

The results of the dark core length measurements of the inner jet of the coaxial jet flow with the new injector are presented in Figure 5.47 and Figure 5.48. The figures show a series of plots with the dark core length measurements on the vertical axis and the different acoustic conditions on the horizontal axis. A secondary axis shows the amplitude of the pressure oscillations as a fraction of the recorded mean chamber pressure for that case. The first value on the horizontal axis is the baseline measurement without acoustics followed by the measurements of the dark core length with acoustics starting with a 0° phase angle between acoustic sources and then in steps of 45° until a full cycle is achieved at 360° . All the values are normalized by the baseline condition of the case, which is the length of the dark core without acoustics. The error bars show the composite uncertainty of the non-dimensional length variable, $L_{\text{acoustics}}/L_{\text{no acoustics}}$, using one standard deviation as the uncertainty of each measured variable.

In some cases, particularly the ones with lower momentum flux ratios, the dark core extended beyond the vertical length of the examination window used for these tests at some or all phase angles. In order to highlight those acoustic conditions, zero, one or two asterisks were placed next the phase angles on the horizontal axis labels. No asterisks indicate that less than 10% of the images had a dark core length that extended beyond the field of view. One asterisk means that between 10% and 50% of the images had dark cores that were longer than the field of view and two asterisks mean that the dark core was longer than the field of view in 50% or more of the images used to extract its length. The values of the dark core lengths for the tests at subcritical pressures are shown in Figure 5.47. These tests at subcritical pressures represent a two-phase coaxial jet flow, where the inner jet is in liquid state at a temperature below the critical temperature of N_2 , and the outer jet is in a gaseous state at a temperature above the critical temperature of N_2 . The dark core length for the coaxial jet obtained with the new injector was analyzed using a new routine in MATLAB based on the one used to analyze the cases with the original injector so that spreading angles could be measured even if the dark core length was not quantifiable, since the previous routine was not designed to process images with dark cores that extended beyond the field of view. The set of plots in Figure 5.47 show the dark core length for the subcritical cases.

The behavior of the case with J equal to 0.089 had very long dark cores even when acoustic excitation was applied. The only condition that showed a short core length was the 315° phase angle. Images from this case can be seen in Figure 5.37. In the following two cases, with $J = 0.43$ and 2.0 the dark core length was measurable for half

of the phase angles. The conditions for which the dark core was too long were those near the pressure node as indicated by the pressure data shown in the plots. Of relevance here is the dark core reduction at the rest of the conditions (see Figure 5.38 and Figure 5.39). These cases show dark core lengths between 50% and 60% that of the baseline for the phase angles away from the pressure node. The reduction in dark core length for the acoustic cases is actually larger since the length of the baseline cases was limited by the examination window. This means that the baselines of both cases are in fact longer and the relative dark core lengths at the acoustic conditions away from the pressure antinode are smaller.

For the next two plots in Figure 5.47, for J equal to 3.4 and 5.2, the same trend with phase angle can be observed. Most dark core lengths away from the pressure node show a 60% reduction compared to the dark core length of the baseline condition for both cases. The dark core length then increases as the phase angle approaches the pressure node location, where it reaches a maximum. In fact, the dark core length for the cases between $J = 0.43$ and 5.2 show the same qualitative behavior. Also, the plots for $J = 0.43$ and 2.0 appear as truncated versions of the ones for $J = 3.4$ and 5.2. Whether the qualitative behavior between these 4 cases is the same is uncertain but the fact that the dark core lengths in the baseline cases for $J = 0.43$ and 2.0 are longer indicate that the qualitative results shown in their respective plots are conservative and could potentially match the reduction seen for the following two cases at $J = 3.4$ and 5.2.

The last three plots in Figure 5.47 show the reduction in the dark core length for $J = 7.8, 12$ and 18. Images for two of these cases are shown in Figure 5.40 and Figure 5.41.

These plots show a smaller reduction in dark core length compared to the baseline case than the reduction in the lower momentum flux ratio cases. The dark core lengths for the higher J value cases were reduced between 58% and 93% of their corresponding baseline. Considering all the different conditions, the dark core length reduction in the $J = 7.8$ case was not as large as the reduction in the $J = 12$ and 18 cases. This effect might be due to transitional behavior between low and moderate momentum flux ratio cases and the high momentum flux ratio cases.

The general trend observed in these measurements consists of longer dark cores near the pressure node and very short ones near the pressure antinode. The reason for this behavior is not well understood and in fact is contrary to what was expected from experiments with the original injector. One of the possible explanations might involve the lack of recirculation zone in the new injector. The recirculation zone could be responsible for the bending of the jet at high velocity fluctuations but in the case of the new injector this recirculation zone is non-existent and the bending does not take place, thus a straight dark core is observed.

The following set of plots (Figure 5.48) show the behavior of the dark core length for the cases obtained when the pressure was above the critical point. The lower four momentum flux ratio cases have flat profiles, indicating that the dark core lengths were always as long as the baseline case. In fact, all conditions for these four momentum flux ratios showed dark cores longer than the field of view, explaining the results. Images for three of these four cases can be seen in Figure 5.42, Figure 5.43 and Figure 5.46. Pressure profiles show that the coaxial jet was exposed to maxima and minima in pressure

perturbations ranging from 0.2% to 1% of the mean chamber pressure; however, no effect on the dark core was seen. There were some instances, as in the 315° condition for the nearcritical case with $J = 0.50$ (see Figure 5.42), where the acoustic excitation modified significantly the mechanics of the jet. Dark core lengths and spreading angles were not reported for such cases because the jet behavior departed significantly from the rest of the conditions. This behavior was observed at various J values near the pressure antinode condition at sufficiently high acoustic amplitudes. The nature of this phenomena is still not well understood and it is believed that the lack of recirculation zone near the injector exit allows the high pressure fluctuations to interact with the inner jet leading to a violent disintegration of the dark core.

The results of the remaining three nearcritical cases; however, show very interesting trends that match those of the subcritical results of the new injector. For instance, the nearcritical case with $J = 4.6$ shows a very large reduction in the dark core for conditions near the pressure antinode, with the value of the dark core length with acoustics close to 40% that of the baseline condition. In fact, this percentage could be even lower because the dark core length was underestimated for the baseline of this case, similar to the results for the $J = 2.0$ subcritical case. As the pressure node condition is approached, the dark core increases its length, reaching a maximum near a 180° phase angle. This behavior was also observed for the subcritical cases with momentum flux ratios of 3.4 and 5.2 (see Figure 5.47).

The nearcritical case at $J = 9.4$ followed the same trend as the $J = 4.6$ case and reached a maximum near the pressure node. The greatest reduction of the dark core

happened at the pressure antinode and was almost 50% of the dark core length of the baseline. This behavior is similar to the subcritical case at $J = 12$. Finally, the nearcritical case at $J = 19$ had a smaller reduction in the dark core length, with the minimum dark core length consisting of two-thirds of the baseline length and being located again at the pressure antinode location. The maximum dark core length with acoustics was obtained for a phase angle of 180° , very close to the pressure node indicated by the pressure measurements.

A comparison of the dark core length behavior for a given momentum flux ratio between the subcritical and nearcritical pressure regimes is shown in Figure 5.49. A remarkable feature of these plots is the agreement in the relative dark core lengths between subcritical and nearcritical cases. For a J value close to 5, the maximum pressure oscillations normalized by the mean chamber pressure are almost twice as much for the subcritical case compared to that of the nearcritical case. In contrast, for J near 20, the relative acoustic forcing is almost the same. Nonetheless, for each momentum flux ratio, the maxima and minima in normalized dark core length between subcritical and nearcritical pressures are very similar, regardless of the relative pressure oscillation. Therefore, the relative effect of the acoustics on the dark core length with the new injector for similar momentum flux ratios agrees with the results obtained with the original injector (see Figure 5.32). Given the differences between the inner jet characteristics of the original and the new injector (inner post thickness, inner jet diameter, inner jet velocity and temperature), the agreement in dark core length results for the same J values indicates that this parameter could in fact reduce the data for a

given geometry regardless of its characteristics. Further evidence of this observation could have important repercussions in shear coaxial injector design.

A plot of the difference between the shortest dark core length for a given case and its corresponding baseline is shown in Figure 5.50. This graph shows agreement between subcritical and nearcritical cases with $J > 3$ with the new injector. Except for the subcritical case with $J = 7.8$, all cases follow a trend that steadily decreases from over 60% change for moderate momentum flux ratio cases to under 40% for high momentum flux ratio cases. The low value of this maximum change in dark core length for the subcritical case with $J = 7.8$ could point to a transitional behavior between momentum flux ratio cases up to 5 and cases at J values near 10 and above. Further tests in the $5 < J < 10$ range will be needed to assess whether the results obtained from the $J = 7.8$ case are an isolated phenomenon or the indication of a transition region between moderate and high momentum flux ratio jets.

When the results of both injectors are compared, (see Figure 5.51) two very distinct trends can be observed for each injector. If the subcritical, $J = 7.8$ case with the new injector is neglected, it seems that the new injector allows for a larger reduction in dark core length for any given outer to inner jet momentum flux ratio. There could be various mechanisms that will enhance the reduction with the new injector, chief among them the lack of a recirculation zone that dampens the effect of the acoustics on the inner jet. If the conclusions from these results and those from Figure 5.32 and Figure 5.49 are combined, it seems that the geometry of the coaxial injector is a more relevant factor than

the chamber pressure when analyzing the effects of acoustic perturbations (and therefore acoustic instabilities) in the dynamics of a coaxial jet.

5.3.3 Spreading Angle Results with and without Acoustic Excitation

The spreading angle results for the new injector identify certain trends observed qualitatively in the images obtained from the high-speed camera. One of the most important features of the new injector is the tendency of the inner jet to decrease its size significantly at moderate momentum flux ratios and display a very exotic behavior with structures that are shed perpendicularly from the direction of flow with very strong atomization at the exit of the injector at or near the pressure antinode. In contrast, at the pressure node location the jet becomes very long and sometimes surpasses the length of the baseline. The large velocity fluctuations might cancel the effect of the outer jet on the inner jet allowing it to extend past its no acoustics length. The spreading angles are able to capture this behavior as it can be seen at the pressure node locations in most subcritical and some nearcritical plots at various momentum flux ratios (see Figure 5.52 and Figure 5.53).

The first set of plots show the spreading angles for the subcritical cases in Figure 5.52. Despite having long dark core lengths, spreading angles from the low momentum flux ratio were measured successfully, showing very interesting behavior. For instance, for the first two subcritical cases show peaks at phase angles of 45° and 315° , close to pressure antinode locations. These spreading angles go as high as 25° for $J = 0.089$ and 15° for $J = 0.43$. They also show a minimum spreading angle of 0° near a phase angle of

135°, which is the location of the pressure node for these cases. Overall, the lowest momentum flux ratio ($J = 0.089$) shows a trend of decreasing spreading angle as the pressure node is approached. The second plot, which corresponds to a J equal to 0.43, does not show a trend but some response to the varying acoustic field can be observed from the results of some conditions near the pressure and velocity nodes.

Compared to the rest of the cases, the spreading angles for $J = 2.0$ show a weak response to acoustics. The minimum angle at 225° does not quite coincide with the pressure node at 135°. The rest of the spreading angles do not vary much (between 4° and 10°) and do not follow a discernable trend. In contrast, the spreading angles for $J = 3.4$ and 5.2 show an enhanced response to the acoustic field. It is easy to differentiate the baseline and the angles near a pressure node from the rest for these two cases. The minimum spreading angle near 5° in both instances coincides with the location of the pressure node at a phase angle of 225°. The next smallest are those near the pressure node and the baseline cases. The rest of the spreading angles for those cases are higher than the minimum by approximately 10°.

The following case is similar in behavior to $J = 2.0$ since the angles do not show any response to the applied acoustic field. All angles for $J = 7.8$ vary between 3° and 6° with the maximum spreading angle happening at the baseline condition. In contrast, the spreading angles for the highest two momentum flux ratios behave quite similarly to the lowest two cases. They both have minima near their respective pressure nodes with a spreading angle of 5° for $J = 12$ and 7° for $J = 18$. As the phase angle changes toward a pressure antinode, the spreading angles increase reaching values over 15° for $J = 12$ and

close to 25° for $J = 18$, indicating a strong response of the coaxial jet to the imposed acoustic field.

In contrast to the rich behavior observed in the range of subcritical cases, the long and straight dark core lengths of the first four lower momentum flux ratio cases of the cases above the critical point shown in Figure 5.53 produced results that did not show any response to the imposed acoustic field. The trend lines in these cases were almost horizontal with spreading angles for all phases ranging from 5° to 10° for almost all conditions. At moderate momentum flux ratios the trends did not improve much. For $J = 4.6$ and 9.4 the spreading angles varied from 2° to 11° and no clear response to phase angle variation or pressure node or antinode conditions was observed. The only case above the critical point that showed a clear response to the externally imposed acoustic field was $J = 19$. For this case, the smallest spreading angle was 5° at a phase angle of 180° and then 8° for a phase angle of 225° with one condition at and the other near the pressure node location. The next smallest spreading angle was the baseline with 10° . The rest of the spreading angles were all higher than 15° . The trend formed by these angles was a coarse sinusoidal shape, showing the only clear response by the spreading angles to the acoustic field for a nearcritical or supercritical case with the new injector.

For a detailed summary of all the experimental data obtained with the original injector, refer to Table C.5 in Appendix C.

5.4 Stability of Coaxial Jet Flows

The purpose of this section is to present a qualitative analysis of the stability characteristics of the coaxial jet flow presented in this study. In the present work two type of flow conditions were observed. One of them is the flow of a liquid with a coaxial gas stream around it. This flow was obtained at subcritical conditions. The second one was the flow of a jet supercritical fluid with high density surrounded by a coaxial stream of supercritical flow at a lower density. The latter was obtained when the pressure of the system was raised over the critical pressure of the fluid used in the experiments. This observation is important because instabilities might behave in a different manner when the surface tension varies greatly. For instance, Leib and Goldstein (49) report that Weber number impact the onset of absolute instability, a substance in its subcritical liquid phase can present a very different stability behavior than its corresponding supercritical phase.

As mentioned in the introduction chapter, previous researchers point out that geometry, momentum thickness and the effects of the vorticity layer could affect the stability characteristics of a flow. In these experiments both the momentum thickness of the gaseous flow and the shear layer between the two coaxial streams seem to play an important role in the development of instabilities, since one of the mechanisms which might be dampening (or perhaps enhancing) these instabilities is the large recirculation region that is created between the inner and outer streams right at the exit of the original injector. It is difficult to say that the recirculation region aids or dampens the instability, since Figure 5.34 shows that both $J = 2.6$ and $J = 9.6$ are

greatly affected by acoustics; however, Figure 5.20, shows a very thin inner jet at $J = 2.6$ which seems not to feel any recirculation zone at all whereas Figure 5.21 shows a very thick jet at $J = 9.6$ that quickly expands into the recirculation zone due to the large momentum flux of the outer jet.

Overall, in the experimental results obtained using the original injector geometry at subcritical pressures (see Figure 5.33 and Figure 5.34), there seems to be a range of momentum flux ratios between 2 and 10 for which the coaxial jet responds very well to acoustics. This provides evidence of a convectively unstable coaxial jet flow at these conditions. In the case of nearcritical and supercritical pressures (Figure 5.33, Figure 5.35 and Figure 5.36) the range of momentum flux ratios for which the jet responds better to acoustics seems to be smaller ($2 < J < 5$). However, there is some evidence from this work (see Figure 5.28) that even at higher momentum flux ratios for supercritical pressures the coaxial jet responds to acoustics. The response for this supercritical case is not as clear at this higher momentum ratio case as compared to its subcritical case counterpart because the supercritical dark core is quickly combined with the outer jet and surrounding fluid as it exits the injector. However, the mixed jet flowing downstream, which has a dark grey color in the images, presents the same oscillatory behavior.

This observation would effectively extend the range in which coaxial jet flows can be characterized as convectively unstable at conditions above the critical pressure of the fluid. Further support for this claim is provided by the fact that acoustic forcing at this pressure regime produces maximum peak-to-peak pressure

perturbations that are less than one percent of the mean pressure chamber but still are able to generate a response in the coaxial jet. It is just difficult to characterize this response of the coaxial jet to acoustics using the inner jet due to the size of its dark core region at these high momentum flux ratios.

In the tests conducted with the new injector, a completely different response to acoustics was observed. The same level of acoustic forcing applied to the old injector geometry was used in the new injector cases. The subcritical cases (Figure 5.37 to Figure 5.41) showed a strong response to the applied acoustic field, with visible differences between the pressure antinode or velocity node location (315° , 360° and 0° conditions) and the pressure node or velocity antinode location (135° and 180° conditions). In contrast, the nearcritical cases and the subcritical case showed mostly a weak or no response to acoustics (Figure 5.42 to Figure 5.46). The only cases that showed some level of excitation were those with a momentum flux ratio near or above 10.

Aside from that, the only other instance that showed excitation was observed at the 315° condition for a J value near 0.5 in the nearcritical regime. This was a particularly violent reaction of the inner jet as it can be observed in Figure 5.42 where dark core particles covered the entire image for that particular condition. A possible explanation for this effect is that there exists an amplitude threshold beyond which the inner jet becomes highly unstable, and that for this particular case the 315° condition was the closest one to the pressure antinode, which reaches the highest pressure perturbations. Thus, the larger pressure oscillations might have surpassed

this excitation threshold and produced such a dramatic effect on the dark core behavior of the inner jet.

The results with the new injector geometry show that at the current forcing conditions the coaxial jet shows a strong response to all the momentum flux ratios at subcritical pressures (see Figure 5.37 to Figure 5.41). The new geometry could be extending the convective instability range of the flow to reach both higher and lower momentum flux ratios as compared to the old injector. One can argue that the thinner shear layer between the inner jet and the outer jet without a recirculation region allows more energy from the acoustic forcing to reach the inner jet and disturb it. However, the nearcritical and supercritical regimes seem to have no significant response to acoustic forcing (see Figure 5.42 to Figure 5.46), when one would expect at least a small range of moderate J values for which the nearcritical and supercritical regimes would show an effect. One potential cause for this lack of response is the need for higher acoustic amplitudes. It is possible that the near and supercritical cases were not being forced at sufficiently high relative amplitudes to visibly excite the coaxial jet. Further testing with the new injector will be necessary to support this claim.

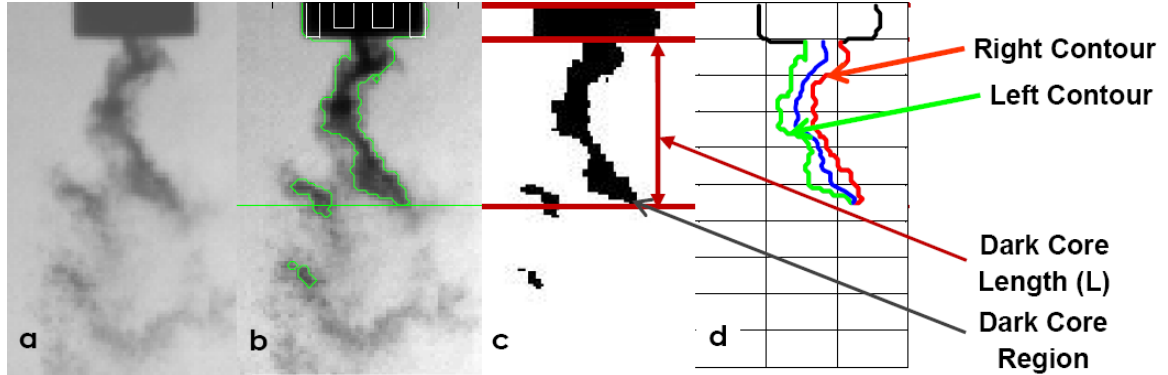


Figure 5.1. (a) Raw image from high-speed camera. (b) Dark core boundary extracted from the raw image using the image processing routine. (c) Black and white image after image processing threshold had been applied. (d) Schematic of the left and right contours used in this study to obtain inner jet spreading angles.

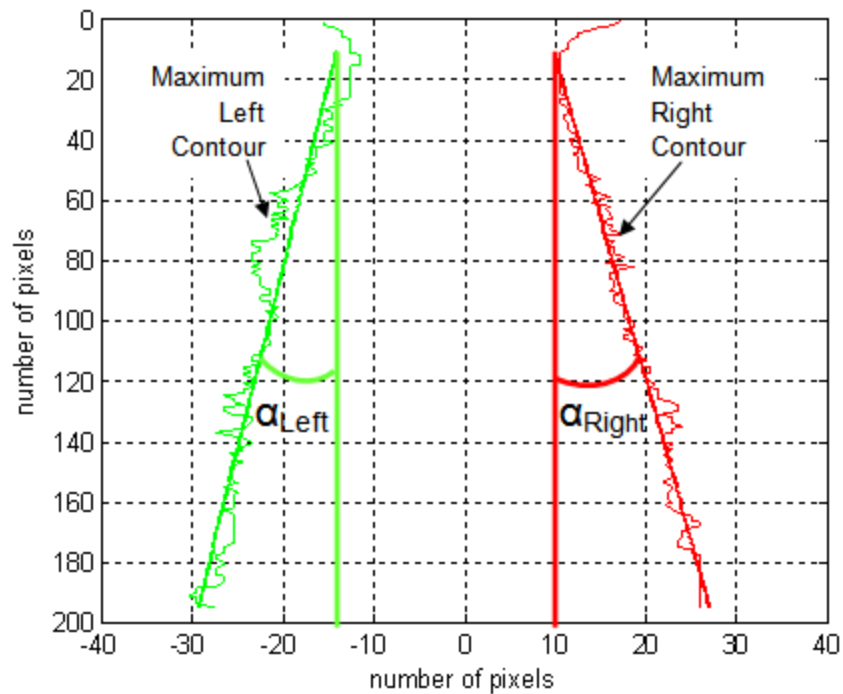


Figure 5.2. Left and right angles derived using the maximum displacement of the dark core region at each row over a sample of 998 images.

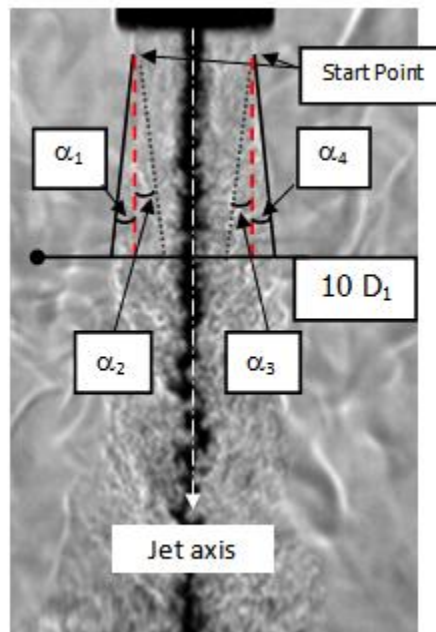


Figure 5.3. Image showing how outer jet spreading angles are measured.

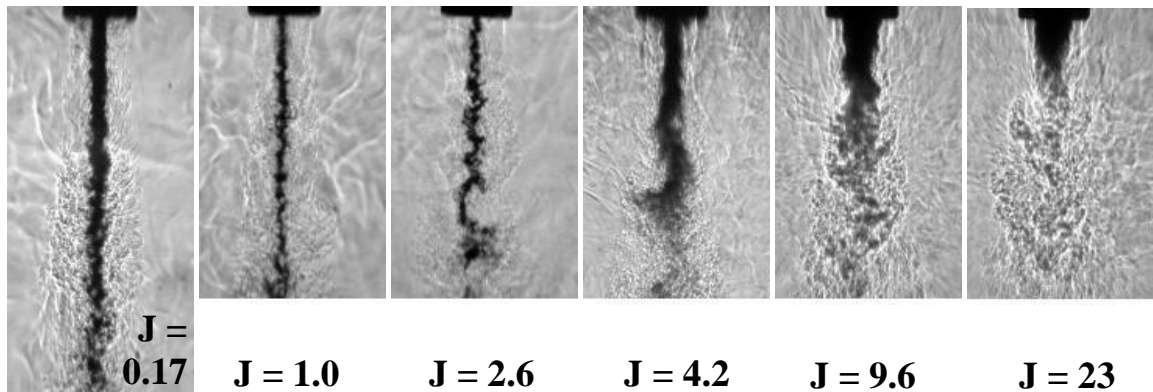


Figure 5.4. Collection of coaxial jet images without acoustic forcing at subcritical pressure from lowest to highest J . Original injector geometry.

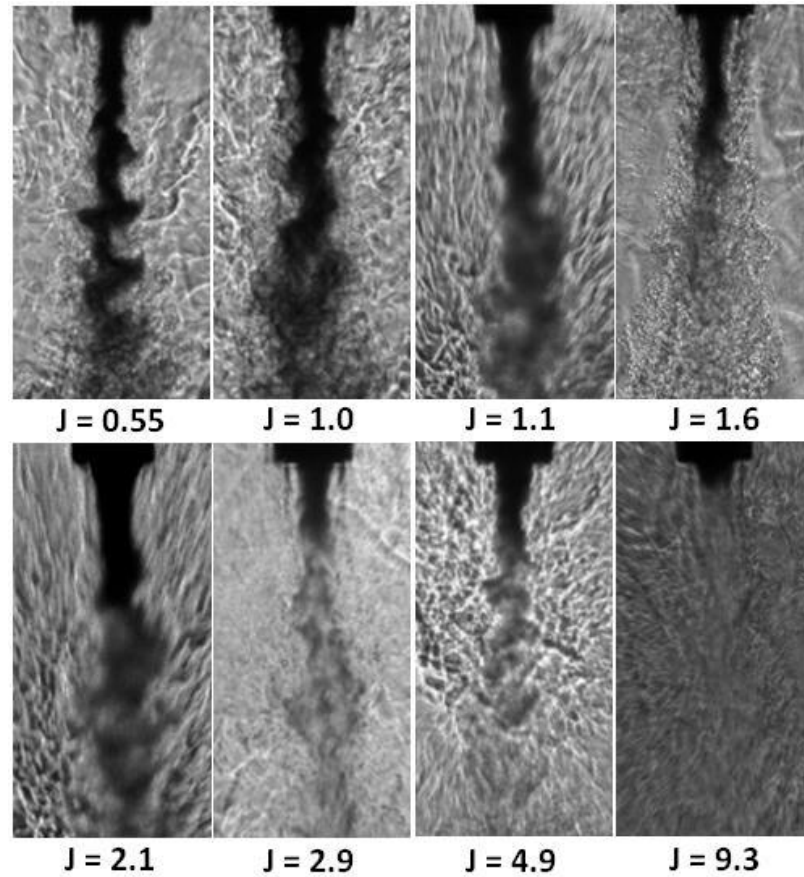


Figure 5.5. Collection of coaxial jet images without acoustic forcing at nearcritical pressure from lowest to highest J . Original injector geometry.

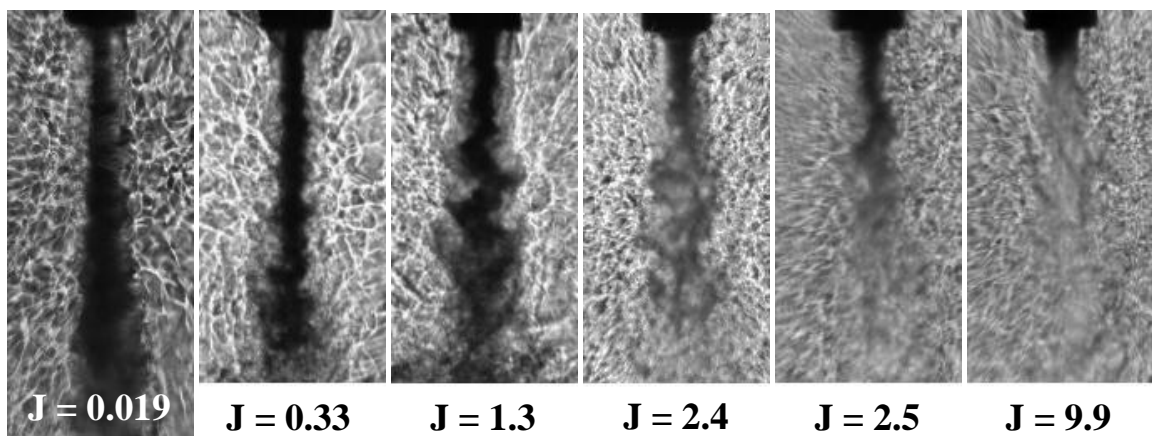


Figure 5.6. Collection of coaxial jet images without acoustic forcing at supercritical pressure from lowest to highest J . Original injector geometry.

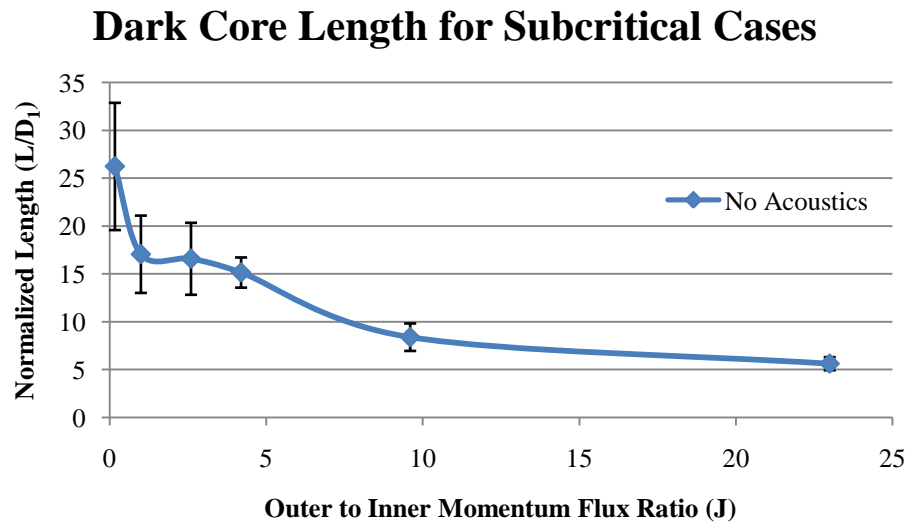


Figure 5.7. Dark core length normalized by the inner jet post inner diameter, L/D_1 , for the subcritical pressure regime. The results shown are for all the cases studied with the original injector geometry.

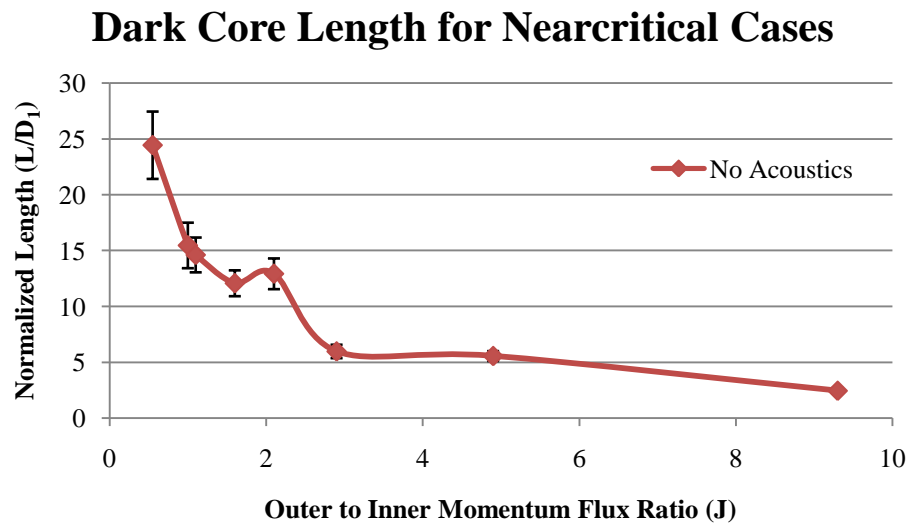


Figure 5.8. Dark core length normalized by the inner jet post inner diameter, L/D_1 , for the nearcritical pressure regime. The results shown are for all the cases studied with the original injector geometry.

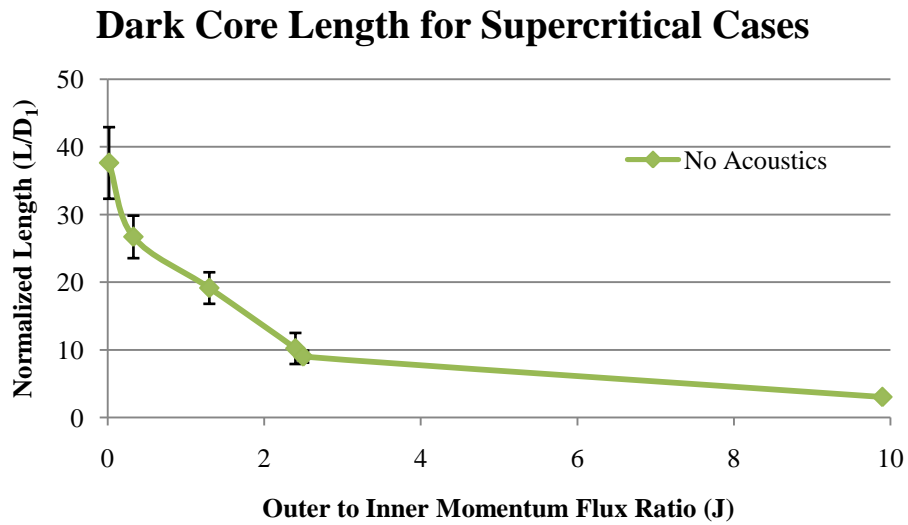


Figure 5.9. Dark core length normalized by the inner jet post inner diameter, L/D_1 for the supercritical pressure regime. The results shown are for all the cases studied with the original injector geometry.

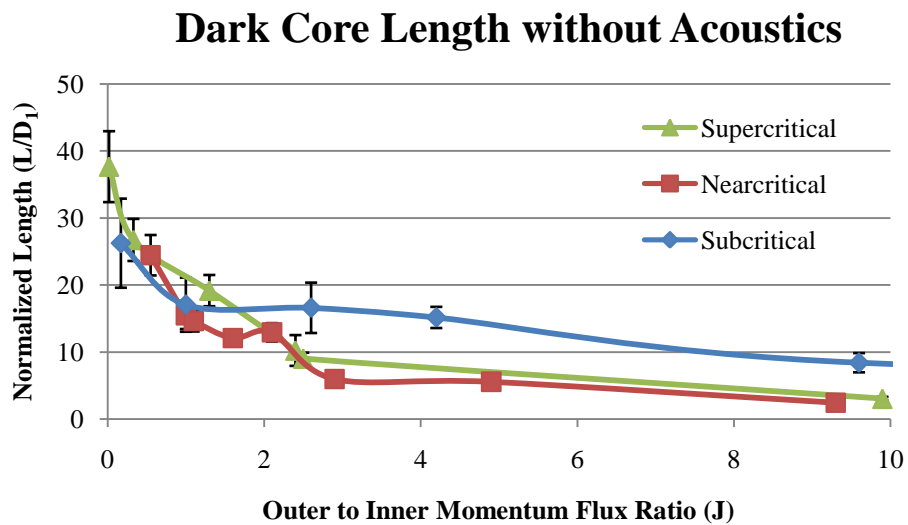


Figure 5.10. Dark core length normalized by the inner jet post inner diameter, L/D_1 for all pressure regimes using the original injector geometry. Results are shown in the $0.02 < J < 10$ range.

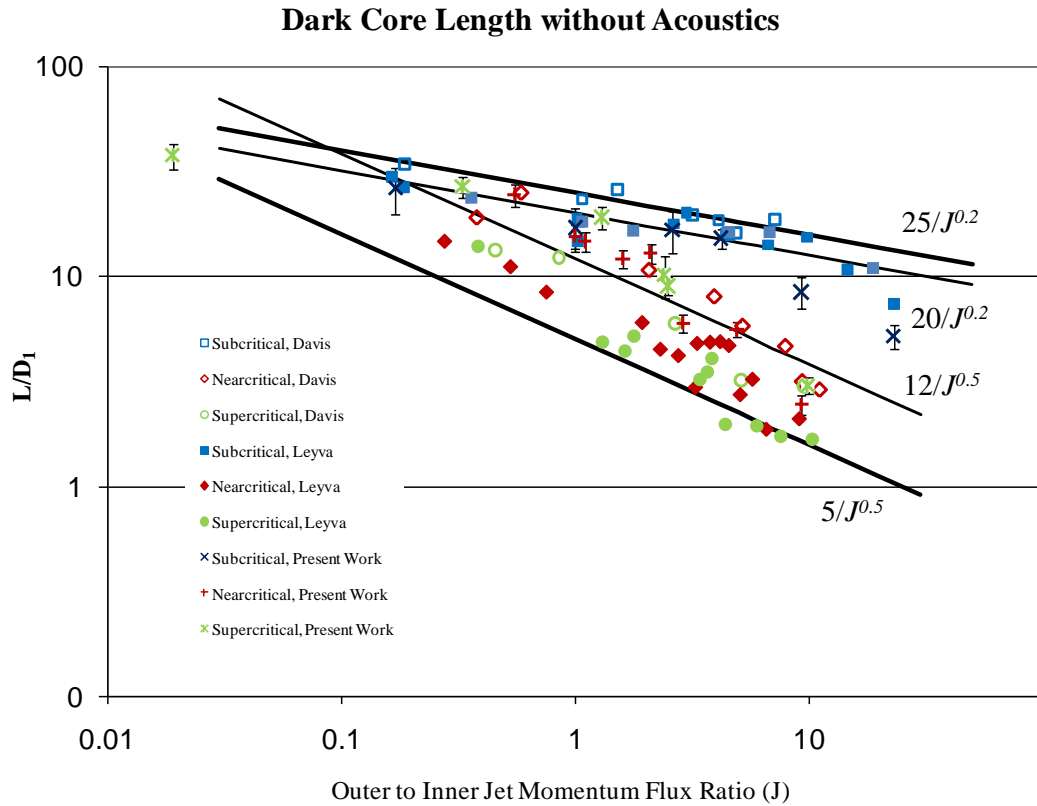


Figure 5.11. Dark core length normalized by the inner jet post inner diameter, L/D_1 for all pressure regimes. Results include previous research work using the original injector geometry in the same facility this study was performed.

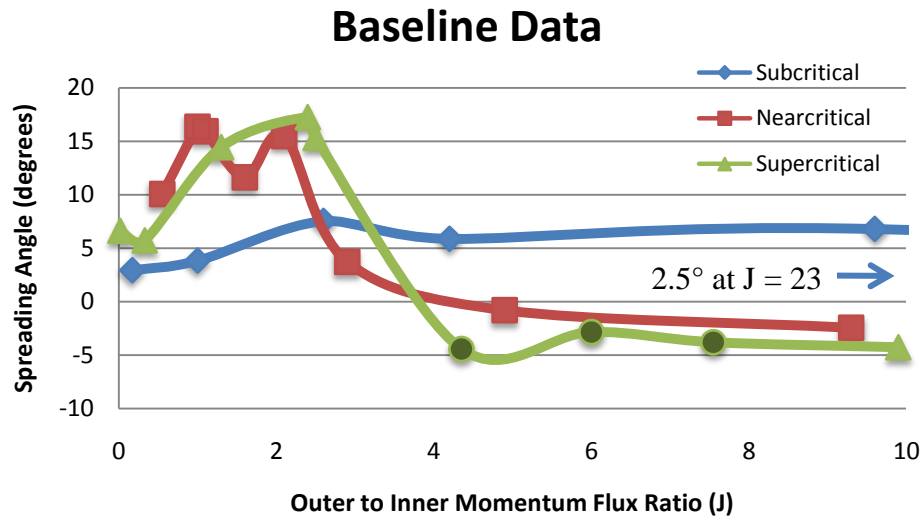


Figure 5.12. Spreading angle of the inner jet in degrees for all pressure regimes using the original injector geometry. Dark circular markers are data points from Leyva et al. (22).

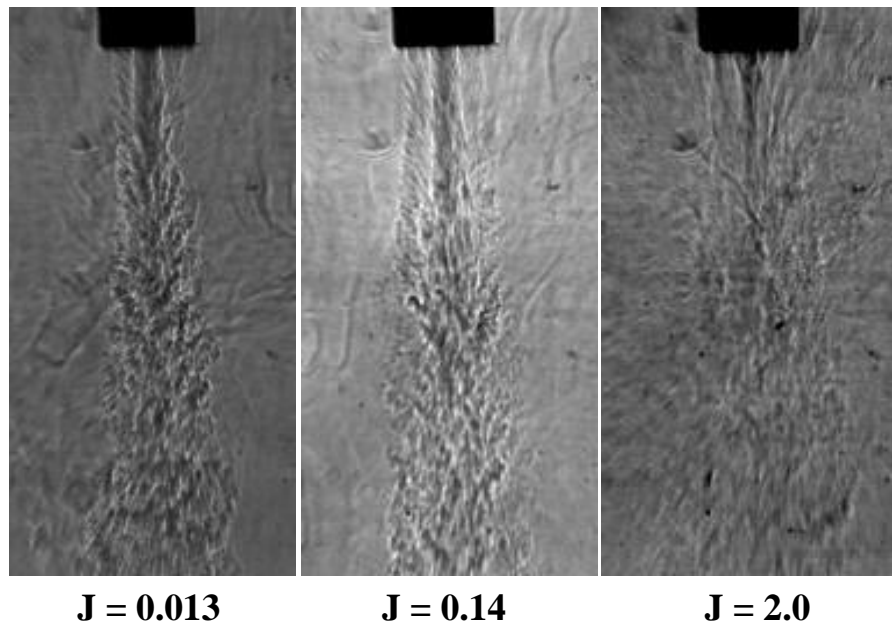


Figure 5.13. Single phase coaxial jet images without acoustic excitation at subcritical pressures. Original injector geometry.

Single Phase Outer Jet Spreading Angle ($\alpha_1 + \alpha_4$) vs. J for Subcritical Pressures

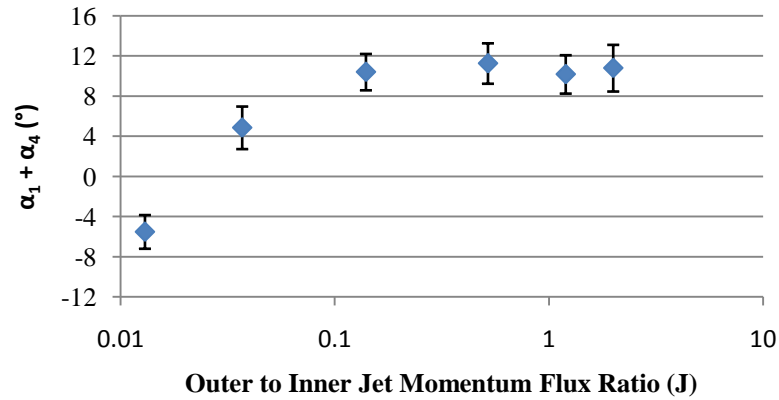


Figure 5.14. Outer jet spread angle measurements with original injector geometry for one-phase coaxial jet at subcritical pressures. The bars indicate one standard deviation above and below the mean spreading angle.

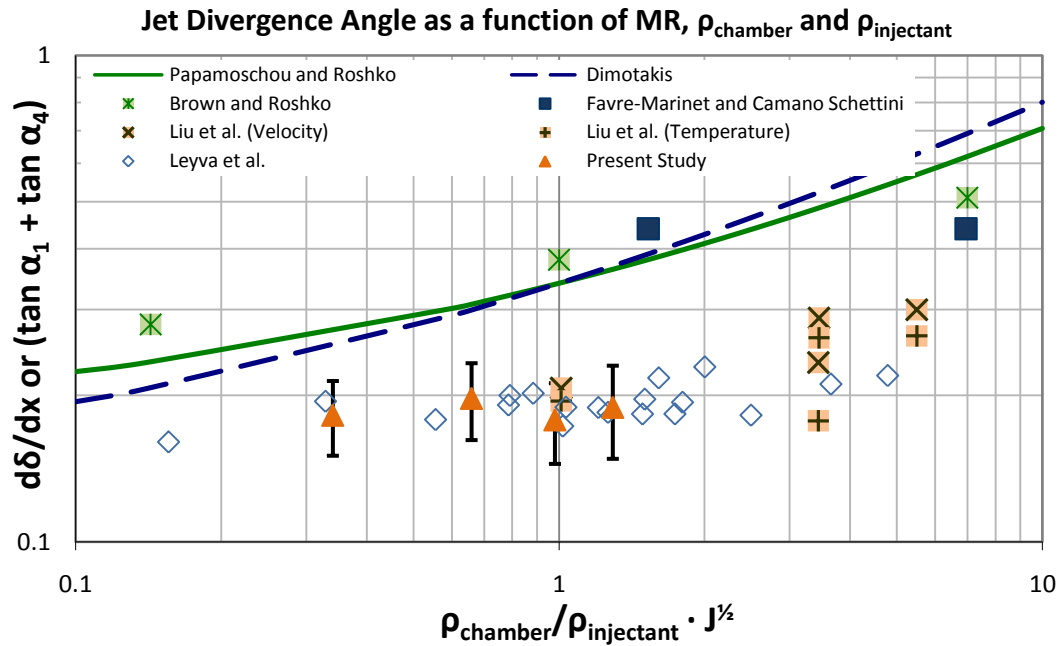


Figure 5.15. Outer jet spread angle measurements compared to jet divergence angle theoretical predictions and other single jet and coaxial jet spreading angle experimental data.

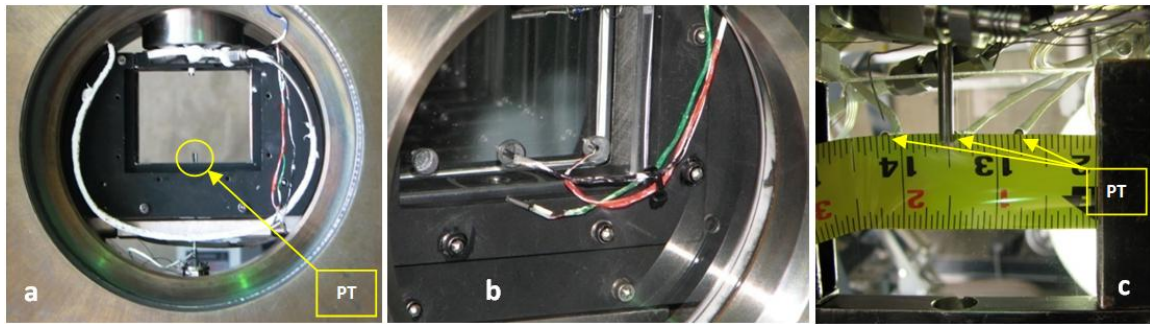


Figure 5.16. (a) Approximate location during testing of the absolute pressure transducer used to measure the acoustic field inside the inner chamber. (b) Absolute pressure transducers used to quantify the pressure oscillations at three different transversal locations within the inner chamber for tests performed with the original injector. (c) Differential pressure transducers used to quantify the pressure oscillations within the inner chamber for tests performed with the new injector.

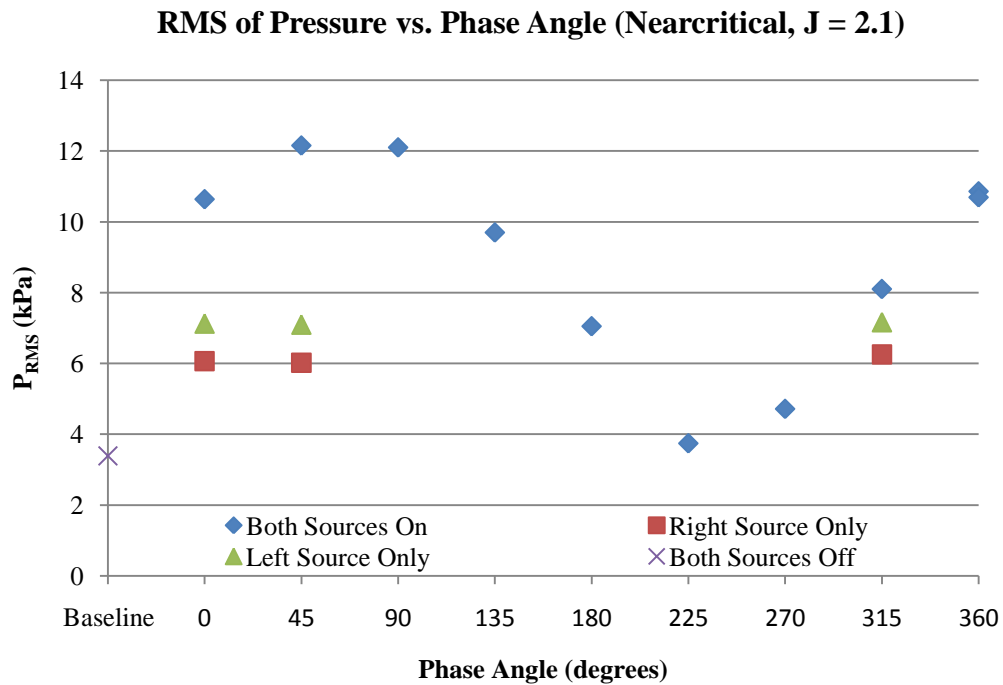


Figure 5.17. RMS of chamber pressure fluctuations measured at the bottom of the inner chamber versus phase angle between acoustic sources for the nearcritical case with $J = 2.1$ with the original injector geometry. The data with only one acoustic source on was obtained immediately before recording data with both sources on for the corresponding phase angle on which they are plotted.

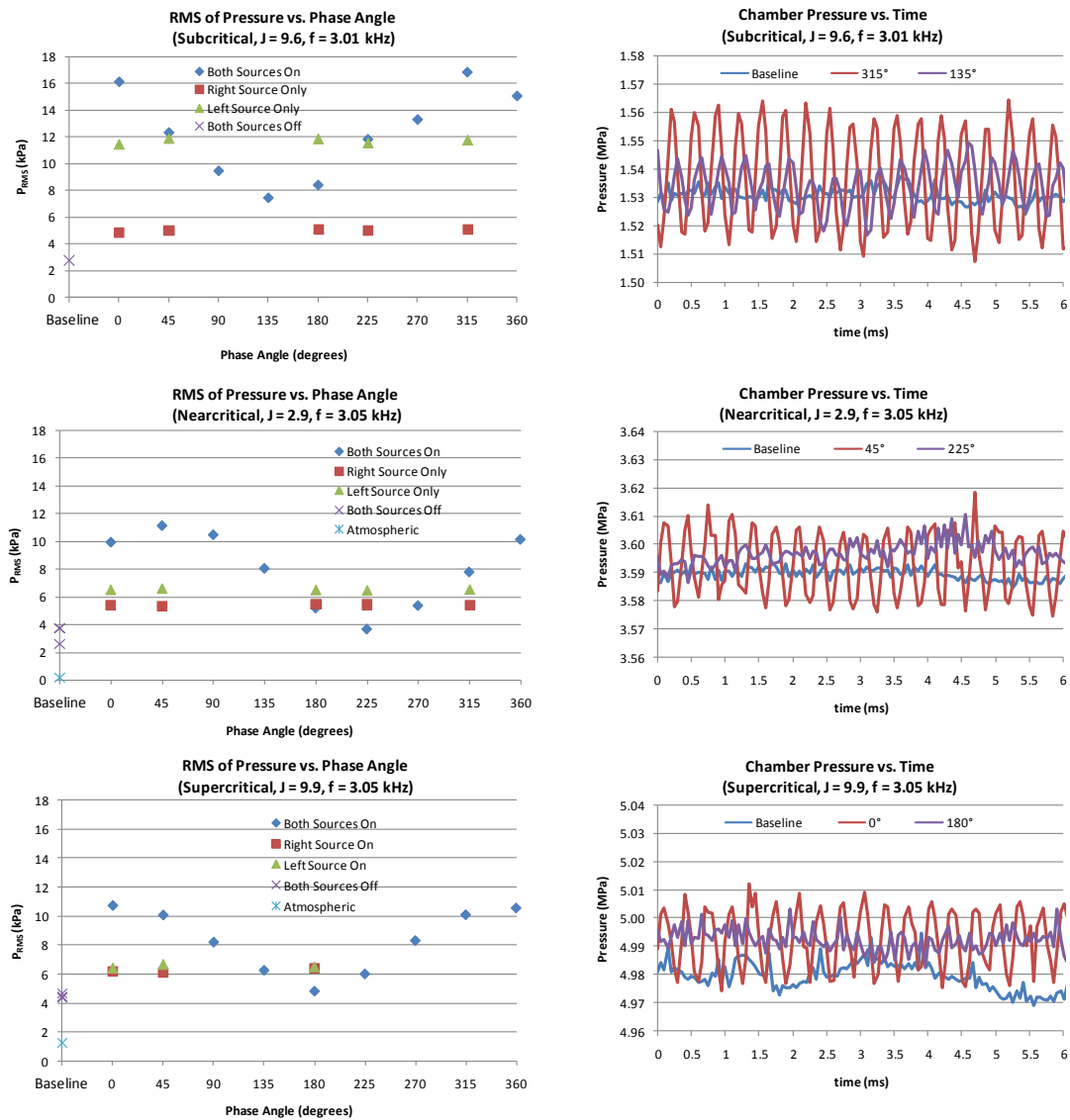


Figure 5.18. Graphs of the RMS value of the chamber pressure fluctuations at different phase angles between the acoustic sources on the left with chamber pressure as a function of time on the right for one subcritical case, one nearcritical case and one supercritical case with the original injector geometry.

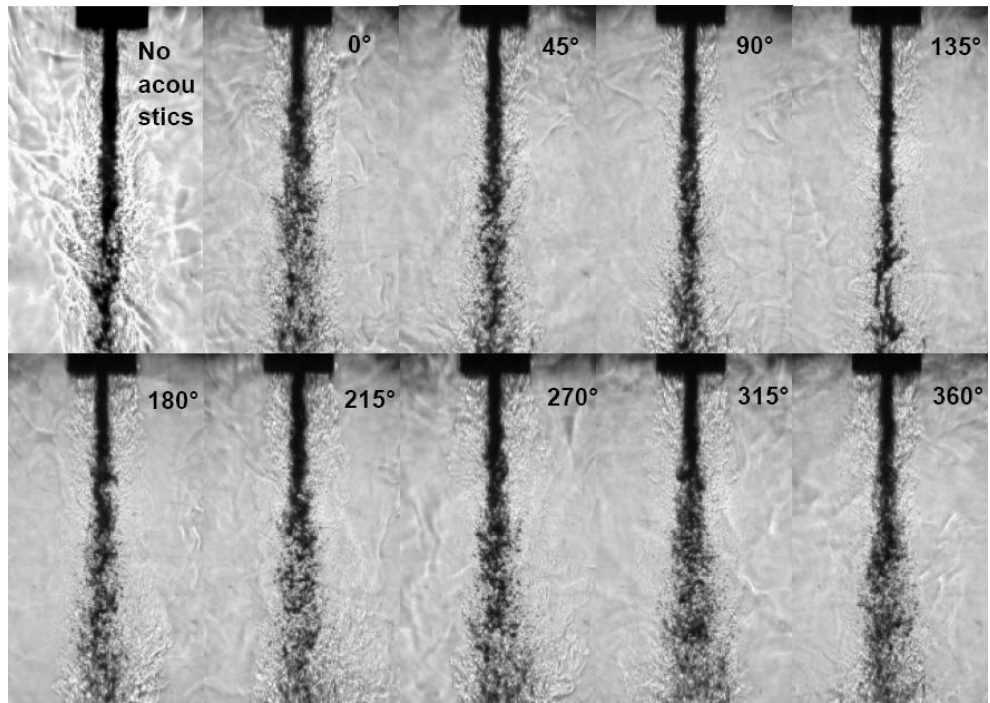


Figure 5.19. Collection of subcritical coaxial jet images at $P_{\text{chamber}} = 1.50 \text{ MPa}$, $J = 0.17$. Original injector geometry

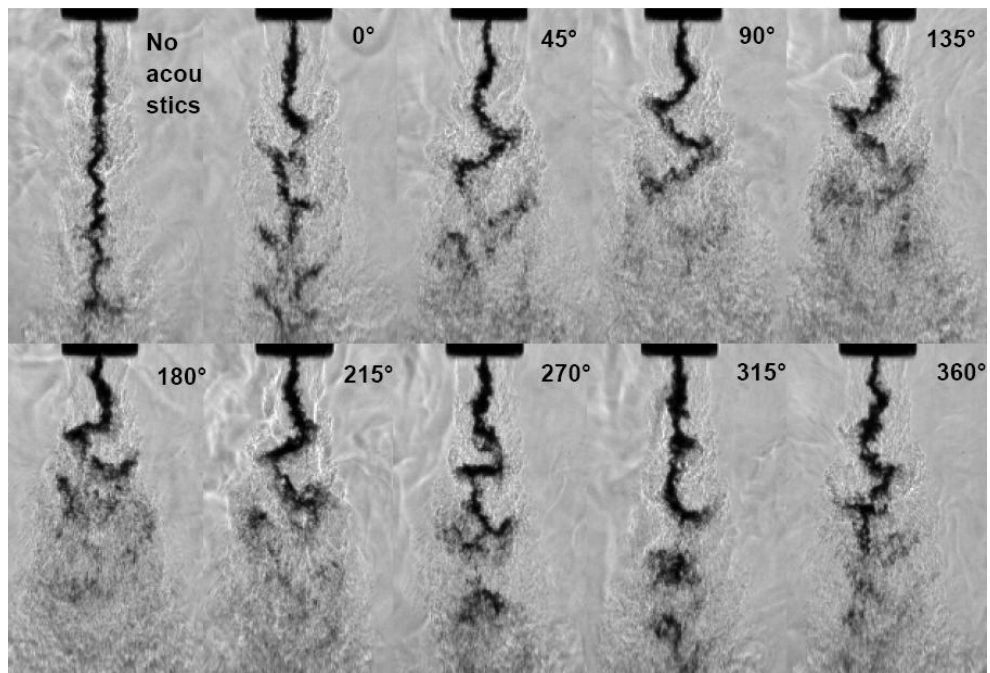


Figure 5.20. Collection of subcritical coaxial jet images at $P_{\text{chamber}} = 1.45 \text{ MPa}$, $J = 2.6$. Original injector geometry.

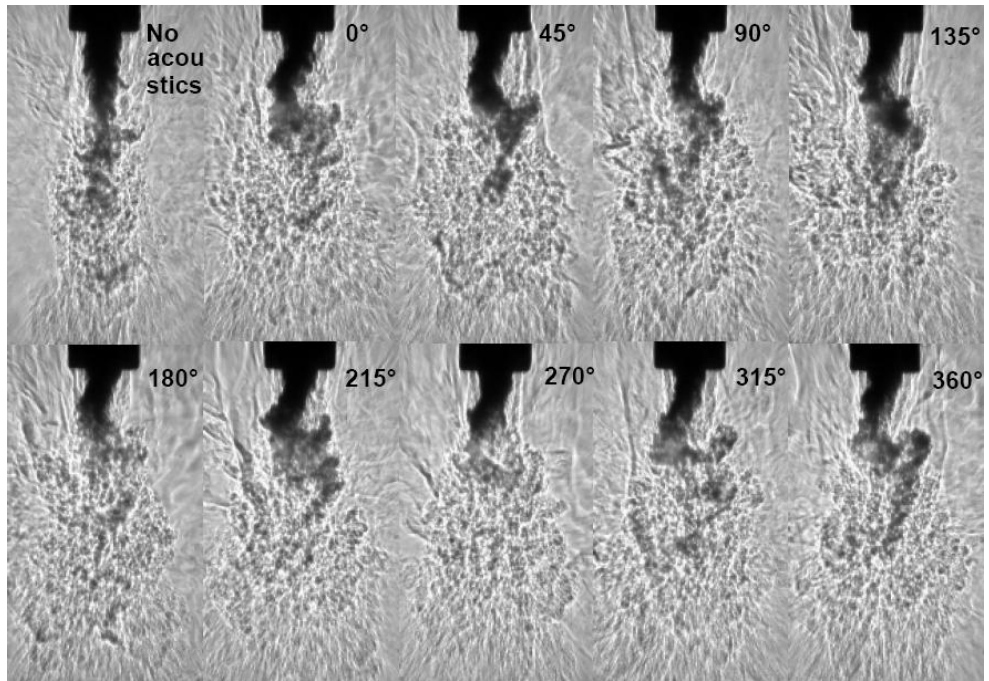


Figure 5.21. Collection of subcritical coaxial jet images at $P_{\text{chamber}} = 1.50 \text{ MPa}$, $J = 9.6$. Original injector geometry.

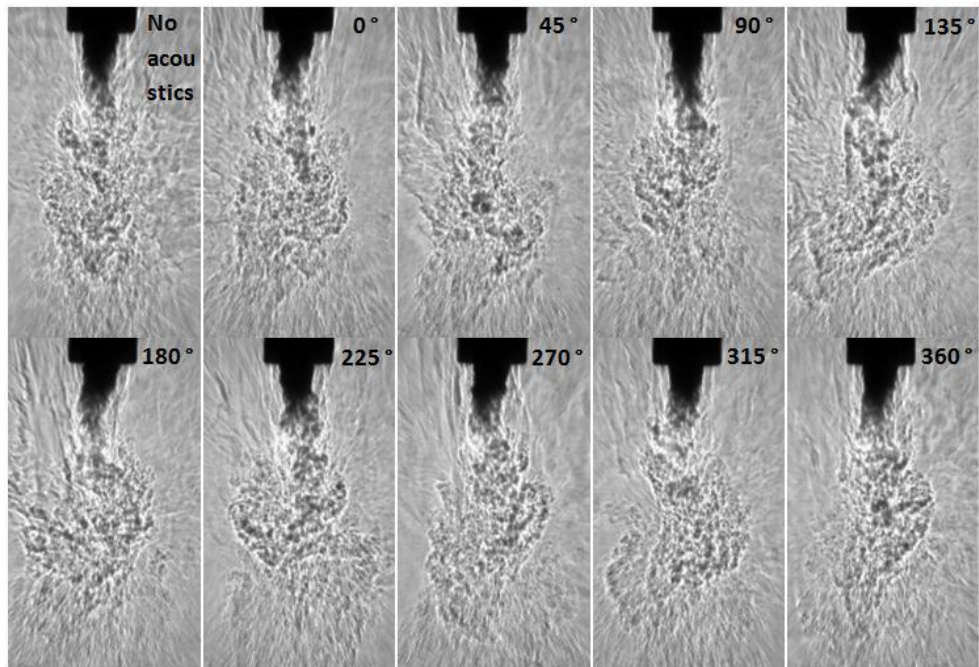


Figure 5.22. Collection of subcritical coaxial jet images at $P_{\text{chamber}} = 1.50 \text{ MPa}$, $J = 23$. Original injector geometry.

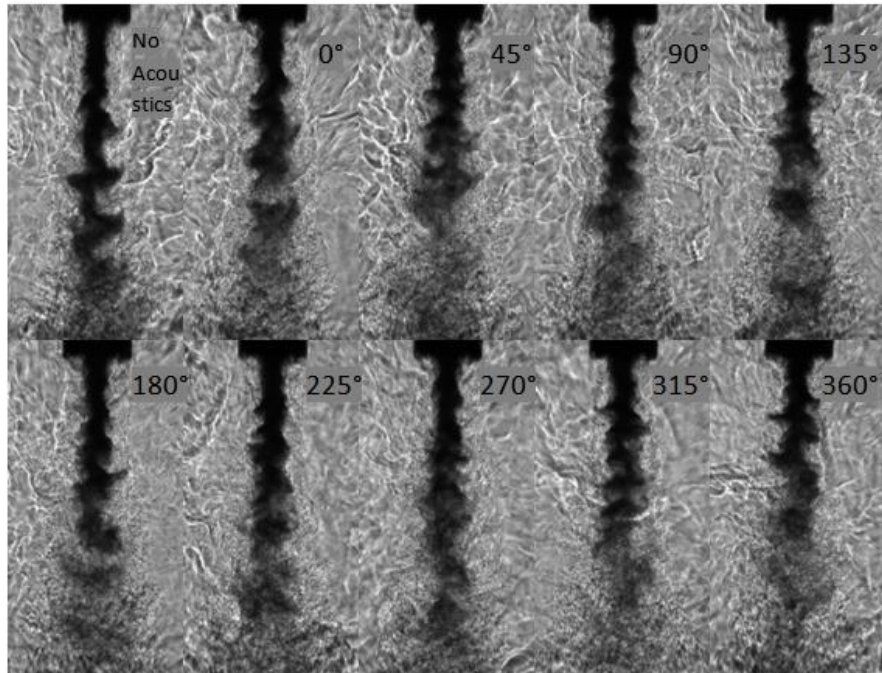


Figure 5.23. Collection of nearcritical coaxial jet images at $P_{\text{chamber}} = 3.58 \text{ MPa}$, $J = 0.55$. Original injector geometry.

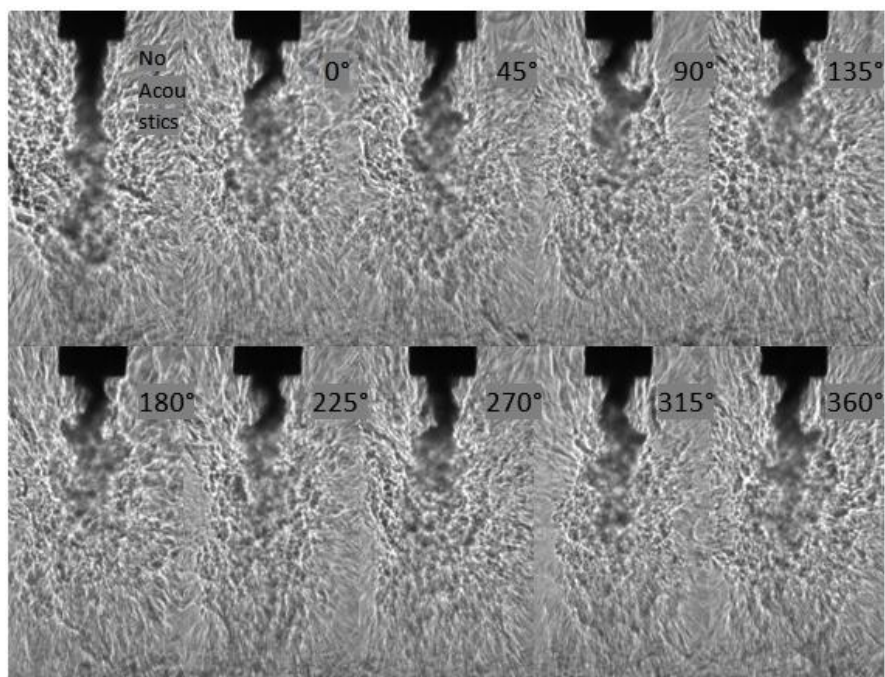


Figure 5.24. Collection of nearcritical coaxial jet images at $P_{\text{chamber}} = 3.56 \text{ MPa}$, $J = 4.9$. Original injector geometry.

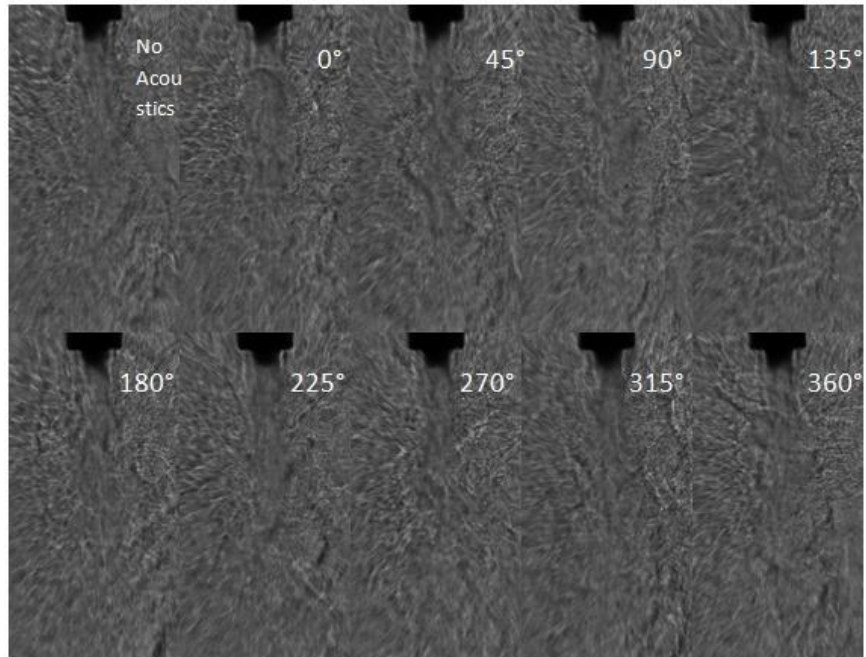


Figure 5.25. Collection of nearcritical coaxial jet images at $P_{\text{chamber}} = 3.56 \text{ MPa}$, $J = 9.3$. Original injector geometry.

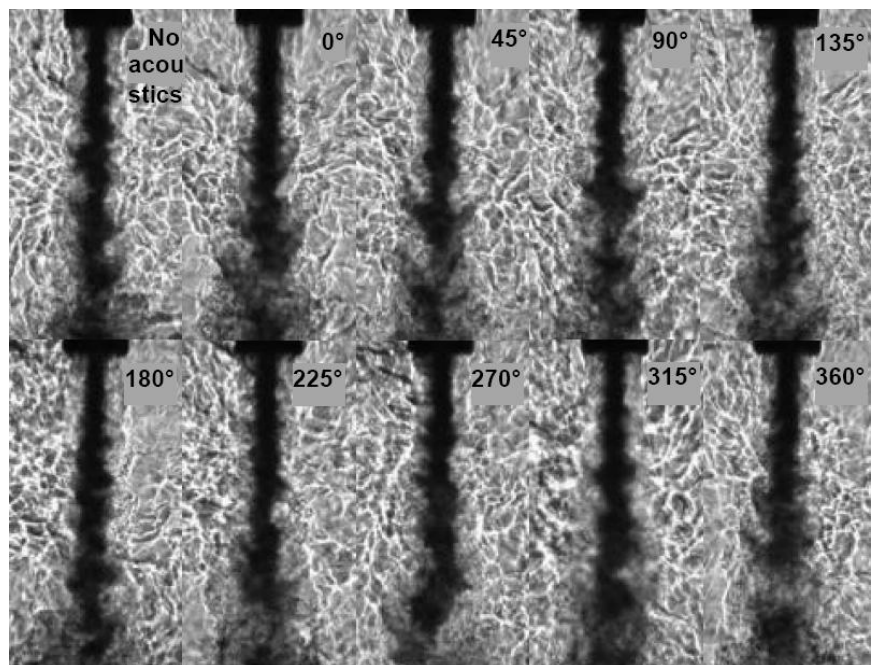


Figure 5.26. Collection of supercritical coaxial jet images at $P_{\text{chamber}} = 4.96 \text{ MPa}$, $J = 0.33$. Original injector geometry.

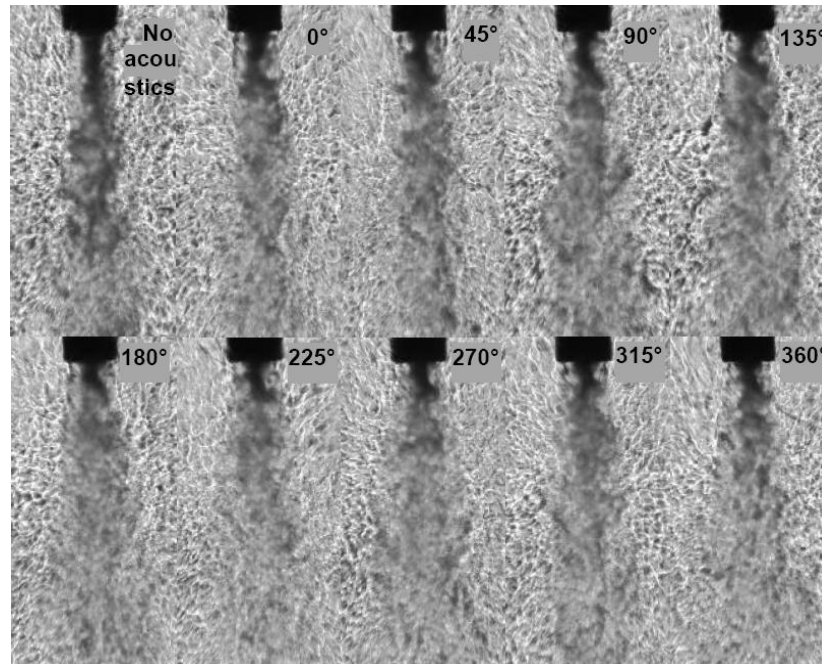


Figure 5.27. Collection of supercritical coaxial jet images at $P_{\text{chamber}} = 4.96 \text{ MPa}$, $J = 2.4$. Original injector geometry.

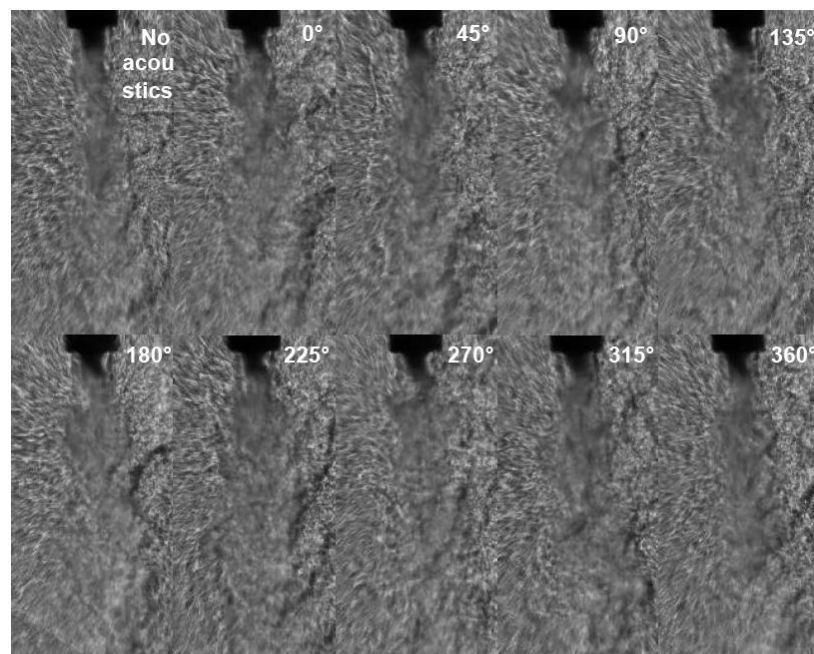


Figure 5.28. Collection of supercritical coaxial jet images at $P_{\text{chamber}} = 4.96 \text{ MPa}$, $J = 9.9$. Original injector geometry.

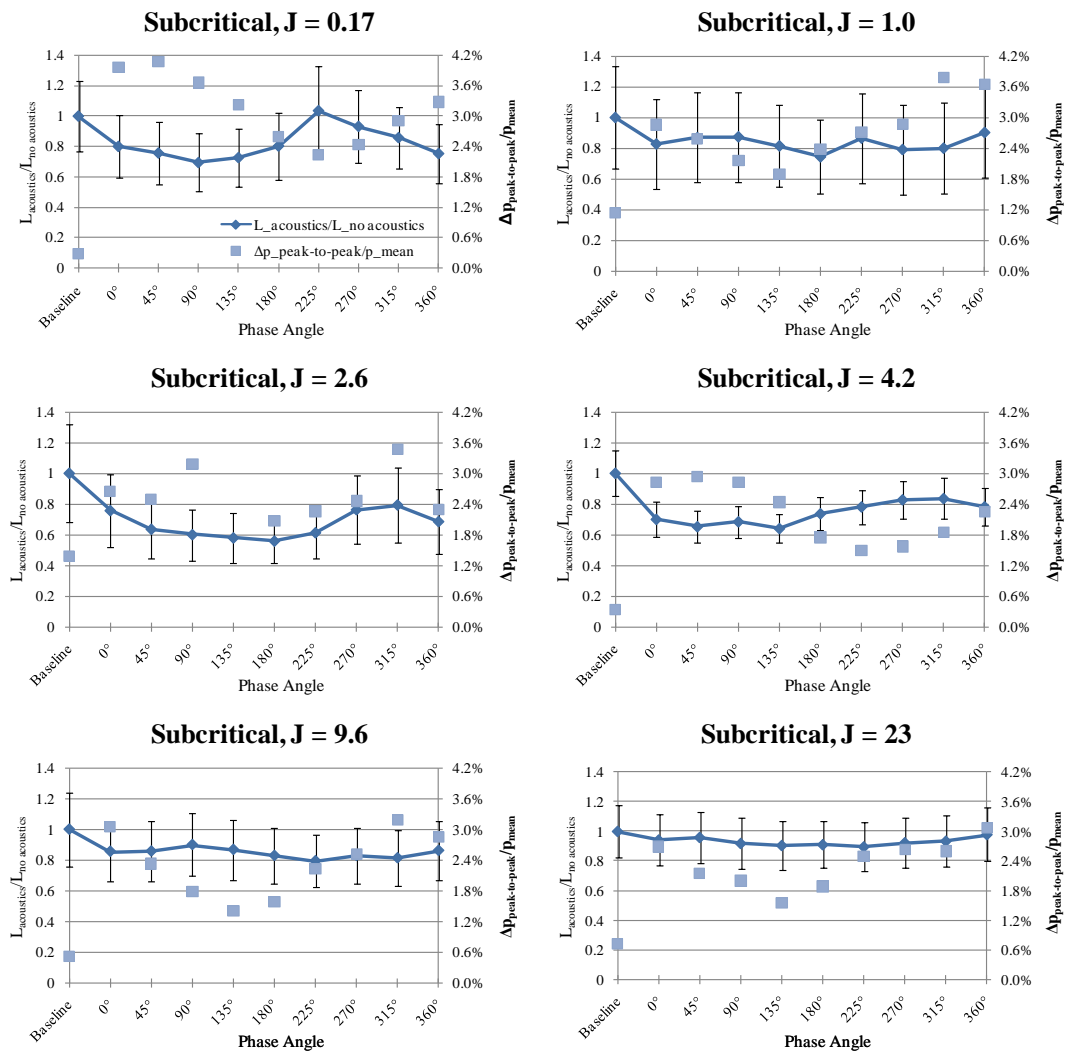


Figure 5.29. Dark core length with acoustics ($L_{\text{acoustics}}$) over dark core length without acoustics ($L_{\text{no acoustics}}$), shown in diamonds, versus phase angle between acoustic sources for subcritical pressures. The the peak-to-peak pressure perturbation as a percentage of the mean chamber pressure ($\Delta p_{\text{peak-to-peak}}/p_{\text{mean}}$), in squares, is also plotted. Original injector geometry.

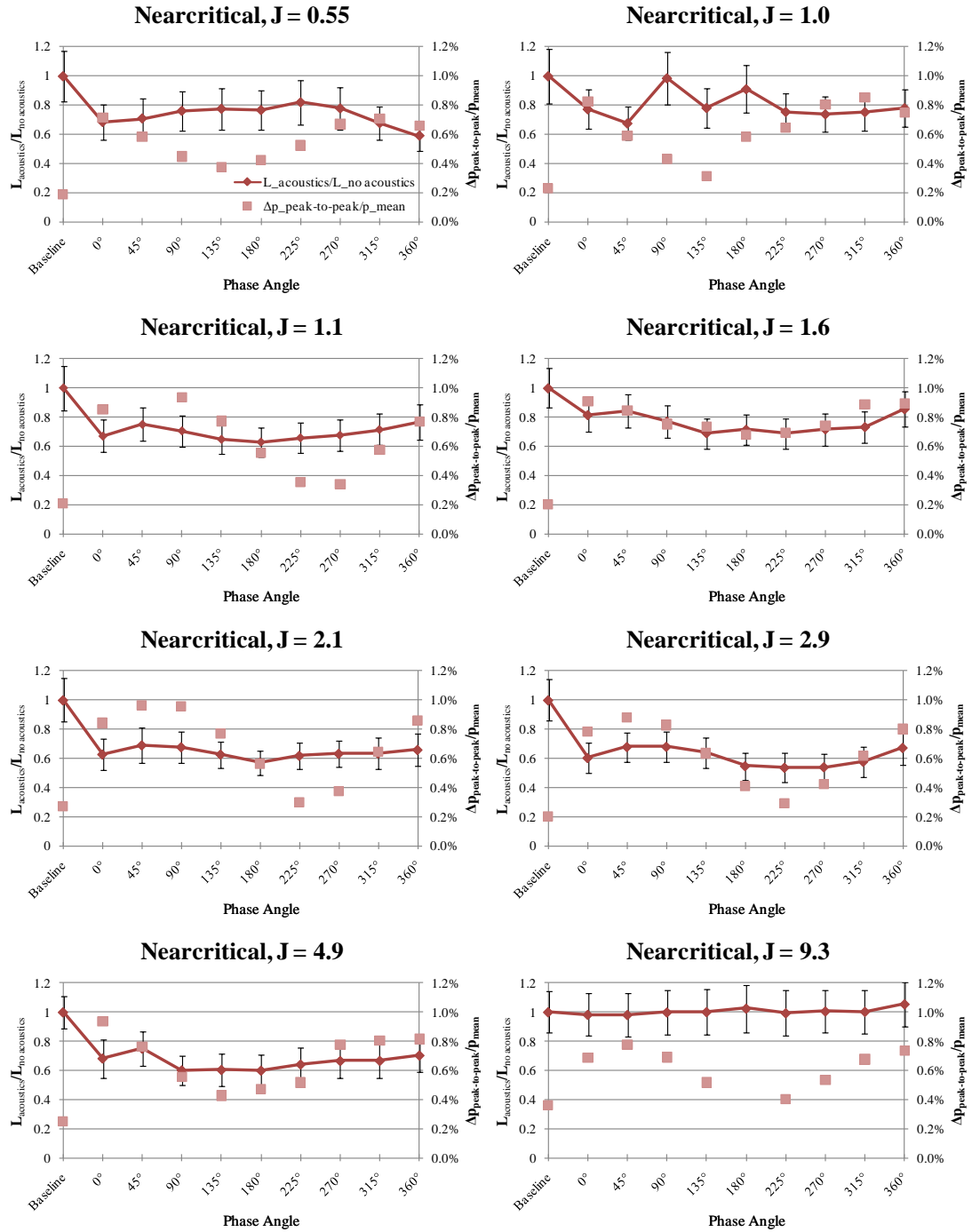


Figure 5.30. Dark core length with acoustics ($L_{\text{acoustics}}$) over dark core length without acoustics ($L_{\text{no acoustics}}$), shown in diamonds, versus phase angle between acoustic sources for nearcritical pressures. The the peak-to-peak pressure perturbation as a percentage of the mean chamber pressure ($\Delta p_{\text{peak-to-peak}}/p_{\text{mean}}$), in squares, is also plotted. Original injector geometry.

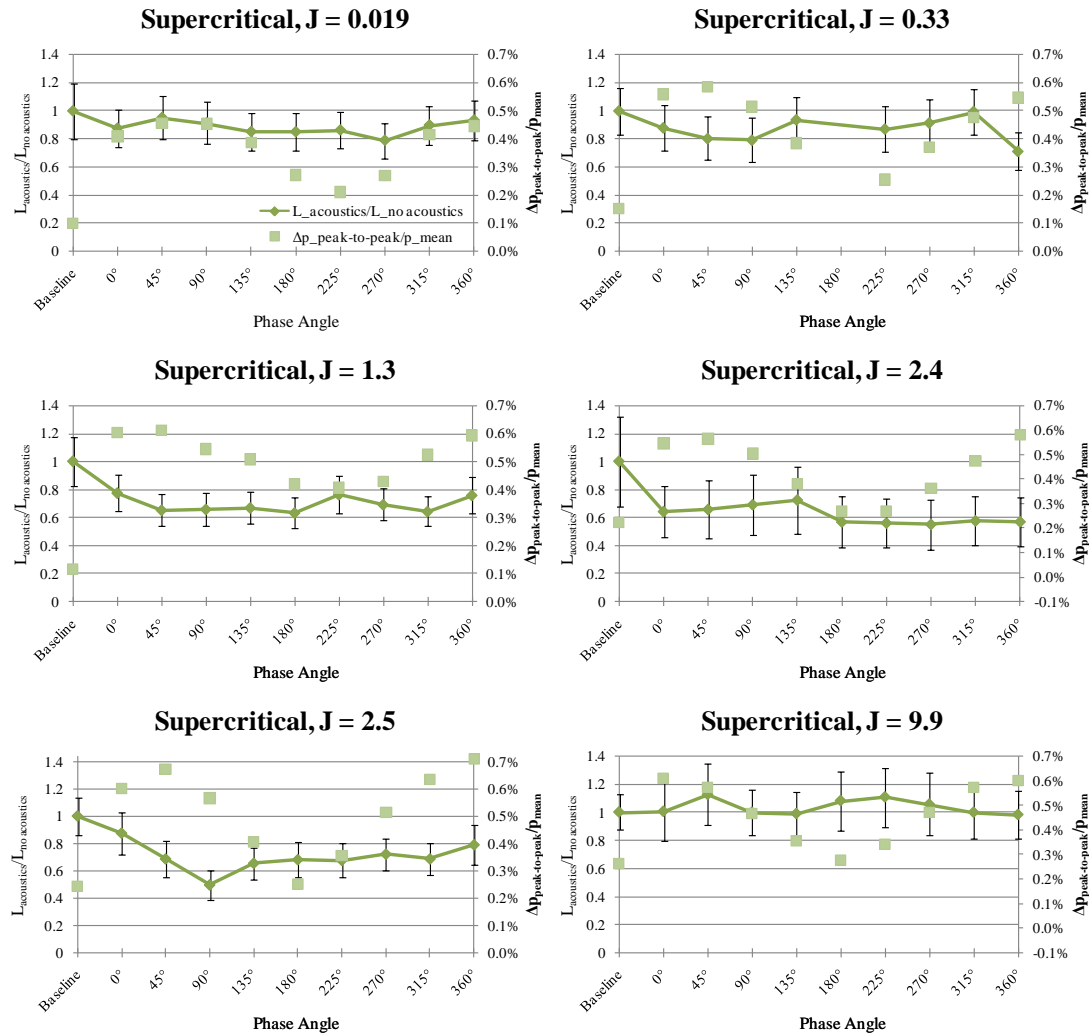


Figure 5.31. Dark core length with acoustics ($L_{\text{acoustics}}$) over dark core length without acoustics ($L_{\text{no acoustics}}$), shown in diamonds, versus phase angle between acoustic sources for supercritical pressures. The the peak-to-peak pressure perturbation as a percentage of the mean chamber pressure ($\Delta p_{\text{peak-to-peak}}/p_{\text{mean}}$), in squares, is also plotted. Original injector geometry.

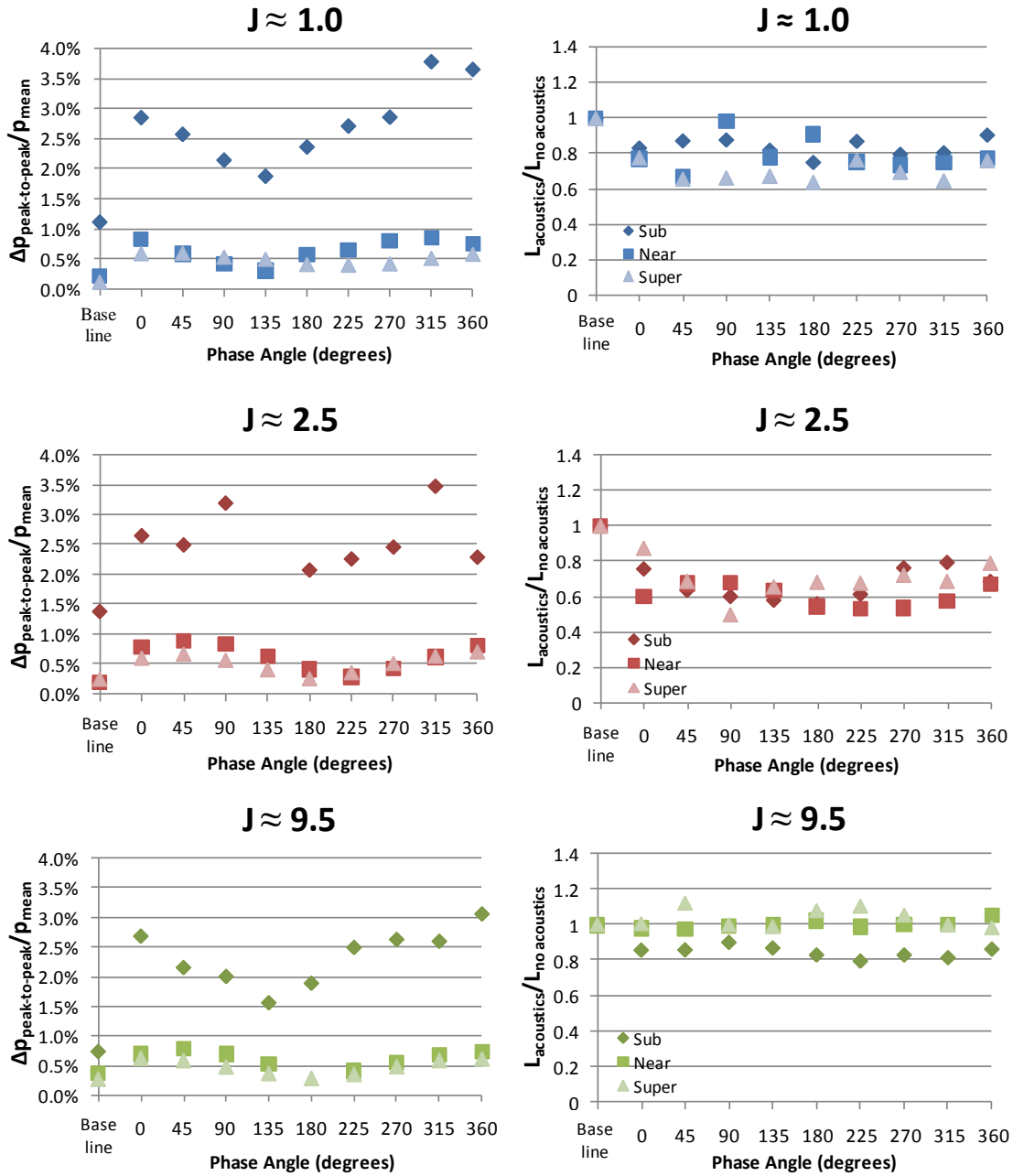


Figure 5.32. Peak-to-peak pressure perturbation ($\Delta p_{\text{peak-to-peak}}$) as a percentage of the mean chamber pressure (p_{mean}) and dark core length with acoustics ($L_{\text{acoustics}}$) over dark core length without acoustics ($L_{\text{no acoustics}}$) versus phase angle between acoustic sources for sub, near and supercritical pressures at $J \approx 1.0$, 2.5 and 9.5 for the original injector geometry.

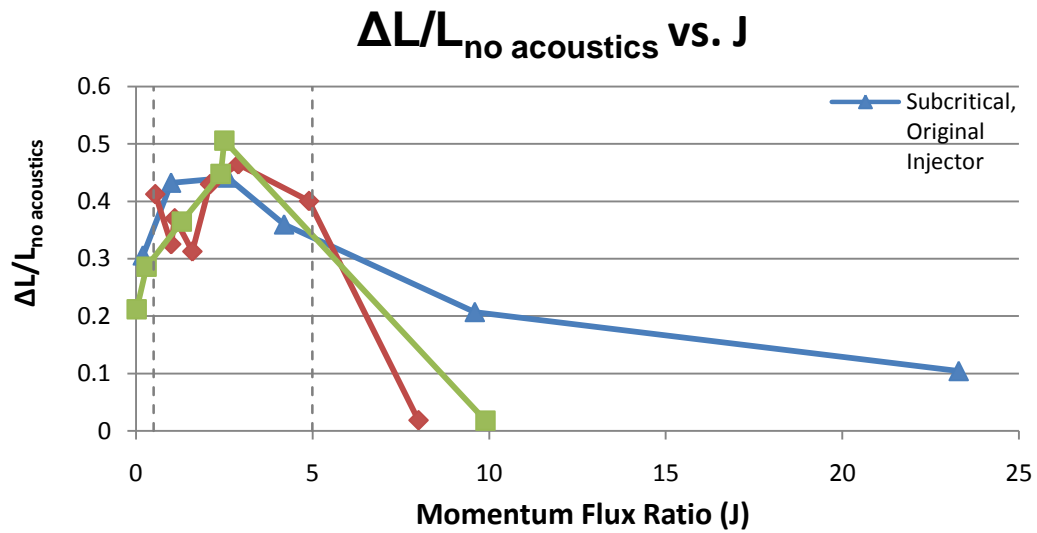


Figure 5.33. Maximum dark core length reduction between dark core length without acoustics and dark core length with acoustics for all phase angles $(L_{\text{no acoustics}} - L_{\text{acoustics}})_{\text{MAX}}$ for a given case divided by the dark core length without acoustics $(L_{\text{no acoustics}})$ as a function of J for all cases obtained with the original injector in this study.

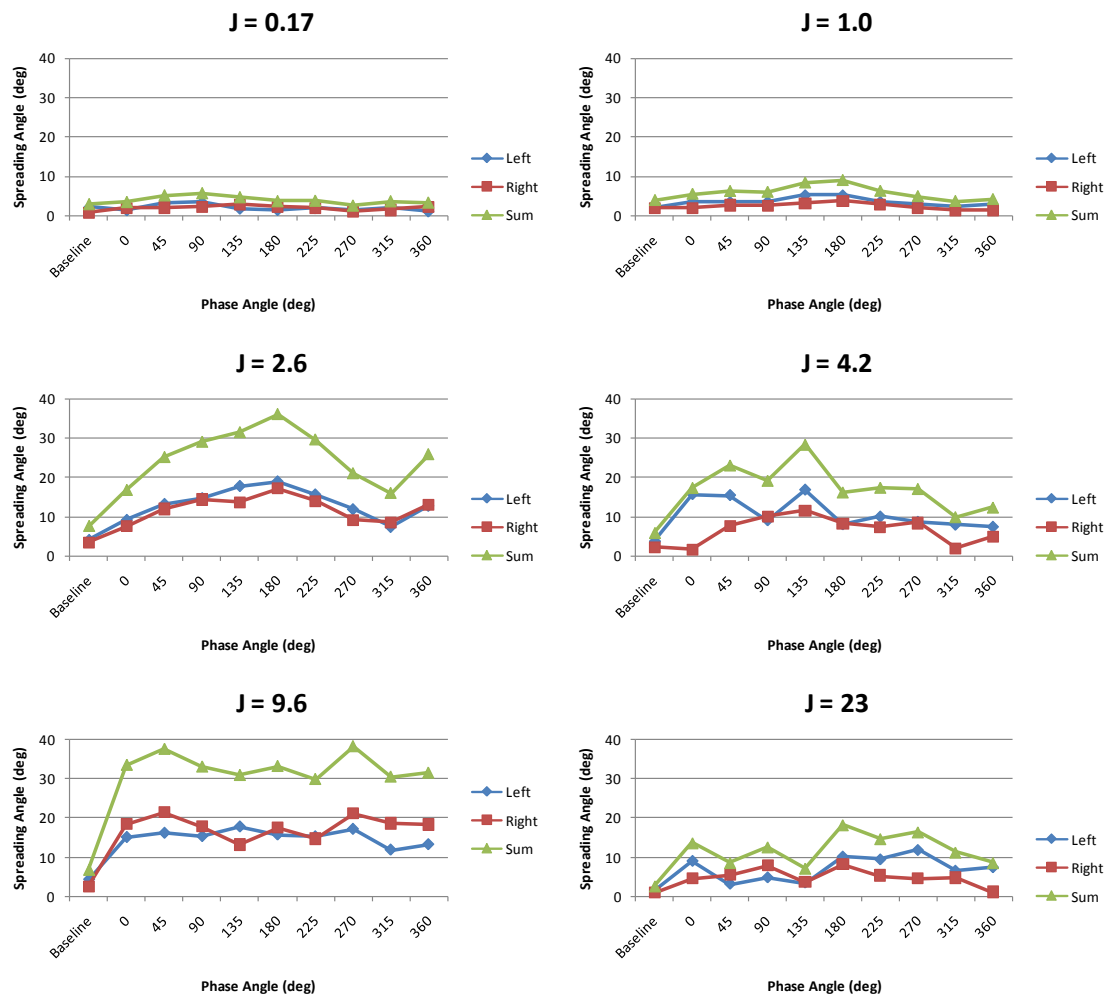


Figure 5.34. Maximum spread angles as a function of acoustic phase angle for different J values at subcritical pressures for original injector geometry.

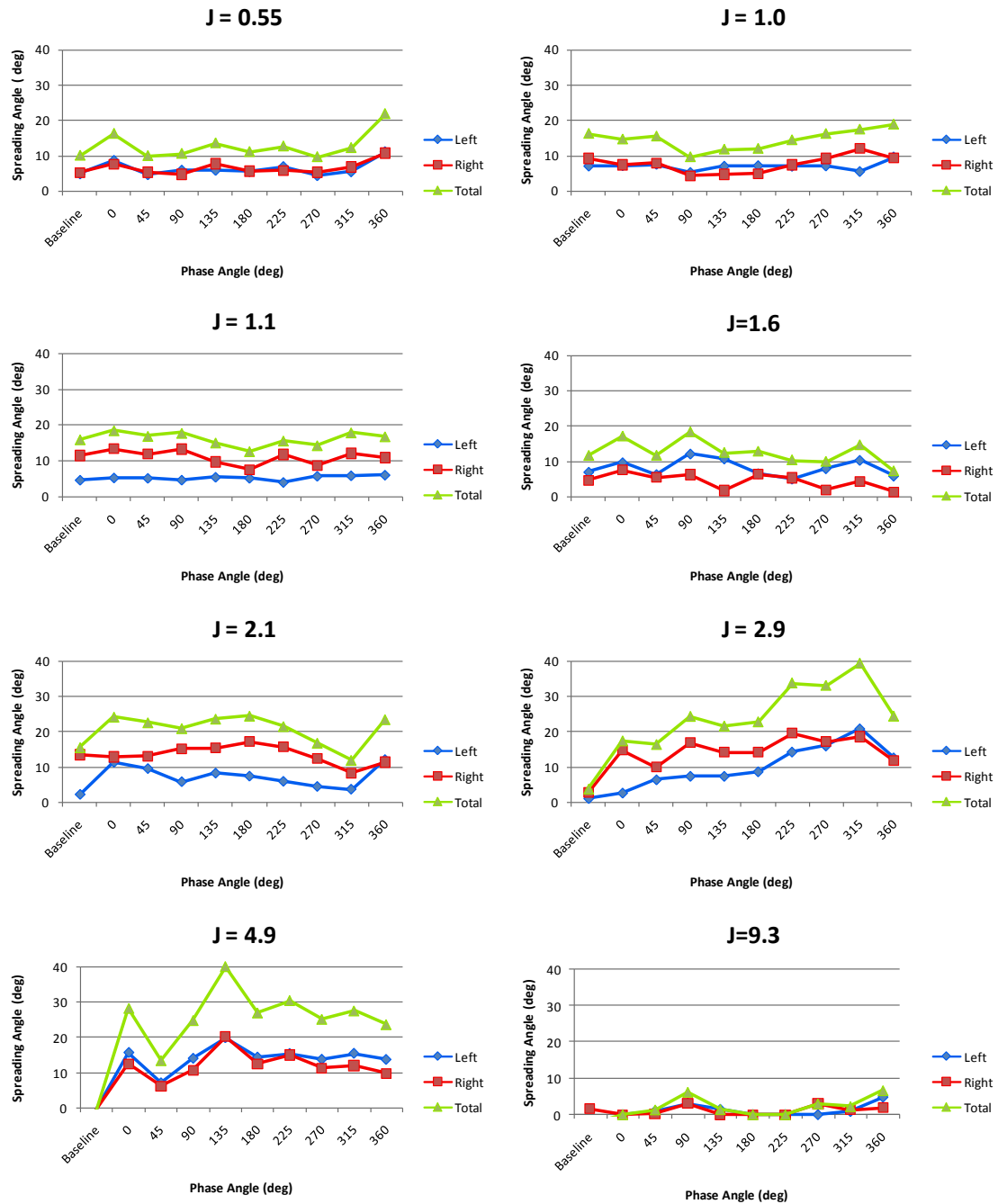


Figure 5.35. Maximum spread angles as a function of acoustic phase angle for different J values at nearcritical pressures for original injector geometry.

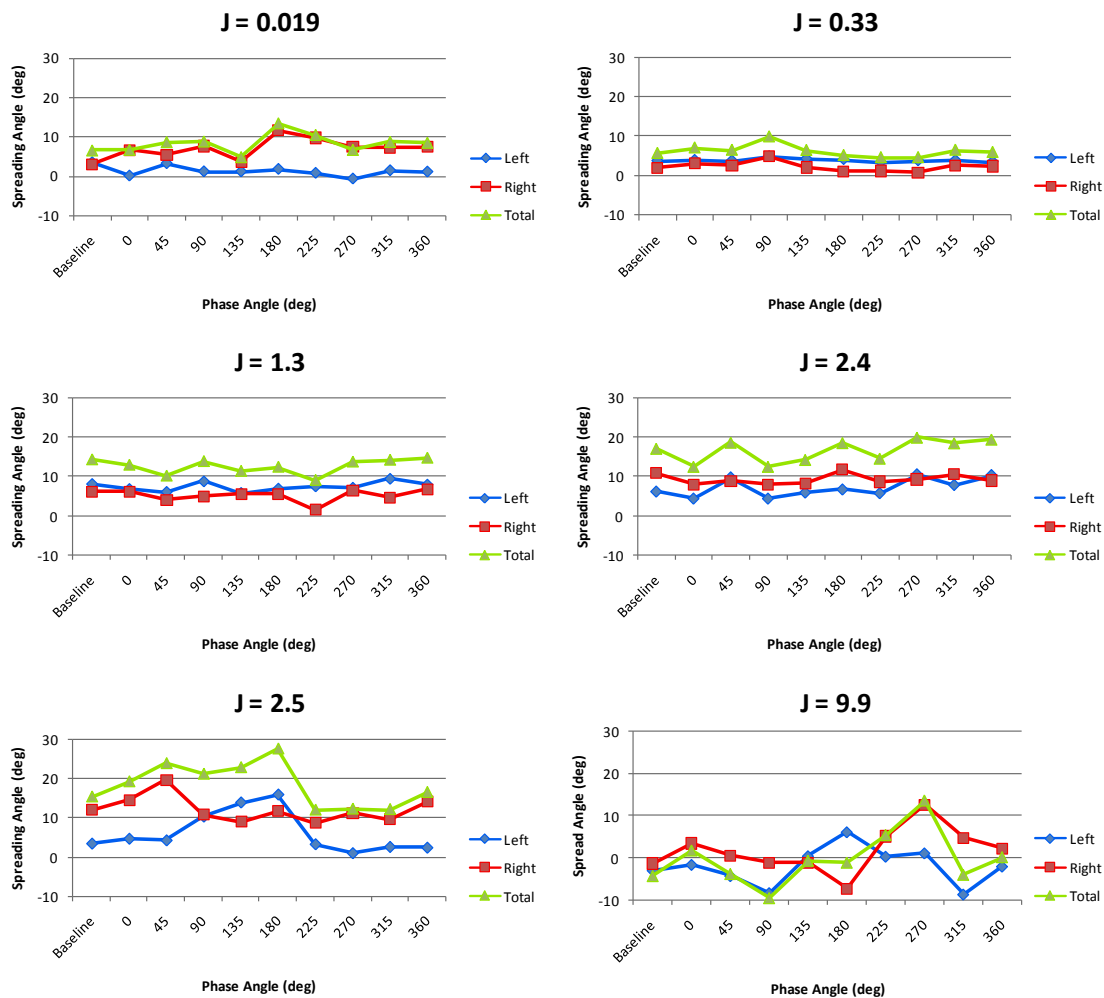


Figure 5.36. Maximum spread angles as a function of acoustic phase angle for different J values at supercritical pressures for original injector geometry.

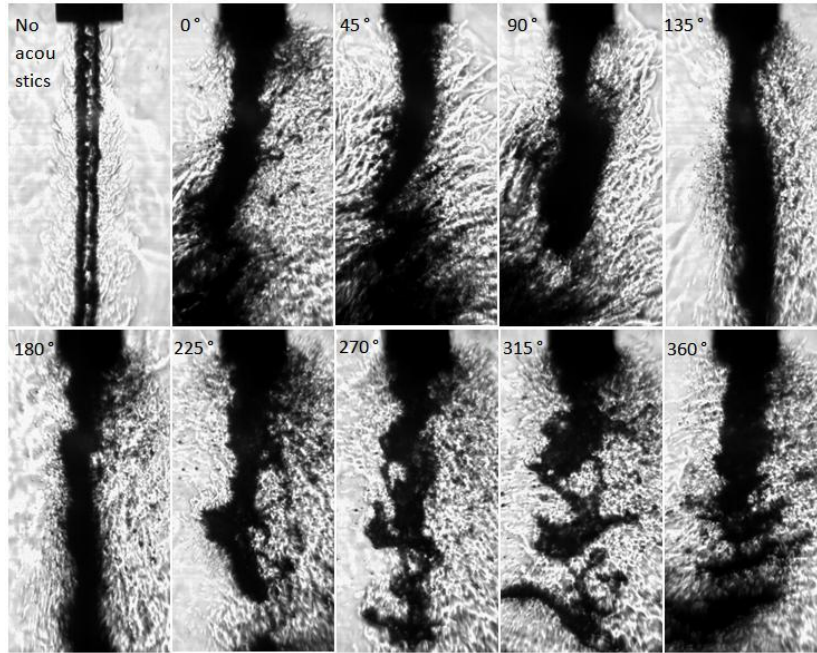


Figure 5.37. Coaxial jet images with the new injector at subcritical pressure ($P_{\text{chamber}} = 1.48 \text{ MPa}$, $J = 0.089$).

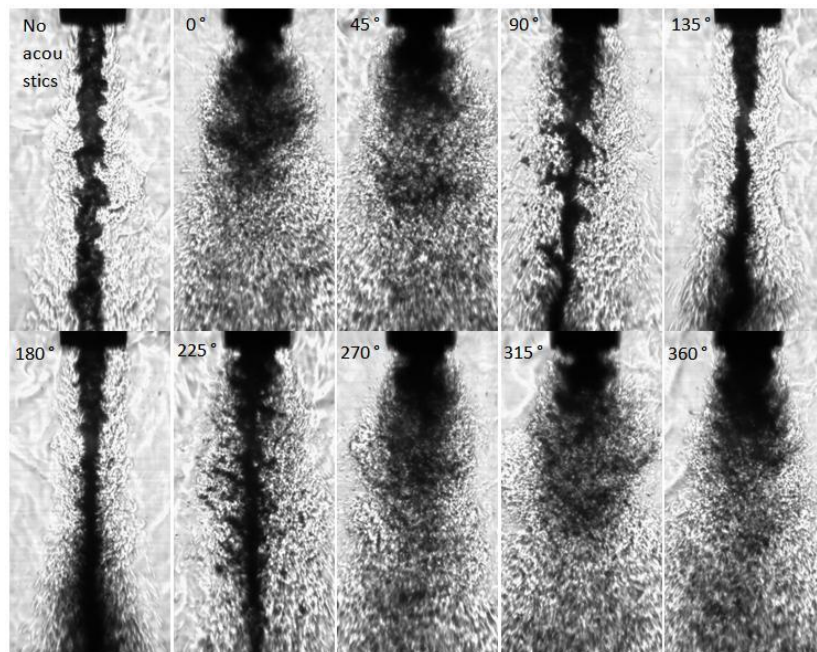


Figure 5.38. Coaxial jet images with the new injector at subcritical pressure ($P_{\text{chamber}} = 1.49 \text{ MPa}$, $J = 0.43$).

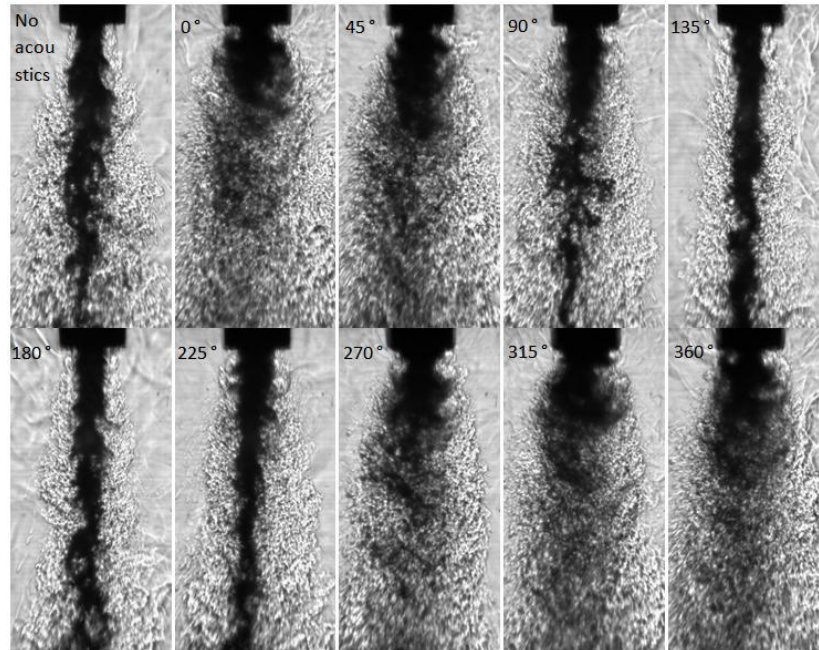


Figure 5.39. Coaxial jet images with the new injector at subcritical pressure ($P_{\text{chamber}} = 1.49 \text{ MPa}$, $J = 2.0$).

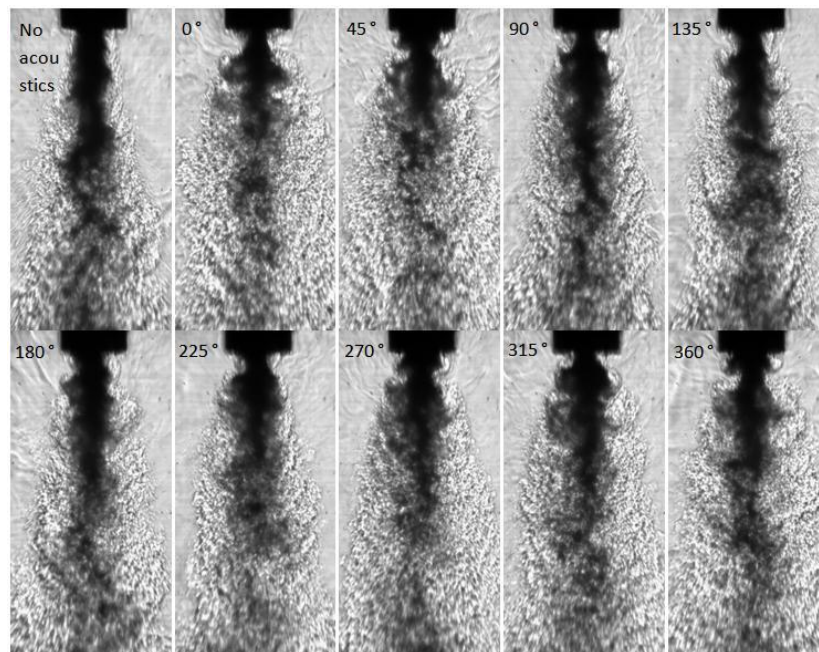


Figure 5.40. Coaxial jet images with the new injector at subcritical pressure ($P_{\text{chamber}} = 1.49 \text{ MPa}$, $J = 7.8$).

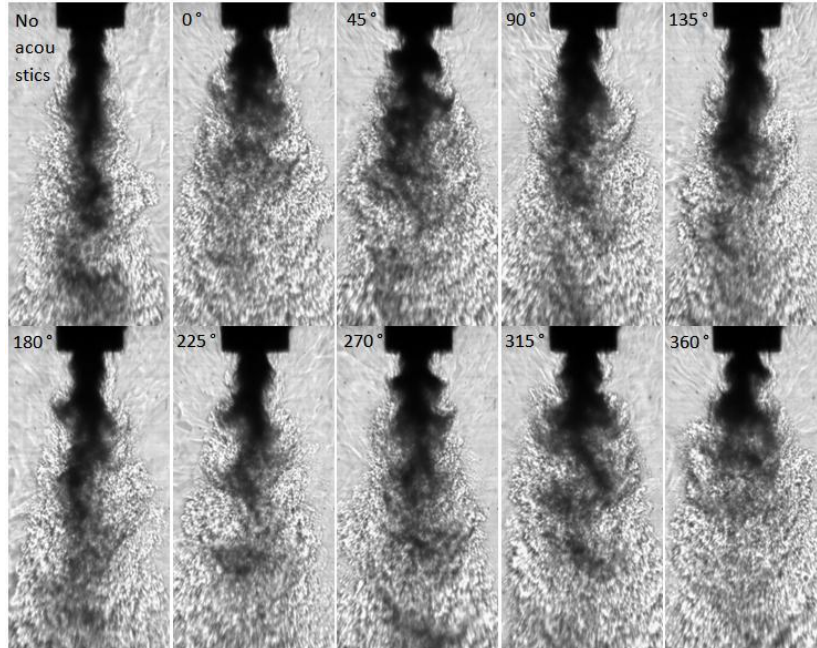


Figure 5.41. Coaxial jet images with the new injector at subcritical pressure ($P_{\text{chamber}} = 1.48 \text{ MPa}$, $J = 18$).

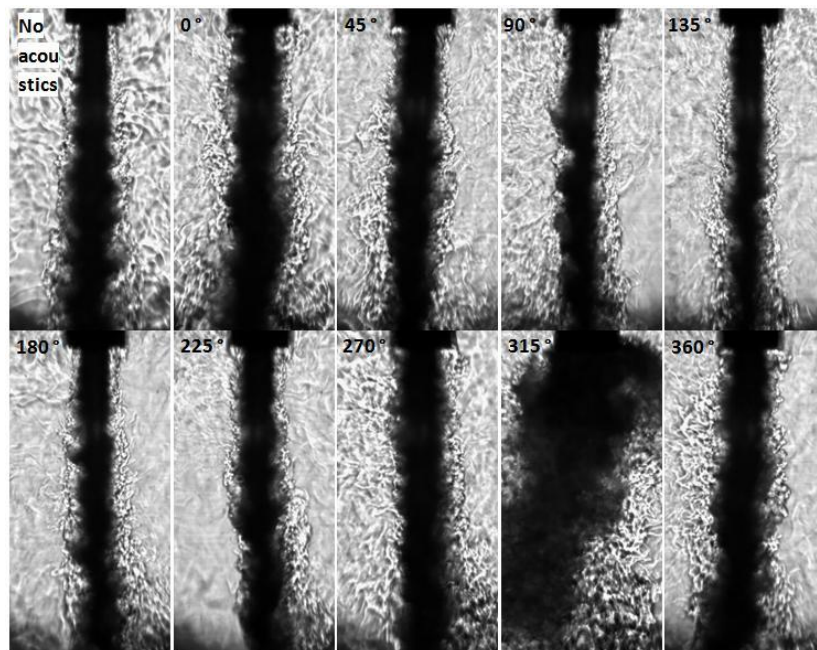


Figure 5.42. Coaxial jet images with the new injector at nearcritical pressure ($P_{\text{chamber}} = 3.56 \text{ MPa}$, $J = 0.50$).

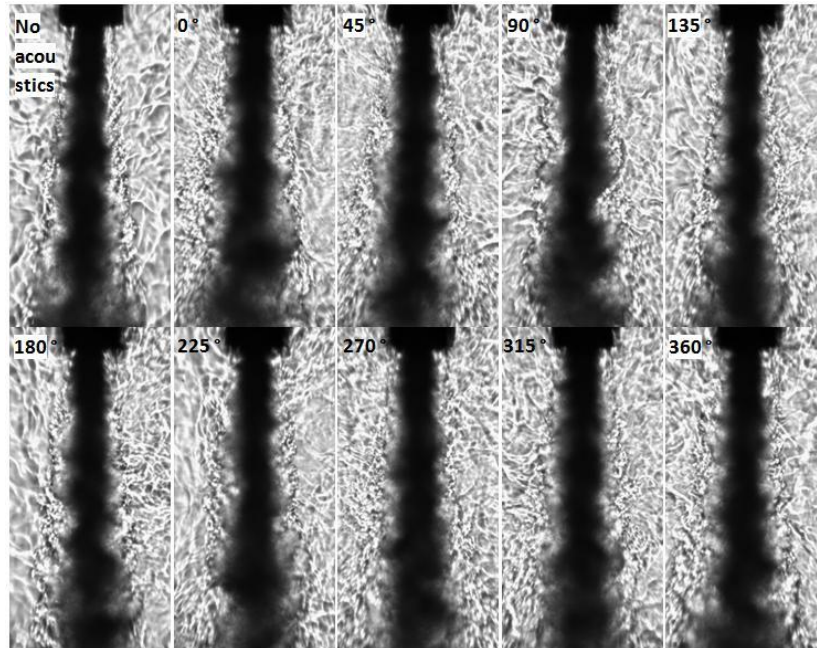


Figure 5.43. Coaxial jet images with the new injector at nearcritical pressure ($P_{\text{chamber}} = 3.58 \text{ MPa}$, $J = 2.2$).

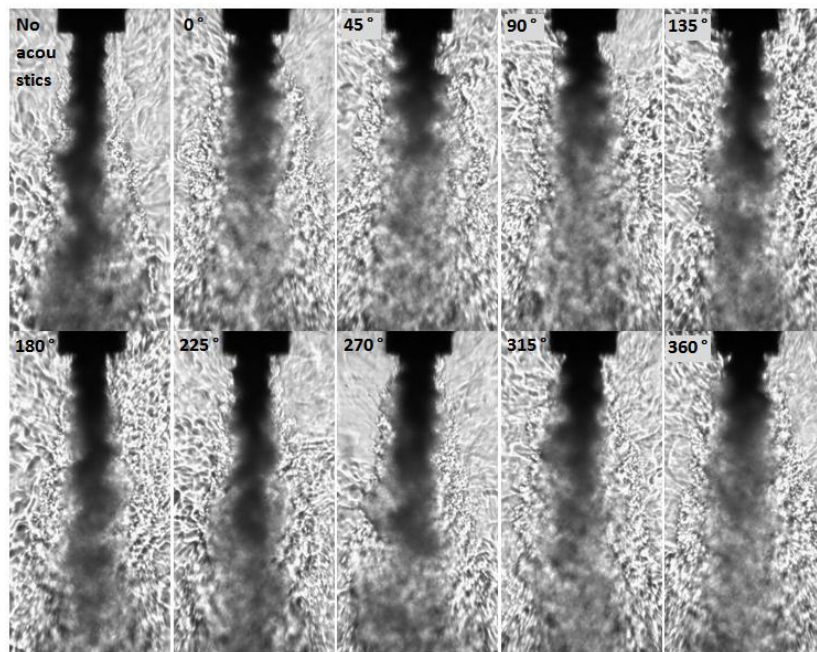


Figure 5.44. Coaxial jet images with the new injector at nearcritical pressure ($P_{\text{chamber}} = 3.58 \text{ MPa}$, $J = 9.4$).

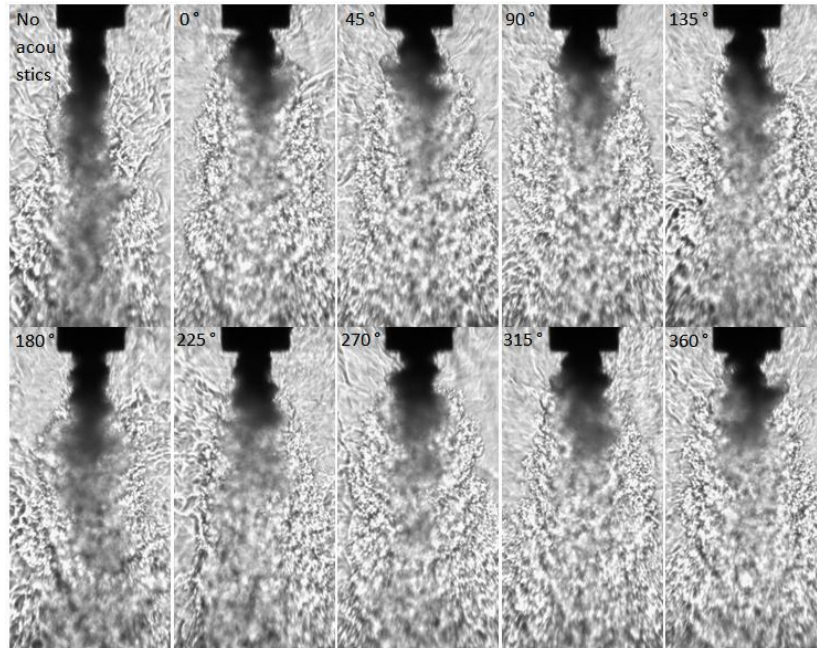


Figure 5.45. Coaxial jet images with the new injector at nearcritical pressure ($P_{\text{chamber}} = 3.56 \text{ MPa}$, $J = 19$).

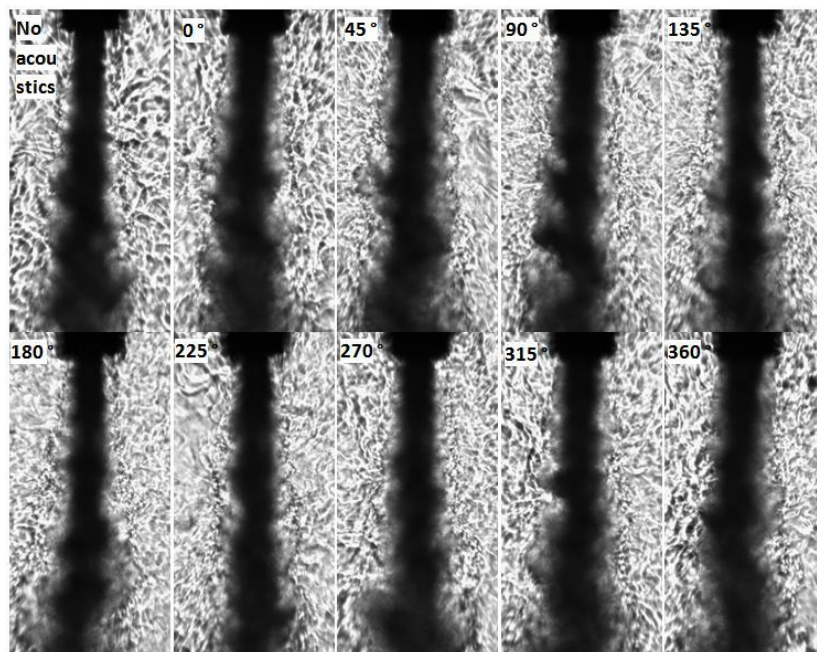


Figure 5.46. Coaxial jet images with the new injector at supercritical pressure ($P_{\text{chamber}} = 4.95 \text{ MPa}$, $J = 2.6$).

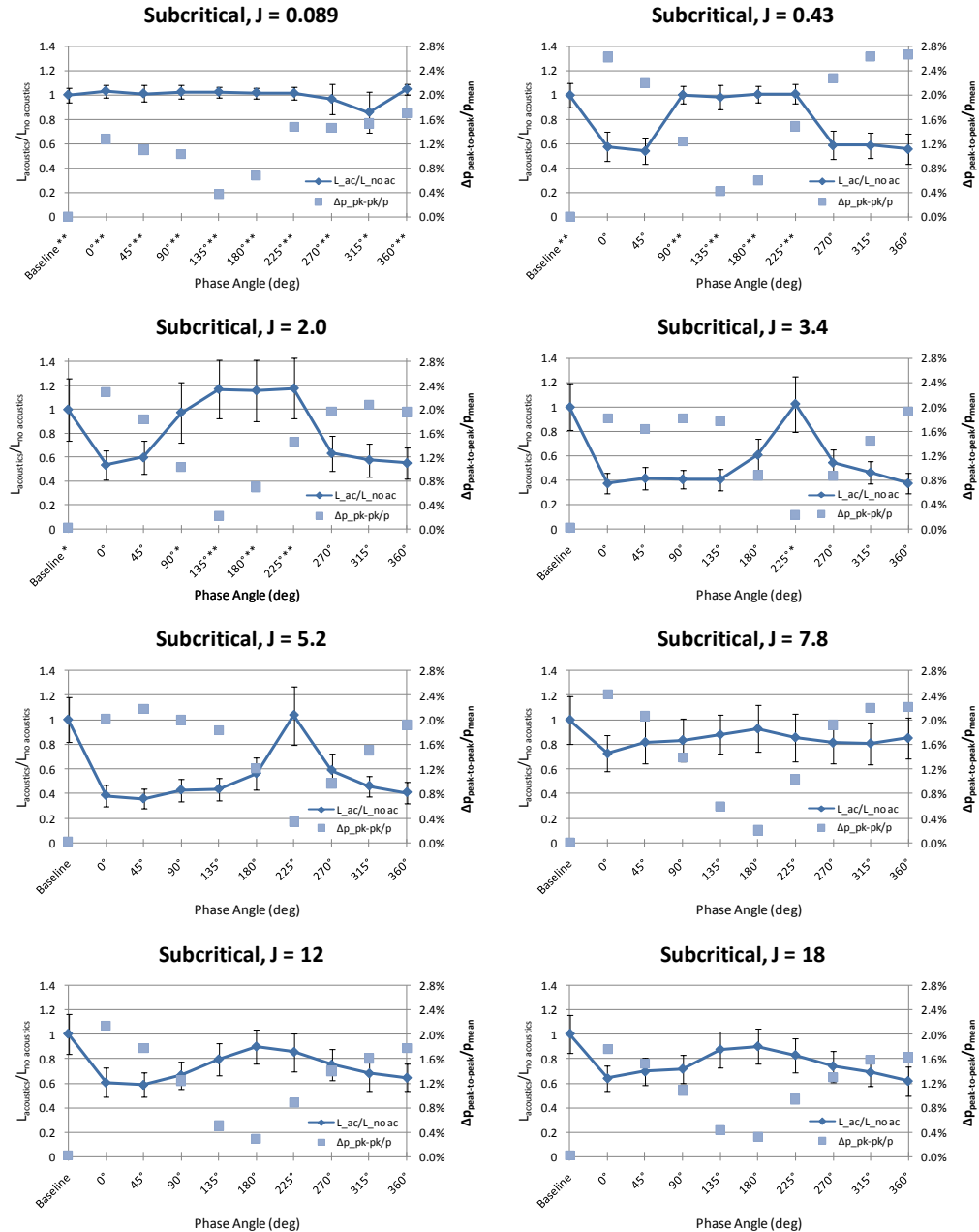


Figure 5.47. Dark core length with acoustics ($L_{\text{acoustics}}$) over dark core length without acoustics ($L_{\text{no acoustics}}$), shown in diamonds, versus phase angle between acoustic sources for subcritical pressures. The the peak-to-peak pressure perturbation as a percentage of the mean chamber pressure ($\Delta p_{\text{peak-to-peak}}/p_{\text{mean}}$), in squares, is also plotted. The cases which had their x coordinate marked with an asterisk (*) denote cases that had a dark core length that was longer than the field of view in more than 10% but less than 50% of the images. The ones marked with two asterisks (**) had dark cores larger than the examination window for at least half of the images. New injector geometry.

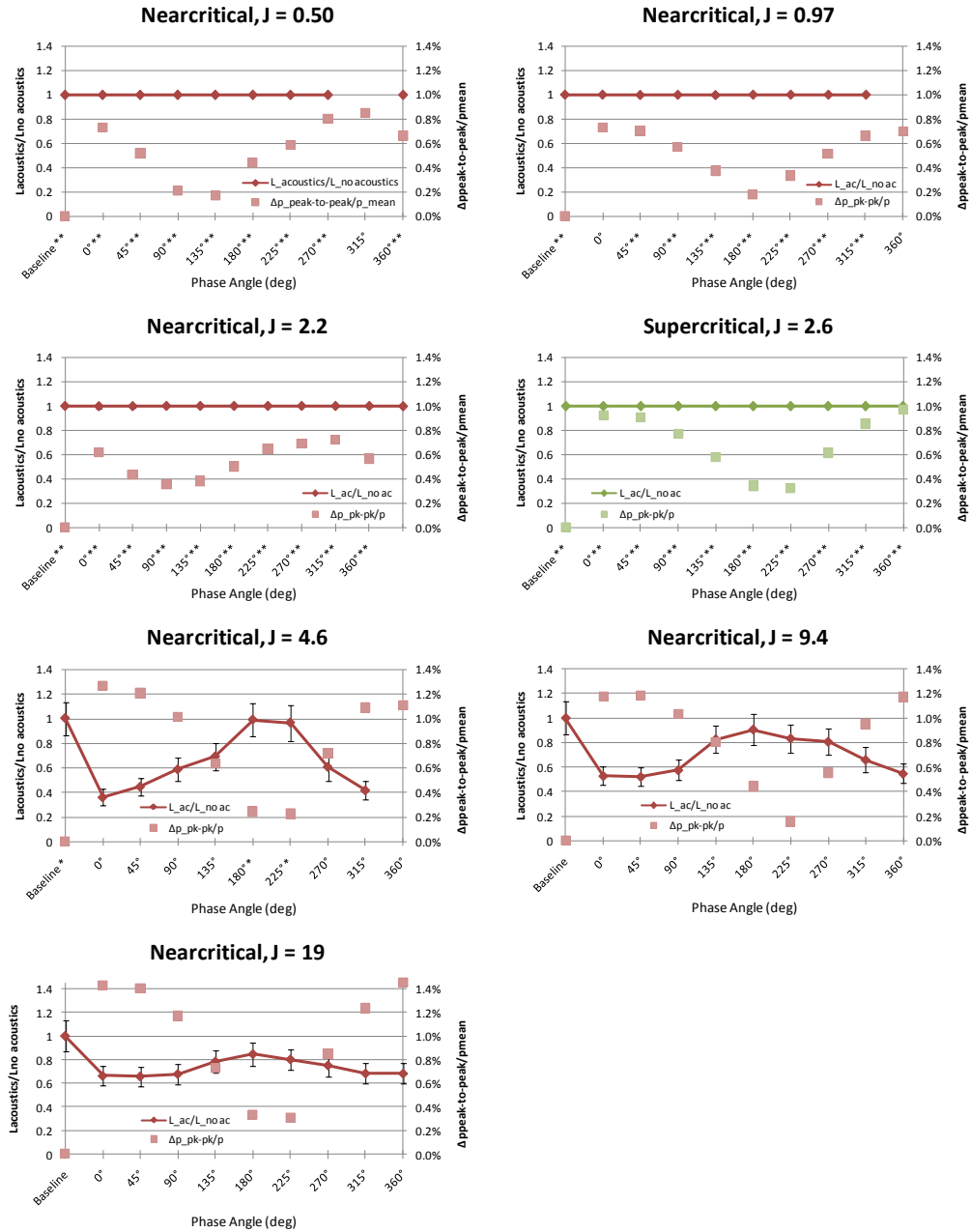


Figure 5.48. Dark core length with acoustics ($L_{acoustics}$) over dark core length without acoustics ($L_{no\ acoustics}$), shown in diamonds, versus phase angle between acoustic sources for pressures above the critical point. The the peak-to-peak pressure perturbation as a percentage of the mean chamber pressure ($\Delta p_{peak-to-peak}/p_{mean}$), in squares, is also plotted. See caption of Figure 5.47 for further details. New injector geometry.

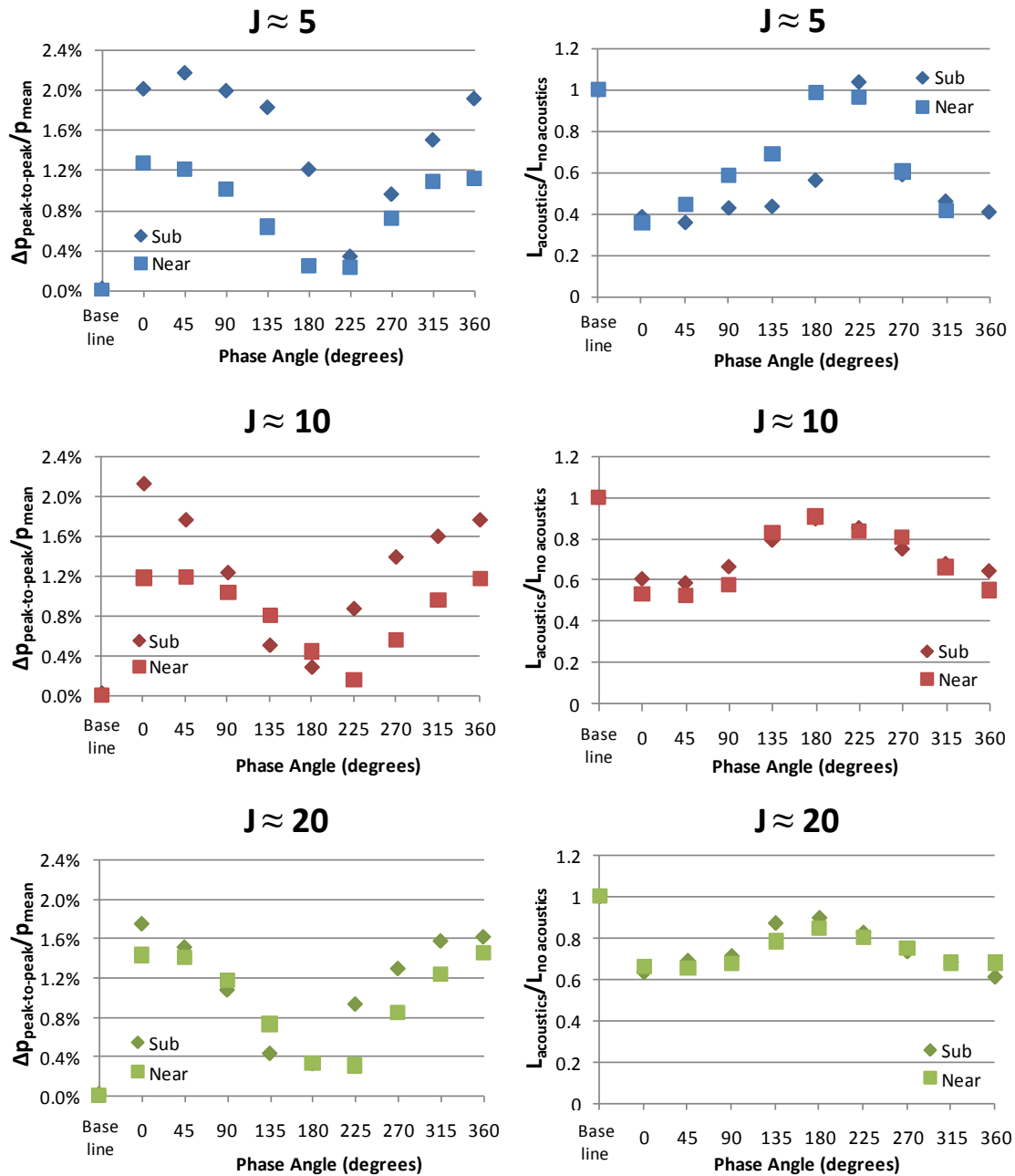


Figure 5.49. Peak-to-peak pressure perturbation ($\Delta p_{\text{peak-to-peak}}$) as a percentage of the mean chamber pressure (p_{mean}) and dark core length with acoustics ($L_{\text{acoustics}}$) over dark core length without acoustics ($L_{\text{no acoustics}}$) versus phase angle between acoustic sources for sub, near and supercritical pressures at $J \approx 5, 10$ and 20 for the new injector geometry.

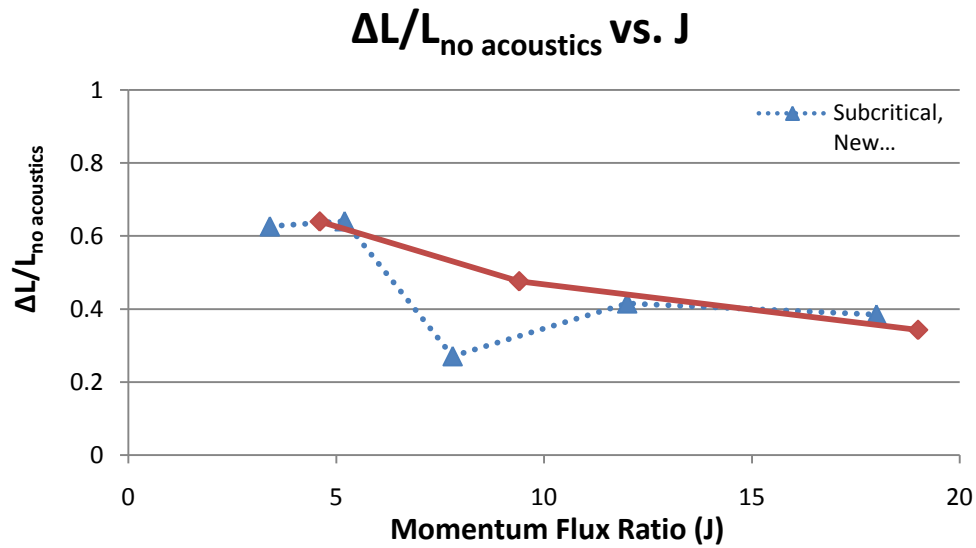


Figure 5.50. Maximum dark core length reduction between dark core length without acoustics and dark core length with acoustics for all phase angles $(L_{no\ acoustics} - L_{acoustics})_{MAX}$ for a given case divided by the dark core length without acoustics $(L_{no\ acoustics})$ as a function of J for moderate and higher momentum flux ratio cases obtained with the new injector.

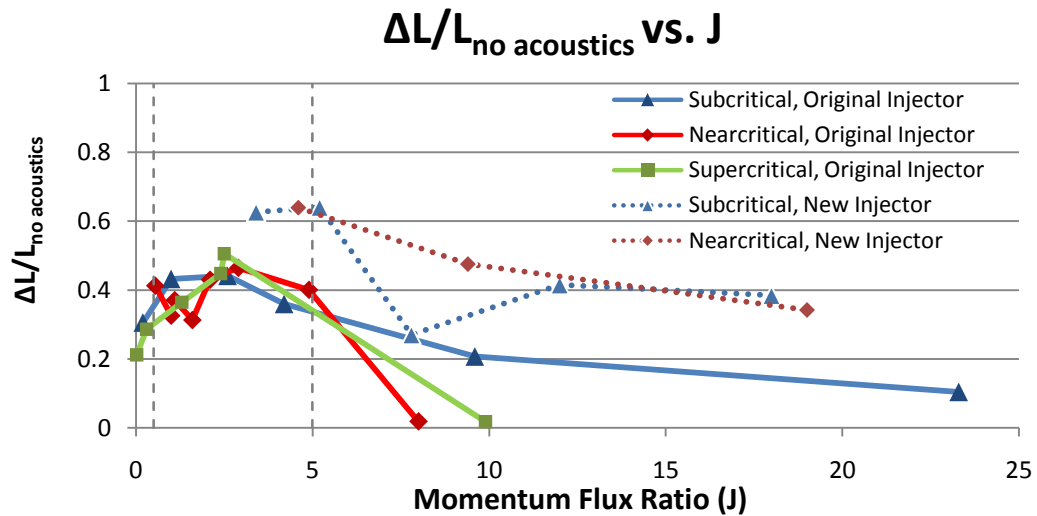


Figure 5.51. Comparison of the maximum dark core length reduction as a function of momentum flux ratio between the original injector geometry and the new injector geometry.

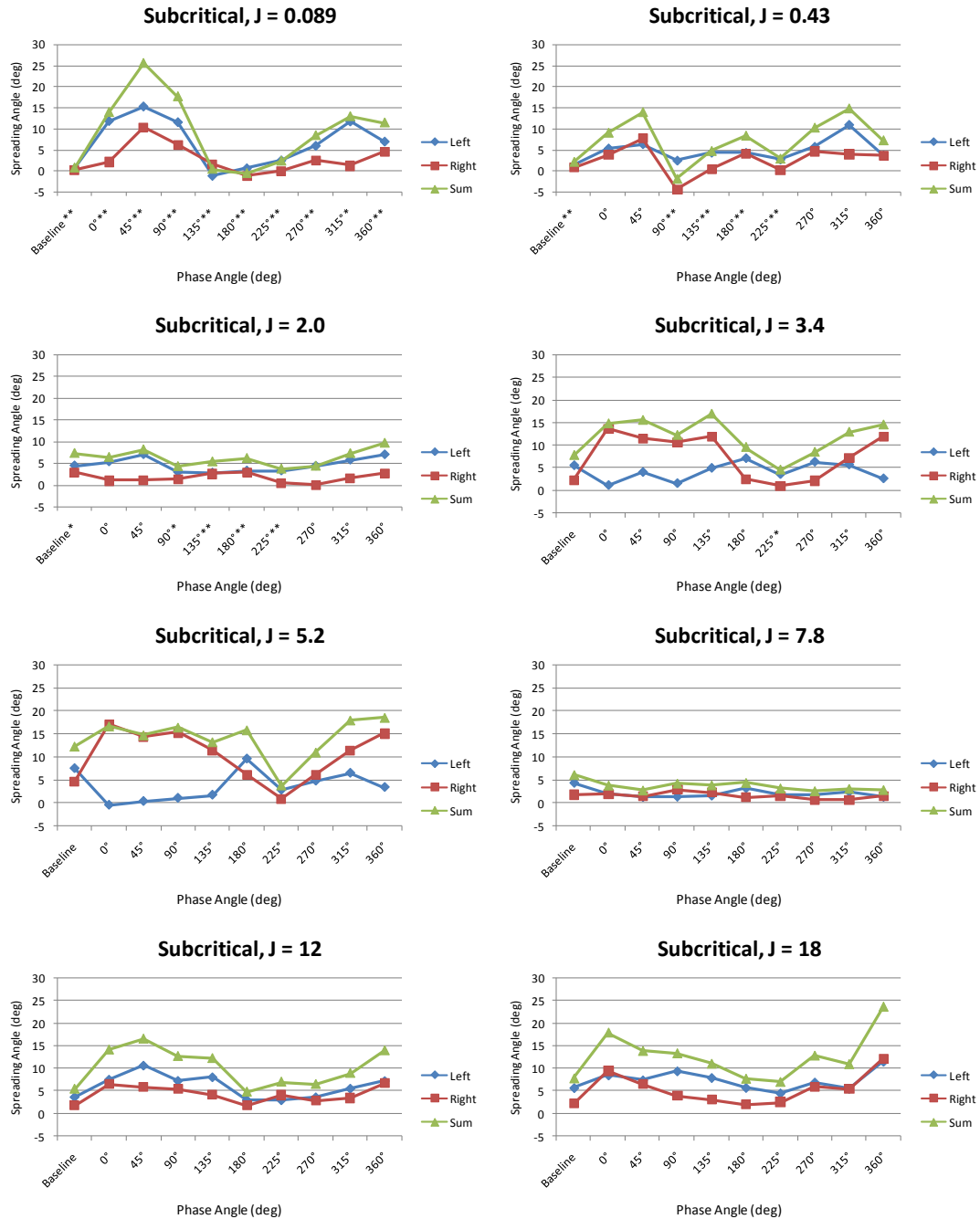


Figure 5.52. Maximum spread angles as a function of acoustic phase angle for different J values at subcritical pressures for the new injector geometry. The cases which had their x coordinate marked with an asterisk (*) denote cases that had a dark core length that was longer than the field of view in more than 10% but less than 50% of the images. The ones marked with two asterisks (**) had dark cores larger than the examination window for at least half of the images.

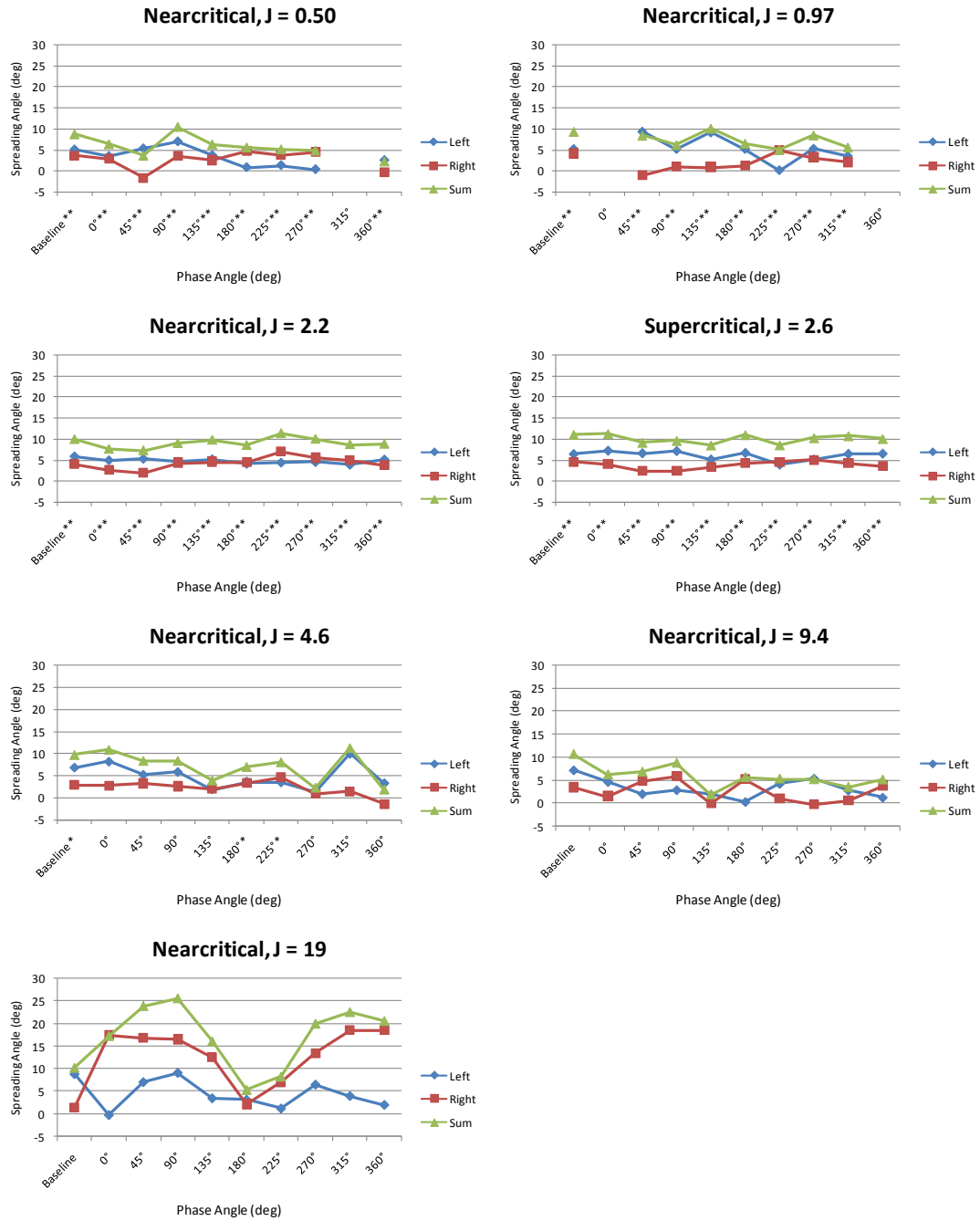


Figure 5.53. Maximum spread angles as a function of acoustic phase angle for different J values at near and supercritical pressures for the new injector geometry. See caption of Figure 5.52 for further details.

CHAPTER 6

Conclusions and Future Work

With the motivation being an improved understanding of fundamental acoustic coupling with condensed-phase combustion and other multiphase transport processes relevant to Liquid Rocket Engines, the present dissertation has described experimental studies on relevant phenomena in both droplet combustion and in coaxial, cryogenic jets. Both sets of experiments have elucidated important phenomenological features of this coupling.

6.1 Acoustically Coupled Droplet Combustion

The present experiments quantified changes that can occur in mean burning rate constants and flame structures associated with a single burning fuel droplet during acoustic excitation for several different fuels and for a range of excitation conditions. The effects of the acoustic excitation with the droplet placed in the vicinity of a pressure node and a pressure antinode have confirmed noticeable increases in burning rates for different alternative fuels. Effective acoustic accelerations, estimated to be on the order of $g_a \approx 2$ m/s^2 or less, were observed to have an effect on flame deformation and droplet burning rates. Despite the fact that natural convection is predominant in a normal gravity environment, these acoustic excitation levels had a noticeable effect on the combustion behavior of the droplet. For instance, at sufficiently high acoustic intensities, strong flame

deflection and distortion were routinely observed for burning droplets away from the pressure node or pressure antinode. Thus, the current configuration provides a useful setup for a systematic testing of the response of different fuels during combustion to an acoustically resonant environment. Increases in burning rate, changes in ignition and extinction phenomena and altered flame response can be quantified and were explored for different condensed phase fuels.

During acoustic excitation of droplets situated in the vicinity of a pressure node or antinode, flame orientation was consistent with the sign of an acoustic radiation force acting on the burning system, per the theory proposed by Tanabe, et al (11; 12). This type of acoustic excitation created conditions where the flame deflection switched, depending on the relative location of the droplet. It is noted that later droplet experiments by Teshome et al. (66) in our group, in which two speakers at either end of the waveguide were incorporated, a more symmetric acoustic field was created, and hence somewhat greater consistency with the theory of Tanabe was observed. Yet, in the present experiments, increases in burning rates were observed as the droplet was moved further from the pressure node or antinode for high amplitude acoustic excitation, consistent with the theory. Moreover, the degree of increase in droplet burning rate was slightly different for different fuels, in some cases as high as 20% above the unforced burning rate. With respect to the preliminary estimates of extinction strain rates, it appeared that the Fischer-Tropsch and aviation fuels, JP-8 and Jet A, tended to have lower extinction strain rates, of the order 300 s^{-1} , than did the alcohol fuels (ethanol and methanol, of the order 400 s^{-1}).

It is important to note, however, that for some conditions, the differences were within the uncertainty of the rough estimation of strain rate. Further studies of extinction phenomena have been ongoing, examined by Sophonias Teshome at the Energy and Propulsion Research Laboratory at UCLA. His findings were recently presented at the 61st Annual Meeting of the APS Division of Fluid Dynamics in San Antonio, Texas (66).

6.2 Acoustic Driving of Coaxial Jets

6.2.1 Summary and Conclusions

This present study complemented previous work done at AFRL on shear coaxial jet spreading angles and dark core length measurements from subcritical to supercritical pressures. With a second acoustic source to generate a variable phase acoustic field, the present study on coaxial jet behavior spanned a range of outer to inner jet momentum flux ratios from 0.019 to 23, obtaining results for at least 6 different J values at each pressure condition. Acoustic forcing at 3 kHz was utilized to maximize the pressure fluctuations within the chamber, reaching maximum values between 1 to 4% of the mean chamber pressure. The coaxial jet was exposed to pressure node (velocity antinode) conditions, where pressure perturbations are small and velocity perturbations large; to pressure antinode (velocity node) conditions, where pressure fluctuations are large and velocity fluctuations are small; and other acoustic conditions in between by carefully varying the phase angle between the two acoustic sources.

The inner jet dark core length analysis showed reduction of dark core length with acoustic excitation in the $1 < J < 5$ range for all pressure regimes and up to 10 for the subcritical regime. The effect of acoustics at lower or higher momentum flux ratios did not have significant effects on the behavior of the dark core length. This observation was supported by analyzing the behavior of the inner jet spreading angle for all conditions. Also, the single phase gas-gas coaxial jet experiments found that the outer jet spreading angle remains constant for $J > 0.1$, in agreement with previous results showing essentially a constant angle for liquid-gas subcritical conditions, and a wide variety of supercritical conditions.

Also, a new coaxial injector design was tested, providing evidence that different geometries for coaxial injectors of similar size could have an impact on the dynamics of a coaxial jet. The new injector data extended the range at which acoustics had a noticeable effect on the coaxial flow for momentum flux ratios as low as 0.1 and up to 10. The qualitative enhancement in mixing and atomization of the inner jet dark core with the surrounding outer jet and chamber obtained with the new injector was evident. In contrast, testing at nearcritical and supercritical pressures yielded very little or no response of the jet to acoustic excitation; however, it is believed that the relative acoustic forcing could be increased in future test to reveal similar effects in the near and supercritical regime as those observed in the subcritical pressure tests.

A quantitative analysis of the data for the new injector showed that the longest dark cores with acoustic excitation were observed at or near the pressure antinode location both at subcritical and supercritical conditions. The location of the pressure

antinode varied between 135° to 225° phase angle due to small changes in the excitation frequency and boundary conditions. In addition, the highest reduction in dark core length for the tests with the new coaxial injector geometry took place at moderate J values which supports similar evidence obtained with the original injector. The results for the new injector also show that for a given outer to inner jet momentum flux ratio, the normalized values of the dark core length between subcritical and nearcritical cases agree remarkably well.

A noticeable difference between the original injector results and the new injector results is the effect of the phase angle on the dark core. In general, phase angle had a weak effect on most results obtained with the original injector geometry. On those cases that the effect was clear, being at a pressure node shortened the dark core length. In contrast, the results with the new injector showed a clear phase angle effect with the longest dark cores occurring at the pressure node. However, when considering the maximum reduction of the dark core length between the baseline condition and a condition with the acoustics on, regardless of phase angle, the results of the new coaxial injector geometry agreed well with the original injector data. Both the original and the new injector showed the same large effect on the dark core at moderate J values and as the momentum flux ratio is increased the maximum reduction decreases. All these results were found to be independent of the relative acoustic pressure the coaxial jets were exposed to.

The fact that the relative acoustic pressure did not have an effect on the behavior of the dark core length points to the possibility of having a limit cycle where only a small

perturbation, smaller than the amplitudes used in this study, is needed to achieve the same large reduction outcome of the dark core. If the previous proposition is true, even small pressure perturbations will have a large impact on the stability behavior of LRE injectors and other applications of coaxial flows. Also, by analyzing coaxial injector with a very large and a very small inner jet post thickness we have covered both ends of the spectrum in coaxial jet flows. One injector with a very large recirculation zone and another with a very thin wall with no recirculation expected.

As a complement of the previous finding, a discussion on stability of liquid jets and coaxial flows was presented, and using local/global and convective/absolute instability concepts the response of the two coaxial jet geometries to acoustic excitation was roughly assessed. It is very possible that there exists a range of values of the momentum flux ratio or a similar parameter for which the coaxial jet behaves as a convectively unstable flow, given the response of the coaxial jet to acoustic forcing outlined above.

Given the discrepancy in the dark core length behavior at the pressure node and antinodes and the qualitative differences observed between the two injectors, it is possible that a different non-dimensional number not used in this study exists which can reduce the data from the original and new injector in a more ordered fashion. However, from an overall perspective, the momentum flux ratio, J , has proven to be a very good parameter to systematically describe the relative change in dark core lengths and spreading angles for acoustically excited coaxial injector flows.

6.2.2 Future Work

Testing at the Supercritical Cryogenic Experimental Cell EC 4 at AFRL in Edwards, AFB will continue with the new coaxial injector design presented in this dissertation. Other parameters and regimes such as outer jet spreading angles and single phase subcritical (gas-gas) conditions could also be explored. A quantitative investigation of the instability of the coaxial jet with the current geometry is recommended to identify parameters that might lead to weaker or stronger response of the flow to acoustic excitation

Preliminary work has been started to study the effects of the recess length between the inner jet and the outer jet posts. All the cases presented in this thesis with both the old and new injector had a recess length of one half the inner diameter of the inner jet post ($1/2 D_{ii}$ as shown in Figure 1.4). A systematic study will be performed to look at the effect of this distance in the coaxial jet dynamics. Data will be gathered when there is no recess and both posts are “flushed”, and potentially when there is negative recess, where the inner jet post ends after the outer jet post does.

CFD simulations that model exact or similar conditions and geometries have been available from other groups closely related to our experimental research. An effort to develop a computer model readily available to the group at AFRL in Edwards, AFB has been underway. If fully implemented, this project could evolve into a very successful experimental design tool for new injectors and flow models and provide supporting evidence to experiments performed at the Supercritical Cryogenic Facility.

A method to obtain instantaneous velocity measurements at the exit of the injector would aid in understanding the flow behavior where the two coaxial streams meet and the effect of the acoustics on the trajectory of fluid particles. However, given the current configuration of the facility, this diagnostics method might be very difficult to implement.

Using a different fluid, such as helium, for either the inner or outer jet would increase the range of conditions that can be tested in EC 4 and provide experimental cold flow data with different species at the unique conditions this facility offers such as supercritical pressures and variable phase transversal acoustic excitation to be available for the research community.

Finally, a plan to construct a new supercritical chamber at AFRL in Edwards, AFB that will study reactive flows under the effects of acoustic excitation is in progress. It is currently at its preliminary stages and when it is finished it will have the capability to test many of the injector configurations that have been tested with the current, non-reactive facility. The versatility to test the behavior of a coaxial injector both in a non-reactive and a reactive environment will give the researcher the possibility to understand which acoustic effects are due to the fluid mechanics of the flow alone and which are enhanced by the energy release and combustion processes of the propellants in a LRE.

APPENDIX

The appendix consists of three sections. Appendix A presents a detailed schematic of the flow systems used in the experiments performed at the Supercritical Cryogenic Facility EC 4 at AFRL in Edwards AFB, CA. It shows the version that was used for the tests with the original injector. Figure 4.2 in the Experimental Setup chapter shows the upgrades performed when the new injector was installed. Appendix B lists the standard operating procedures that were followed in the EC 4 facility for every test. Appendix C provides a summary of the coaxial jet experimental data presented in this dissertation.

APPENDIX A

Detailed Schematic of Coaxial Jet Experimental Facility

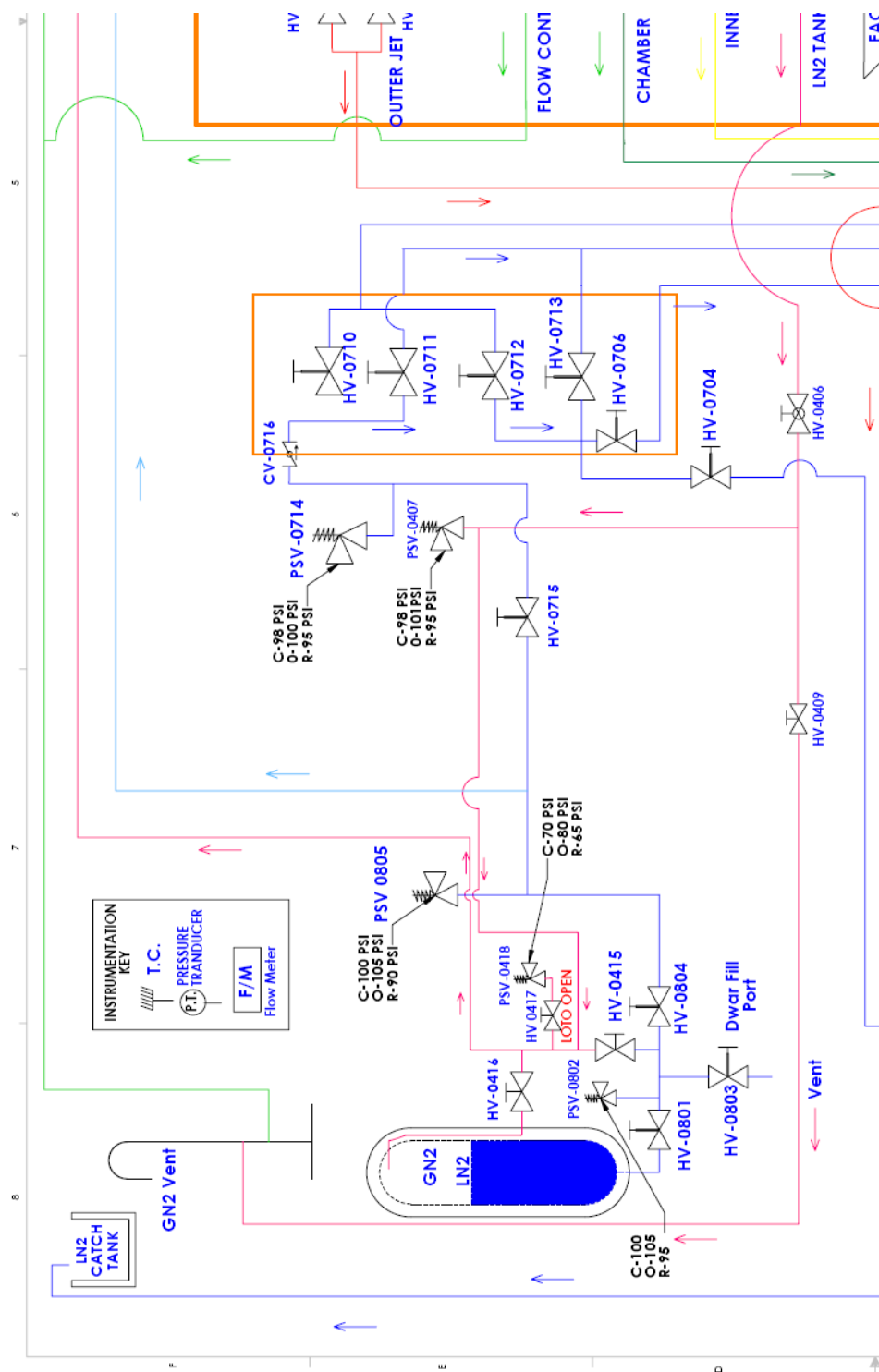


Figure A.2. Expanded view of the upper left section of the flow path schematic in Figure A.1.

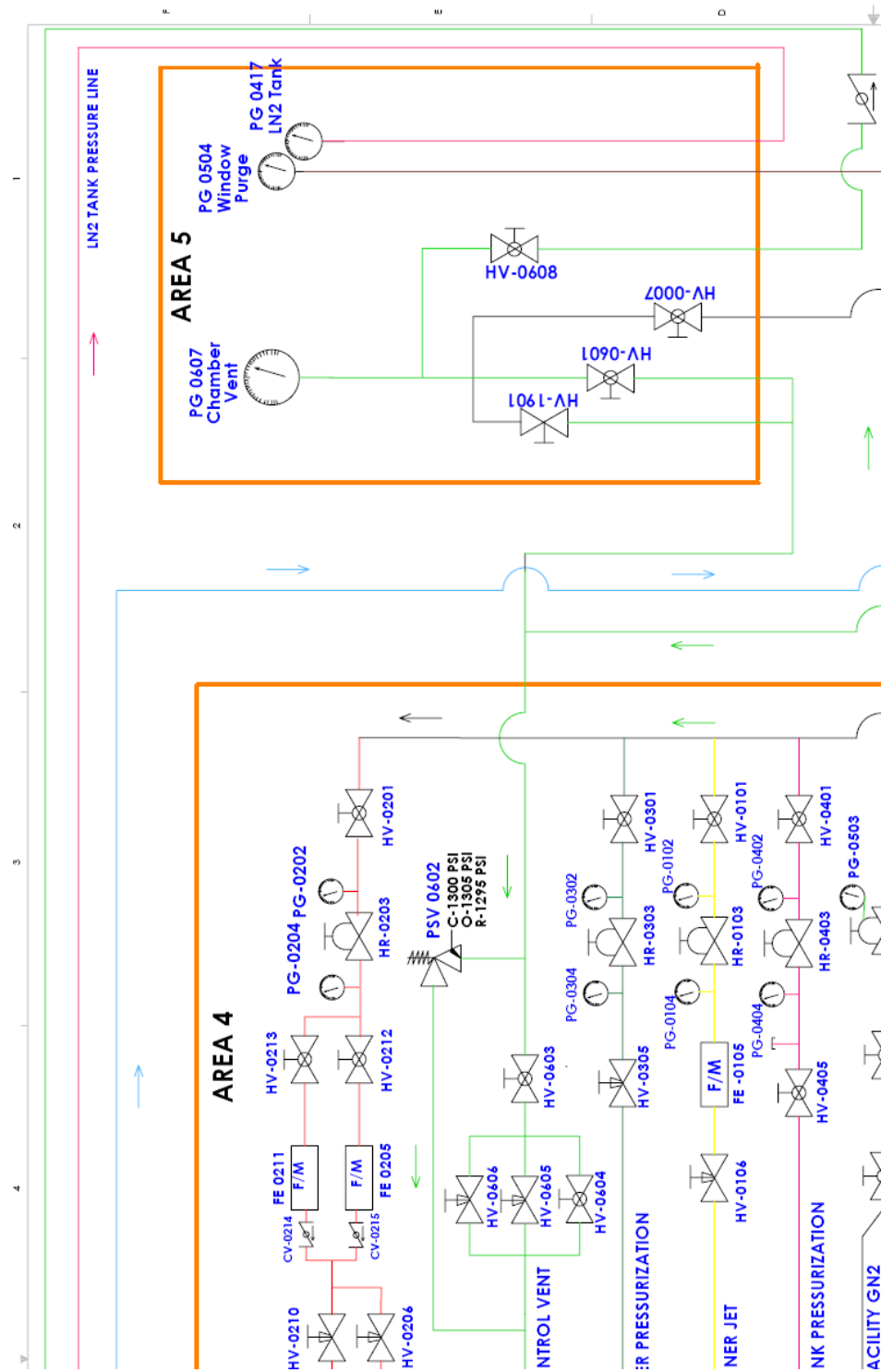


Figure A.3. Expanded view of the upper right section of the flow path schematic in Figure A.1.

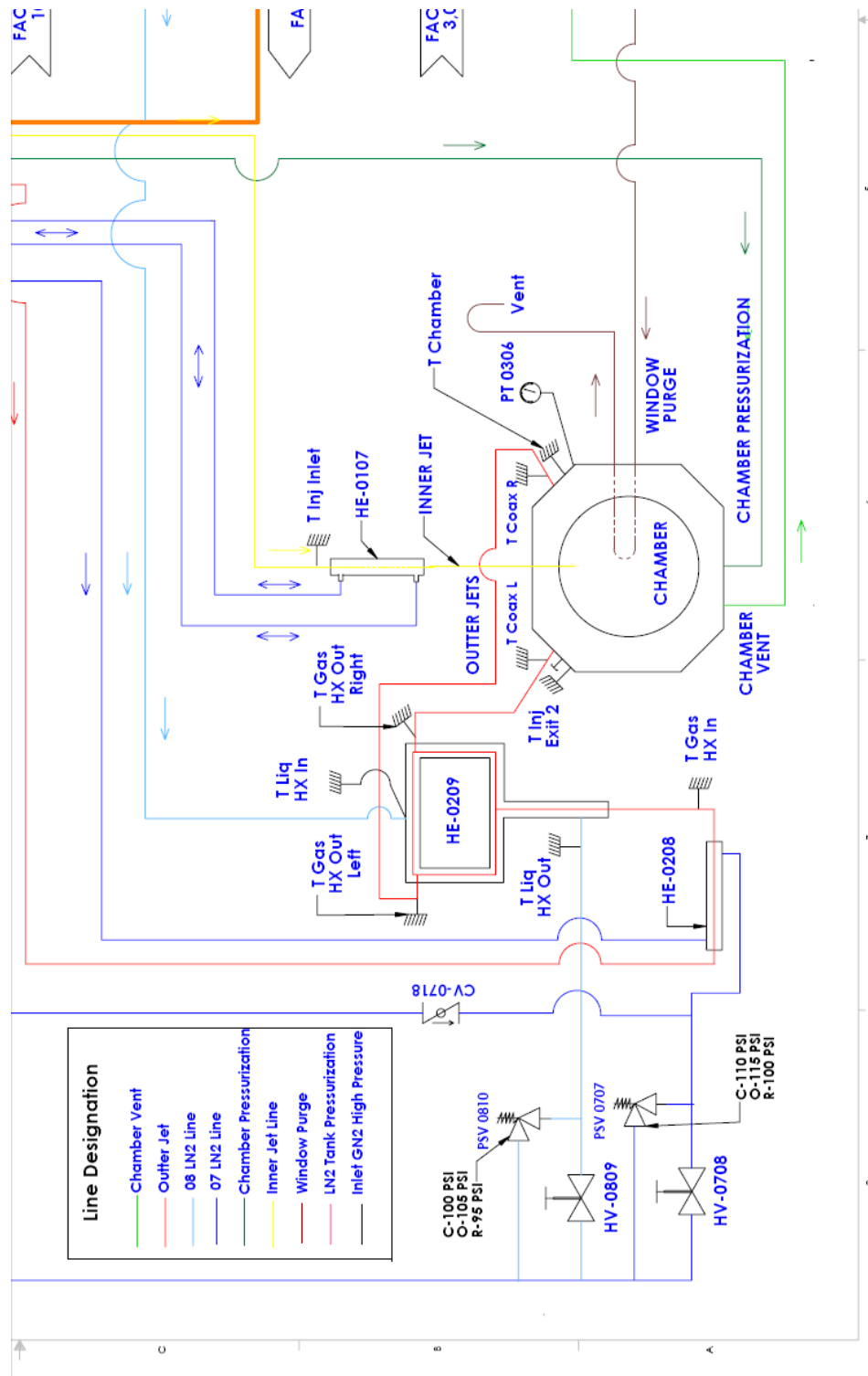


Figure A.4. Expanded view of the lower left section of the flow path schematic in Figure A.1.

Figure A.5. Expanded view of the lower right section of the flow path schematic in Figure A.1.

APPENDIX B

Coaxial Jet Experimental Procedures

**BUILDING 8451
EXPERIMENTAL CELL, EC-4
AIR FORCE RESEARCH LABORATORY
EDWARDS AFB, CA**

**PROCEDURE: SOP-RZSA-EC4-0001
REVISION: 2.4
DATE REVISED: September 4, 2008
No. OF PAGES: 23**

**BUILDING 8451
EXPERIMENTAL CELL, EC-4
OPERATIONS**

PROCEDURE TITLE

**SUPERCRITICAL COLD FLOW
OPERATIONS using LN2/GN2**

PREPARED BY:

Ivett Leyva, Principal Investigator, PRSA

DATE

REVIEWED BY:

Doug Talley, Program Manager, PRSA

DATE

COORDINATED BY:

Randy Harvey, Red Crew Leader, ERC

DATE

Tim Auyeung, System Safety Engineer, Det 7/SES

DATE

APPROVED BY:

David Campbell, Program Manager, ERC

DATE

Ingrid Wysong, Branch Chief, PRSA

DATE

Debra Fuller, Branch Chief, Det 7/SE

DATE

Revision	Notes	Prepared By
0	- Initial procedure written	D. Davis, 24 June 2004
1	- Added more details on the operation of the facility - Deleted Dewar steps and LN2 mass flow meter	I. Leyva, 12 May 2006
2	- Modified procedures to account for a different arrangement of hand valves	J. Rodriguez, 30 July 2007
2.1	- Slight modifications to order of instructions in general procedure	J. Rodriguez, 31 July 2007
2.2	- Minor changes in preparation steps before pressurization	J. Rodriguez, 22 August 2007
2.3	- Slight modifications to instructions - Added explanatory notes to some steps	J. Rodriguez, 10 October 2007
2.4	- Modified procedures to account for rearrangement of flow elements	J. Rodriguez, 4 September 2008

PERSONNEL

EXPERIMENTAL CELL EC-4

DATE

AEROPHYSICS BRANCH, BLDG 8451

WORK

AUTHORIZATION#

The following personnel are designated as test team members, and are charted to perform their assignment as follows:

Test Conductor (TC) – Responsible for the timely performance of the test as written and for overall facility and test safety. This includes coordinating and directing the activities of the Red Crew and other test support teams. TC is responsible for coordinating all pretest activities and outside support required, including (but not limited to) security, fire, medical, and safety. TC is responsible for initialing completion on each step of the master test procedure and ensuring all test goals are met and all critical data is acquired. Has authority to perform real-time redlines on test procedures as required to ensure test requirements and goals are met. All safety-related redlines will be coordinated and approved by AFRL and/or ERC Safety.

Name_____ Signature_____

Red Crew Leader (RCL) – Responsible for directing the activities of Red Crew members. Reports directly to the TC and ensures all Red Crew tasks are completed. Responsible for ensuring all RCM's have all required certifications and training. Responsible for ensuring all required equipment is available, accessible, and serviceable.

Name_____ Signature_____

Other Test Team Members – Responsible for performing ancillary duties in support of test, support of anomaly resolution, and other necessary activities.

Name_____ Signature_____

Name_____ Signature_____

ALL TEST TEAM MEMBERS – Responsible for the safe performance of the test. Have read and understood all portions of the test procedure. Any Test Team Member can declare an emergency or unsafe condition.

_____1.

ABBREVIATIONS AND ACRYONMS

CPR	- Cardiopulmonary Resuscitation
CV	- Check Valve
EC	- Experimental Cell
ER	- Engineering Request
FE	- Flow Element
FLTR	- Filter
FLX	- Flexible Line
FOD	- Foreign Object Debris
GN2	- Gaseous Nitrogen
HE	- Heat Exchanger
He	- Helium
HR	- Hand Regulator
HV	- Hand Valve
LN2	- Liquid Nitrogen
N2	- Nitrogen
PC	- Chamber Pressure
PG	- Pressure Gauge
PI	- Principal Investigator
PM	- Program Manager
PPE	- Personal Protective Equipment
PSV	- Pressure Safety Valve
PT	- Pressure Transducer
QA	- Quality Assurance
RCL	- Red Crew Leader
RD	- Rupture Disk
SCF	- Supercritical Facility
SOCC	- Site Operations Control Center
SOP	- Standard Operating Procedure
TC	- Test Conductor
TOP	- Test Operation Procedure

_____ 2.		TEST DESCRIPTION AND OBJECTIVES
_____ 2.1.		<p>PURPOSE</p> <p>This procedure performs a stand-alone operation of the EXPERIMENTAL CELL, EC-4. This procedure may be used in conjunction with other Test Operation Procedures (TOP) or Work Authorizations (WA) as required to support operations or checkouts.</p>
_____ 2.2.		<p>SCOPE</p> <p>This procedure will verify proper configuration before operation including purges and valve configuration and sequential steps to perform the Supercritical Cold Flow (SCF) Operation. Securing the SCF post operation and emergency shutdown are also included in the procedure.</p>
_____ 3.		DOCUMENTATION
		<p>The completion of each applicable event shall be verified by marking to the left of the item number by the TC. Deviations from these procedures will be coordinated with the Test Engineer, TC, RCL</p>
_____ 3.1.		<p>APPLICABLE DOCUMENTS</p> <p>AFRL/PR OI 91-202, Environmental, Safety, and Occupational Health (ESOH) Programs, 7 Aug 2000.</p> <p>Space & Missile Propulsion Division, Chemical Hygiene Plan (CHP), Bldg 8451.</p>
_____ 3.2.		REFERENCE DOCUMENTS: NONE
_____ 3.3.		<p>SPECIFICATIONS</p> <p>Nitrogen Purge Gas: Pressurizing agent, nitrogen, Grade B, Type I, Spec. Mil-P-27401.</p> <p>Water: Facility domestic water supply</p>
_____ 3.4.		<p>DRAWINGS</p> <p>EC4-001, EC-4 Supercritical Facility</p>

4.

4.1.

4.2.

4.3.

4.4.

TEST REQUIREMENTS AND RESTRICTIONS

TRAINING

The following training is required for personnel using these procedures:

CPR & First Aid

High Pressure

Noise

Initial HAZCOM

Cryogenics

Job Site HAZCOM

Lock-Out/Tag-Out

MAXIMUM PERSONNEL ALLOWED IN EC-4:

Five (5): Workers – (3) (RCL and TC),
Supervision – (1) (PI, PM, etc.),
Casual (Bio, Safety, QA, etc) – (1)

LIST OF EQUIPMENT

Vapor Detection Equipment: two (2) portable oxygen sensors (one for each worker in the cell).

Mechanics Tool Kit, Torque Wrench, Caliper, Digital Thermometer and Multimeter.

Ensure all tools associated with this experiment/test/operation are accounted for prior to initiating system/item test. Assure all trash, debris, and FOD is picked up from around the test stand.

METEOROLOGICAL LIMITATIONS/ RESTRICTIONS

A. No hazardous operations will be started when thunderstorms are within 25 nautical miles (28.75 miles) of AFRL unless the operation can meet the requirements for stopping the operation for lightning within 10 nautical miles. Operations in progress may be completed if it is safe to do so; however supervisors must assess individual operations to determine the appropriate action.

B. All hazardous operations will be stopped when thunderstorms are within 10 nautical miles (11.5 miles) of AFRL. The operation should be secured and personnel evacuated to Bldg 8451 and remain indoors.

C. All outside work must stop when thunderstorms are within 5 nautical miles (5.75 miles) of AFRL and all personnel must seek safety in Bldg 8451 until the lightning warning is cancelled.

_____ 5.	SAFETY REQUIREMENTS
_____ 5.1.	<p>TEST HAZARDS:</p> <p>Nitrogen gas (GN2) is used for pressurization of the chamber and production of the supercritical jet in the chamber. Nitrogen gas can cause asphyxiation hazards to personnel working in EC-4. Oxygen deficiency monitors will be used to warn personnel working in EC-4 of the hazard.</p> <p>Liquid nitrogen (LN2) is used for temperature conditioning of the supercritical jet in the chamber. This presents a cryogenic hazard to test crew working inside and outside EC-4. LN2 will also convert to GN2.</p> <p>The Acoustic test can produce hazardous noise levels (>120 dB). Personnel are required to wear ear muffs to reduce exposure.</p>
_____ 5.2.	<p>PERSONNEL PROTECTIVE CLOTHING REQUIREMENTS</p> <p>Test PPE: Lab coat or coveralls, safety goggles, safety shoes, and ear muffs (noise protection as required).</p> <p>Cryogenic PPE: Cryogenic gloves.</p>
_____ 5.3.	<p>TEST AREA ACCESS DURING OPERATIONS</p> <p>EC-4 GREEN: Normal test preparation activities. There are no pressure or chemical hazards in the test cell. The RCL will limit access to the affected operational area of interest.</p> <p>EC-4 AMBER: Hazardous chemicals in the test cell. No pressure or flows (static condition). RCL will monitor the Test Cell entrance, and prevent access to the cell. Personnel will not be allowed access to the test area unless cleared by the RCL and TC.</p> <p>EC-4 RED Hazardous test operations including propellant chill downs and purging operations. The TC will maintain access control to the area. Personnel will not be allowed access to EC-4 unless cleared by the TC.</p>

_____ 6.		EXPLOSIVE LIMITS: NONE
_____ 7.		EMERGENCY PROCEDURES In the event of a major nitrogen leak or other emergency that jeopardizes the safety of the operators or other personnel perform Section 20 emergency procedures at the end of this document.
_____ 8.		SPECIAL INSTRUCTIONS Red Crew Member shall notify Test Engineer of any leaks from the system. Any lines, which require maintenance or re-torquing, should be coordinated with Test Engineering to maintain SCF system cleanliness. Work must be authorized in order to break into clean and sealed systems.
_____ 9.		PRETEST PREPARATIONS
_____ 9.1.	ALL	DON Test PPE listed in step 5.2
_____ 9.2.	RCL	Verify portable oxygen sensors are operational and calibrated.
_____ 9.3.	RCL	Turn ON or Verify ON EC-4 Air Handler ventilation system.
_____ 9.4.	RCL	Turn OFF Air Handler.
_____ 9.5.	ALL	UNLOCK EC-4 outside door.
_____ 9.6.	ALL	NOTE any potential hazards in and outside EC-4
_____ 9.7.	ALL	Verify GREEN, AMBER, and RED lights are functional and return to GREEN.
_____ 9.8.	TC	If Acoustic Testing Verify Gain or Turn Gain on Amplifier to the ZERO position.
_____ 9.9.	TC	If Acoustic Testing, Turn ON Amplifier to allow warm up as per ER_____
_____ 9.10.	RCL	If Acoustic Testing, POST "HEARING PROTECTION REQUIRED" signs on the outside of the doors to EC-4, Room 19, foam door and adjacent hallway.
_____ 9.11.	TC	Turn on Data Acquisition System and System Electronics.
_____ 9.12.	RCL	Position "DO NOT ENTER" sign on exterior door near LN2 catch tank.
_____ 9.13.	RCL	Position "DO NOT ENTER" signs in rooms 39 and 41.
_____ 9.14.	RCL	Place chain in front of entrance to horseshoe.

_____10.		INITIAL SETUP
_____10.1.	RCL	OPEN / Verify OPEN HV-0001 (EC-3, EC-4 Primary Facility Isolation Valve) - Area 3
_____10.2.	RCL	CLOSE / Verify CLOSED HV-0003 (EC-4 Secondary Facility Isolation Valve) - Area 3
_____10.3.	RCL	CLOSE / Verify CLOSED HV-0008 (EC-4 Low Pressure Facility Isolation Valve) - Area 3
_____10.4.	RCL	CLOSE / Verify CLOSED HV-0009 (EC-3 Secondary Facility Isolation Valve) - Area 3
_____10.5.	RCL	CLOSE / Verify CLOSED HV-0406 (Tank GN2 Pressurization Isolation Valve) - Area 2
_____10.6.	RCL	CLOSE / Verify CLOSED HV-0409 (Dewar Pressurization Vent Isolation Valve) - Area 2
_____10.7.	RCL	OPEN / Verify OPEN HV-0715 (Direct LN2 Supply Valve) - Area 2
_____10.8.	RCL	CLOSE / Verify CLOSED HV-0801 (Tank LN2 Isolation Valve) – Area1
_____10.9.	RCL	OPEN / Verify OPEN HV-0803 (Local Dewar Fill Isolation Valve) – Area1
_____10.10.	RCL	CLOSE / Verify CLOSED HV-0804 (Tank-Dewar Separation Valve) – Area 1
_____10.11.	RCL	CLOSE / Verify CLOSED HV-0415 (Vacuum Jacketed Line Purge Valve) – Area 1 NOTE: In case the LN₂ line needs to be broken, moisture could get in. This valve permits purging of the line after it is reconnected
_____10.12.	RCL	CLOSE / Verify CLOSED HV-0416 (Tank GN2 Pressurization Valve) – Area 1
_____10.13.	RCL	CLOSE / Verify CLOSED HV-1901 (He System Isolation Valve) - Area 5
_____10.14.	RCL	CLOSE / Verify CLOSED HV-0601 (PC Vent PG Isolation Valve) - Area 5
_____10.15.	RCL	OPEN / Verify OPEN HV-0608 (Gauge Vent Valve) - Area 5
_____10.16.	RCL	CLOSE / Verify CLOSED HV-0007 (Upstream Regulator Pressure Valve) - Area 5
_____10.17.	RCL	OPEN / Verify OPEN HV-0603 (Chamber Pressure Build Valve) - Area 4

_____10.18.	RCL	OPEN / Verify OPEN HV-0604 (Primary Chamber Pressure Vent Valve) - Area 4
_____10.19.	RCL	CLOSE / Verify CLOSED HV-0605 (Secondary Chamber Pressure Vent Valve) - Area 4
_____10.20.	RCL	CLOSE / Verify CLOSED HV-0606 (Tertiary Chamber Pressure Vent Valve) - Area 4
_____10.21.	RCL	CLOSE / Verify CLOSED HV-0708 (Heat Exchanger LN2 Throttle Vent Valve) – ceiling between Area 4 & Area 5
_____10.22.	RCL	CLOSE / Verify CLOSED HV-0809 (Coax Heat Exchanger LN2 Throttle Vent Valve) – ceiling between Area 4 & Area 5
_____10.23.	RCL	OPEN / Verify OPEN HV-0704 (Heat Exchanger LN2 Bypass Valve) – Area 3
_____10.24.	RCL	CLOSE / Verify CLOSED HV-0706 (Heat Exchanger Flow Valve) – Area 3
_____10.25.	RCL	CLOSE / Verify CLOSED HV-0710 (Primary Co-Flow Valve) – Area 4
_____10.26.	RCL	OPEN / Verify OPEN HV-0711 (Primary Counter Flow Valve) – Area 4
_____10.27.	RCL	OPEN / Verify OPEN HV-0712 (Secondary Counter Flow Valve) – Area 4
_____10.28.	RCL	CLOSE / Verify CLOSED HV-0713 (Secondary Co-Flow Valve) – Area 4
_____10.29.	RCL	CLOSE / Verify CLOSED HV-0806 (Coax LN2 Flow Meter Isolation Valve) – Area 4
_____10.30.	RCL	OPEN / Verify OPEN HV-0808 (Coax LN2 Flow Meter Bypass Valve) – Area 4
_____10.31.	RCL	Verify PG-0607 (Chamber Pressure Gauge) reads 0 psig– Area 5
_____10.32.	RCL	Verify PG-0004 (EC-4 System Inlet Pressure Gauge) reads 0 psig – Area 5
_____10.33.	RCL	DECREASE FULLY / Verify FULLY DECREASED HR-0005 (EC-4 Facility Pressure Regulator) – Area 5
_____10.34.	RCL	Verify PG-0006 (EC-4 System Outlet Pressure Gauge) reads 0 psig – Area 5
_____10.35.	RCL	CLOSE / Verify CLOSED HV-0101 (Center Jet GN2 Isolation Valve) – Area 4

_____10.36.	RCL	Verify PG-0102 (Center Jet GN2 System Inlet Pressure Gauge) reads 0 psig – Area 4
_____10.37.	RCL	DECREASE FULLY / Verify FULLY DECREASED HR-0103 (Center Jet GN2 Pressure Regulator) – Area 4
_____10.38.	RCL	Verify PG-0104 (Center Jet GN2 Regulated Pressure Gauge) reads 0 psig – Area 4
_____10.39.	RCL	CLOSE / Verify CLOSED HV-0106 (Center Jet GN2 Throttle Valve) – Area 4
_____10.40.	RCL	CLOSE / Verify CLOSED HV-0201 (Coax Jet GN2 Isolation Valve) – Area 4
_____10.41.	RCL	Verify PG-0202 (Coax Jet GN2 System Inlet Pressure Gauge) reads 0 psig – Area 4
_____10.42.	RCL	DECREASE FULLY / Verify FULLY DECREASED HR-0203 (Coax Jet GN2 Pressure Regulator) – Area 4
_____10.43.	RCL	Verify PG-0204 (Coax Jet GN2 Regulated Pressure Gauge) reads 0 psig – Area 4
_____10.44.	RCL	CLOSE / Verify CLOSED HV-0212 (Outer Jet Low Flow Isolation Valve) – Area 4
_____10.45.	RCL	CLOSE / Verify CLOSED HV-0213 (Outer Jet High Flow Isolation Valve) – Area 4
_____10.46.	RCL	CLOSE / Verify CLOSED HV-0206 (fine Coax Jet GN2 Throttle Valve) – Area 4
_____10.47.	RCL	CLOSE/ Verify CLOSED HV-0210 (coarse Coax Jet GN2 Throttle valve) – Area 4
_____10.48.	RCL	CLOSE / Verify CLOSED HV-0301 (Chamber Pressurization Isolation Valve) – Area 4
_____10.49.	RCL	Verify PG-0302 (Chamber Pressurization System Inlet Pressure Gauge) reads 0 psig – Area 4
_____10.50.	RCL	DECREASE FULLY / Verify FULLY DECREASED HR-0303 (Chamber Pressurization Regulator) – Area 4
_____10.51.	RCL	Verify PG-0304 (Chamber Pressure Regulated Pressure Gauge) reads 0 psig – Area 4
_____10.52.	RCL	CLOSE / Verify CLOSED HV-0305 (Chamber Pressurization Throttle Valve) – Area 4
_____10.53.	RCL	CLOSE / Verify CLOSED HV-0401 (Dewar and Tank Pressurization Isolation Valve) – Area 4

_____ 10.54.	RCL	Verify PG-0402 (Dewar and Tank GN2 System Inlet Pressure Gauge) reads 0 psig – Area 4
_____ 10.55.	RCL	DECREASE FULLY / Verify FULLY DECREASED HR-0403 (Dewar and Tank GN2 Pressure Regulator) – Area 4
_____ 10.56.	RCL	Verify PG-0404 (Dewar and Tank Pressurization Pressure Gauge) reads 0 psig – Area 4
_____ 10.57.	RCL	CLOSE / Verify CLOSED HV-0405 (Dewar LN2 Supply Dewar Tank Isolation Valve) – Area 4
_____ 10.58.	RCL	CLOSE / Verify CLOSED HV-0501 (Window Purge Isolation Valve) – Area 4
_____ 10.59.	RCL	Verify PG-0504 (Window Purge Pressure Gauge) reads 0 psig – Area 5
_____ 10.60.	RCL	DECREASE FULLY / Verify FULLY DECREASED HR-0502 (Window Purge Pressure Regulator) – Area 4
_____ 10.61.	RCL	Verify PG-0417 (LN2 Tank Pressure Gauge) reads 0 psig – Area 5 If not: A – OPEN HV-0409 – Area 2 B – CLOSE HV-0409 – Area 2

_____ 11.		WINDOW PURGE
_____ 11.1.	TC	Notify SOCC via hotline in EC-1, EC-2 or EC-3 control room that EC-4 is going into a RED condition for SCF testing.
_____ 11.2.	ALL	Verify all personnel are wearing Test PPE
_____ 11.3.	RCL	Change EC-4 light to RED
_____ 11.4.	TC	Record Time _____
_____ 11.5.	RCL	Verify window purge apparatus is in satisfactory condition.
_____ 11.6.	RCL	OPEN HV-0008 (EC-4 Low Pressure Facility Isolation Valve) – Area 3
_____ 11.7.	RCL	OPEN HV-0501 (Window Purge Isolation Valve) – Area 4 CAUTION: Do NOT Increase HR-0502 so that PG-0504 reads greater than 5 psig as it will damage PG-0504
_____ 11.8.	RCL	INCREASE HR-0502 (Window Purge Pressure Regulator) until PG-0504 (Window Purge Pressure Gauge) reads 1.5 psig +/- 0.5 psig – Area 4
_____ 11.9.	RCL	Permit window purge to continue according to ER _____

_____ 12.		FACILITY GN2 SETUP
_____ 12.1.	RCL	<i>Slowly</i> OPEN HV-0003 (EC-4 Facility Isolation Valve) – Area 3
_____ 12.2.	RCL	Verify PG-0004 (EC-4 System Inlet Pressure Gauge) reads a pressure greater than 2000 psig – Area 4 _____
_____ 12.3.	RCL	OPEN HV-0007 (Upstream Regulator Pressure Valve) – Area 5
_____ 12.4.	RCL	CLOSE HV-0608 (Gauge Vent Valve) – Area 5
_____ 12.5.	RCL	INCREASE HR-0005 (EC-4 Facility Pressure Regulator) until PG-0607 (Chamber Pressure Gauge) reads 2000 psig +/- 50 psig – Area 5
		NOTE: Open and quickly close HV-0608 to check if PG-0607 actually reads 2000 psig
_____ 12.6.	RCL	CLOSE HV-0007 (Upstream Regulator Pressure Valve) – Area 5
_____ 12.7.	RCL	<i>Slowly</i> OPEN HV-0608 (Gauge Vent Valve) – Area 5
_____ 12.8.	RCL	Verify PG-0607 (Chamber Pressure Gauge) reads 0 psig – Area 5
_____ 12.9.	RCL	CLOSE HV-0608 (Gauge Vent Valve) – Area 5
_____ 12.10.	RCL	OPEN HV-0601 (PC Vent PG Isolation Valve) – Area 5
_____ 12.11.	RCL	Verify PG-0607 (Chamber Pressure Gauge) reads 0 psig – Area 5
_____ 12.12.	RCL	Turn ON Air Handler

_____ 13.		CHAMBER PURGE
_____ 13.1.	TC	Record Time _____
_____ 13.2.	TC	Record zero values for Pressure Transducer (Agilent Ch. 103), Incoming Mass Flow Meter (Agilent Ch. 104) and Outgoing Mass Flow Meter (Agilent Ch. 102).
_____ 13.3.	RCL	<i>Slowly</i> OPEN HV-0301 (Chamber Pressurization Isolation Valve) – Area 4
_____ 13.4.	RCL	Verify PG-0302 (Chamber Pressurization System Inlet Pressure Gauge) reads 2000 psig +/- 150 psig – Area 4 _____
_____ 13.5.	RCL	INCREASE HR-0303 (Chamber Pressure GN2 Pressure Regulator) until PG-0304 (Chamber Pressure Regulated Pressure Gauge) reads _____ psig +/-100 psig as per ER – Area 4
_____ 13.6.	RCL	OPEN HV-0305 (Chamber Pressurization Throttle Valve) as per ER _____ – Area 4 NOTE: Perform next 3 steps in quick succession
_____ 13.7.	RCL	CLOSE HV-0603 (Chamber Pressure Build Valve) – Area 4
_____ 13.8.	RCL	Verify PG-0607 (Chamber Pressure Gauge) indicates that PC is increasing to indicate purge is flowing. – Area 5
_____ 13.9.	RCL	OPEN HV-0603 (Chamber Pressure Build Valve) – Area 4
_____ 13.10.	RCL	Go to Chamber Pressurization Section if taking ambient T measurements with no flows
_____ 14.		CENTER JET PURGE
_____ 14.1.	RCL	<i>Slowly</i> OPEN HV-0101 (Center Jet GN2 Isolation Valve) – Area 4
_____ 14.2.	RCL	Verify PG-0102 (Center Jet GN2 System Inlet Pressure Gauge) reads 2000 psig +/- 150 psig – Area 4 _____
_____ 14.3.	RCL	INCREASE HR-0103 (Center Jet GN2 Pressure Regulator) until PG-0104 (Center Jet GN2 Regulated Pressure Gauge) reads _____ psig +/-100 psig as per ER – Area 4
_____ 14.4.	RCL	OPEN HV-0106 (Center Jet GN2 Throttle Valve) as per ER _____ – Area 4 NOTE: Check chamber pressure periodically Ch. 103 in Agilent (at least every 500 mg/s)
_____ 14.5.	TC	Verify FE-0105 (Center Jet GN2 Flow Meter) indicates purge is flowing NOTE: Ch. 104 in Agilent

_____15.		COAXIAL JET PURGE
_____15.1.	RCL	<i>Slowly</i> OPEN HV-0201 (Coax Jet GN2 Isolation Valve) – Area 4
_____15.2.	RCL	Verify PG-0202 (Coax Jet GN2 System Inlet Pressure Gauge) reads 2000 psig +/- 150 psig – Area 4 _____
_____15.3.	RCL	Open HV-0212 (Outer Jet Low Flow Isolation Valve) for use with FE-0205 (flow rate up to 3500 mg/s) or HV-0213 (Outer Jet High Flow Isolation Valve) for use with FE-0211 (higher flow rates) as per ER _____
_____15.4.	RCL	INCREASE HR-0203 (Coax Jet GN2 Pressure Regulator) until PG-0204 (Coax Jet GN2 Regulated Pressure Gauge) reads _____ psig +/-100 psig as per ER – Area 4 NOTE: 1100 psig is the high limit for PG-0204. The calibration curve available does not go beyond this pressure.
_____15.5.	RCL	OPEN HV-0206 (Coax Jet GN2 Throttle Valve) as per ER _____ – Area 4 NOTE: Check chamber pressure periodically Ch. 103 in Agilent (at least every 500 mg/s).
_____15.6.	TC	Verify FE-0205 (Coax Jet GN2 Flow Meter) indicates purge is flowing NOTE: Ch. 102 in Agilent.

_____16.		CHAMBER PRESSURIZATION
_____16.1.	RCL	OPEN HV-0605 (Secondary Chamber Pressure Vent Valve) – Area 4
_____16.2.	RCL	OPEN HV-0606 (Tertiary Chamber Pressure Vent Valve) 7 turns – Area 4
_____16.3.	RCL	CLOSE HV-0604 (Primary Chamber Pressure Vent Valve) – Area 4
_____16.4.	RCL	ADJUST HV-0605 (Secondary Chamber Pressure Vent Valve) and HV-0606 (Tertiary Chamber Pressure Vent Valve) until PG-0607 (Chamber Pressure Gauge) reads INITIAL CHAMBER PRESSURE as per ER _____ – Area 4
_____16.5.	RCL	Wait for required time to elapse from step 13.1 as per ER _____
_____16.6.	RCL	IF taking measurements at room temperature A - Take measurements B - Reduce chamber pressure after measurements C - Return to “Center Jet Purge” section

_____17.		SYSTEM CHILL DOWN
_____17.1.	TC	Verify Red Crew has donned Cryogenic PPE as outlined in Step 5.2
_____17.2.	RCL	CLOSE HV-0803 (Local Dewar Fill Isolation Valve) – Area 1
_____17.3.	RCL	OPEN HV-0801 (Tank LN2 Isolation Valve) – Area 1
_____17.4.	RCL	OPEN HV-0804 (Tank-Dewar Separation Valve) – Area 1
_____17.5.	RCL	OPEN HV-0416 (pressurize tank with GN2) – Area 1
_____17.6.	RCL	Remove Cryogenic PPE and don Test PPE as listed in Step 5.2
_____17.7.	RCL	<i>Slowly</i> OPEN HV-0401 (Dewar and Tank Pressurization Isolation Valve) – Area 4
_____17.8.	RCL	Verify PG-0402 (Dewar and Tank GN2 System Inlet Pressure Gauge) reads 2000 psig +/-150 psig – Area 4 _____
_____17.9.	RCL	Increase HR-0403 (Dewar and Tank GN2 Pressure Regulator) until PG-0404 (Dewar and Tank Pressurization Pressure Gauge) reads as per ER – Area 4 _____
_____17.10.	RCL	OPEN HV-0405 (Dewar LN2 Supply Dewar Tank Isolation Valve) – Area 4
_____17.11.	RCL	OPEN HV-0406 (Tank GN2 Pressurization Isolation Valve) – Area 2
_____17.12.	TC	Record Time _____
_____17.13.	RCL	OPEN HV-0809 (Coax Heat Exchanger LN2 Throttle Vent Valve) as per ER_____ ceiling between Area 4 & 5 NOTE: Rotate valve ¼ of a turn and wait 10 minutes
_____17.14.	RCL	OPEN HV-0708 (Heat Exchanger LN2 Throttle Vent Valve) as per ER_____ ceiling between Area 4 & 5 NOTE: Rotate valve ¼ of a turn and wait 10 minutes
_____17.15.	ALL	Wait Required time for chill down as per ER_____

_____18.		TESTING
_____18.1.	RCL	If acoustic testing, place foam door into position
_____18.2.	TC	Verify all personnel are wearing ear muffs if acoustic testing.
_____18.3.	RCL	Adjust HR-0103 (Center Jet GN2 Pressure Regulator) to maintain desired flow rates NOTE: Ch. 104 in Agilent
_____18.4.	RCL	Adjust HR-0203 (Coax Jet GN2 Pressure Regulator) to maintain desired flow rates NOTE: Ch. 102 in Agilent
_____18.5.	RCL	Adjust HV-0606 (Tertiary Chamber Pressure Vent Valve) and HV-0605 (Secondary Chamber Pressure Vent Valve) to maintain desired pressure chamber NOTE: Ch. 103 in Agilent
_____18.6.	TC	Direct RCL to operate system as per test needs
_____18.7.	RCL	OPERATE System as directed by test conductor

_____19.	RCL	SHUT DOWN
_____19.1.	RCL	CLOSE HV-0003 (EC-4 Secondary Facility Isolation Valve) – Area 2
_____19.2.	RCL	CLOSE HV-0008 (EC-4 Low Pressure Facility Isolation Valve) – Area 2
_____19.3.	RCL	Turn off air handler
_____19.4.	RCL	DON Cryogenic PPE
_____19.5.	RCL	CLOSE HV-0801 (Tank LN2 Isolation Valve) – Area 1
_____19.6.	RCL	CLOSE HV-0416 (Tank GN2 Pressurization Isolation Valve) – Area 1
_____19.7.	RCL	REMOVE Cryogenic PPE
_____19.8.	RCL	OPEN HV-0409 (Dewar Pressurization Vent Isolation Valve) – Area 2
_____19.9.	RCL	Wait for PG-0004 (EC-4 System Inlet Pressure Gauge) to read 0 psig – Area 5
_____19.10.	RCL	Fully DECREASE HR-0005 (EC-4 Facility Pressure Regulator) – Area 5
_____19.11.	RCL	Verify PG-0006 (EC-4 System Regulated Pressure Gauge) reads 0 psig – Area 5
_____19.12.	RCL	Verify PG-0102 (Center Jet GN2 System Inlet Pressure Gauge) reads 0 psig – Area 4
_____19.13.	RCL	CLOSE HV-0101 (Center Jet GN2 Isolation Valve) – Area 4
_____19.14.	RCL	Fully DECREASE HR-0103 (Center Jet GN2 Pressure Regulator) – Area 4
_____19.15.	RCL	Verify PG-0104 (Center Jet GN2 Regulated Pressure Gauge) reads 0 psig – Area 4
_____19.16.	RCL	CLOSE HV-0106 (Center Jet GN2 Throttle Valve) – Area 4
_____19.17.	RCL	Verify PG-0202 (Coax Jet GN2 System Inlet Pressure Gauge) reads 0 psig – Area 4
_____19.18.	RCL	CLOSE HV-0201 (Coax Jet GN2 Isolation Valve) – Area 4
_____19.19.	RCL	Fully DECREASE HR-0203 (Coax Jet GN2 Pressure Regulator) – Area 4
_____19.20.	RCL	Verify PG-0204 (Coax Jet GN2 Regulated Pressure Gauge) reads 0 psig – Area 4
_____19.21.	RCL	CLOSE HV-0212 (Outer Jet Low Flow Isolation Valve) – Area 4

_____19.22.	RCL	CLOSE HV-0213 (Outer Jet High Flow Isolation Valve) – Area 4
_____19.23.	RCL	CLOSE HV-0206 (coarse Coax Jet GN2 Throttle Valve) – Area 4
_____19.24.	RCL	CLOSE HV-0210 (fine Coax Jet GN2 Throttle Valve) – Area 4
_____19.25.	RCL	Verify PG-0302 (Chamber Pressurization System Inlet Pressure Gauge) reads 0 psig – Area 4
_____19.26.	RCL	CLOSE HV-0301 (Chamber Pressurization Isolation Valve) – Area 4
_____19.27.	RCL	Fully DECREASE HR-0303 (Chamber Pressurization Regulator) – Area 4
_____19.28.	RCL	Verify PG-0304 (Chamber Pressure Regulated Pressure Gauge) reads zero psig () – Area 4
_____19.29.	RCL	CLOSE HV-0305 (Chamber Pressurization Throttle Valve) – Area 4
_____19.30.	RCL	Verify PG-0402 (Dewar and Tank GN2 System Inlet Pressure Gauge) read 0 psig – Area 4 NOTE: Current readout sticks
_____19.31.	RCL	CLOSE HV-0401 (Dewar and Tank Pressurization Isolation Valve) – Area 4
_____19.32.	RCL	Fully DECREASE HR-0403 (Dewar and Tank GN2 Pressure Regulator) – Area 4
_____19.33.	RCL	Verify PG-0404 (Dewar and Tank Pressurization Pressure Gauge) reads 0 psig – Area 4
_____19.34.	RCL	OPEN HV-0405 (Dewar LN2 Supply Dewar Tank Isolation Valve) – Area 4
_____19.35.	RCL	OPEN/Verify OPEN HV-0406 (Tank GN2 Pressurization Isolation Valve) – Area 2
_____19.36.	RCL	Verify PG-0504 (Window Purge Pressure Gauge) reads 0 psig – Area 5
_____19.37.	RCL	CLOSE HV-0501 (Window Purge Isolation Valve) – Area 4
_____19.38.	RCL	Fully DECREASE HR-0502 (Window Purge Pressure Regulator) – Area 4
_____19.39.	RCL	OPEN HV-0608 (Gauge Vent Valve) – Area 5
_____19.40.	RCL	Verify PG-0607 (Chamber Pressure Gauge) reads 0 psig – Area 5
_____19.41.	RCL	CLOSE HV-0601 (PC Vent PG Isolation Valve) – Area 5

_____19.42.	RCL	OPEN / Verify OPEN HV-0603 (Chamber Pressure Build Valve) – Area 4
_____19.43.	RCL	OPEN HV-0604 (Primary Chamber Pressure Vent Valve) – Area 4
_____19.44.	RCL	CLOSE HV-0605 (Secondary Chamber Pressure Vent Valve) – Area 4
_____19.45.	RCL	CLOSE HV-0606 (Tertiary Chamber Pressure Vent Valve) – Area 4
_____19.46.	RCL	OPEN HV-0708 (Heat Exchanger LN2 Throttle Vent Valve) – ceiling between Area 4&5
_____19.47.	RCL	OPEN HV-0809 (Coax Heat Exchanger LN2 Throttle Vent Valve) – ceiling between Area 4&5
_____19.48.	RCL	OPEN / Verify OPEN HV-0715 (Direct LN2 Supply Valve) - Area 2
_____19.49.	RCL	Don Cryogenic PPE
_____19.50.	RCL	CLOSE HV-0804 (Tank-Dewar Separation Valve) – Area 1
_____19.51.	RCL	OPEN HV-0803 (Local Dewar Fill Isolation Valve - vent trapped LN2 between 0801 and 0804) - Area 1
_____19.52.	RCL	Remove Cryogenic PPE
_____19.53.	RCL	Verify PG-0417 (LN2 Tank Pressure Gauge) reads 0 psig – Area 5
_____19.54.	TC	Notify SOCC EC-4 is going back to green condition
_____19.55.	ALL	Turn off portable O ₂ sensors
_____19.56.	RCL	Turn EC-4 lights back to green
_____19.57.	RCL	Remove “DO NOT ENTER” and “HEARING PROTECTION REQUIRED” signs
_____19.58.	RCL	Remove chain from entrance to horseshoe

_____20.	RCL	EMERGENCY PROCEDURE (GN₂ or LN₂ line leak or burst)
		IF OXYGEN DEFICIENCY MONITORS ALARMS:
_____20.1.	ALL	Exit the facility to a safe zone given in safety brief.
_____20.2.	TC	Contact SOCC 5-5632 and report the emergency. Have SOCC contact the Fire Dept. 5-5181
_____20.3.	TC	Contact the Facility Manager and isolate the cell or area.
		IF POSSIBLE AND WHEN SAFE, DO THE FOLLOWING:
_____20.4.	RCL	CLOSE HV-0001 (EC-3, EC-4 Primary Facility Isolation Valve)
_____20.5.	RCL	CLOSE HV-0701 (LN2 Isolation Valve)
_____20.6.	RCL	CLOSE HV-0801 (Tank LN2 Isolation Valve)
		NOTE: WHEN SAFE TO DO SO COMPLETE THE STEPS OF THE "SHUT DOWN" SECTION 19

APPENDIX C

Summary of Coaxial Jet Experimental Data

Table C.1. Summary of experimental conditions for tests performed with the original injector including single phase subcritical experimental conditions and results.

	T_{chamber} (K)	ρ_{chamber} (kg/m ³)	P_{chamber} (MPa)	T_{outer} (K)	$\dot{\gamma}_{\text{outer}}$ (mg/s)	ρ_{outer} (kg/m ³)	U_{outer} (m/s)	T_{inner} (K)	$\dot{\gamma}_{\text{inner}}$ (mg/s)	ρ_{inner} (kg/m ³)	U_{inner} (m/s)	$F_{\text{req.}}$ (kHz)	$P_{\text{gas max}}$ (kPa)	VR	J
SUB															
sub1	233	22.0	1.50	191	310	22.0	4.30	109	279	630	2.2	2.98	21.5	2.0	0.17
sub2	231	22.2	1.50	183	790	28.8	11.0	109	283	630	2.2	3.06	20.1	4.8	1.0
sub3	226	21.9	1.45	183	1230	27.8	16.9	109	284	630	2.2	3.06	17.8	7.6	2.6
sub4	226	22.9	1.51	185	1560	28.7	20.9	109	279	630	2.2	2.96	15.7	9.5	4.2
sub5	210	24.9	1.50	182	2400	29.3	31.3	109	279	630	2.2	3.01	16.9	14	9.6
sub6	216	24.1	1.50	191	3640	27.7	50.3	109	279	630	2.2	3.02	16.3	23	23
NEAR															
near1	223	56.6	3.58	180	1060	75.4	5.38	123	290	520	2.8	3.08	9.04	2.0	0.55
near2	207	62.0	3.57	152	1570	101	5.95	117	289	590	2.4	3.04	10.8	2.5	1.0
near3	228	55.1	3.58	185	1590	72.4	8.40	126	293	440	3.3	3.00	11.8	2.6	1.1
near4	223	56.1	3.55	184	2170	72.3	11.5	127	294	360	4.0	3.01	11.4	2.8	1.6
near5	230	54.2	3.56	199	2120	65.1	12.5	126	292	440	3.3	3.03	12.1	3.8	2.1
near6	229	54.5	3.56	183	2690	73.1	14.1	126	292	420	3.4	3.05	11.1	4.1	2.9
near7	219	57.6	3.56	194	3080	67.4	17.5	125	289	480	3.0	3.06	11.8	5.9	4.9
near8	213	59.6	3.56	192	6460	68.3	36.2	128	295	220	6.6	2.93	9.73	5.5	9.3
SUPER															
super1	231	76.1	4.96	198	292	93.9	1.19	136	291	300	4.8	3.05	8.01	0.25	0.019
super2	231	76.1	4.96	193	997	97.7	3.90	130	292	460	3.1	3.01	10.2	1.2	0.33
super3	221	80.4	4.95	180	2050	109	7.19	128	291	490	2.9	3.01	10.7	2.5	1.3
super4	222	80.1	4.96	182	3110	107	11.1	134	288	360	3.9	3.05	10.1	2.8	2.4
super5	222	80.3	4.97	191	2820	99.5	10.8	131	293	440	3.3	3.09	12.5	3.3	2.5
super6	211	85.8	4.96	187	5820	103	21.6	132	286	410	3.4	3.05	10.7	6.3	9.9
SUB															
angle1	276	18.0	1.47	250	304	20	5.8	145	281	38	36	0.16	0.013	-0.10	
angle2	276	18.8	1.53	254	506	21	9.2	145	281	40	35	0.27	0.037	0.08	
angle3	276	18.2	1.48	254	1000	20	19	150	281	36	39	0.50	0.14	0.18	
angle4	270	19.2	1.53	245	2000	21	36	155	282	36	39	0.94	0.52	0.20	
angle5	270	18.8	1.50	246	3010	21	55	148	282	38	37	1.5	1.2	0.18	
angle6	261	20.1	1.54	242	4500	22	78	190	281	28	50	1.6	2.0	0.19	

	T_{chamber} (K)	ρ_{chamber} (kg/m ³)	P_{chamber} (MPa)	T_{outer} (K)	$\dot{\gamma}_{\text{outer}}$ (mg/s)	ρ_{outer} (kg/m ³)	U_{outer} (m/s)	T_{inner} (K)	$\dot{\gamma}_{\text{inner}}$ (mg/s)	ρ_{inner} (kg/m ³)	U_{inner} (m/s)	VR	J	$\tan \alpha_1 + \tan \alpha_4$
SUB														
angle1	276	18.0	1.47	250	304	20	5.8	145	281	38	36	0.16	0.013	-0.10
angle2	276	18.8	1.53	254	506	21	9.2	145	281	40	35	0.27	0.037	0.08
angle3	276	18.2	1.48	254	1000	20	19	150	281	36	39	0.50	0.14	0.18
angle4	270	19.2	1.53	245	2000	21	36	155	282	36	39	0.94	0.52	0.20
angle5	270	18.8	1.50	246	3010	21	55	148	282	38	37	1.5	1.2	0.18
angle6	261	20.1	1.54	242	4500	22	78	190	281	28	50	1.6	2.0	0.19

Table C.2. Summary of two-phase subcritical experimental results for tests performed with the original injector.

SUBCRITICAL

sub1 (J = 0.17)					sub2 (J = 1.0)				
	L/D ₁	STD L/D ₁	$\Delta p_{\text{peak-to-peak}}/p_{\text{mean}}$	$\alpha_{\text{Left}} + \alpha_{\text{Right}} (^{\circ})$		L/D ₁	STD L/D ₁	$\Delta p_{\text{peak-to-peak}}/p_{\text{mean}}$	$\alpha_{\text{Left}} + \alpha_{\text{Right}} (^{\circ})$
Baseline	15.09	2.45	0.28%	2.93	Baseline	16.59	3.76	1.13%	3.83
0°	13.88	2.15	3.96%	3.46	0°	12.56	2.77	2.86%	5.44
45°	13.80	2.10	4.06%	5.12	45°	10.55	2.13	2.58%	6.15
90°	13.43	1.86	3.65%	5.65	90°	9.96	1.59	2.16%	5.95
135°	13.52	1.81	3.22%	4.65	135°	9.61	1.54	1.89%	8.32
180°	14.99	2.27	2.58%	3.66	180°	9.26	1.18	2.37%	8.95
225°	17.71	3.29	2.23%	3.78	225°	10.17	1.48	2.72%	6.20
270°	15.25	2.65	2.44%	2.58	270°	12.66	2.32	2.86%	4.83
315°	13.75	2.10	2.91%	3.64	315°	13.17	2.83	3.78%	3.59
360°	13.56	1.90	3.27%	3.32	360°	11.38	2.37	3.65%	4.07

sub3 (J = 2.6)					sub4 (J = 4.2)				
	L/D ₁	STD L/D ₁	$\Delta p_{\text{peak-to-peak}}/p_{\text{mean}}$	$\alpha_{\text{Left}} + \alpha_{\text{Right}} (^{\circ})$		L/D ₁	STD L/D ₁	$\Delta p_{\text{peak-to-peak}}/p_{\text{mean}}$	$\alpha_{\text{Left}} + \alpha_{\text{Right}} (^{\circ})$
Baseline	17.06	4.04	1.37%	7.53	Baseline	15.15	1.58	0.33%	5.88
0°	14.14	3.67	2.64%	16.68	0°	10.61	1.31	2.81%	17.35
45°	14.84	3.53	2.49%	25.05	45°	9.89	1.13	2.93%	23.09
90°	14.93	3.54	3.19%	28.94	90°	10.37	1.14	2.82%	19.19
135°	13.93	3.23	n/a	31.36	135°	9.70	1.01	2.43%	28.37
180°	12.72	2.81	2.07%	35.97	180°	11.16	1.15	1.74%	16.22
225°	14.79	3.56	2.25%	29.53	225°	11.84	1.18	1.49%	17.42
270°	13.53	3.82	2.45%	20.93	270°	12.54	1.29	1.56%	17.10
315°	13.68	3.82	3.47%	15.94	315°	12.66	1.54	1.85%	9.91
360°	15.41	3.49	2.28%	25.78	360°	11.85	1.41	2.24%	12.36

sub5 (J = 9.6)					sub6 (J = 23)				
	L/D ₁	STD L/D ₁	$\Delta p_{\text{peak-to-peak}}/p_{\text{mean}}$	$\alpha_{\text{Left}} + \alpha_{\text{Right}} (^{\circ})$		L/D ₁	STD L/D ₁	$\Delta p_{\text{peak-to-peak}}/p_{\text{mean}}$	$\alpha_{\text{Left}} + \alpha_{\text{Right}} (^{\circ})$
Baseline	8.40	1.44	0.52%	6.80	Baseline	5.19	0.65	0.72%	2.47
0°	7.18	1.10	3.04%	33.33	0°	4.89	0.64	2.69%	13.49
45°	7.19	1.13	2.33%	37.37	45°	4.98	0.65	2.15%	8.43
90°	7.55	1.12	1.79%	32.90	90°	4.77	0.66	2.00%	12.45
135°	7.28	1.08	1.41%	30.76	135°	4.70	0.63	1.55%	7.00
180°	6.95	0.96	1.59%	33.04	180°	4.73	0.56	1.88%	18.12
225°	6.66	0.87	2.23%	29.76	225°	4.65	0.64	2.49%	14.56
270°	6.95	0.91	2.51%	38.03	270°	4.79	0.65	2.63%	16.29
315°	6.82	0.99	3.18%	30.36	315°	4.85	0.64	2.60%	11.12
360°	7.23	1.08	2.84%	31.36	360°	5.08	0.68	3.06%	8.42

Table C.3. Summary of nearcritical experimental results for tests performed with the original injector.

NEARCRITICAL

near 1 (J = 0.55)					near2 (J = 1.0)				
	L/D ₁	STD L/D ₁	$\Delta p_{\text{peak-to-peak}}/p_{\text{mean}}$	$\alpha_{\text{Left}} + \alpha_{\text{Right}} (^{\circ})$		L/D ₁	STD L/D ₁	$\Delta p_{\text{peak-to-peak}}/p_{\text{mean}}$	$\alpha_{\text{Left}} + \alpha_{\text{Right}} (^{\circ})$
Baseline	24.44	3.02	0.19%	10.06	Baseline	15.47	2.04	0.23%	16.34
0°	16.67	2.09	0.72%	16.23	0°	11.94	1.35	0.83%	14.72
45°	17.29	2.61	0.59%	9.96	45°	10.43	1.11	0.59%	15.57
90°	18.56	2.39	0.45%	10.59	90°	15.25	1.95	0.43%	9.64
135°	18.92	2.52	0.37%	13.57	135°	12.08	1.35	0.31%	11.83
180°	18.70	2.34	0.42%	11.11	180°	14.09	1.66	0.58%	12.05
225°	20.02	2.71	0.52%	12.67	225°	11.66	1.16	0.65%	14.51
270°	18.98	2.58	0.67%	9.64	270°	11.41	1.19	0.81%	16.31
315°	16.49	1.86	0.71%	12.21	315°	11.63	1.33	0.85%	17.57
360°	14.35	1.76	0.66%	21.81	360°	12.06	1.23	0.75%	18.98

near3 (J = 1.1)					near4 (J = 1.6)				
	L/D ₁	STD L/D ₁	$\Delta p_{\text{peak-to-peak}}/p_{\text{mean}}$	$\alpha_{\text{Left}} + \alpha_{\text{Right}} (^{\circ})$		L/D ₁	STD L/D ₁	$\Delta p_{\text{peak-to-peak}}/p_{\text{mean}}$	$\alpha_{\text{Left}} + \alpha_{\text{Right}} (^{\circ})$
Baseline	14.62	1.56	0.21%	15.94	Baseline	12.08	1.16	0.20%	11.63
0°	9.79	1.23	0.85%	18.48	0°	9.83	1.00	0.91%	17.18
45°	10.96	1.21	n/a	16.89	45°	10.19	0.99	0.84%	11.67
90°	10.32	1.12	0.93%	17.75	90°	9.30	1.00	0.75%	18.39
135°	9.47	1.09	0.77%	15.05	135°	8.32	0.97	0.73%	12.49
180°	9.20	1.09	0.55%	12.61	180°	8.61	0.98	0.68%	12.84
225°	9.62	1.12	0.35%	15.59	225°	8.30	1.01	0.69%	10.36
270°	9.88	1.19	0.34%	14.28	270°	8.64	1.08	0.74%	9.93
315°	10.45	1.12	0.57%	17.88	315°	8.83	0.99	0.89%	14.68
360°	11.23	1.29	0.77%	16.79	360°	10.33	1.06	0.89%	7.21

near5 (J = 2.1)					near6 (J = 2.9)				
	L/D ₁	STD L/D ₁	$\Delta p_{\text{peak-to-peak}}/p_{\text{mean}}$	$\alpha_{\text{Left}} + \alpha_{\text{Right}} (^{\circ})$		L/D ₁	STD L/D ₁	$\Delta p_{\text{peak-to-peak}}/p_{\text{mean}}$	$\alpha_{\text{Left}} + \alpha_{\text{Right}} (^{\circ})$
Baseline	12.93	1.38	0.27%	15.49	Baseline	5.98	0.60	0.21%	3.72
0°	8.10	1.12	0.84%	24.17	0°	3.60	0.51	0.79%	17.33
45°	8.91	1.24	0.97%	22.58	45°	4.05	0.45	0.88%	16.31
90°	8.75	1.02	0.96%	20.91	90°	4.06	0.45	0.83%	24.24
135°	8.09	0.77	0.77%	23.62	135°	3.80	0.50	0.64%	21.51
180°	7.37	0.73	0.56%	24.46	180°	3.26	0.47	0.41%	22.70
225°	7.98	0.76	0.30%	21.51	225°	3.20	0.51	0.29%	33.69
270°	8.15	0.80	0.37%	16.77	270°	3.22	0.47	0.43%	33.02
315°	8.18	1.06	0.64%	11.87	315°	3.44	0.50	0.62%	39.27
360°	8.50	1.09	0.86%	23.47	360°	4.01	0.56	0.80%	24.31

near7 (J = 4.9)					near8 (J = 9.3)				
	L/D ₁	STD L/D ₁	$\Delta p_{\text{peak-to-peak}}/p_{\text{mean}}$	$\alpha_{\text{Left}} + \alpha_{\text{Right}} (^{\circ})$		L/D ₁	STD L/D ₁	$\Delta p_{\text{peak-to-peak}}/p_{\text{mean}}$	$\alpha_{\text{Left}} + \alpha_{\text{Right}} (^{\circ})$
Baseline	5.56	0.44	0.25%	-0.81	Baseline	2.45	0.25	0.36%	-2.45
0°	3.80	0.67	0.94%	28.21	0°	2.41	0.26	0.68%	0.00
45°	4.17	0.55	0.76%	13.41	45°	2.40	0.26	0.77%	1.36
90°	3.34	0.50	0.56%	24.76	90°	2.45	0.28	0.69%	6.24
135°	3.36	0.57	0.43%	40.03	135°	2.45	0.28	0.51%	1.43
180°	3.33	0.54	0.47%	26.91	180°	2.51	0.31	n/a	0.00
225°	3.57	0.56	0.52%	30.41	225°	2.43	0.29	0.40%	0.00
270°	3.70	0.60	0.78%	25.12	270°	2.46	0.25	0.53%	3.00
315°	3.71	0.59	0.81%	27.49	315°	2.46	0.27	0.67%	2.26
360°	3.91	0.54	0.82%	23.60	360°	2.58	0.27	0.73%	6.67

Table C.4. Summary of supercritical experimental results for tests performed with the original injector.

SUPERCRITICAL

super1 (J = 0.019)					super2 (J = 0.33)				
	L/D ₁	STD L/D ₁	$\Delta p_{\text{peak-to-peak}}/p_{\text{mean}}$	$\alpha_{\text{Left}} + \alpha_{\text{Right}} (^{\circ})$		L/D ₁	STD L/D ₁	$\Delta p_{\text{peak-to-peak}}/p_{\text{mean}}$	$\alpha_{\text{Left}} + \alpha_{\text{Right}} (^{\circ})$
Baseline	37.66	5.29	0.10%	6.63	Baseline	26.72	3.14	0.15%	5.74
0°	32.95	2.06	0.41%	6.79	0°	23.52	3.43	0.56%	7.12
45°	35.84	2.63	0.46%	8.73	45°	21.49	3.26	0.58%	6.54
90°	34.41	2.82	0.46%	8.90	90°	21.19	3.46	0.51%	9.91
135°	32.02	2.14	0.39%	4.93	135°	25.04	3.13	0.38%	6.48
180°	31.98	2.36	0.27%	13.50	180°	n/a	n/a	n/a	5.20
225°	32.45	1.79	0.21%	10.57	225°	23.30	3.32	0.26%	4.65
270°	29.67	2.26	0.27%	6.78	270°	24.44	3.31	0.37%	4.66
315°	33.80	2.20	0.42%	8.79	315°	26.60	2.97	0.48%	6.55
360°	35.17	2.04	0.45%	8.58	360°	19.07	2.76	0.55%	5.98

super3 (J = 1.3)					super4 (J = 2.4)				
	L/D ₁	STD L/D ₁	$\Delta p_{\text{peak-to-peak}}/p_{\text{mean}}$	$\alpha_{\text{Left}} + \alpha_{\text{Right}} (^{\circ})$		L/D ₁	STD L/D ₁	$\Delta p_{\text{peak-to-peak}}/p_{\text{mean}}$	$\alpha_{\text{Left}} + \alpha_{\text{Right}} (^{\circ})$
Baseline	19.16	2.33	0.12%	14.43	Baseline	10.23	2.30	0.22%	17.24
0°	14.86	1.66	0.60%	13.04	0°	6.57	1.17	0.55%	12.65
45°	12.54	1.52	0.61%	10.23	45°	6.73	1.49	0.56%	18.79
90°	12.65	1.56	0.54%	13.98	90°	7.07	1.53	0.50%	12.65
135°	12.85	1.48	0.51%	11.46	135°	7.41	1.83	0.38%	14.39
180°	12.17	1.52	0.42%	12.52	180°	5.82	1.33	0.27%	18.68
225°	14.63	1.90	0.41%	9.11	225°	5.75	1.24	0.27%	14.72
270°	13.28	1.42	0.43%	13.85	270°	5.64	1.30	0.36%	20.07
315°	12.36	1.36	0.52%	14.33	315°	5.90	1.17	0.47%	18.63
360°	14.55	1.73	0.59%	14.86	360°	5.83	1.20	0.58%	19.57

super5 (J = 2.5)					super6 (J = 9.9)				
	L/D ₁	STD L/D ₁	$\Delta p_{\text{peak-to-peak}}/p_{\text{mean}}$	$\alpha_{\text{Left}} + \alpha_{\text{Right}} (^{\circ})$		L/D ₁	STD L/D ₁	$\Delta p_{\text{peak-to-peak}}/p_{\text{mean}}$	$\alpha_{\text{Left}} + \alpha_{\text{Right}} (^{\circ})$
Baseline	9.02	0.88	0.25%	15.31	Baseline	3.04	0.27	0.26%	-4.28
0°	7.88	1.16	0.60%	19.19	0°	3.05	0.58	0.61%	1.80
45°	6.18	1.03	0.67%	23.83	45°	3.42	0.60	0.57%	-3.78
90°	4.46	0.85	0.57%	21.13	90°	3.03	0.42	0.47%	-9.52
135°	5.89	0.91	0.41%	22.79	135°	3.00	0.39	0.36%	-0.63
180°	6.13	0.97	0.25%	27.58	180°	3.28	0.57	0.27%	-1.09
225°	6.08	0.96	0.36%	11.95	225°	3.36	0.57	0.34%	5.46
270°	6.49	0.86	0.51%	12.20	270°	3.21	0.61	0.47%	13.67
315°	6.18	0.83	0.64%	12.08	315°	3.03	0.51	0.57%	-3.96
360°	7.11	1.12	0.71%	16.45	360°	2.98	0.44	0.60%	0.21

Table C.5. Summary of experimental conditions for tests performed with the new injector.

	T_{chamber} (K)	ρ_{chamber} (kg/m ³)	P_{chamber} (MPa)	T_{outer} (K)	\dot{m}_{outer} (mg/s)	ρ_{outer} (kg/m ³)	u_{outer} (m/s)	T_{inner} (K)	\dot{m}_{inner} (mg/s)	ρ_{inner} (kg/m ³)	u_{inner} (m/s)	Freq. (kHz)	VR	J
SUB														
subnew1	235	22	1.48	199	90	26	1.6	105	920	660	0.91	3.01	1.5	0.089
subnew2	237	22	1.49	197	200	26	3.0	106	925	655	0.92	2.96	3.3	0.43
subnew3	246	21	1.49	195	450	27	6.6	109	925	630	0.96	2.97	6.9	2.0
subnew4	224	23	1.49	189	600	28	8.5	110	925	620	0.97	3.04	8.7	3.4
subnew5	217	24	1.49	184	750	29	10	110	925	620	0.97	3.02	11	5.2
subnew6	228	22	1.49	193	880	27	13	108	925	640	0.94	2.96	14	7.8
subnew7	222	23	1.49	194	1100	27	16	108	925	640	0.94	2.92	17	12
subnew8	217	24	1.48	201	1300	26	20	109	925	630	0.96	2.90	21	18
NEAR														
neame w1	228	55	3.56	213	330	60	2.2	109	925	650	0.93	2.98	2.3	0.50
neame w2	226	55	3.56	209	460	61	3.0	109	925	650	0.93	3.06	3.2	0.97
neame w3	230	54	3.58	198	730	66	4.3	108	925	655	0.92	3.00	4.7	2.2
neame w4	216	59	3.58	199	1030	65	6.3	109	925	650	0.93	3.11	6.7	4.6
neame w5	214	59	3.58	203	1460	63	9.2	109	925	650	0.93	3.07	9.9	9.4
neame w6	215	59	3.56	207	2060	62	13	111	925	635	0.95	3.09	14	19
SUPER														
supnew1	219	81	4.95	212	890	85	4.1	111	925	650	0.93	3.11	4.4	2.6

REFERENCES

1. *A Review of Active Control of Combustion Instabilities*. **McManus, K. R., Poinso, T., Candel, S. M.** 1, s.l. : Elsevier Science, 1993, Prog. Energy Comb. Sci., Vol. 19, pp. 1-29.
2. *Measurements in an Acoustically Driven Coaxial Jet under Sub-, Near-, and Supercritical Conditions*. **Davis, D. W. and Chehroudi, B.** 2007, J. Propul. Power, Vol. 23, pp. 364-374.
3. *Recent Advances in Droplet Vaporization and Combustion*. **Law, C. K.** 1982, Prog. Energy Comb. Sci., Vol. 8, p. 171.
4. *Opportunities and Challenges of Combustion in Microgravity*. **Law, C. K. and Faeth, G. M.** 1994, Prog. Energy Comb. Sci., Vol. 20, pp. 65-113.
5. *On Calculating Burning Rates during Fibre Supported Droplet Combustion*. **Struk, P. M., Ackerman, M., Nayagam, V., Dietrich, D. L.** 4, 1998, Micrograv. Sci. Technology, Vol. XI, pp. 144-151.
6. *Acoustically Disturbed Fuel Droplet Combustion*. **Blaszczak, J.** 1991, Fuel, Vol. 70, pp. 1023-1025.
7. *Experimental Investigation of the Evaporation of Droplets in Axial Acoustic Fields*. **Sujith, R. I., Waldherr, G. A., Jagoda, J. I., Zinn, B. T.** 2000, J. Propul. Power, Vol. 16, pp. 278-285.
8. *Evaporation and Combustion of a Single Fuel Droplet in Acoustic Fields*. **Saito, M., Sato, M., Suzuki, I.** 1994, Fuel, Vol. 73, pp. 349-353.
9. *Enhancement of Evaporation/Combustion Rate Coefficient of a Single Fuel Droplet by Acoustic Oscillation*. **Saito, M., Hoshikawa, M., Sato, M.** 1996, Fuel, Vol. 75, pp. 669-674.

10. *Combustion of Single Droplets and Droplet Pairs in a Vibrating Field Under Microgravity.* **Okai, K., Moriue, O., Araki, M., Tsue, M., Kono, M., Sato, J., Dietrich, D. L., Williams, F. A.** 2000, Proc. Combustion Inst., Vol. 28, pp. 977-983.
11. *Influence of Standing Sound Waves on Droplet Combustion.* **Tanabe, M., Morita, T., Aoki, K., Satoh, K., Fujimori, T., Sato, J.** 2000, Proc. Combustion Inst., Vol. 28, pp. 1007-1013.
12. *Droplet Combustion in Standing Sound Waves.* **Tanabe, M., Kuwahara, T., Satoh, K., Fujimori, T., Sato, J., Kono, M.** 2005, Proc. Combustion Inst., Vol. 30, pp. 1957-1964.
13. *On the Circulation of Air Observed in Kundt's Tubes, and on Some Allied Acoustical Problems.* **Rayleigh, Lord.** 1884, Phil. Trans. Roy. Soc., Vol. 175, pp. 1-21.
14. **Dattarajan, S.** Acoustically Excited Droplet Combustion in Normal Gravity and Microgravity. *Ph. D. Dissertation.* s.l. : Department of Mechanical and Aerospace Engineering, UCLA, 2004.
15. *Acoustic Excitation of Droplet Combustion in Microgravity and Normal Gravity.* **Dattarajan, S., Lutomirski, A., Lobbia, R., Smith, O. I., Karagozian, A. R.** 2006, Comb. and Flame, Vol. 144, pp. 299-317.
16. **Karagozian, A. R., Dahm, W. J. A., Glasgow, E., Howe, R., Kroo, I., Murray, R., Shyu, H.** Technology Options for Improved Air Vehicle Fuel Efficiency. *SAB-TR-06-04.* s.l. : Air Force Scientific Advisory Board Report, May 2006.
17. **Fischer, F.** *The Conversion of Coal.* s.l. : Ernst Benn, Ltd., 1925.
18. **Harrison, W.** OSD Clean Fuel Initiative and Air Force Fuels. December 12, 2005. Presented to the Air Force Scientific Advisory Board.
19. B-52 Flight Uses Synthetic Fuel in All Eight Engines. *Air Force AIM Points.* December 2006. <http://www.af.mil/news/story.asp?storyID=123035568>.

20. **Vingert, L., Gicquel, P., Lourme, D., Ménoret, L.** Coaxial Injector Atomization. [ed.] V., Anderson, W. Yang. *Liquid Rocket Engine Combustion Instability*. s.l. : Progress in Astronautics and Aeronautics, AIAA, 1995, pp. 145-190.
21. *Shear-Coaxial Jets from a Rocket-Like Injector in a Transverse Acoustic Field at High Pressures*. **Davis, D. W., Chehroudi, B.** Reno, NV : s.n., 9-12 Jan 2006. 44th AIAA Aerospace Sciences Meeting & Exhibit.
22. *Dark-Core Analysis of Coaxial Injectors at Sub-, Near-, and Supercritical Conditions in a Transverse Acoustic Field*. **Leyva, I. A., Chehroudi, B., Talley, D.** Cincinnati, OH : s.n., 8-11 Jul. 2007. 43rd AIAA/ASME/SAE/ASEE Joint Propulsion Conference & Exhibit.
23. **Harrje, D. T., Reardon, F. H., [ed.].** *Liquid Propellant Rocket Combustion Instability*. s.l. : NASA, 1972. pp. 17-19. Vols. SP-194.
24. *Critical Lines and Phase Equilibria in Binary van der Waals Mixtures*. **van Konynenburg, P. H., Scott, R. L.** 1980, Phil. Trans. R. Soc. London, Vol. 298, p. 495.
25. *Injection of Fuels into Supercritical Environments*. **Oschwald, M., Smith, J. J., Branam, R., Hussong, J., Schik, A., Chehroudi, B., Talley, D.** 2006, Combust. Sci. and Tech., Vol. 178, pp. 49-100.
26. **Sutton, G. P.** *Rocket Propulsion Elements*. 6th Ed. New York : John Wiley & Sons, Inc., 1992.
27. *Experimental and Computational Investigation of Combustor Acoustics and Instabilities, Part II: Transverse Modes*. **Marshall, W., Pal, S., Woodward, R., Santoro, R. J., Smith, R., Xia, G., Sankaran, V., Merkle, C. L.** Reno, NV : s.n., 9-12 Jan. 2006. 44th AIAA Aerospace Sciences Meeting & Exhibit.
28. *Interactions Between Propellant Jets and Acoustic Modes in Liquid Rocket Engines: Experiments and Simulations*. **Richecoeur, F., Scoufflaire, P., Ducruix, S., Candel,**

- S. Sacramento, CA : s.n., 9-12 Jul. 2006. 42nd AIAA/ASME/SAE/ASEE Joint Propulsion Conference and Exhibit.
29. *Mixing Enhancement in Coaxial Supersonic Jets*. **Gutmark, E., Schadow, K. C., Wilson, K. J.** Buffalo, NY : s.n., 12-14 Jun. 1989. AIAA 20th Fluid Dynamics, Plasma Dynamics and Lasers Conference.
30. *Simulation of Flow and Mixing from a Cryogenic Rocket Injector*. **Gautam, V., Gupta, A. K.** 2007, J. Propul. Power, Vol. 23, pp. 123-130.
31. *A Numerical Study of High-Pressure Oxygen/Methane Mixing and Combustion of a Shear Coaxial Injector*. **Zong, N., Yang, V.** Reno, NV : s.n., 10-13 Jan. 2005. 43rd AIAA Aerospace Sciences Meeting & Exhibit.
32. *The Flow Region Near the Nozzle in Double Concentric Jet*. **Chigier, N. A., Beér, J. M.** 1964, Journal of Basic Engineering, Vol. 86, pp. 797-804.
33. **Romiti, A.** *Fluid Dynamics of Jet Amplifiers*. Udine : Springer-Verlag, 1970.
34. **Reitz, R. D., Bracco, F. V.** Mechanisms of Breakup of Round Liquid Jets. [ed.] N. P. Cheremisinoff. *Encyclopedia of Fluid Mechanics*. 1986, Vol. 3, pp. 233-249.
35. *A Review of Atomization in Liquid Rocket Engines*. **Ghafourian, A., Mahalingam, S., Dindi, H., Daily, J. W.** Reno, NV : s.n., 7-10 Jan. 1991. 29th Aerospace Sciences Meeting.
36. *Liquid Jet Instability and Atomization in a Coaxial Gas Stream*. **Lasheras, J. C., Hopfinger, E. J.** 2000, Annu. Rev. Fluid Mech., Vol. 32, pp. 275-308.
37. **Lin, S. P.** *Breakup of Liquid Sheets and Jets*. Cambridge : Cambridge University Press, 2003.
38. *Atomization Characteristics on the Surface of a Round Liquid Jet*. **Mayer, W. O. H., Branam, R.** 2004, Experiments in Fluids, Vol. 36, pp. 528-539.

39. *Investigation of the Primary Breakup of Round Turbulent Liquid Jets Using LES/VOF Technique.* **Srinivasan, V., Salazar, A., Saito, K.** San Francisco, CA : s.n., 5-8 Jun. 2006. 36th AIAA Fluid Dynamics Conference and Exhibit.
40. *The Effects of Pressure and Acoustic Field on a Cryogenic Coaxial Jet.* **Davis, D. W., Chehroudi, B.** Reno, NV : s.n., 5-8 Jan. 2004. 42nd AIAA Aerospace Sciences Meeting & Exhibit.
41. **Davis, D. W.** On the Behavior of a Shear-Coaxial Jet, Spanning Sub- to Supercritical Pressures, With and Without an Externally Imposed Transverse Acoustic Field. *Ph. D. Dissertation.* s.l. : Department of Mechanical and Nuclear Engineering, Pennsylvania State University, 2006.
42. *On Density Effects and Large Structure in Turbulent Mixing Layers.* **Brown, G., Roshko, A.** 1974, J. Fluid Mech., Vol. 64, p. 775.
43. *Two-Dimensional Shear-Layer Entrainment.* **Dimotakis, P. E.** 1986, AIAA Journal, Vol. 21, p. 1791.
44. *The Compressible Turbulent Shear Layer: An Experimental Study.* **Papamoschou, D., Roshko, A.** 1988, J. Fluid Mech., Vol. 197, p. 453.
45. *Initial Growth Rate and Visual Characteristics of a Round Jet into a Sub- to Supercritical Environment of Relevance to Rocket, Gas Turbine, and Diesel Engines.* **Chehroudi, B., Talley, D., Coy, E.** Reno, NV : s.n., 11-14 Jan. 1999. 37th AIAA Aerospace Sciences Meeting and Exhibit.
46. *Fractal Geometry and Growth Rate Changes of Cryogenic Jets Near the Critical Point.* **Chehroudi, B., Talley, D., Coy, E.** Los Angeles, CA : s.n., 20-24 Jun. 1999. 35th AIAA/ASME/SAE/ASEE Joint Propulsion Conference & Exhibit.
47. *Characterization of Cryogenic Injection at Supercritical Pressure.* **Mayer, W., Telaar, J., Branam, R., Schneider, G.** Salt Lake City, UT : s.n., 9-11 Jul. 2001. 37th AIAA/ASME/ASEE Joint Propulsion Conference and Exhibit.

48. *Fluid Dynamics and Diffusion Calculation for Laminar Liquid Jets*. **Scriven, L. E., Pigford, R. L.** 1959, AIChE Journal, Vol. 5, pp. 397-402.
49. *Convective and Absolute Instability of a Viscous Liquid Jet*. **Leib, S. J., Goldstein, M. E.** 1986, Phys. Fluids, Vol. 29, pp. 952-954.
50. *Local and Global Instabilities in Spatially Developing Flows*. **Huerre, P., Monkewitz, P. A.** 1990, Annu. Rev. Fluid Mech., Vol. 22, pp. 473-537.
51. **Raynal, L.** Instabilité et entraînement à l'interface d'une couche de mélange liquide-gaz. *Thèse de Doctorat*. Grenoble : Université Joseph Fourier, 1997.
52. *Linear Stability of a Compressible Coaxial Jet with Continuous Velocity and Temperature Profiles*. **Perrault-Joncas, D., Maslowe, S. A.** 2008, Phys. Fluids, Vol. 20.
53. **Heidmann, M. F.** *Oxygen Jet Behavior During Combustion Instability*. NASA. 1965. TN D-2725.
54. *The Effect of Ambient Pressure Oscillations on The Disintegration and Dispersion of a Liquid Jet*. **Miesse, C. C.** 1955, Jet Propulsion, Vol. 25, pp. 525-530, 534.
55. *Response of Turbulent Liquid Jets to Transverse Acoustic Fields*. **Buffum, F. G., Williams, F. A.** 1967. Heat Transfer and Fluid Mechanics Institute. pp. 247-276.
56. *Cryogenic Shear Layers: Experiments and Initial Growth Rates of Round Cryogenic Jets at Subcritical and Supercritical Pressures*. **Chehrودي, B., Cohn, R., Talley, D. G.** 2002, International Journal of Heat and Fluid Flow, Vol. 23, pp. 554-563.
57. *Acoustically Driven Droplet Combustion with Alternative Liquid Fuels*. **Rodriguez, J., Teshome, S., Mao, H.-S., Pezeshkian, A., Smith, O. I., Karagozian, A. R.** Reno, NV : s.n., 2008. 46th AIAA Aerospace Sciences Meeting and Exhibit.
58. *Effects of Flow Transients on the Burning Velocity of Laminar Hydrogen/Air Premixed Flames*. **Im, H. G., Chen, J. H.** 2000. Proc. Combustion Inst. Vol. 28, pp. 1833-1840.

59. *REFPROP, Reference Fluid Thermodynamic and Transport Properties*. [Software Package] Ver. 7.0, Gaithersburg, MD : NIST, U. S. Department of Commerce, 2002.
60. *Thermophysical Properties of Fluid Systems*. [Online] NIST, U. S. Department of Commerce, 2005. <http://webbook.nist.gov/chemistry/fluid>.
61. *A Threshold Selection Method from Gray-Level Histograms*. **Otsu, N.** 1, 1979, IEEE Transactions on Systems, Man and Cybernetics, Vol. 9, pp. 62-66.
62. **Taylor, J. R.** *An Introduction to Error Analysis*. Mill Valley : University Science Books, 1982.
63. **Coleman, H. W., Steele, Jr., W. G.** *Experimentation and Uncertainty Analysis for Engineers*. s.l. : Wiley Interscience, 1989.
64. *The Density Field of Coaxial Jets with Large Velocity Ratio and Large Density Differences*. **Favre-Marinet, M., Camano Schettini, E. B.** 2001, Int. J. of Heat and Mass Transfer, Vol. 44, pp. 1913-1924.
65. *Dynamics of Shear-Coaxial Cryogenic Nitrogen Jets with Acoustic Excitation under Supercritical Conditions*. **Liu, T., Zong, N., Yang, V.** Reno, NV : s.n., 9-12 Jan. 2006. 44th AIAA Aerospace Sciences Meeting and Exhibit.
66. *Influence of Standing Acoustic Waves on Combustion of Alternative Fuels*. **Teshome, S., Pezeshkian, A., Smith, O., Karagozian, A.** San Antonio, TX : s.n., 23–25 Nov., 2008. 61st Annual Meeting of the APS Division of Fluid Dynamics.